# University of Technology of Troyes

**Light, Nanomaterials, Nanotechnologies (L2n)**

**Speciality: Materials, Mechanics, Optics and Nanotechnologies**

*In cotutelle with*

# Eberhard Karls University of Tübingen

**Institute for Applied Physics**

**Speciality: Physics**

Thesis presented for obtention of the Title Ph.D.

## Wei TAO

# Active Tuning of LSPR and SLR for Au Nanoring Metasurfaces and Hybrids via Flexible Plasmonics

## Jury

| | | |
|---|---|---|
| M. FINOT Eric | Professeur des Universités | Reviewer |
| Ms. STAUDE Isabelle | Professorin | Reviewer |
| M. ADAM Pierre-Michel | Professeur des Universités | Examiner |
| M. MEIXNER Alfred J. | Professor | Examiner |
| M. MAURER Thomas | Professeur des Universités | Supervisor |
| Ms. FLEISCHER Monika | Professorin | Supervisor |

# Active Tuning of LSPR and SLR for Au Nanoring Metasurfaces and Hybrids via Flexible Plasmonics

**Dissertation**

der Mathematisch-Naturwissenschaftlichen Fakultät

der Eberhard Karls Universität Tübingen

zur Erlangung des Grades eines

Doktors der Naturwissenschaften

(Dr. rer. nat.)

vorgelegt von

Wei Tao

aus Hefei/China

Tübingen

2023

# Acknowledgments

# Abstract

Recent advances in nanofabrication have stimulated research efforts in the field of flexible plasmonics by integrating functional metasurfaces onto mechanically flexible substrates. In this thesis, we report on the fabrication of flexible metasurfaces composed of gold regular and elliptical nanoring arrays embedded in polydimethylsiloxane (PDMS), using state-of-the-art electron beam lithography and wet-etching transfer techniques. In-situ dark-field reflection spectra are monitored on the flexible systems by implementing a homemade micro-stretcher inside the spectroscope. The feasibility of pattern transfer and reliability of optical measurement are further confirmed by subsequent SEM characterizations on PDMS. The spectral behavior of thin-width nanoring square arrays exhibits a significant shift towards longer wavelengths due to in-situ shape changes under strain. The shape-altering ability is carefully demonstrated through optical/SEM measurements and numerical simulations, which is further understood by a purposed squeezing mechanism. On the other hand, the spectral evolution of elliptical nanorings in square and triangular arrays presents interesting polarization dependence and spectral blueshift under strain. The square array subjected to high strain values exhibits also surface lattice resonances with Fano features due to the coupling between the grating and plasmonic modes. Additionally, we demonstrate Fano resonances in ring-disc-pair hybrid systems on a rigid substrate. The ring-disc-pair system shows significantly enhanced Fano features and surface-enhanced Raman signals with a decreasing gap, predicting well an active spectral tuning once they are transferred onto flexible substrates in future work. In general, this thesis expands the possibilities of conventional gap-altering flexible plasmonics by investigating plasmonic spectral shifts corresponding to NPs shape-altering, surface lattice resonances, and Fano coupling under strain. It provides valuable insights into strain sensing, flexible color displays, and wearable electronics with high sensitivity and selectivity.

**Keywords:** Plasmons (physics), gold nanoparticles, polydimethylsiloxane, lithography, electron beam, optical properties

# Résumé

Les récents progrès en nanofabrication ont stimulé les efforts de recherche dans le domaine de la plasmonique flexible en intégrant des métasurfaces fonctionnelles sur des substrats mécaniquement flexibles. Dans cette thèse, nous rendons compte de la fabrication de métasurfaces flexibles composées de réseaux de nano-anneaux réguliers et elliptiques en or incorporés dans du polydiméthylsiloxane (PDMS), en utilisant des techniques de lithographie électronique à faisceau d'électrons de pointe et de transfert par gravure humide. Les spectres de réflexion en champ sombre in-situ sont obtenus à partir d'un dispositif optique maison intégrant une micromachine de traction. La faisabilité du transfert de motifs et la fiabilité des mesures optiques sont ensuite confirmées par des caractérisations ultérieures effectuées avec un microscope électronique à balayage (MEB) sur le PDMS. Le comportement spectral des réseaux carrés de nano-anneaux de faible largeur présente un décalage significatif vers des longueurs d'onde plus longues en raison des changements de forme induits in-situ sous contrainte. Les déformations des nanostructures sont alors mises en évidence par la confrontation entre mesures optiques/MEB et simulations numériques. D'autre part, l'évolution spectrale des nano-anneaux elliptiques dans des réseaux carrés et triangulaires présente une dépendance intéressante à la polarisation et un décalage spectral vers le bleu sous contrainte. Le réseau carré soumis à des valeurs élevées de contrainte présente également des résonances de réseau de surface avec des caractéristiques Fano en raison du couplage entre le réseau et les modes plasmoniques. En outre, nous mettons en évidence des résonances de Fano dans des systèmes hybrides de paires d' anneaux et de disques sur un substrat rigide. Le système de paires d'anneaux et de disques présente des caractéristiques de Fano considérablement améliorées et des signaux de Raman amplifiés en surface avec un espacement décroissant, prévoyant ainsi une réponse spectrale active une fois qu'ils seront transférés sur des substrats flexibles dans des travaux futurs. De manière générale, cette thèse élargit les possibilités de transfert technologique de la plasmonique flexible. Elle fournit des connaissances précieuses sur la détection de contraintes, les affichages couleur flexibles et l'électronique portable à haute sensibilité et sélectivité.

**Mots-clés**: Plasmons, nanoparticules d'or, diméticone, lithographie par faisceau d'électrons, propriétés optiques

# Zusammenfassung

Die jüngsten Fortschritte in der Nanofertigung haben Forschungsanstrengungen im Bereich der flexiblen Plasmonik angeregt, indem funktionale Metasurfaces auf mechanisch flexible Substrate integriert wurden. In dieser Arbeit berichten wir über die Herstellung flexibler Metasurfaces, die aus regelmäßigen und elliptischen Nanoring-Arrays aus Gold bestehen, die in Polydimethylsiloxan (PDMS) eingebettet sind. Hierfür wurden hochmoderne Elektronenstrahllithographie- und Nassätztechniken verwendet. In-situ-Dunkelfeld-Reflexionsspektren werden auf den flexiblen Systemen über einen selbstgebauten Mikro-Streckapparat im Spektrometer überwacht. Die Machbarkeit des Mustertransfers und die Zuverlässigkeit der optischen Messungen werden durch nachfolgende SEM-Charakterisierungen an PDMS weiter bestätigt. Das spektrale Verhalten von quadratischen dünnen Nanoring-Arrays zeigt aufgrund von in-situ-Formänderungen unter Belastung eine signifikante Verschiebung zu längeren Wellenlängen. Die Fähigkeit zur Formänderung wird durch optische/SEM-Messungen und numerische Simulationen sorgfältig demonstriert und durch einen vorgeschlagenen Kompressionsmechanismus weiter verstanden. Andererseits zeigt die spektrale Entwicklung elliptischer Nanoringe in quadratischen und dreieckigen Arrays eine interessante Polarisationsabhängigkeit und einen spektralen Blauverschiebungseffekt unter Zugspannung. Das quadratische Array bei hohen Dehnungswerten zeigt auch eine Fano-Kopplung aufgrund der Hybridisierung zwischen verschiedenen Oberflächen-Gitterresonanzen. Zusätzlich zeigen wir Fano-Resonanzen in Ring-Scheiben-Paar-Hybridsystemen auf einem starren Substrat. Das Ring-Scheiben-Paar-System zeigt deutlich verbesserte Fano-Merkmale und oberflächenverstärkte Raman-Signale bei abnehmendem Spalt, was eine aktive spektrale Abstimmung in zukünftigen Arbeiten auf flexiblen Substraten erwarten lässt. Insgesamt erweitert diese Arbeit die Möglichkeiten der konventionellen flexiblen Plasmonik mt variablen Lücken, indem sie plasmonische spektrale Verschiebungen untersucht, die mit der Veränderung der Form von Nanopartikeln, Oberflächen-Gitterresonanzen und Fano-Kopplung unter Dehnung zusammenhängen. Sie liefert wertvolle Erkenntnisse für die Spannungsmessung, flexible Farbdisplays und tragbare Elektronik mit hoher Empfindlichkeit und Selektivität.

**Schlüsselwörter**: Plasmonen, Goldnanopartikel, Polydimethylsiloxan, Lithografie,

Elektronenstrahl, optische Eigenschaften

# Contents

# Nomenclature

| | |
|---|---|
| PDMS | polydimethylsiloxane |
| NP | Nanoparticle |
| LSPR | Localized Surface Plasmonic Resonance |
| SPP | Surface Plasmon Polaritons |
| FDTD | Finite-Difference Time-Domain |
| CDA | Coupled dipole approximation |
| FEM | Finite element method |
| EBL | Electron beam lithography |
| Au | gold |
| NR | nanoring |
| SEM | Scanning Electron Microscopy |
| SLR | Surface Lattice Resonance |
| PET | polyethylene terephthalate |
| AFM | Atomic Force Microscopy |
| Si | silicon |
| Cr | chromium |
| ENR | elliptical nanoring |
| SERS | surface-enhanced Raman scattering |
| ITO | indium tin oxide |
| CNRS | *Centre national de la recherche scientifique* |
| CTP | charge transfer plasmon |
| PH | plasmonic hybridization |
| NCRDC | nonconcentric ring-disk cavity |
| WRA | Wood-Rayleigh Anomaly |
| EOT | extraordinary optical transmission |
| IPA | isopropanol |
| PMMA | Poly-methyl methacrylate |
| MIBK | methyl isobutyl ketone |
| MPTS | (3-Mercaptopropyl) triethoxysilane |
| R6G | Rhodamine 6G |
| NA | numerical aperture |
| TFSF | total-field scattered-field |
| PML | perfectly matched layer |

| | |
|---|---|
| TP | transverse polarization |
| LP | longitudinal polarization |
| AR | aspect ratio |
| BFAST | Broadband Fixed Angle Source Technique |
| RDC | ring-disc cavities |
| RDP | ring-disc pair |
| FoM | figure of merit |
| CR | contrast ratio |

# Chapter 1 Introduction

As a young branch in optics, plasmonics studies the light-excited collective oscillations of free electrons localized at the surface of sub-wavelength metallic nanoparticles (NPs) or electromagnetic waves propagating at a dielectric-metal interface, namely Localized Surface Plasmonic Resonances (LSPRs), [1-5] and Surface Plasmon Polaritons (SPPs). [6-10] The application of LSPRs can be traced back to stained glass in Roman times, yet only recently there has been a scientific understanding of how impurities such as gold and cobalt suspended in glass play a role in plasmonic color displaying. Historically speaking, the discovery of the electron in 1897 spurred the study of its electrodynamic behavior in materials, [11] which established a theoretical basis for plasmonics. Early work may include but is not limited to the mathematical description of surface wave functions propagating on metal surfaces by Sommerfeld in 1899, [12] and the Mie theory of absorption by gold nanospheres excited by plane wave incidence in 1908. [13] After half a century of development, pioneers Pines and Bohm in 1952 for the first time described the collective behavior of electron gas as "plasma" oscillations. [14] Since then, the concept of plasmonic resonance regarding collective electron oscillation was widely accepted in the 1960s and 1970s. [15-18] The late decades of the last century witnessed rapid growth in plasmonics in various fields. Electron microscopy and surface-sensitive spectroscopy have enabled researchers to explore an experimental verification of the behaviors of surface plasmons at the nanoscale. [19-23] Numerical methods, such as Finite-Difference Time-Domain (FDTD), [24-27] Coupled Dipole Approximation (CDA), [28-29] and Finite Element Method (FEM), [30-31] have also emerged as versatile techniques to not only calculate the dispersion relations of surface plasmons but also to design plasmonic devices for applications in sensing, [32-34] imaging, [35] solar energy, [36] and nanoscale electronics. [37]

Fast forward to today, state-of-the-art nanofabrication of LSPR structures has made significant advances, utilizing both bottom-up colloidal self-assembly, [38-39] and top-down methods such as optical tweezers, [40-41] ion beam milling, [42-43] and electron beam lithography (EBL). [44-46] These fabrication techniques, combined with numerical simulations, allow for precise geometric control of plasmonic NPs and a comprehensive understanding of both near-field enhancement and far-field properties depending on the medium refractive index, [47] NP compositions, [48] geometric sizes, [49]

and particularly their shapes. [50-53] Figure 1-1 depicts gold nanorings (Au NRs) fabricated through top-down lithography and bottom-up colloidal synthesis in response to advanced fabrication techniques. Compared with the dipolar momentum for traditional plasmonic nanospheres, [50] nanorods or NRs with a long aspect ratio of length/perimeter to width exhibit complex multipolar LSPR modes spanning the visible and mid-infrared region when excited with linear polarization. [52-53] Furthermore, the inherent symmetry and hollow feature enable NRs of uniform near-field enhancement in the cavity, [54] lower plasmon damping effects, [55] and relatively high refractive index sensitivities, [56] giving a strong interest in sensing applications. [57] Additionally, NRs can be easily integrated with other nanophotonic structures such as waveguides and resonators to achieve sharp Fano resonances and realize more complex functionalities. [58-62]
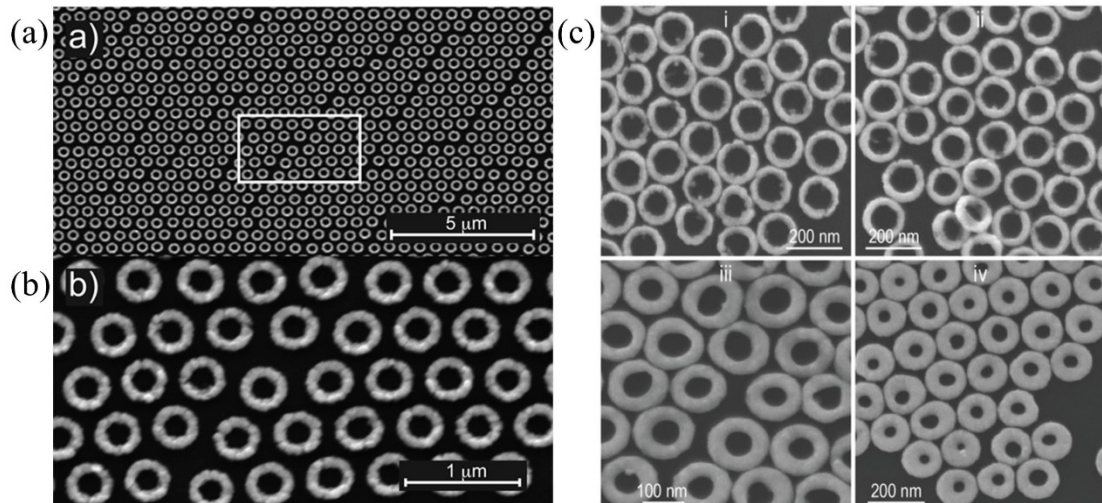


Figure 1-1 Scanning Electron Microscopy (SEM) images of Au NRs fabricated via top-down nanosphere lithography (a-b), and bottom-up colloidal synthesis (c). Figures (a-b) and (c) are adapted from Ref [[63-64]].

Given advances in nanofabrication, another research focus lies in plasmonic metasurfaces consisting of 2D gratings of subwavelength-thick resonators. [65-68] In contrast to single plasmonic NPs, a grating of resonators supports a strong coupling between the LSPR of individual NPs and their diffraction mode, [69-71] and the resulting Surface Lattice Resonance (SLR) exhibits more dominant near-field enhancement and ultra-narrow features in the far-field spectrum. [72-73] Consequently, metasurfaces have shown remarkable advantages in different areas, such as quantum plasmonics, [74] nonlinear optics, [75] ultra-thin lenses, [76] and bio-medical sciences. [77] Jung et al. provide a comprehensive overview of plasmonic metasurfaces in terms of their types and

optical properties, [66] as depicted schematically in Figure 1-2. These versatile metasurfaces range from dielectric Mie scatterers to metallic antennas and nanohole arrays, with advantages in manipulating the far-field spectrum, phase delay, bandwidth, nonlinear coefficients, etc.
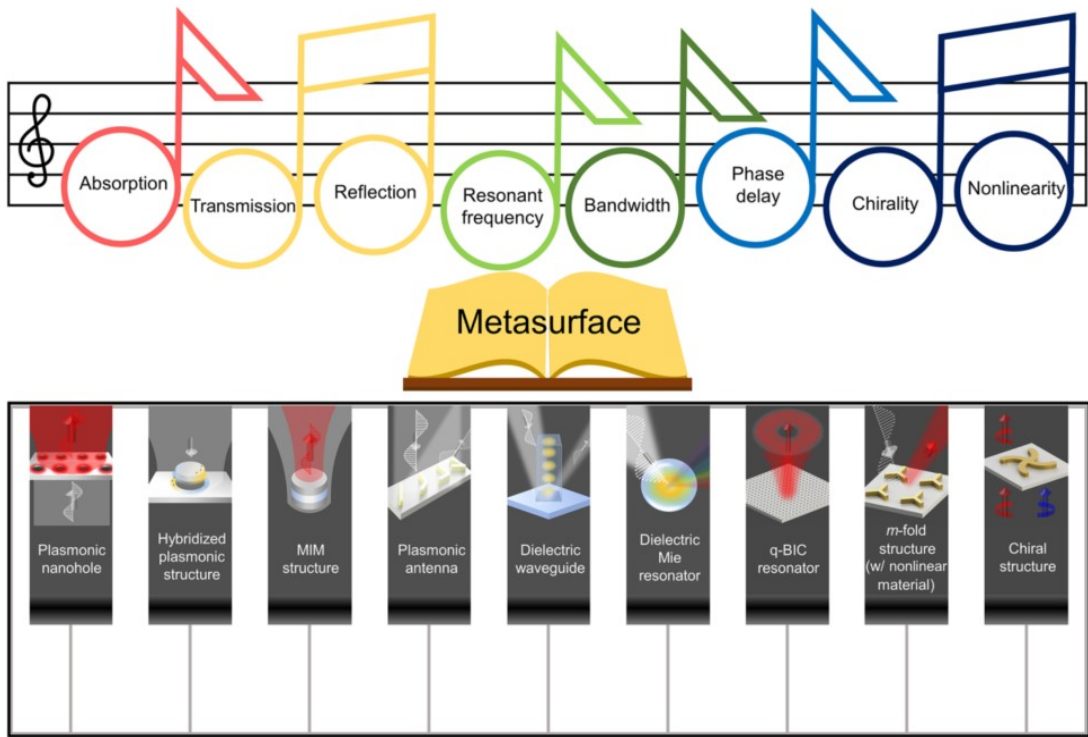


Figure 1-2 Schematic diagram of diversity and optical functionality of metasurfaces. The figure is adapted from Ref [[66]]

However, conventional metasurfaces are usually designed on planar and rigid substrates, which limits the potential applications in biomedicine, wearable technology, and flexible electronics. Recently, the demand to actively control optical properties through macroscopic stimuli (e.g., light, heat, electricity, chemistry and mechanics) has motivated research on flexible metasurfaces. [78-82] Fu et al. published a nice review concerning the fabrication, characterization, multi-functional property, and potential application of soft plasmonic systems, [83] as schematically shown in Figure 1-3. The field of flexible plasmonics studies the dynamic optical response of plasmonic NPs under mechanical bending, twisting, and stretching, by integrating them onto flexible substrates such as polydimethylsiloxane (PDMS), [84-85] polyethylene terephthalate (PET), [86] and liquid crystals. [87] Among them, PDMS is widely used because of its good optical transparency, mechanical ductility, and bio/chemical compatibility. [88] However, due to the charge accumulation effect on the

dielectric surfaces of flexible substrates, most top-down fabrication methods such as EBL are not feasible. [85] Consequently, recent literature has explored various pattern transfer techniques on different substrates, where the geometry of the metasurface is well-controlled by initial photolithography or colloidal synthesis. [89-92] Examples of these techniques include the peeling-off approach reported by Du et al., [91] which transfers lithography-fabricated Au gratings from silicon to PDMS. Similarly, Tseng et al. presented an approach aimed at transferring aluminum metasurfaces. [92] Such methods also enable NPs fabrication on the stretched/wavy surfaces of PDMS by exploiting its elasticity during the modeling process. [53, 93]
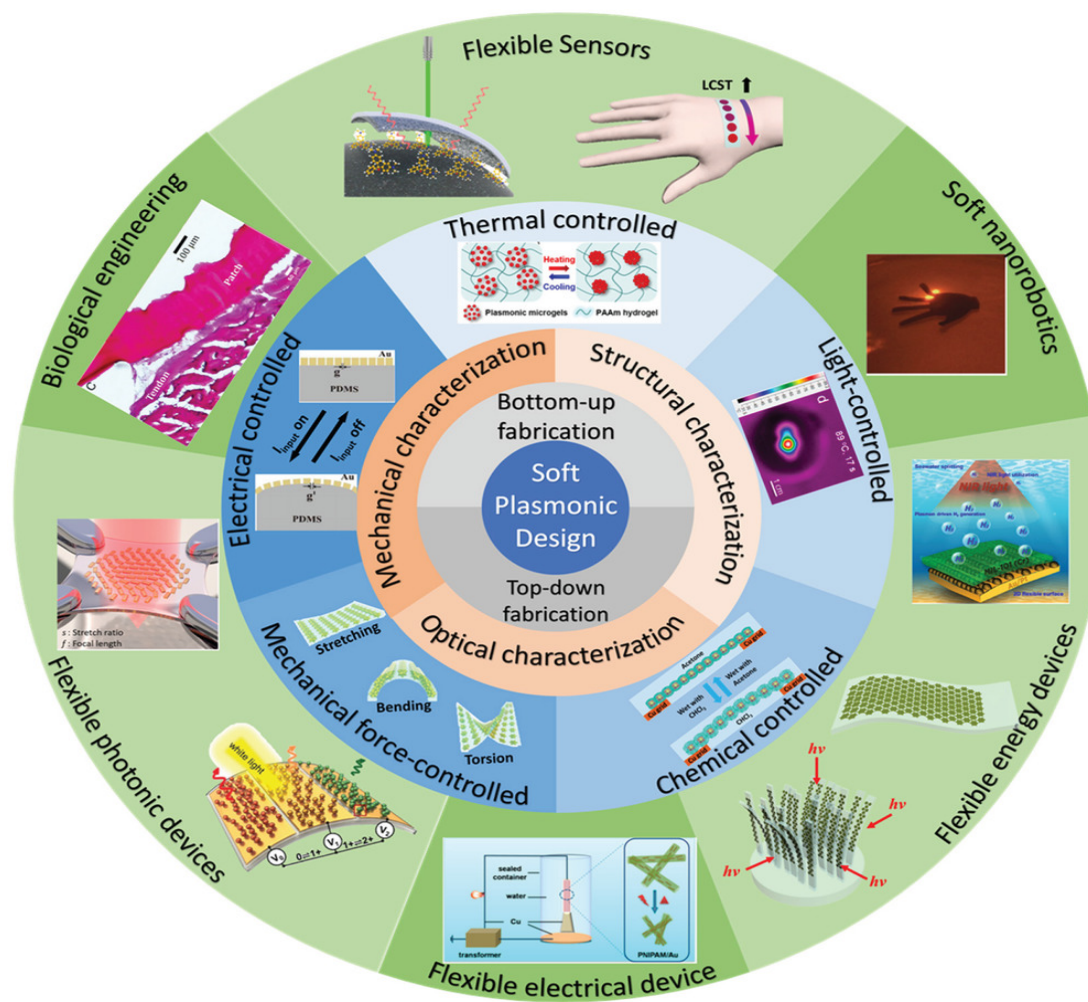


Figure 1-3 Schematic diagram of soft plasmonic systems in terms of fabrication, characterization, mechanoplasmonic property, and application. The figure is adapted from Ref [83].

The principle of flexible plasmonics is based on modifying the spacing between adjacent NPs through mechanical stimuli, so as to monitor the plasmonic coupling in the direction of the nanogap. [70] Figure 1-4 (a) illustrates dipolar-dipolar or gap-mode coupling between two spherical NPs depending on the gap and geometric radius variations. Changes in near-field coupling also result in spectral shifts in the far-field spectrum, such as absorption, transmission, and extinction. For example, with applied uniaxial strain, the gap between the NPs in the dimer system that is parallel to the stretching will increase, leading to a weakening near-field coupling and a redshifting far-field spectrum under a perpendicular polarization. [94] In this context, extensive literature has reported studies on the strain-induced spectral evolution of gap-altering flexible plasmonics, including randomly distributed NPs, [95] 1D linear, [96] 2D square, [80] and 2D triangular metasurfaces, [79] as shown in Figures 1-4 (b-e), respectively. All these samples exhibit clear LSPR spectral shifts, while Figure 1-4 (c) shows also SLR shifts due to the controlled geometry. However, conventional gap-altering flexible plasmonics represented by these systems still have limitations, such as ineffective control over NP size/regularity, isotropic shapes of most NPs, and exclusive consideration of strain-induced spacing changes without accounting for NPs' shape variations. Therefore, recent literature also explores the possibilities of flexible plasmonics by investigating the manipulation of solid nanoparticle shapes, such as spheres and triangles, [85, 97] along with the modification of refractive indices under mechanical compression and stretching. [98-99]
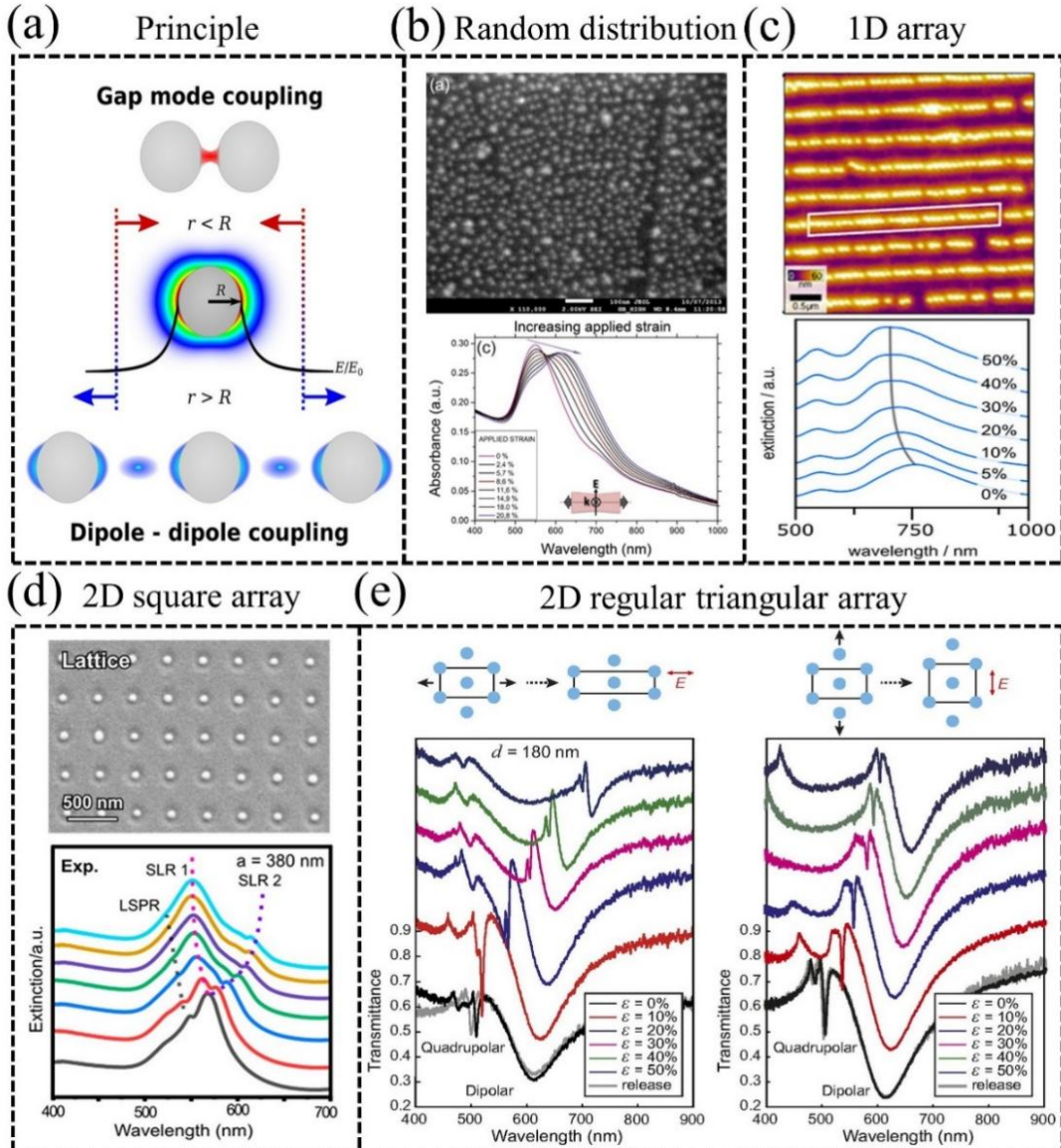
Figure 1-4 Conventional gap-altering flexible plasmonics. (a) The principle of plasmonic coupling between two spherical NPs along the gap direction; (b) SEM image and absorption spectra of randomly distributed NPs on PDMS; (c) Atomic Force Microscopy (AFM) image and extinction spectra of 1D NP array on PDMS; (d) SEM images and extinction spectra of 2D square NP array on PDMS; and (e) transmission spectra under horizontal and perpendicular polarizations of 2D regular triangular NP array on PDMS. The figure is adapted from Ref [70, 79-80, 95-96].

Herein, this thesis presents a method for fabricating flexible metasurfaces by adopting EBL on a rigid silicon (Si) substrate coated with a sacrificial chromium (Cr) layer, followed by a wet-etching transfer onto PDMS. Compared with the peeling-off method mentioned above, this state-of-the-art technique offers a more universal

approach to transfer any ordered 2D pattern. After fabrication, the PDMS sample is subjected to uniaxial stretching, and dark-field reflection spectra of the transferred patterns are measured in situ. The quality of transfer and reliability of optical measurements are confirmed via subsequent SEM tests on PDMS. In contrast to conventional gap-sensitive flexible metasurfaces composed of solid/isotropic NPs, the thesis focuses on studying the strain-induced optical response of Au NR arrays, anisotropic elliptical nanoring (ENR) arrays, and ring-disc hybrid systems. By monitoring the distinguished LSPR spectral shifts under NR shape-altering, SLRs, and Fano coupling under strain, we aim to pave a new path in the field of flexible plasmonics. The organization of this thesis is as follows.

In the first two chapters, we present a general introduction and theoretical framework of the thesis. Chapter 2 systematically illustrates the optical responses of single, pair, and grating configurations of NPs. The size, gap, and polarization dependences in these systems are discussed in response to strain-induced parameter variations via flexible plasmonics.

Chapter 3 presents the experimental methods and setups. The fabrications concerning EBL and transfer techniques are briefly introduced. Optical setups involving dark-field reflection/transmission spectrometers and surface-enhanced Raman scattering (SERS) instruments and SEM tests are also discussed. The grating strain and simulation conditions are also elaborated in this chapter.

Chapters 4 and 5 experimentally explore the potential for flexible plasmonics in different efforts. By fabricating a square NR array with thin width, Chapter 4 demonstrates a shape-altering NR metasurface on PDMS with a strong spectral redshift under strain. Chapter 5 discusses the strain-induced spectral evolution of LSPR and SLR signals of both square and regular triangular ENR arrays. The dependence on polarization and grating distribution is carefully illustrated.

Chapter 6 focuses on the Fano coupling in a ring/disc hybrid system. Despite the transmission spectra being monitored on a rigid glass/indium tin oxide (glass/ITO) substrate, the strong gap-dependent Fano coupling and SERS enhancements predict a strong spectral guiding on PDMS in future work.

Finally, in the last Chapter 7, we conclude the thesis work and provide an outlook on future work.

# Chapter 2 Theoretical Foundations

In this chapter, we review the theoretical foundations for the localized surface plasmons of sub-wavelength particles of varying dimensions and distributions. More detailed mathematical descriptions concerning electrodynamics can be found in Ref [100-102]. To start with, we introduce two common approximations, i.e., the quasi-static approximation and Mie theory, to describe the optical modes of the single particle reaching resonance conditions. We then proceed to explain the plasmonic coupling in the near- and far-field regimes for a combined dimer system. The geometry and polarization dependence, as well as the plasmonic ruler equation, are systematically reviewed. Furthermore, we provide an overview of Fano coupling in plasmonic hybrid structures, e.g., nanoring-disc cavities, and explain the underlying reason involving near-field hybridization and far-field spectral interference. When these individual nanoparticles are distributed in a lattice, the emerging grating modes, such as Wood-Rayleigh Anomalies and Surface Lattice Resonance, are subsequently described.

## 2.1. Optical modes for single sub-wavelength particles

### 2.1.1 Quasi-static approximation

The quasi-static approximation describes the optical response of an isotropic nanosphere that is significantly smaller in size than the incident wavelength (usually of a scale of ~nm) and embedded in a uniform medium. [103-105] The model is schematically depicted in Figure 2-1. The quasi-static approximation relies on several assumptions: the electric field impinging on the entire nanosphere remains constant without any spatial variations, and all multi-polar modes higher than the dipolar are neglected. The dielectric constants of the medium and sphere are namely $\varepsilon_d$ and $\varepsilon_s$. The scattered light is observed at the point of $P\ (r,\ \theta)$.
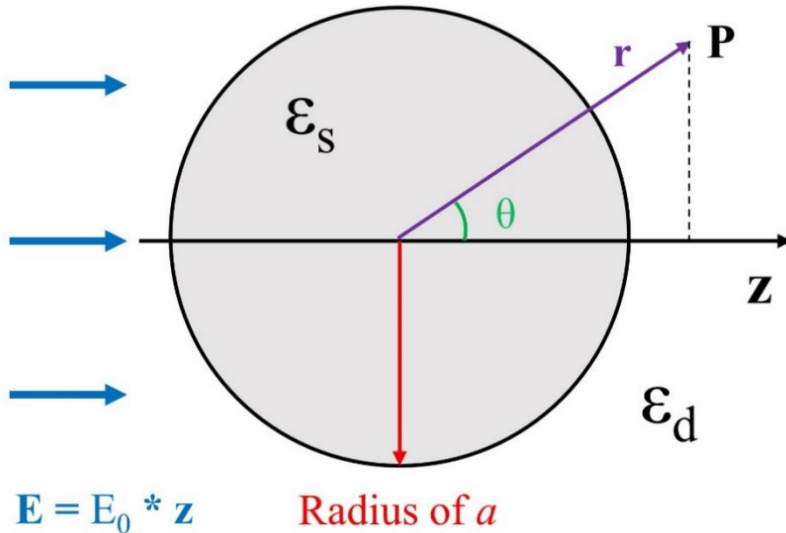
Figure 2-1. A simplified 2D spherical model of an isotropic nanosphere embedded in a uniform dielectric medium.

We start by giving the *Laplace Equation* for the potential $\Phi$ as there is no charge density $(\rho = 0)$ in this approach,

$$\nabla^2 \Phi = -\frac{\rho}{\varepsilon_0} = 0 \tag{2-1}$$

Such an equation in 3D spherical coordinates (r, θ, φ) can be written as

$$\frac{1}{r}\frac{\partial^2}{\partial r^2}(r\Phi) + \frac{1}{r^2 \sin\theta}\frac{\partial}{\partial\theta}\left(\sin\theta\frac{\partial\Phi}{\partial\theta}\right) + \frac{1}{r^2 \sin^2\theta}\frac{\partial^2\Phi}{\partial^2\varphi} = 0 \tag{2-2}$$

The azimuthal symmetry of the homogeneous nanosphere enables simplified 2D coordinates (r, θ), and thus general solutions considering potentials inside and outside the nanosphere ($\Phi_{in}$ and $\Phi_{out}$) read

$$\Phi_{in}(r,\theta) = \sum_{l=0}^{\infty} A_l r^l P_l(\cos\theta) \tag{2-3}$$

$$\Phi_{out}(r,\theta) = \sum_{l=0}^{\infty}\left[ B_l r^l + C_l r^{-(l+1)} \right] P_l(\cos\theta) \tag{2-4}$$

where $\theta$ is the angle between the position vector and the horizontal axis, and $P_l(\cos\theta)$ are the Legendre Polynomials of order $l$. The external potential in Equation (2-4) follows the form of $\Phi_{out} = \Phi_0 + \Phi_{scat}$, indicating the potentials from the incoming and nanosphere's scattering part.

We now apply two boundary conditions to Equations (2-3) and (2-4), namely, that the external potential is equal to the background potential at infinity ($r \to \infty$), and that the differential of the internal and external potentials in the normal and tangential directions should also be equal at the nanosphere's surface ($r = a$)

$$\lim_{r \to \infty} \left\{ \sum_{l=0}^{\infty} \left[ B_l r^l + C_l r^{-(l+1)} \right] P_l (\cos \theta) \right\} = \lim_{r \to \infty} \left( -E_0 r \cos \theta \right) \tag{2-5}$$

$$\frac{\partial}{\partial \theta} \left[ \sum_{l=0}^{\infty} A_l r^l P_l (\cos \theta) \right] \Bigg|_{r=a} = \frac{\partial}{\partial \theta} \left\{ \sum_{l=0}^{\infty} \left[ B_l r^l + C_l r^{-(l+1)} \right] P_l (\cos \theta) \right\} \Bigg|_{r=a} \tag{2-6}$$

$$\varepsilon_s \frac{\partial}{\partial r} \left[ \sum_{l=0}^{\infty} A_l r^l P_l (\cos \theta) \right] \Bigg|_{r=a} = \varepsilon_d \frac{\partial}{\partial r} \left\{ \sum_{l=0}^{\infty} \left[ B_l r^l + C_l r^{-(l+1)} \right] P_l (\cos \theta) \right\} \Bigg|_{r=a} \tag{2-7}$$

Here, one can directly calculate the coefficients of $B_1 = -E_0$ and $A_l = B_l = C_l = 0$

for $l \neq 1$. By connecting the remaining $A_1$ and $B_1$ with Equations (2-3) and (2-4), the two potentials are obtained as

$$\Phi_{in} = -\frac{3\varepsilon_d}{\varepsilon_s + 2\varepsilon_d} r E_0 \cos \theta \tag{2-8}$$

$$\Phi_{out} = -r E_0 \cos \theta + \frac{\varepsilon_s - \varepsilon_d}{\varepsilon_s + 2\varepsilon_d} \frac{a^3}{r^2} E_0 \cos \theta = -r E_0 \cos \theta + \frac{\mathbf{p} \cdot \mathbf{r}}{4\pi \varepsilon_s \varepsilon_d r^3} \tag{2-9}$$

$$\text{with} \quad \mathbf{p} = 4\pi \varepsilon_s \varepsilon_d a^3 \frac{\varepsilon_s - \varepsilon_d}{\varepsilon_s + 2\varepsilon_d} \mathbf{E_0} \tag{2-10}$$

The nanosphere's scattering part of the external potential can be also described with the dipolar moment $\mathbf{p}$ as

$$\frac{\varepsilon_s - \varepsilon_d}{\varepsilon_s + 2\varepsilon_d} \frac{a^3}{r^2} E_0 \cos \theta = \frac{\mathbf{p} \cdot \mathbf{r}}{4\pi \varepsilon_0 \varepsilon_d r^3} \tag{2-11}$$

Since the polarizability $\alpha$ to the dipolar moment $\mathbf{p}$ reads

$$\mathbf{p} = \varepsilon_0 \varepsilon_d \alpha \mathbf{E_0} \tag{2-12}$$

the dipolar polarizability is then simplified as

$$\alpha = 4\pi a^3 \frac{\varepsilon_s - \varepsilon_d}{\varepsilon_s + 2\varepsilon_d} \tag{2-13}$$

Thus, in the quasi-static approximation, the absorption cross section $\sigma_{abs}$ of the

nanosphere can be derived from Poynting's theorem, and the scattering cross section $\sigma_{scat}$ can be defined by the ratio of total radiated power of the dipole $P$ to the intensity of the exciting wave $I$, where

$$P = \frac{\omega^4 |\mathbf{p}|^2}{12\pi\varepsilon_0\varepsilon_d^3} \tag{2-14}$$

$$I = \frac{1}{2}c\varepsilon_0\varepsilon_d E_0^2 \tag{2-15}$$

By connecting Equation (2-13) to (2-15) with the wave vector $k = \dfrac{2\pi}{\lambda} = \dfrac{\omega}{c}$, we finally arrive at

$$\sigma_{abs} = \frac{\omega}{c}\operatorname{Im}[\alpha] = 4\pi k a^3 \operatorname{Im}\left[\frac{\varepsilon_s - \varepsilon_d}{\varepsilon_s + 2\varepsilon_d}\right] \tag{2-16}$$

$$\sigma_{scat} = \frac{P}{I} = \frac{8\pi}{3}k^4 a^6 \left|\frac{\varepsilon_s - \varepsilon_d}{\varepsilon_s + 2\varepsilon_d}\right|^2 \tag{2-17}$$

Due to the different scale factors between $\sigma_{abs} \propto a^3$ and $\sigma_{scat} \propto a^6$, it is reasonable that the absorption of smaller particles dominates over the scattering. Since we have not assumed a metallic sphere, the quasi-static approximation is also valid for dielectric nanospheres.

### 2.1.2 Mie Theory

As the size of the nanosphere increases, e.g., to a scale of the wavelength, the quasi-static approximation is no longer valid due to the enhanced phase changes of the driving field over the sphere's volume. In 1908, Gustav Mie by solving Maxwell's equations obtained a strict solution of elastic scattering by a homogeneous sphere in spherical coordinates (r, θ, φ). [13] In the *Mie theory*, a few assumptions are made, i.e., a plane wave propagates toward the positive z-axis with the wavelength of $\lambda$ and electric field parallel to the x-axis; and the scattered light comes from an isotropic homogeneous sphere located at (0, 0, 0), which is further observed at the point of P (r, θ, φ). The sphere's radius is *a*, and its complex refractive index is *m*. The schematic is depicted in Figure 2-2.
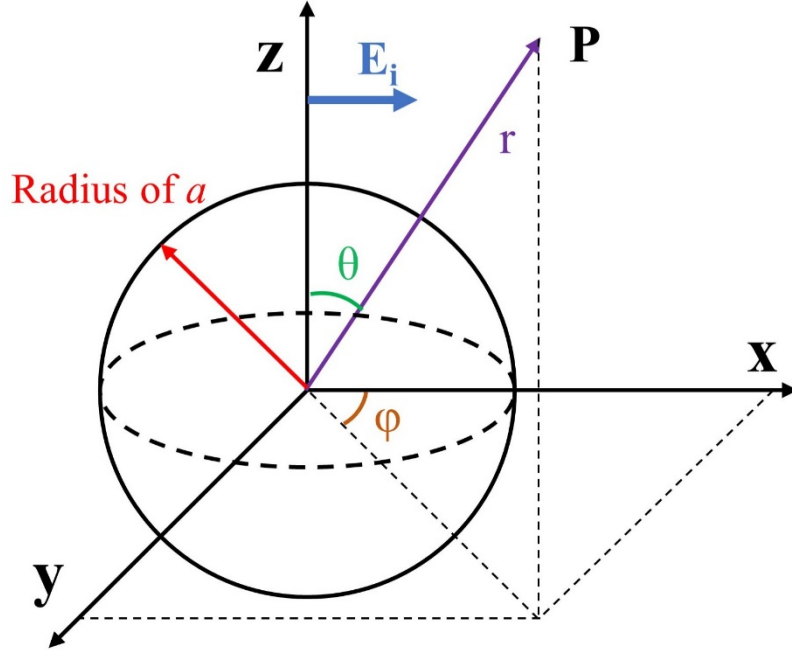
Figure 2-2 3D spherical model of an isotropic nanosphere dispersed in a uniform dielectric medium.

We start our discussion by giving the components of electric fields in spherical coordinates $E\ (r,\ \theta,\ \varphi)$. Since the diffracted field is usually in the far field (i.e., $r > a$), the component $E_r$ inversely proportional to the distance squared is neglected. Thus, the other two components read

$$E_{\varphi} = \frac{i}{kr} e^{-ikr} \sin(\varphi) S_1(\theta) \tag{2-18}$$

$$E_{\theta} = -\frac{i}{kr} e^{-ikr} \cos(\varphi) S_2(\theta) \tag{2-19}$$

The amplitude functions $S_1$ and $S_2$ can be derived by

$$S_1 = \sum_{n=1}^{\infty} \frac{2n+1}{n(n+1)} \left[ a_n \pi_n(\cos\theta) + b_n \tau_n(\cos\theta) \right] \tag{2-20}$$

$$S_2 = \sum_{n=1}^{\infty} \frac{2n+1}{n(n+1)} \left[ a_n \tau_n(\cos\theta) + b_n \pi_n(\cos\theta) \right] \tag{2-21}$$

where $a_n$ and $b_n$ are the Mie coefficients, i.e.,

$$a_n = \frac{\psi_n(\alpha)\psi_n'(m\alpha) - m\psi_n'(\alpha)\psi_n(m\alpha)}{\zeta_n(\alpha)\psi_n'(m\alpha) - m\zeta_n'(\alpha)\psi_n(m\alpha)} \tag{2-22}$$

$$b_n = \frac{m\psi_n(\alpha)\psi_n'(m\alpha) - \psi_n'(\alpha)\psi_n(m\alpha)}{m\zeta_n(\alpha)\psi_n'(m\alpha) - \zeta_n'(\alpha)\psi_n(m\alpha)} \tag{2-23}$$

$$\text{with the size parameter } \quad \alpha = \frac{2\pi a}{\lambda} \tag{2-24}$$

In Equations (2-22) and (2-23), the $\psi_n(z)$ and $\zeta_n(z)$ are Ricatti-Bessel functions derived by

$$\psi_n(z) = \left(\frac{\pi z}{2}\right)^{1/2} J_{n+\frac{1}{2}}(z) \tag{2-25}$$

$$\zeta_n(z) = \left(\frac{\pi z}{2}\right)^{1/2} \left[ J_{n+\frac{1}{2}}(z) + i(-1)^n J_{-n-\frac{1}{2}}(z) \right] \tag{2-26}$$

where $J_{n+\frac{1}{2}}(z)$ is the half-integral order Bessel function. Also, in Equations (2-20) and (2-21), $\pi_n(\cos\theta)$ and $\tau_n(\cos\theta)$ can be calculated by the Legendre functions $P_n(\cos\theta)$ as follows

$$\pi_n(\cos\theta) = \frac{P_n^{(1)}(\cos\theta)}{\sin\theta} \tag{2-27}$$

$$\tau_n(\cos\theta) = \frac{dP_n^{(1)}(\cos\theta)}{d\theta} \tag{2-28}$$

where $P_n^{(1)}(\cos\theta)$ is the Legendre function of the first kind. Thus, the efficiency factors for absorption and scattering of a sphere can be calculated by Mie coefficients of $a_n$ and $b_n$ as shown as follows,

$$Q_{abs} = \frac{2}{\alpha^2} \sum_1^\infty (2n+1)\left\{ \mathrm{Re}\left\{ a_n + b_n \right\} - |a_n|^2 - |b_n|^2 \right\} \tag{2-29}$$

$$Q_{scat} = \frac{2}{\alpha^2} \sum_1^\infty (2n+1)\left\{ |a_n|^2 + |b_n|^2 \right\} \tag{2-30}$$

The above discussion gives solutions for the four parameters in *Mie theory*, namely $a_n$, $b_n$, $\pi_n$ and $\tau_n$. It can be seen that the calculation of these parameters requires the use of Bessel functions and Legendre functions, which are not elaborated here but can be found in Ref [106-109] due to space limitations. In fact, as the sphere's size increases, the number of items $n$ to be calculated will also increase. Thanks to the development of computer science, we can now simply calculate the efficiency of Mie absorption/scattering of any metallic or dielectric spheres of different material and

sizes through simulation. To show the size applicability of the *Mie theory*, Figure 2-3 presents a comparison of the scattering power of Au nanospheres with different sizes calculated by Mie theory and simulated by the *Lumerical FDTD solutions*. When the particle size is small, the result of Mie scattering matches well with the FDTD theoretical calculation in the low wavelength region. Specifically, for radii of a = 5 *nm* and a = 50 *nm*, the corresponding wavelength ranges for which the agreement holds are approximately 200 nm < λ < 300 nm and 200 nm < λ < 450 nm, respectively. However, as the radius increases to a = 350 *nm*, the Mie scattering efficiency at the high wavelength region (~700 nm < λ < ~1200 nm) is more related to the FDTD theoretical calculation. Finally, when the particle is too large (i.e., *a = 1000 nm*), there is a larger deviation between the Mie theory and the FDTD simulation result.
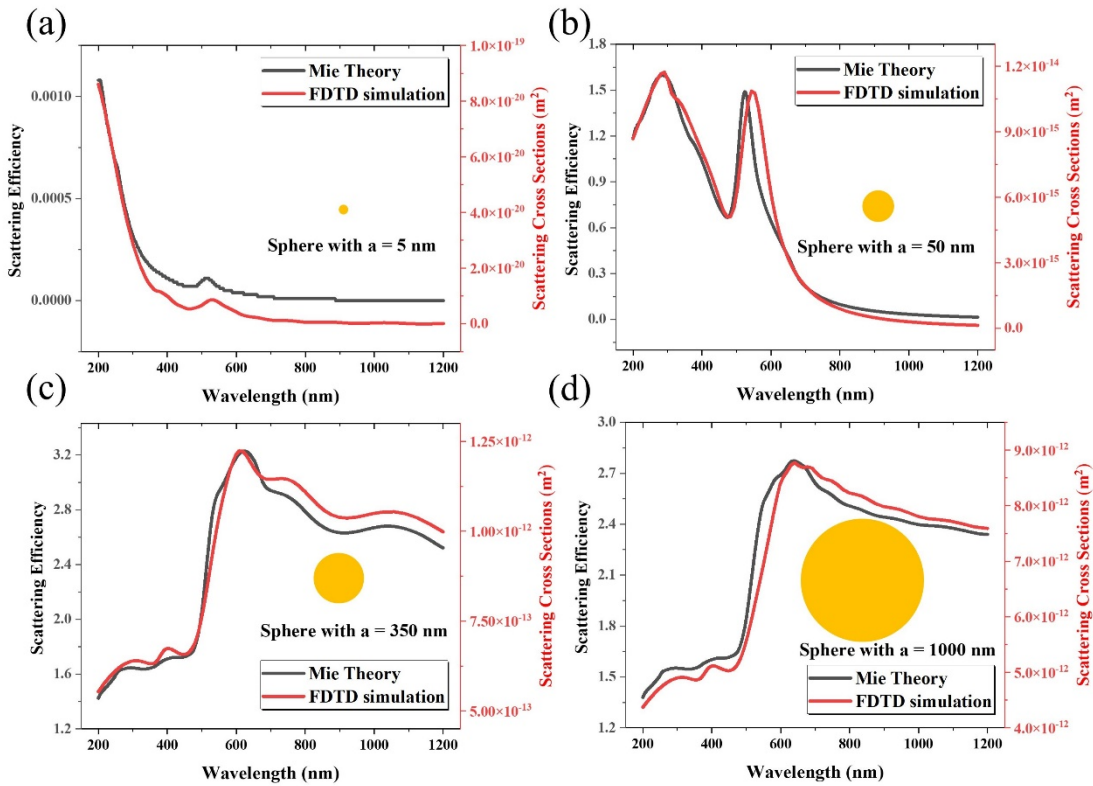


Figure 2-3 Comparison of scattering spectra between the Mie theory and FDTD simulation. The Au spheres' sizes are namely 5, 50, 350, and 1000 nm (a-d, respectively). The Mie scattering efficiency is calculated by a *Javascript Mie scattering calculator* provided by *Centre national de la recherche scientifique* (CNRS), via https://saviot.cnrs.fr/mie/index.en.html

## 2.2 Plasmonic coupling in a dimer system

### 2.2.1 Gap and size dependence: a quasi-static approximation

The gap and size dependence of the optical response in the dimer system is firstly studied via quasi-static approximation. More details of this part can be found in Ref [110-111]. Here we move beyond the Equation (2-13), and give a universal Clausius-Mossotti dipole polarizability for an isolated metal nanoparticle embedded in a uniform dielectric medium

$$\alpha = V(1+\kappa)\frac{\varepsilon_s - \varepsilon_d}{\varepsilon_s + \kappa\varepsilon_d} \tag{2-31}$$

where $V$ is the nanoparticle's volume and $\kappa$ remains constant depending on the nanoparticles' geometries. Note that $\kappa_{sphere} = 2$ refers to a spherical particle. By assuming a negligible imaginary part of the dielectric medium, the resonance condition reaches

$$\mathrm{Re}\left[\varepsilon_s\right] = -\kappa\varepsilon_d \tag{2-32}$$

We now consider the case of the dimer system with center-to-center distance $d$, electric field $\mathbf{E'}$, and dipolar momentum $\mathbf{p'}$ compared with the single particle system with $\mathbf{E}$ and $\mathbf{p}$. When the incidence is polarized along the gap direction, $\mathbf{E'}$ becomes

$$\mathbf{E'} = \mathbf{E} + \frac{\mathbf{p'}}{2\pi\varepsilon_d\varepsilon_0 d^3} \tag{2-33}$$

By connecting Equations (2-12) and (2-33), the polarizability of the dimer systems reads

$$\alpha' = \frac{\alpha}{1 - \dfrac{\alpha}{2\pi d^3}} \tag{2-34}$$

Since the volume for a sphere follows

$$V = \frac{\pi D^3}{6} \tag{2-35}$$

where D refers to the diameter, Equations (2-31), (2-34) and $\kappa_{sphere} = 2$ lead to

$$\alpha' = \frac{2\pi D^3 \left( \varepsilon_s - \varepsilon_d \right)}{\varepsilon_s \left( 4 - \dfrac{D^3}{d^3} \right) + \varepsilon_d \left( 8 + \dfrac{D^3}{d^3} \right)} \tag{2-36}$$

Here, the edge-to-edge gap $s$ is introduced to the dimer system, i.e., $s = d - D$. By connecting resonance conditions for the dimer system observed at the maximum $\alpha'$ with Equation (2-32), the effective $\kappa_{di}$ in the dimer system arrives at

$$\kappa_{di} = \frac{8 \left( s/D + 1 \right)^3 + 1}{4 \left( s/D + 1 \right)^3 - 1} \tag{2-37}$$

In such a nanospheres' dimer system, when the two particles are far away from each other (i.e., $s \to \infty$), $\kappa_{di} = 2$ indicates a same optical response as for the isolated nanosphere. As the scaling ratio of $s/D$ decreases, one can observe a significantly increased $\kappa_{di}$, implying an enhanced coupling in the dimer system. Comparing the dimer system with the isolated nanosphere, the red shift value $\Delta\lambda$ due to the coupling can be approximated to be proportional to the difference between $\mathrm{Re}[\varepsilon_s']$

and $\mathrm{Re}[\varepsilon_s]$ at the resonance conditions, which reads

$$\Delta\lambda \propto \varepsilon_d \left( \kappa_{di} - \kappa_{sphere} \right) = \varepsilon_d \left( \frac{3}{4 \left( s/D + 1 \right)^3 - 1} \right) \tag{2-38}$$

Note that the above Equation indicates a near-exponential decay of $\Delta\lambda$ vs. $s/D$, which predicts and confirms the empirical plasmonic ruler equation as discussed in the following section.

## 2.2.2 Gap and size dependence: a plasmonic ruler equation

In experimental studies of plasmonic dimer systems, it is also reported that a significantly enhanced dipole feature is confined to the gaps between the nanoparticles under the gap-directed polarization, as the edge-to-edge gap remains a few nanometers. [112-113] The physical mechanism is that the enhanced near-field of one particle can couple with that of the other one in close proximity, resulting in the surface charge oscillation together. Consequently, the far-field spectrum of the coupled dimer system usually presents exponential growth in the spectral shift to a longer wavelength as the gap decreases, compared with the LSPR peak of the single structure. [94] In 2007, Jain et al. fabricated a series of Au nanodisc dimers via EBL, and studied the LSPR spectral shifts of Au dimer systems with different sizes and gaps

under the parallel polarization. [114] The results plotted in Figure 2-4 (a) illustrate that the dimer systems of different discs' sizes all show exponential growth of the spectral shift with respect to the decreasing gap. Furthermore, as the spectral shift $\Delta\lambda$ and the mutual gap $s$ are scaled by the single disc's maximum plasmonic wavelength $\lambda_0$ and diameter $D$, one can observe a universal exponential decay of $\Delta\lambda / \lambda_0$ vs. $s/D$ independent of the discs' size in Figure 2-4 (b). Similar behavior can also be found in the experimental results as shown in Figure 2-4 (c).
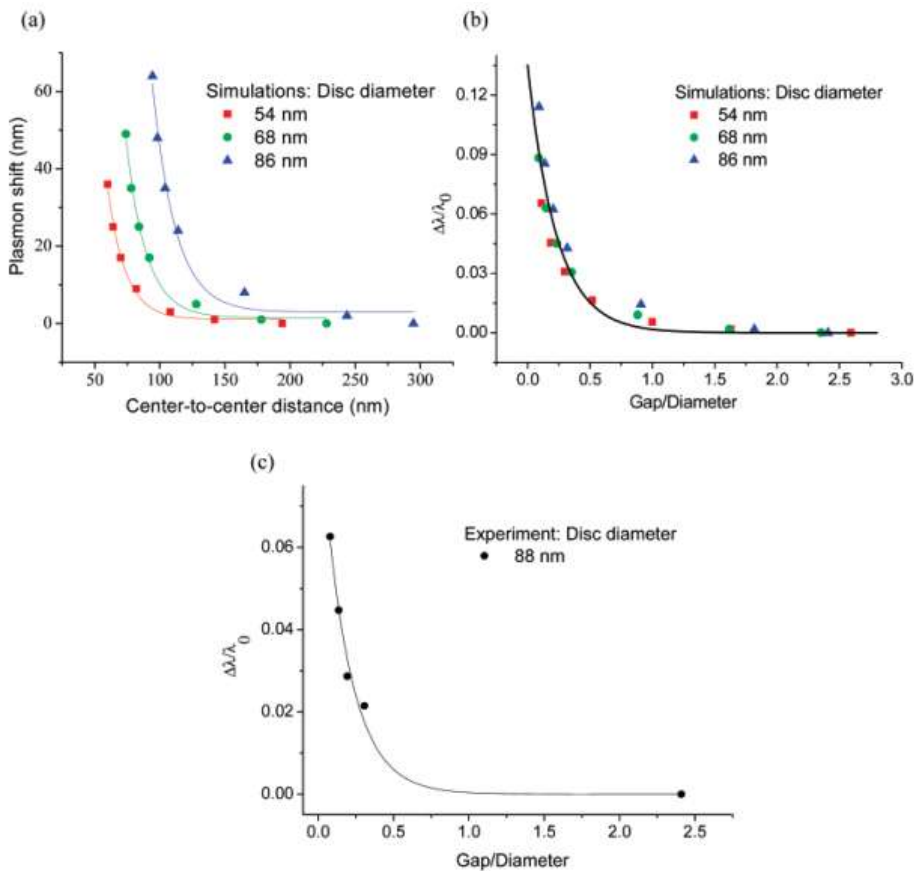


Figure 2-4 (a) Simulation results of the LSPR peaks' shift as a function the center-to-center distance, indicating three different exponential decay fitting-lines; (b) Simulation plots of the fractional LSPR shift vs the ratio of the gap to diameter; and (c) experimental figures of the scaling plot. The figure is adapted from Ref [114]

Therefore, the authors introduced the so-called plasmonic ruler equation to describe the exponential decay on account of the scaling as follows

$$\frac{\Delta\lambda}{\lambda_0} = A * \exp\left[\frac{-(s/D)}{\tau}\right] \qquad (2\text{-}39)$$

where $A$ and $\tau$ are the amplitude and decay constant, which remain constant in their

cases, i.e., $A = 0.18$ and $\tau = 0.23$. Furthermore, the authors declared that the decay constant calculated in the current Au nanodisc dimer system matches well with that measured in different metallic systems (e.g., Ag dimer system), [115] and geometric shapes (e.g., bow-tie system). [116] Such behaviors indicate that on the basis of the dipolar-dipolar coupling model, the plasmonic ruler equation manifests a universal scaling behavior in explaining gap and size dependence in a dimer system.

However, such a ruler equation is not valid for dimer systems with ultra-narrow separations, as the strong coupling across the ultrathin gap can also inhibit the inherent oscillations of each individual nanoparticle. [117-118] Zuloaga el al. explained the underlying reason is due to the emerging charge transfer plasmon (CTP) mode where conduction electrons are flowing back and forth in the dimer system when the gap is reaching the quantum region of ~1 nm. [119] Specifically, in the crossover regime (i.e., the edge-to-edge gap is from 0.5 nm to 1 nm), the classical plasmonic ruler equation breaks down, and the quantum mechanical effect begins to influence the optical behavior in the dimer system. The CTP occurring at the junction reduces mutual electromagnetic interaction, leading to smaller hybridization and a less pronounced redshift for the dipole plasmons in the dimer system. When the gap is reduced to 0.5 nm, the Fermi energy of the dimer system becomes higher than the electron potential barrier separating the two nanoparticles, and the conductive regime redefined as the conductive junction becomes large. Consequently, the CTP dominates in this region, and its far-field signals strongly blue-shift as the gap keeps decreasing. Figure 2-5 (a) shows the plot of plasmon energy as a function of the ratio of gap to radius, calculated via the time-dependent local density approximation. The red and blue lines indicate two systems with respective radii $R$ of 16 and 24 $b$ (where the unit $b$ is with respect to a Wigner-Seitz radius of $r_s = 3$ $b$ in their theoretical studies). The solid and dashed black lines refer to the classical exponential decay of the dipolar and quadrupolar modes. In their work, the quadrupolar mode for the big sphere with $R = 24$ $b$ follows the classical exponential decay, while the dipolar modes in both systems all witness a significant increase for the plasmon energy in the CTP regime ($d < 4$ $b$). Furthermore, similar anomalies in the quantum region are also observed in some experimental studies. For example, Chat et al. reported a self-assembly method in fabricating Au nanoparticles adsorbed on a glass substrate. [120] The results in Figure 2-5 (b-c) show a classical exponential decay of LSPR peaks vs. edge-to-edge gap when the gap is larger than 1 nm. However, once the gap is reaching the quantum

region, the resonance peaks in the dimer system become broadened and begin to show a distinct blueshift (followed by a redshift) in the wavelength domain.
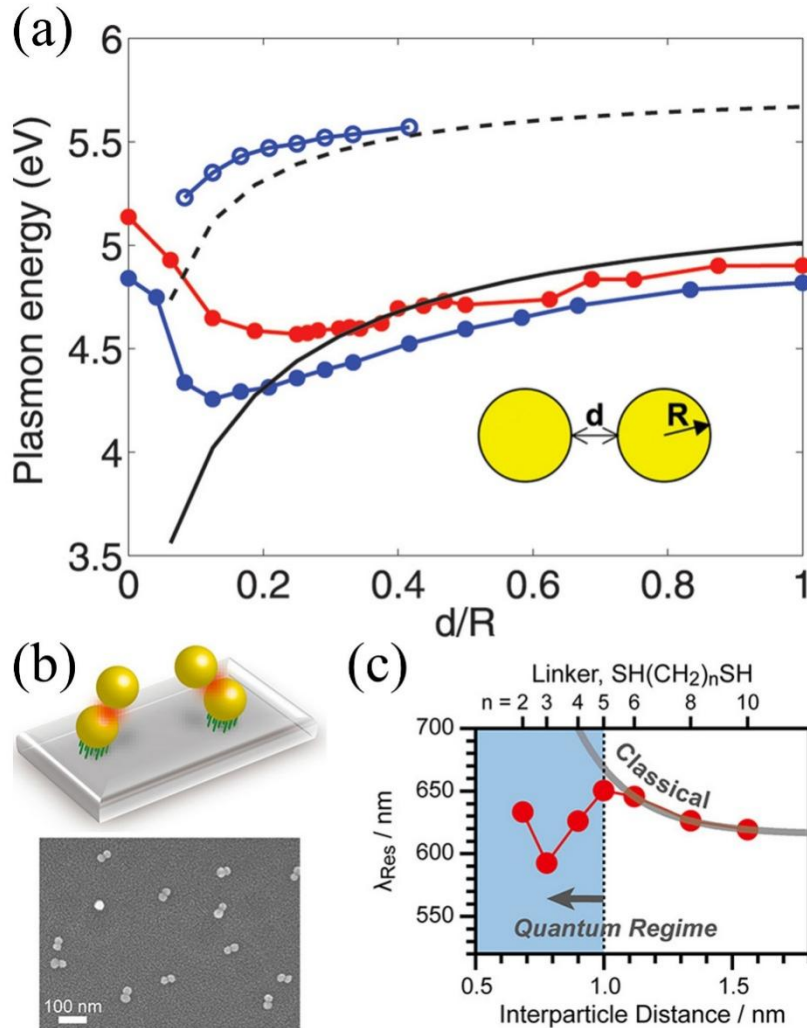


Figure 2-5. (a) Plot of plasmonic energy as a function of the scaling factor of gap to radius. The dipolar (full circles) and quadrupolar (open circles) modes in two different sizes of spheres, R = 16 (red) and 24 $b$ (blue), are systematically compared with the dipolar (solid lines) and quadrupolar (dashed lines) in classical exponential models. (b-c) Experimental study of the plasmonic coupling in the quantum region for gold sphere dimer systems deposited on a glass substrate. Figures (a) and (b-c) are adapted from Ref [119-120].

### 2.2.3 Plasmonic hybridization and polarization dependence

While isolated and isotropic nanospheres exhibit similar dipolar moments under linear polarization, the finite cluster systems composed of them display complex optical

modes, thus exhibiting different polarization dependences. Deng et al. [121] introduced the plasmonic hybridization (PH) model to explain the diverse optical modes in dimer systems, specifically focusing on longitudinal polarization where the incident electric field is polarized along the gap direction. As depicted in Figure 2-6(a), the hybridization between two dipolar disks results in four distinct surface charge distributions: in-phase bonding and anti-bonding modes, as well as out-of-phase bonding and anti-bonding modes. The in-phase coupling of these modes manifests as spectral peak features in the far field, which are referred to "bright" modes. In contrast, the out-of-phase coupling appears relatively "dark" due to the cancellation of dipole moments in opposite directions. Therefore, it is evident that these modes possess different polarization dependences. For the purpose of this discussion, we only focus on the polarization dependence of the simplest mode, where each particle exhibits a uniform dipolar characteristic corresponding to the external electric field. Importantly, this mode of lowest energy state demonstrates the most pronounced spectral features in the far field compared to other bright/dark modes. To better illustrate the influence of polarization on the simplest modes, we schematically plot the electric field distribution of a horizontally oriented trimer system under both transverse and longitudinal polarization conditions as shown in Figures 2-6 (b-c), respectively. Classical electrostatic analysis reveals that under transverse polarization, a decreasing gap leads to denser electric field lines along the gap direction. As a result, the system's energy increases, leading to a blueshift in the far-field spectrum. However, under longitudinal polarization, the electric field lines along the gap direction weaken each other when the gap decreases, resulting in a redshift in the spectrum. This spectral phenomenon, characterized by a sharp contrast in different polarizations, is nowadays widely accepted in the literature. [122-123]
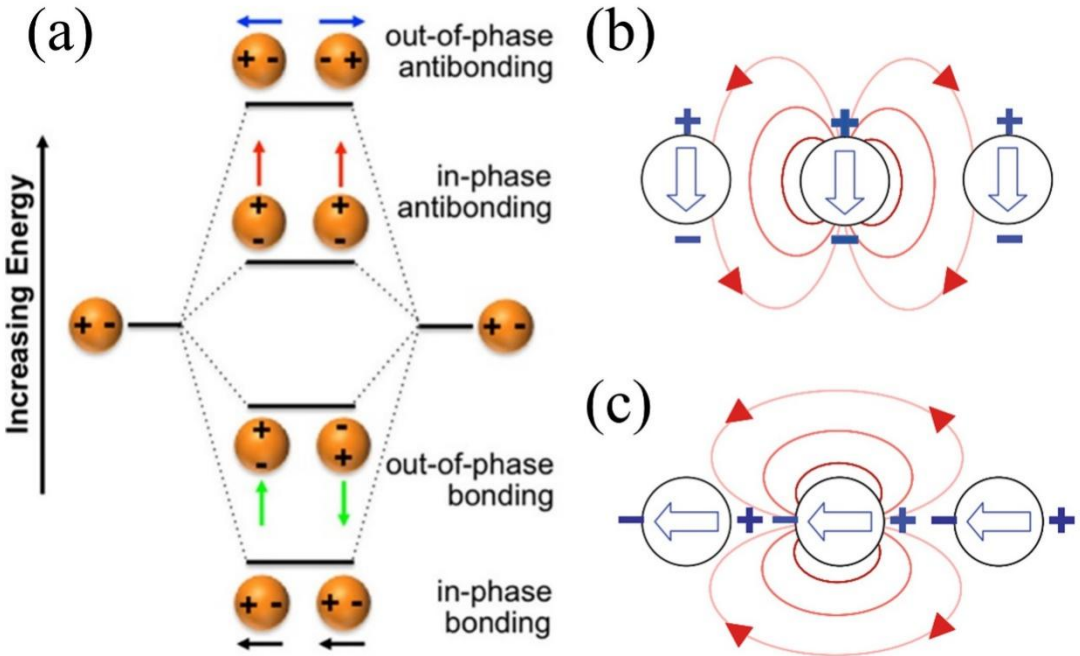
Figure 2-6. (a) Plasmonic hybridization model explaining the multiple charges in the dimer system. (b-c) Schematic of electric field distribution of a trimer system under transverse and longitudinal polarizations. Figure (a) is adapted from Ref [121], and Figures (b-c) are modified after Ref [103]

A quantitative study on the polarization dependence can be visualized by the plasmonic ruler equations. Note that such an equation is not only valid for the dipole-dipole interaction in the nanosphere dimer system, but also valid for the interaction between dipole and higher-order LSPR modes as well as in different dimer systems. [124-125] In the context of the current thesis, we give an example of a plasmonic ruler equation model of a nanoring dimer system under both polarizations. Near et al. reported a set of extinction spectra of different Au nanoring dimers fabricated via EBL, [44] as shown in Figure 2-7. A strong redshift of ~60 nm is observed under parallel polarization, while the perpendicular polarization leads to a slight blueshift of few nanometers with respect to decreasing the gaps from ~239.2 to ~17.8 nm. When the fractional spectral shift is fitted to the gap over the outer diameter of the nanoring, both experimental data match well with the plasmonic ruler equations. Quantitatively speaking, the shape of the exponential decay in the parallel polarization results in a higher absolute value for the amplitude ($A_1$) and low absolute decay constant ($\tau$) in this dimer system, where $A_1 = 0.085$ and $\tau = 0.27$ under the parallel polarization, and $|A_1| = 0.031$ and $|\tau| = 0.6$ refer to the perpendicular polarization, respectively.
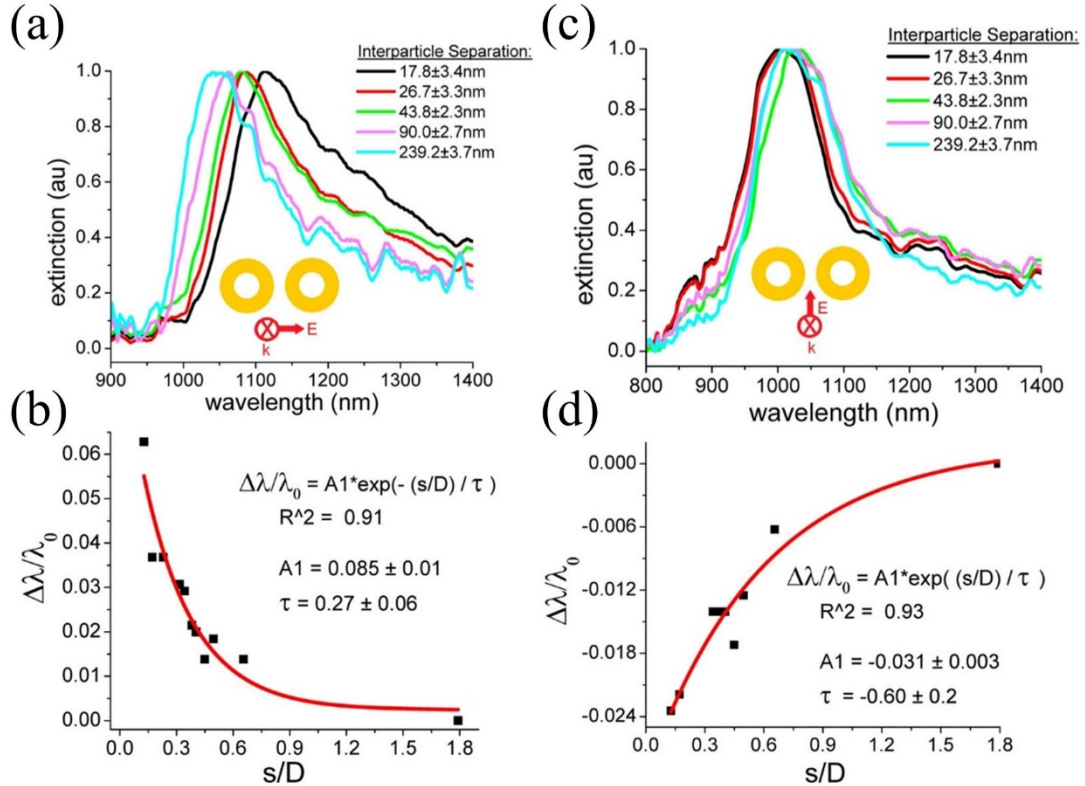
Figure 2-7 Experimental extinction spectra for nanoring dimers of varying gaps under polarizations either parallel (a) or perpendicular (c) to the gap-direction. Plots of the fractional shift against the geometric ratio of the gap to the outer diameter of the nanoring under parallel (b) and perpendicular (d) polarizations. The figure is adapted from Ref [44].

## 2.3 Fano coupling in a hybrid system

### 2.3.1 Spectral interference

In contrast to the above resonances which can be described with a Lorentzian function, Fano resonances with inherent asymmetric lineshape have shown appealing applications in various contexts, such as quantum probes detecting low-dimensional structures, Fano-transistors and Fano-filters for polarized electrons. [126-128] Historically speaking, Ugo Fano firstly studied such an asymmetric resonance, which now bears his name, [129-130] via a perturbation approach by considering a coupling between discrete and continuum states, as shown in Figure 2-8 (a). In his mathematical mode, the Fano resonance in scattering cross section $\sigma$ reads

$$\sigma = \frac{(\varepsilon + q)^2}{\varepsilon^2 + 1} \qquad (2\text{-}40)$$

where $q$ is the shape parameter, and the reduced energy $\varepsilon$ refers to $2(E - E_F)/\Gamma$

( $E_F$ and $\Gamma$ set the resonant energy and the width of the autoionized state). Equation

(2-40) indicates two eigensolutions, namely the Fano dip $\sigma_{min} = 0$ at $\varepsilon = -q$ and the

Fano peak $\sigma_{max} = 1 + q^2$ at $\varepsilon = 1/q$. Although this mathematical description of the

scattering cross section does not correspond to any specific physical situation, it is

then widely accepted that the Fano resonance arises from interference between a

discrete resonance and a broad continuum. Physically, Fano resonances can also be

found in a weakly-coupled dimer system consisting of two harmonic oscillators ($\omega_1 \ll$

$\omega_2$) as plotted in Figure 2-8 (b), [131] where the left one is excited with a periodic force

of $\cos(\omega t)$. In such a dimer system, two resonances $\omega_-$ and $\omega_+$ are located close to the

eigen-frequencies $\omega_1$ and $\omega_2$ for the two oscillators. The symmetric and broad $\omega_-$ in the

two oscillators shows a typical Lorentzian profile, while the sharp $\omega_+$ in the first

oscillator presents instead a Fano feature. In contrast to the Lorentzian resonance

where a single harmonic oscillator produces an enhanced response under external

excitation of a specific frequency, the Fano resonance in the dimer system results

from a destructive interference of oscillations from the external force and the second

oscillator, as there is a sudden phase change of $\varphi = \pi/2$ reaching the resonance

conditions.

(a) Discrete state — Mixing — Continuum — Fano resonance

$$\frac{q^2-1}{\epsilon^2+1} \quad + \quad \frac{2q\epsilon}{\epsilon^2+1} \quad + \quad 1 \quad = \quad \frac{(\epsilon+q)^2}{\epsilon^2+1}$$
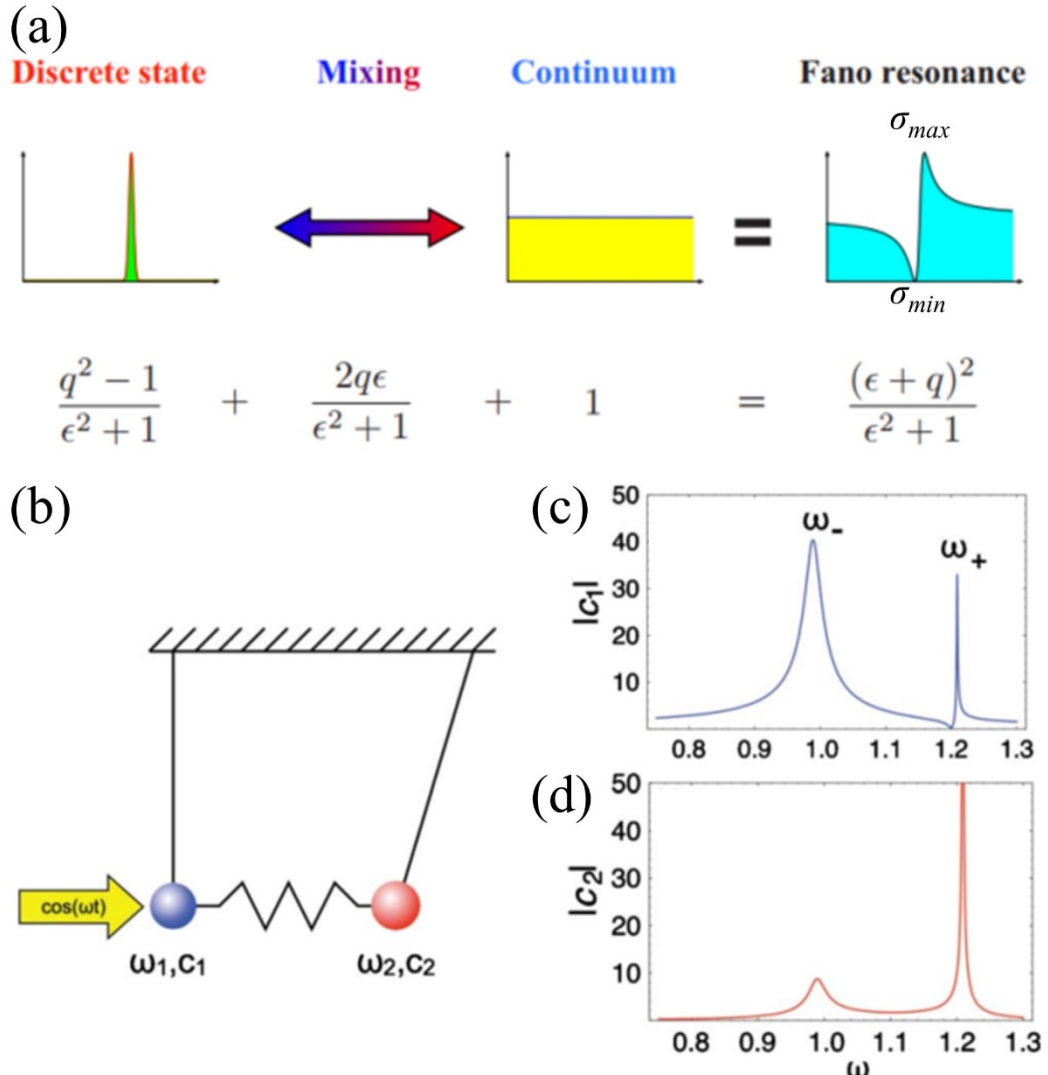
Figure 2-8 (a) Schematic of the Fano resonance resulting from the interference between a discrete state and a continuum. (b) A weakly-coupled model consisting of two harmonic oscillators, where (c) and (d) show the resonant dependence of the amplitude of the left and right oscillators. Figures (a) and (b-d) are adapted from Ref [131-132].

## 2.3.2 Near-field hybridization

In general, Fano resonances in plasmonic structures can be either SPP-based, such as a metal-insulator-metal (MIM) structure consisting of a pair of waveguide and resonator, [133] or LSPR-based. [61, 134] In LSPR systems, Fano resonances are characterized by the spectral interference between a spatially overlapping broad resonance and a narrow one. Typically, the broad resonance corresponds to a dipolar

disc plasmonic mode that exhibits super-radiance, resulting in strong radiation and providing a continuum for the sub-radiant and discrete mode arising from plasmonic hybridizations. [135] Although Fano resonances have been observed in single plasmonic structures with broken symmetry, [124] they are more commonly observed in complex coupled structures such as finite nanoparticle clusters and ring-disc cavities. [60, 136-139]

In a context of the current thesis, we give an example of Fano resonances occurring in a nonconcentric ring-disk cavity (NCRDC), where its symmetry breaking from a concentric one enhances the Fano features. In the work by Hao et al. [139] the extinction spectra of single disc, hybrid NCRDC, and single ring are shown in Figures 2-9 (a-c), respectively. The Fano feature in NCRDC contains the dip and peak located at the plasmon energy of ~0.9 and 0.85 eV, respectively. It is clear that such a Fano resonance is due to the spectral interference between the broad resonance of the disc (peaking at ~1.1 eV) and discrete ring's mode (peaking at ~1.05 eV). On the other hand, Fano resonances in such a system can also be interpreted by the near-field plasmonic hybridization (PH). The blue-dot line in Figure 2-9 depicts the PH between the quadrupolar ring mode and dipolar disk mode responsible for the Fano dip, while the red-dot line shows the PH between the dipolar bonding ring mode and dipolar disc mode. It is observed that the strong coupling effect from the dipolar disc excites an antibonding combination of the dipolar ring and disc resonances (i.e., the Fano peak). When the near-field coupling from the disc is weakened (e.g., at the energy of ~0.5 eV), instead of Fano resonances one can only observe the more discrete superposition mode between the dipolar ring mode and the dipolar disk mode affected by the ring.
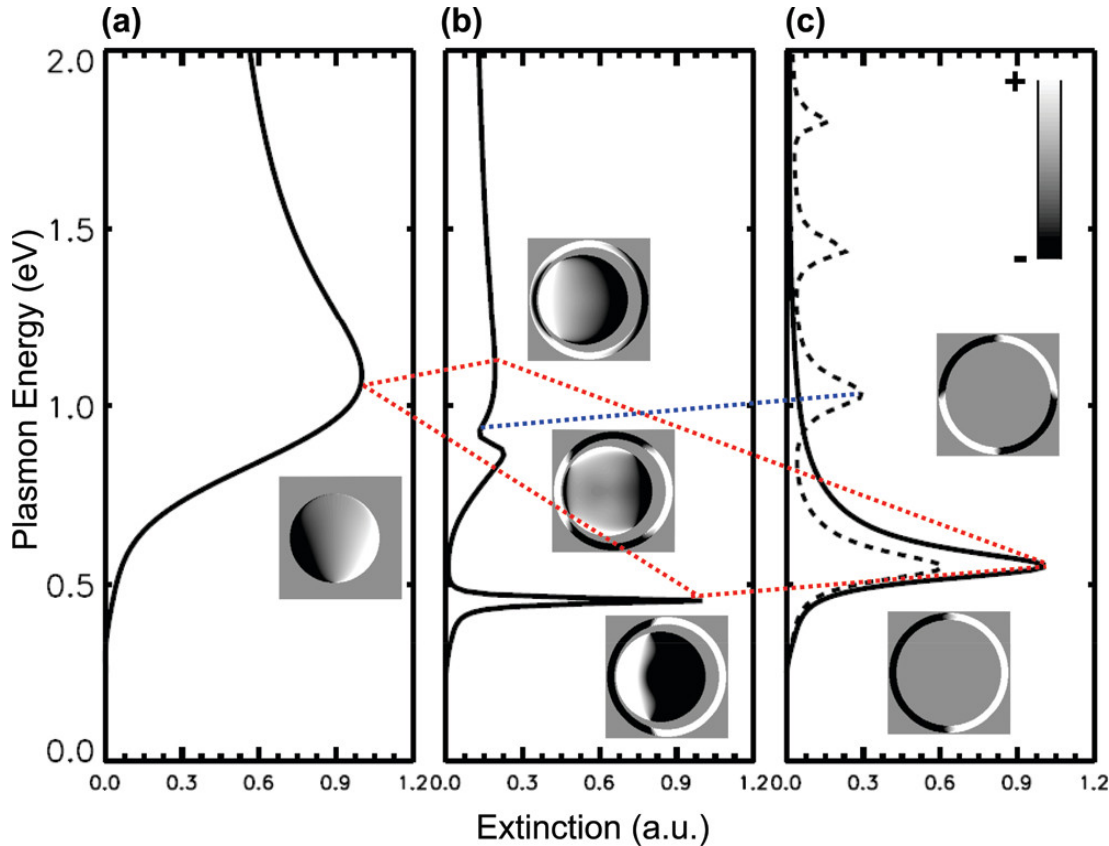
Figure 2-9 PH diagram for the NCRDC system illustrated by the red-dot line. The extinction spectra and top surface charge plots of individual disc (a), NCRDC (b), and single ring (c), where the black-dot line in (c) indicates different dark-modes of the ring. The blue-dot line indicates the quadrupolar ring mode responsible for the Fano feature, while the red-dot line explains the PH between the dipolar bonding ring and dipolar disk modes. The figure is adapted from Ref [138].

## 2.4 WRAs and SLRs for a grating system.

### 2.4.1 Wood-Rayleigh anomalies

As nanoparticles are distributed into a uniform array with a fixed lattice period, the so-called Wood-Rayleigh Anomalies (WRAs) arise within the lattice plane. [140-141] WRAs are firstly observed by Wood in explaining the multiple light transmission mechanisms in metallic diffraction gratings. [142] The arising peaks are due to the diffracted wave propagating tangentially to the grating's surface (within the lattice plane) at a certain wavelength reaching WRA conditions. Furthermore, such anomalies are proved to be independent of the permittivity of nanoparticles, but instead dependent of the lattice period, the incidence wavelength and injection

conditions, and the surrounding refractive indices. [143-144]

Here, we give fundamental mathematical descriptions of WRAs in two different nanosphere gratings under normal incidence, i.e., square and regular triangular gratings, as shown in Figure 2-10. The periods for the two gratings are maintained at $P$, and the corresponding in-plane primitive lattice vectors are $\mathbf{a_1}$, $\mathbf{a_2}$, $\mathbf{d_1}$, and $\mathbf{d_2}$, respectively.
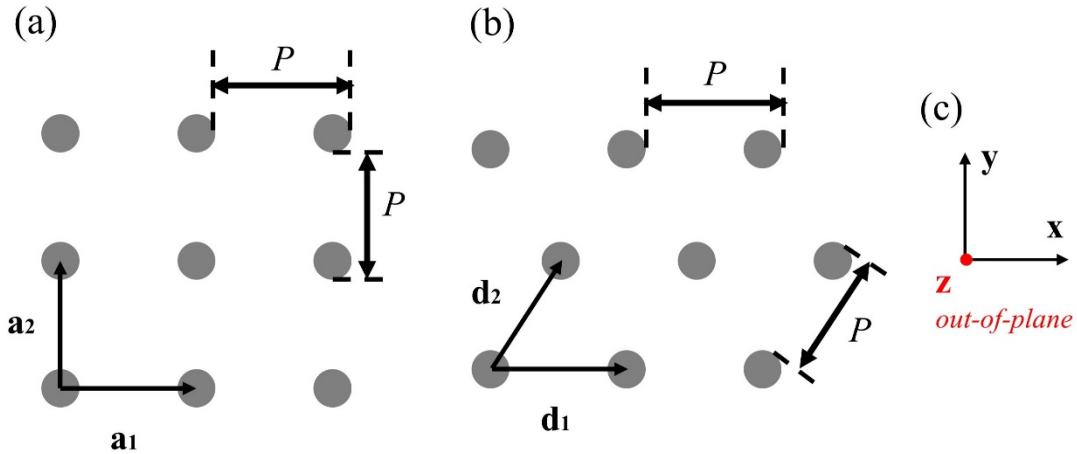


Figure 2-10 Schematic of the 2D square (a) and regular triangular (b) lattices. Constant center-to-center spacing $P$ is maintained in the two cases. $\mathbf{a_1}$, $\mathbf{a_2}$, $\mathbf{d_1}$, and $\mathbf{d_2}$ are the responding lattice vectors. The coordinate system $(\mathbf{x}, \mathbf{y}, \mathbf{z})$ is shown in (c).

As for the square lattice, the primitive lattice vectors are namely

$$\begin{aligned} \mathbf{a}_1 &= P \cdot \mathbf{x} \\ \mathbf{a}_2 &= P \cdot \mathbf{y} \\ \mathbf{a}_3 &= c \cdot \mathbf{z} \end{aligned} \tag{2-41}$$

where $\mathbf{a_3}$ is the out-of-plane vector with $c \to \infty$. Consequently, the in-plane reciprocal lattice vectors are

$$\begin{aligned} \mathbf{b}_1 &= 2\pi \frac{\mathbf{a}_2 \times \mathbf{a}_3}{\mathbf{a}_1 \cdot (\mathbf{a}_2 \times \mathbf{a}_3)} = \frac{2\pi}{P} \mathbf{x} \\ \mathbf{b}_2 &= 2\pi \frac{\mathbf{a}_3 \times \mathbf{a}_1}{\mathbf{a}_1 \cdot (\mathbf{a}_2 \times \mathbf{a}_3)} = \frac{2\pi}{P} \mathbf{y} \end{aligned} \tag{2-42}$$

The WRA signal with grating orders (m, n) appears at the wavelength reaching the grating coupling condition

$$\mathbf{k}_{/\!/} = \left( \mathrm{k}_{/\!/,\mathrm{x}}, \mathrm{k}_{/\!/,\mathrm{y}} \right) = \mathbf{k}_{\mathbf{inc},/\!/} + m\mathbf{b}_1 + n\mathbf{b}_2 \tag{2-43}$$

where $\mathbf{k}_{/\!/} = \left(k_{/\!/,x}, k_{/\!/,y}\right)$ is the surface plasmon wavevector propagating in the 2D lattice plane, and $\mathbf{k}_{inc,/\!/} = 0$ is set by the normal incidence. In the square lattice, the wavevectors follow

$$\left|\mathbf{k}_{/\!/}\right|^2 = (m\mathbf{b_1} + n\mathbf{b_2})^2 = \left(\frac{2\pi}{\lambda_{WRA,sq}}\right)^2 \tag{2-44}$$

Thus, the WRA wavelength in the square lattice reads

$$\lambda_{WRA,sq} = \frac{P}{\sqrt{m^2 + n^2}} \tag{2-45}$$

On the other hand, the primitive and in-plane reciprocal lattice vectors for the regular triangular arrays are

$$\begin{aligned} \mathbf{d_1} &= P \cdot \mathbf{x} \\ \mathbf{d_2} &= \frac{1}{2} P \cdot \mathbf{x} + \frac{\sqrt{3}}{2} P \cdot \mathbf{y} \\ \mathbf{d_3} &= c \cdot \mathbf{z} \left(c \to \infty\right) \end{aligned} \tag{2-46}$$

and

$$\begin{aligned} \mathbf{e_1} &= \frac{2\pi}{P}(\mathbf{x} - \frac{1}{\sqrt{3}}\mathbf{y}) \\ \mathbf{e_2} &= \frac{4\pi}{\sqrt{3}P}\mathbf{y} \end{aligned} \tag{2-47}$$

Since the wavevectors in the regular triangular lattice follow

$$\left|\mathbf{k}_{/\!/}\right|^2 = (m\mathbf{e_1} + n\mathbf{e_2})^2 = \left(\frac{2\pi}{\lambda_{WRA,tri}}\right)^2 \tag{2-48}$$

the corresponding WRA wavelength reads

$$\lambda_{WRA,tri} = \frac{P}{\sqrt{\frac{4}{3}\left(m^2 + n^2 - mn\right)}} \tag{2-49}$$

Note that WRAs observed in a way of transmission for a metallic nanohole array or in a way of reflection for a nanoparticle array can be termed as extraordinary optical transmission (EOT) and Bragg reflection modes, [80, 143, 145] respectively. Since EOT signals propagate at metallic surfaces, one should also consider the dispersion relation of the surface plasmon polaritons (SPPs). Thus, the EOT wavelength locates at

$$\lambda_{EOT} = \lambda_{WRA} \sqrt{\frac{\varepsilon_s \varepsilon_d}{\varepsilon_s + \varepsilon_d}} \tag{2-50}$$

where $\varepsilon_s$ and $\varepsilon_d$ are the permittivity of the metal and dielectric medium.

Furthermore, when the nanoparticle array is dispersed in a uniform medium ($\varepsilon_d$), the Bragg reflection mode reads

$$\lambda_{Bragg} = \lambda_{WRA} \sqrt{\varepsilon_d} \tag{2-51}$$

In contrast to the EOT signals, the Bragg mode is independent of the permittivity of nanoparticles, indicating also the validity for dielectric nanoparticle arrays.

## 2.4.2 Surface lattice resonances

Both WRAs and Surface Lattice Resonances (SLRs) are grating modes, even in some cases SLRs are located closely to (or slightly red-shifted from) WRAs, [144] but they are fundamentally different. To be specific, SLRs are collective resonances in a lattice consisting of metallic nanoparticles with sub-wavelength scale, resulting from the coupling between LSPRs of individual nanoparticles and the WRAs. [146-148] Such collective responses enable a strong far-field signal with ultra-high quality factors (Q-factor). For example, Bin-Alam et al. recently reported a lattice metasurface supporting a Q-factor of 2340 in the telecommunication C band. [73] As shown in Figure 2-11, the lattice consists of a rectangular array of rectangular Au nanostructures, where lattice periods and structure dimensions in the two axes are $P_x$ = 500; $P_y$ = 1060, $L_x$ = 130 and $L_y$ = 200 nm, respectively, and the out-of-plane thickness is $T$ = 20 nm. The transmittance spectra in both FDTD simulation and experiments show two distinct modes, i.e., the LSPR mode at $\lambda_{LSPR}$ = 830 nm and SLR mode at $\lambda_{SLR}$ = 1550 nm. The experimental SLR peak in Figure 2-11 (d) indicates an ultra-narrow linewidth of $\Delta\lambda = 0.66$ nm, corresponding to Q = 2340.

Furthermore, the electric field distributions plotted in Figure 2-11 (b) illustrate that SLR plasmons are not limited to the particle surface, but there is also a propagating plasmon in the lattice plane.
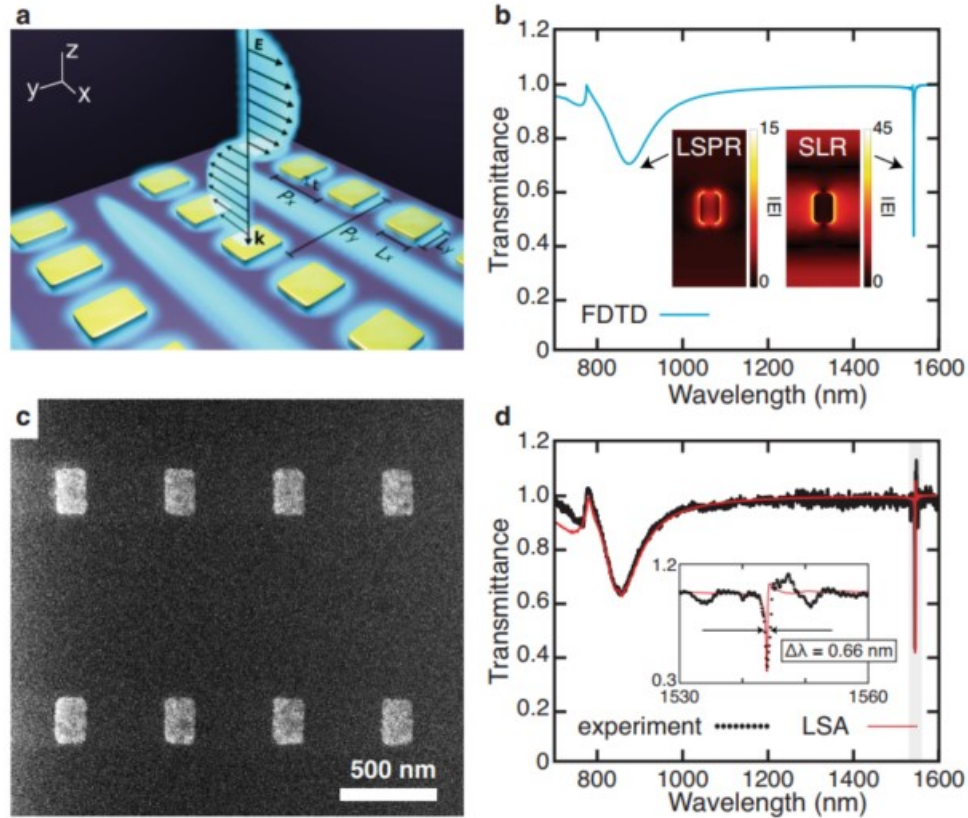
Figure 2-11 Schematic (a) and top-view SEM image (c) of the rectangular lattice consisting of rectangular nanostructures. Simulation (b) and experimental (d) transmittance spectra of the rectangular lattice, where the inset plot in (d) indicates a narrow linewidth of 0.66 nm for the SLR mode. The figure is adapted from Ref [73].

# Chapter 3 Experimental and Characterization Methods

In this chapter, we discuss the main experimental and characterization methods used in this thesis. The well-ordered 2D patterns, such as nanorings, elliptical nanorings, and ring disc cavities, are fabricated via EBL. To achieve flexible metasurfaces, we also design state-of-art techniques to transfer the EBL patterns onto PDMS, including surface functionalization, PDMS modeling, and wet etching. After fabrication, the optical properties of dark-field reflection or scattering spectra are measured in situ. In the following section, we explain the basic principle of the homemade stretcher implemented in the optical set-up and SEM chamber. The applied strain is also quantitatively defined. To specify the local deformation of the transferred patterns on PDMS, we introduce two approaches to perform SEM imaging on PDMS, depending on the existence of an additional conductive layer. In the last section, we briefly present the simulation methods, where the geometries are taken from the SEM results.

## 3.1 Electron beam lithography

Electron beam lithography (EBL) is a nanofabrication method that creates 2D patterns by scanning a focused electron beam across the surface of a photoresist-covered substrate. [149-150] In this thesis, the EBL fabrication mainly consists of six steps as follows:

(1) *Preparation of rigid substrates.* In Chapters 4 and 5, the chromium/silicon (Cr/Si) rigid substrate is made by evaporating a 200 nm thick Cr layer onto a Si wafer. The Cr layer is not only a sacrificial layer for the pattern transfer, but also an adhesion promoter for the evaporated Au to the Si wafer. In Chapter 6, a 30 nm thick transparent layer, such as indium-tin-oxide (ITO), is thermally evaporated onto a cleaned glass substrate. Note that the Cr and ITO layers enhance also the conductivity of the substrate to avoid the electron accumulating effect during the EBL process. [151-152] Both rigid substrates are further cleaned in an ultra-sonic bath containing acetone and isopropanol (IPA) for 5 minutes each, rinsed with deionized water, and dried with nitrogen gas. (Acknowledgement to Dr. Christoph Dreser for his valuable contribution in writing the fabrication handbook on EBL procedures, which is disseminated within the research group led by Prof. Monika Fleischer at Eberhard

Karls University Tübingen (EKUT).)

(2) *Spin-coating of photoresist.* Poly-methyl methacrylate (PMMA) is the most frequently used positive photoresist in EBL. [153] When exposed to electrons, the polymer chains of PMMA have a tendency to break and can be easily dissolved in a developing solution. In this work, the rigid substrate is spin-coated with a 5 v% diluted PMMA/methyl isobutyl ketone (MIBK) solution, which bakes at 150 °C overnight to generate a ~200 nm PMMA layer.

(3) *Lithography.* A *JEOL JSM-6500F* SEM along with a *XENOS* pattern generator is used to carry out the lithography work. Complex and precise pattern designs with sub-micron accuracy are achievable thanks to the high resolution of the SEM imaging and the precise control of the pattern generator. The shape of nanostructures is designed through a self-made pattern involving repeated exposure dots that are regularly arranged. The width or size is further controlled by adjusting the dwelling time and dose during the electron exposure.

(4) *Development.* A 25 v% MIBK / IPA solution serves as the developer for PMMA. The exposure region is selectively dissolved in the above solvent, leaving behind the unexposed PMMA on the substrate. The 75s developing time is carefully chosen to optimize the designed patterns.

(5) *Au evaporation.* A ~50 nm thick Au layer is then thermally evaporated onto the developed substrate via a *Balzers BA510* evaporator.

(6) *Lift-off.* The above sample is further immersed in acetone overnight to lift off all the unexposed areas. Finally, the Au patterns of ~50 nm thickness on the rigid substrate are formed, exhibiting high resolution and fidelity to the pattern design. The dimensions of the resulting structures on Si/Cr are confirmed by further SEM characterizations.

## 3.2 Pattern transfer techniques

To transfer the EBL patterns from initial Cr/Si onto PDMS substrates, the following sequential procedures are performed.

### 3.2.1 Surface functionalization

(3-Mercaptopropyl) triethoxysilane (MPTS) is used as a linking molecule to form a chemical bond between PDMS and the evaporated Au and to enhance the adhesion between them. [154-155] First, the EBL sample is immersed in a 5 v% MPTS/n-hexane solution for 2 hours, allowing the thiol head group (-SH) of MPTS to combine with the evaporated Au. The linking group of Au-MPTS is then strongly formed. Next, the sample is placed in a 50 v% Chloroform/n-hexane solution for at least 3 min to facilitate the $S_N2$-reaction. In this reaction, the ethoxy group (-OCH$_3$) of MPTS is replaced by a hydroxyl group (-OH), which is necessary for the subsequent modeling process because it enables the formation of a siloxane bond (Si-O-Si) between PDMS and MPTS through a condensation reaction. A small amount of deionized water can be used as a catalyst thus accelerating $S_N2$-reation. More details of the above chemical reaction process can be found in Ref [[156-157]] and are not discussed in detail here.

### 3.2.2 Cured/Fluid PDMS modeling

In this thesis, we use two different PDMS modeling approaches. The cured PDMS modeling is literally to model the sample using cured PDMS. For this purpose, a 10:1 w/w PDMS/curing agent mixture is stored at room temperature for 30 minutes and then degassed completely in a vacuum chamber. Next, by first placing the mixture inside the stretching template to half-cure at 150°C for 6 min, the PDMS is demolded and pressed directly onto the MPTS/Au/Cr/Si sample. Finally, the above system is cured at 150°C for another 6 min, thus enabling modeling.

On the other hand, the fluid PDMS modeling is an extension of the above method with the aim of embedding the transferred patterns into PDMS to improve the shape deformability of the embedded NRs under strain. First, three additional silicon wafers are prepared to fix the EBL sample as shown in Figure 3-1 (a). A few drops of PDMS can be placed between the two supporting wafers and the base wafer, and cured to form an adhesive. Then a customized Teflon-made tensile template is attached to the EBL sample and secured in place with two clamps, as shown in Figure 3-1 (b). Note that the EBL patterns should be placed exactly in the middle to achieve uniform elastic deformation under strain in the future. Afterward, the same PDMS mixture is slowly poured into the mold, further degassed in a vacuum chamber, and cured at

120° for 12 minutes. Then, the Teflon template is carefully removed, leaving behind a molded PDMS sample as shown in Figure 3-1 (c). (Acknowledgement to Dr. Florian Laible from the Fleischer group, EKUT, for introducing the cured PDMS modeling method in Ref [85], and to Dr. Abdelhamid Hmima from University of Technology of Troyes (UTT) for establishing the principle of fluid PDMS modeling method which is further improved as shown in Figure 3-1. We also extend our appreciation to William d'Orsonnens (UTT) for the fabrication of the Teflon template.)
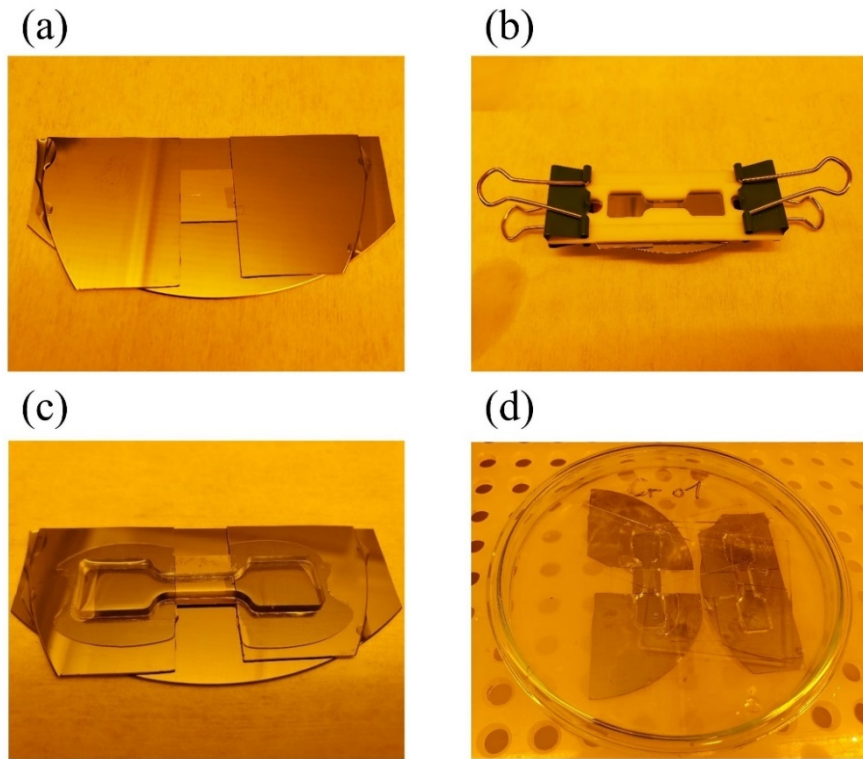


Figure 3-1 Set of photos explaining the process of fluid PDMS modeling. Figure (a) shows the EBL sample that has been secured by additional wafers; Figure (b) shows the fluid modeling system by pouring the fluid PDMS into the template; Figure (c) shows a template-detached sample as PDMS is cured; and Figure (d) indicates the wet etching process for the pattern transfer.

### 3.2.3 Wet etching

In order to remove the sacrificial Cr layer, the modeling sample is carefully immersed in the Cr etchant (TechniStrip Cr01 solution) as shown in Figure 3-1 (d). The sample is also pressed under a loading glass, and covered to prevent the solution from evaporating. The etching process may last for one or two weeks, and one can visually decide if the Cr layer is fully dissolved. Once the etching is completed, the

Au/MPTS/PDMS systems can be easily peeled off from the original substrates, and are ready for optical or mechanical tests after rinsing and drying.

To conclude, Figure 3-2 shows the schematic fabrication methods above discussed, combining the EBL work (as shown in Figures a-f), surface functionalization (Figure g), fluid modeling (Figure h), and wet-etching (Figures i-j) techniques.
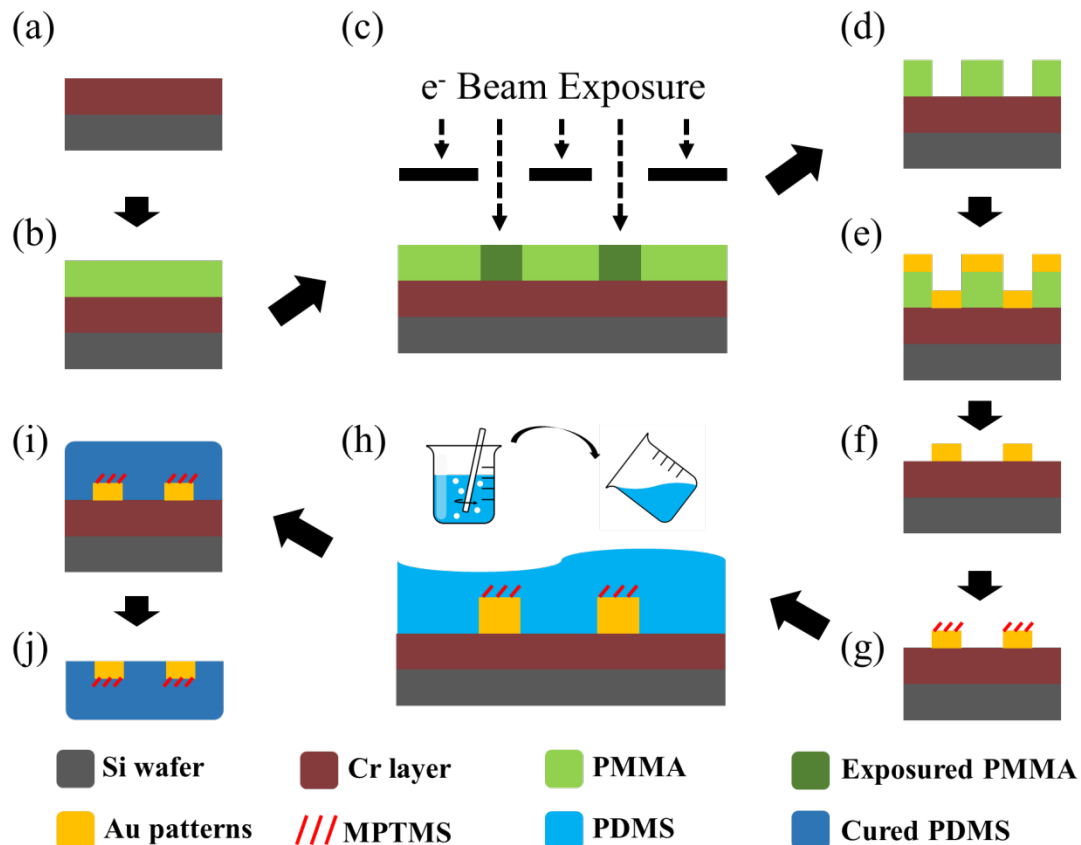


Figure 3-2 Flow map of the fabrication in a case of fluid modeling, containing substrate preparation (a), photoresist coating (b), electron beam exposure (c), development (d), Au evaporation (e), lift-off (f), surface functionalization (g), fluid PDMS modeling (h), PDMS curing (i), and completion of wet-etching (j).

## 3.3 Homemade stretcher and strain definition

Once the Au structures are transferred onto the PDMS, uniaxial strain to PDMS is applied via a homemade micro-stretcher that can be further placed in a Zeiss microscope or SEM chamber for optical or imaging tests. Figure 3-3 (a) shows the strain-less PDMS mounted on this stretcher where Figure 3-3 (b) presents the initial

clamp spacing of 1 cm. As the stretcher nut is rotated, the substrate is stretched uniformly to the final state (Figure 3-3 d) with a spacing of 1.4 cm (Figure 3-3 e). Thus the engineering strain is calculated as $\varepsilon_{engr} = \Delta L / L = (1.4 - 1) / 1 = 40\%$. However, when we observe the transferred Au grating on PDMS before and after stretching with the CCD camera inside the microscope, Figures 3-3 (c, f) show a grating strain of $\varepsilon_{grtg} = 37.5\%$. To avoid ambiguity between the engineering strain and local strain, the strain values in this thesis are defined by the elongation of the grating along the stretching direction, which is also used for related optical simulation. In Figures 3-3 (g, h), we employ FEM mechanical simulation to investigate the local strain distribution of PDMS during uniaxial stretching. The simulation involves fixing one end of the PDMS sample while stretching the other end. The obtained preliminary results depict the distribution of normalized logarithmic strain (i.e., true strain) in the initial ($\varepsilon = 0$) and final state ($\varepsilon = 40\%$), presented at the same scale. Notably, PDMS exhibits distinct strain responses across different areas. However, the middle part of PDMS undergoes homogeneous strain development, indicating the reason for centrally-placed transferred structures as discussed in Section 3.3.2 (Acknowledgement to Dr. Florian Laible (EKUT) and Michel Rebmann (A. Meixner group, EKUT) for the fabrication of the micro-stretcher.).
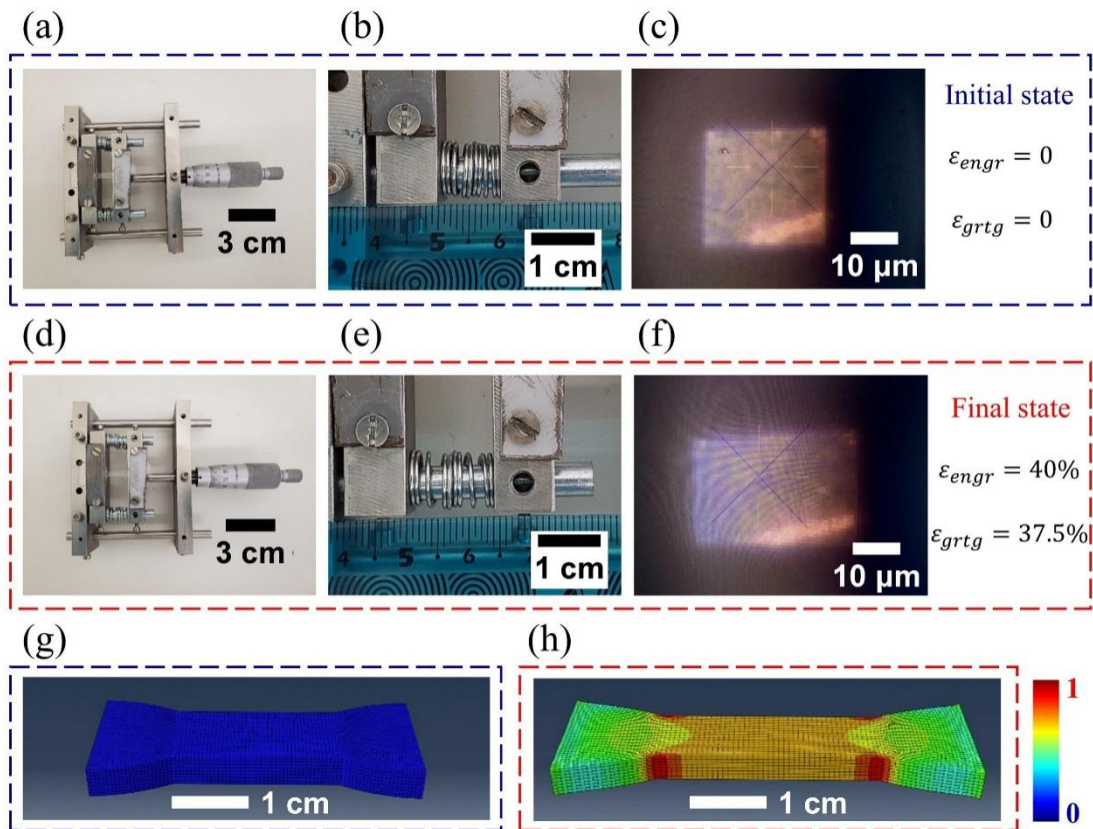


Figure 3-3 Principle of the micro-stretcher. Figures (a-c) and (d-f) show the initial and

final stretching states in sample mounting, clamp spacing, and grating development, respectively. Figures (g, h) show the simulation result of strain distribution in the initial and final state.

## 3.4 Optical characterization

Plasmonic NPs exhibit strong near-field enhancement under excitation, however, monitoring their far-field spectra remains challenging. The main reason is that the far-field signal intensity of individual NPs is rather weak (i.e., low signal-to-noise ratio). Furthermore, the broad plasmonic peaks present a challenge in distinguishing between resonances of different orders, particularly for complex structures such as nanorings. To increase the contrast of the spectra, we adopted dark-field spectroscopy to collect the signals. In Chapters 4 and 5, we monitor the dark-field reflection spectra of Au arrays on PDMS at different strains. Instead in Chapter 6, we use a high-magnification oil lens to improve the resolving power and perform the dark-field scattering spectra. Additional SERS measurement is also illustrated. The details are shown as follows.

### 3.4.1 Dark-field reflection spectroscopy

A *Zeiss Axio Scope A1* reflection microscope combined with a grating spectrometer *LOT SR-303i-B* is used to analyze the plasmonic scattering of Au structure arrays on PDMS in the dark field. Figure 3-4 (a) depicts its schematic diagram, which contains mainly a 100 W halogen lamp, a linear polarizer, a beam splitter, an objective lens, and a spectrometer, respectively. The halogen source light passes through blockers, mirrors, and objectives to form ring-shaped dark-field incidences with an oblique angle of $56.75 \pm 2.25°$. Figure 3-4 (b) shows the operation principle of the *Zeiss EC EPIPLAN 20x/0.4* objective, which focuses the incident dark-field on the object plane and collects its back-scattered light. The collected signal is further analyzed by the grating spectrometer through a focusing lens. Typically, the focusing area of the objective is ~25 $\mu m^2$ and the effective wavelength detection range of the spectrometer is ~500 to 1000 nm. Thus, for Au structure arrays with a period of 400 or 500 nm, both the plasmonic and grating resonances can be monitored. Note that in Chapter 4, the optical spectra correspond to the NR array measured at the central position. In contrast, in Chapter 5, we perform spectral measurements on three distinct regions of

the ENR array to ensure the reproducibility of the SLR properties.
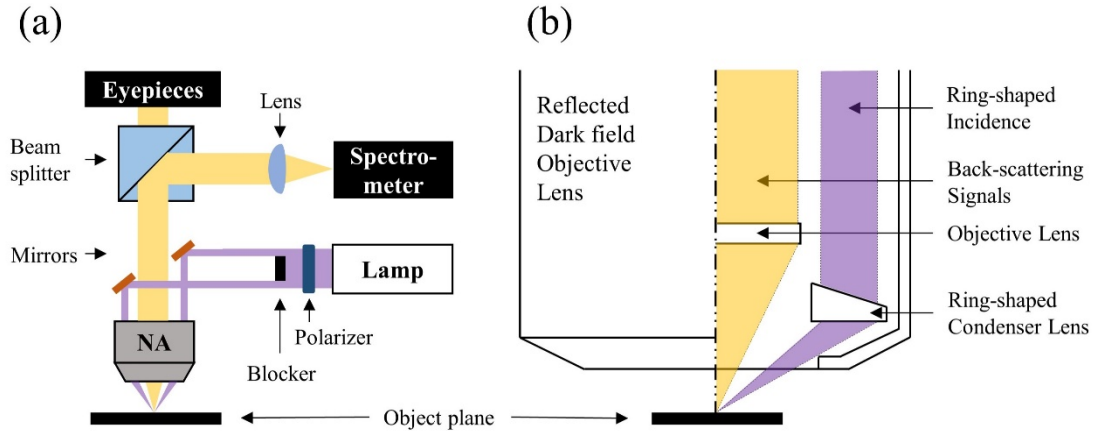


Figure 3-4 Optical path diagram for the dark-field reflection spectroscopy (a), and the working principle of the dark-field objective lens (b).

### 3.4.2 Dark-field transmission spectroscopy

A *Nikon Eclipse Ti* inverted transmission microscope with an external Nikon dark-field condenser (*dry 0.95-0.80*) is used to detect the forward-scattered light from Au samples. The optical path diagram is similar to Figure 3-3 (a), the same halogen light source and spectrometer are used, but the scattered light is collected from the back of the samples. To improve the optical resolution, we use a high magnification objective such as a *Nikon Plan Fluor 100x/0.5-1.3* oil objective and treat the sample with an oil (refractive index of 1.518) immersion. Since the effective detection area of this objective is ~1 $\mu m^2$ for a spectrometer slit width of 100 $\mu m$, the grating effect of Au structures with a period of 5 $\mu m$ can be neglected. Note that in Chapter 6, the spectra of RDPs exhibit a direct correspondence with their structures, which are subsequently characterized by SEM.

To eliminate the effects of sample background noise ($I_{bg}$), light sources ($I_{lamp}$), and dark current ($I_{dc}$) on the spectra of Au structures, the raw data ($I_{raw}$) for all collected back-scattered or forward-scattered signals are normalized as follows.

$$I_{nor} = \frac{I_{raw} - I_{bg}}{I_{lamp} - I_{dc}} \tag{3-1}$$

### 3.4.3 Surface-enhanced Raman spectroscopy

Rhodamine 6G (R6G) is commonly used in SERS measurements due to its robust Raman signals, chemical stability, low cost, and notable affinity for metal surfaces. In this work, R6G is dissolved in triply distilled water. Samples are directly soaked in R6G aqueous solution ($10^{-6}$ **M**) for 4 hours, then rinsed with water. A home-built confocal microscope is used for the measurements. The sample is mounted on a scanning piezo-stage (P-527.3CL, Physics Instruments). A high numerical aperture oil objective lens (NA = 1.46, Carl Zeiss) is used to focus the excitation laser (3.4 mW, 632.8 nm) on the sample. The excitation laser is filtered out by a 633 nm long-pass filter (RazorEdge LP Edge Filter 633 RU, Semrock). Raman signal is collected by the same objective lens, then sent to a spectrometer (SP-2500i, Princeton Instruments) to record a spectrum. All the images and spectra are analyzed with a self-written Matlab script. (Acknowledgment to Dr. Quan Liu and Liangxuan Wang for the SERS measurements, which were conducted as part of the research group led by Prof. Alfred J. Meixner at EKUT.)

### 3.5 SEM characterization on PDMS

Scanning electron microscopy (SEM) enables high-resolution (e.g., 1 nanometer) imaging of material surfaces. However, when scanning a polymer sample, the high-energy electrons may either damage the sample or show a drift in the image due to the charge accumulating effect. In this thesis, we adopt two methods to image Au samples on PDMS surfaces, such as conductive layer coating and low-voltage operation. Note that all imaging tests on PDMS are performed after optical characterizations to avoid the effect of carbon contamination and the PDMS hardening on the spectra evolution.

### 3.5.1 Conductive layer coating

A *Philips XL30* SEM is used for imaging on either Si/Cr or PDMS. As for the PDMS sample, an *Agar Sputter Coater* is adopted to sputter a Au film onto the PDMS surface to reduce electron accumulation. In addition, we test the effect of the thickness of the Au film on PDMS on its SEM imaging, and preliminary results show a large drift in PDMS imaging at the deposition of low-thickness films. Since a thicker

conductive layer will restrict the grating development under strain (i.e., strain-induced variations in grating periods), we select 50 nm as the experimental condition, i.e., not exceeding the Au structure thickness. After acetone immersion and nitrogen blowing, the micro-stretcher is now mounted with the PDMS sample and placed inside the SEM chamber. An acceleration voltage of 5.0 kV is selected and a fast-scan mode is applied to avoid artifacts due to image drifts.

Indeed, SEM imaging on PDMS with conductive layers still presents a challenge. Figures 3-5 (a) and (b) show SEM images of a NR array on PDMS in the strain-less state, acquired using a normal scanning speed (a) and a fast-scan mode for screenshot imaging (b). As shown in Figure (a), a larger aspect ratio deviation during the scanning process is observed due to charge drifts. Nevertheless, even with the fast-scan method used in Figure (b), a slight shift is still noticeable while observing the sample. Furthermore, the soft PDMS presents also hardening effects for the imaging regions under electron exposure. Figures 3-5 (c-d) show a grating development on PDMS at strain $\varepsilon_{engr}$ = 20% and 40%, respectively. As PDMS presents elastic deformation, the sputtered Au film is rather rigid and incapable of responding simultaneously, thus resulting in cracks outside the center imaging region. Such hardening effects not only hinder the grating development under strain but also lead to varied strain response in different regions in the array. Consequently, the initial square array fails to develop into a regular rectangular array, as shown in Figure 3-5 (d) (Acknowledgement to Dr. Florian Laible for conducting the PDMS imaging using the *Philips* SEM.)
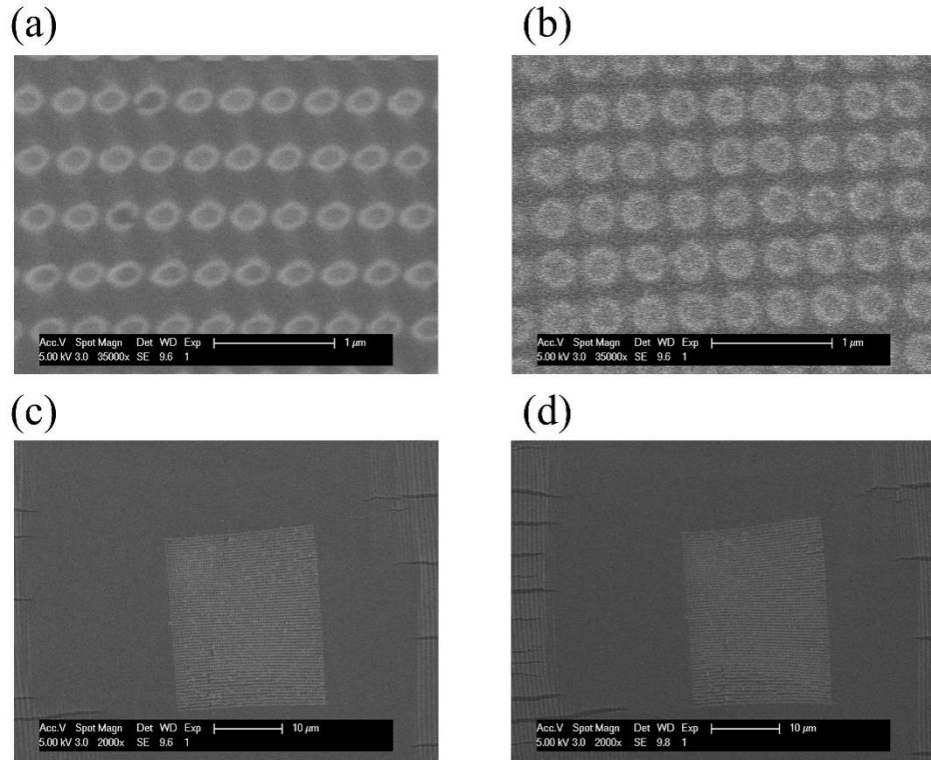
Figure 3-5 Set of SEM images explaining the drifting (a, b) and freezing effects (c, d) on PDMS.

### 3.5.2 Low-voltage operation

A *Zeiss Crossbeam Auriga* 40 SEM is used for imaging on PDMS. To reduce charging effects, an acceleration voltage of 1kV is used. Frame averaging with drift compensation is applied for recording the presented images. However, in order to measure the dimensions of the nanostructures correctly, images without averaging are used to prevent artifacts due to charging or drift. (Acknowledgement to Jonas Haas for introducing me to the *Zeiss* set-up at the NMI Institute in Reutlingen, Germany. His technical support and collaboration have been instrumental in capturing high-quality images on PDMS.)

### 3.6 Simulation methods

The Finite-Difference Time-Domain (FDTD) method is a numerical technique to simulate the electromagnetic behaviors in materials by solving Maxwell's equations. We adopt the commercial software of *Lumerical FDTD Solutions* for FDTD

calculations. The geometric parameters of the Au structures follow the top-view SEM characterizations. The refractive index for Au is taken from Johnson and Christy. [158] Based on experience, the indexes for PDMS and ITO are of constant values of about 1.4 and 1.9, respectively. To simplify the ring-shaped dark-field incidences, four separate oblique total-field scattered-field (TFSF) incidences placed at 90° to each other are set. The incidence angle to the injection axis is $\theta = 56.75°$. In most cases, a 3D perfectly matched layer (PML) boundary condition is introduced. The plasmonic scattering ability is characterized by simulating the full scattering cross section of the structures. By assuming the material as pure plasma, the pre-set *diverging current* script in *Lumerical* plots the charge density distribution on the surface of the structure.

To summarize, we first adopt the EBL method to prepare Au structures on a silicon wafer covered by a sacrificial layer of Cr. Suitable patterns are confirmed via SEM and then selected to transfer onto PDMS by Cr wet-etching. These transferred samples are subsequently mounted on a micro-stretcher, and subjected to in-situ optical tests at various strains. Finally, we employ two strategies to perform the SEM test to visualize transferred patterns on PDMS. In Chapter 4, PDMS is sputtered with an Au film to monitor the mechanical responses of the NR arrays under different strains, while in Chapter 5, PDMS is directly stretched to the final strain, and SEM testing was performed at low voltage without any conductive layer.

# Chapter 4 Active Tuning of LSPR for in-situ Shape-altering Au Nanoring Metasurfaces on PDMS

As stressed in Chapter 1, plasmonic nanoring (NR) antennas have gained considerable research interest due to their inherent symmetric and hollow structure. Conventional studies on NRs are performed on rigid substrates involving fabrication methods ranging from e-beam and nanosphere lithography to recent colloidal synthesis. In this chapter, we fabricate well-ordered Au NR arrays on the PDMS substrate profiting from the advance in flexible plasmonics. The NR arrays are designed with varying widths and radii, and their shape-altering capabilities under stretching the PDMS are investigated in detail. Since the LSPR of NPs significantly depends on their geometries, [159-160] NR arrays with strain-induced changes in aspect ratio can be distinguished by monitoring the far-field spectra. In the following sections, we perform SEM characterizations on PDMS to confirm such in-situ deformation of NRs. Numerical simulations and plasmonic hybridization models are also carried out to explain the optical behavior of the deformed NRs. Finally, we expand the scope of the current study and carefully examine the shape-altering of NRs under different transferring methods or with varying periods and sizes. In general, by comparing the effect of in-situ deformed NRs on their spectral behavior, the main purpose of this chapter is to explore the possibility of shape-altering flexible plasmonics induced by hollow NPs.

Partial results and related figures (Figures 4-1 to 4-5 and Figures 4-7 to 4-10) have been published in the journal article (Reproduced with permission from Springer Nature): [161]

*Tao, W., Laible, F., Hmima, A., Maurer, T., & Fleischer, M. (2023). Shape-altering flexible plasmonics of in-situ deformable nanorings. Nano Convergence, 10(1), 15.*

## 4.1 Dark-field reflection characterization

The geometry of Au NR arrays is schematically depicted in Figure 4-1 (a), controlled by periods along the x- and y-axis of *Px* and *Py*, center diameters of *Dx* and *Dy*, a height of *H*, and a width of *W*. By assuming the x-axis as the future stretching

direction, the aspect ratio (AR) of a NR is determined by AR = $Dx$ / $Dy$. Figures 4-1 (b-d) show the top-view SEM images for three NR arrays deposited on Si/Cr wafers, namely NR1, NR2, and NR3. Table 4-1 presents the nominal and measured geometric parameters of the three NRs. The parameters $Px$, $Py$, $Dx$, and $Dy$ are designed using pattern files in EBL. The parameter $H$ is controlled by the evaporator, while $W$ represents the average widths of all rings measured in both the horizontal and vertical axes on the three SEM images depicted in Figure 4-1. These rules also apply to Table 4-3 and Table 4-4.    Note that the SEM characterizations are performed on Si/Cr, and optical measurements are carried out once these NR arrays are transferred onto PDMS.
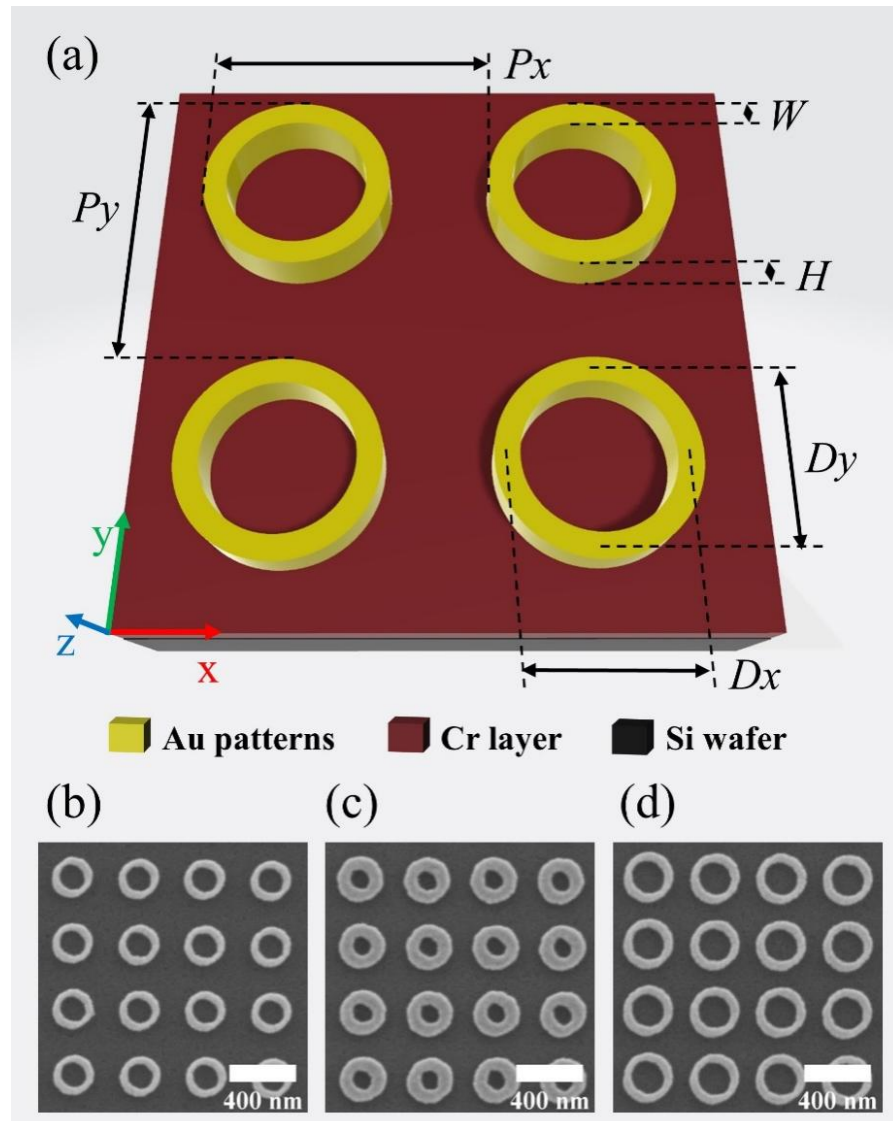


Figure 4-1 Schematic of Au NR arrays deposited on the Si/Cr substrate (a). SEM images of the three NR arrays on Si/Cr, named NR1 (b), NR2 (c), and NR3 (d). The figure is modified after Ref [161].

Table 4-1 Geometric parameters of the three NR arrays in Figure 4-1

| NR arrays | Designed Px [nm] | Designed Py [nm] | Designed Dx [nm] | Designed Dy [nm] | Controlled H [nm] | W [a) [nm] |
|---|---|---|---|---|---|---|
| NR1 | 400 | 400 | 200 | 200 | 50 | 49 ± 7 |
| NR2 | 400 | 400 | 200 | 200 | 50 | 83 ± 6 |
| NR3 | 400 | 400 | 250 | 250 | 50 | 56 ± 6 |

[a)](W = Avg ± Sd, where Avg and Sd are the average and standard deviation values.)

The three NR arrays are then transferred onto PDMS, which is further mounted in a micro-stretcher to measure their optical properties under strain. Two linear polarizations are introduced during the optical characterizations, where transverse and longitudinal polarizations (TP and LP) refer to the polarized directions that are perpendicular or parallel to the uniaxial stretching. Figure 4-2 shows offset plots of dark-field reflection spectra of the three NR arrays under strain, with the polarization conditions schematically illustrated in the top-right figures. Unless otherwise noted, the strain values in the spectral plots in Chapters 4 and 5 exactly refer to grating strains with a step of 10% engineering strain value (e.g., $\varepsilon = \varepsilon_{grtg} = 45\%$ refers to $\varepsilon_{engr} = 50\%$). On the one hand, the spectra in Figure 4-2 outline a set of broad LSPR modes denoted by circles, where the solid ones indicate the highest LSPR intensities. In addition to the main LSPR mode peaking at 680 nm, NR1 shows also a second LSPR mode (marked with an open circle, at 820 nm) at the strain of $\varepsilon = 0$ under both polarizations. These two modes gradually merge into a single peak with applied strains, which further redshifts to a longer wavelength as strain increases. The average redshift value of the main LSPR modes for NR1-TP can be quantified as 2.85 nm per 1% strain ($\Delta\lambda = (804 - 675.8)$ nm / 45% = 2.85 nm/%), which is higher than that observed in conventional gap-altering flexible plasmonic devices, i.e., up to ~2 nm/%. [162] A similar spectral trend can be found for NR1-LP, while the redshift effect shows less sensitivity to a high strain value ($\varepsilon \geq 29\%$). Furthermore, it is observed that the spectral behaviors significantly depend on the geometries of the NR. Increasing the width from ~49 nm (NR1) to ~83 nm (NR2) results in constant LSPR modes upon strain, located at ~750 nm for NR2-TP and ~760 nm for NR2-LP, respectively. Since NR3 shares the same period and a similar width with NR1, its grating and NR shape development exhibit similarities under strain (discussed in the following sections). An increased diameter of NR3 from 200 to 250 nm brings the emergence of three LSPR modes at $\varepsilon = 0$, which display fluctuations in their peak positions as strain develops.

However, in terms of intensity weights, a discernible redshifting trend can still be observed for the main LSPR modes under both polarizations.
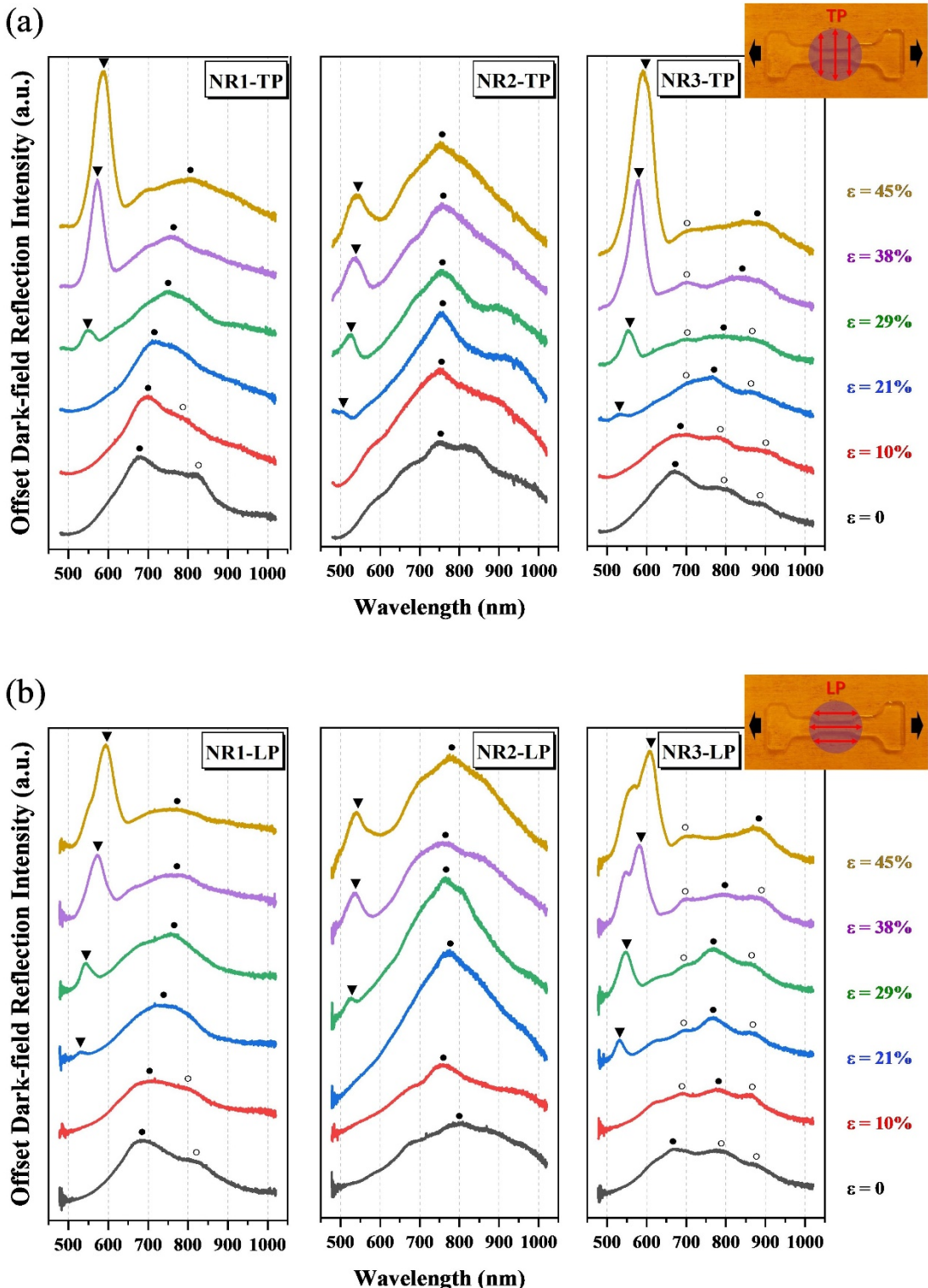


Figure 4-2 Plots of dark-field spectra evolution for NR1, NR2, and NR3 arrays under transverse (a) and longitudinal polarizations (b), with the grating and LSPR modes marked with triangles and circles. The solid and open circles indicate the main and

side LSPR modes. The top-right figures in (a) and (b) display the direction of stretching and polarization conditions using black and red arrows, respectively. The figure is adapted from Ref [161].

To distinguish between the narrower peaks and LSPR ones as depicted in Figure 4-2, we conduct another optical test on EBL-fabricated Au disc arrays deposited on a rigid glass/ITO substrate. Figures 4-3 (a-d) show the top-view SEM images for the four arrays, indicating diameters of $(173 \pm 3)$, $(188 \pm 3)$, $(203 \pm 7)$, and $(463 \pm 11)$ nm, respectively. These statistic values are obtained by measuring and averaging the diameters of all discs in the SEM images in the horizontal and vertical directions. These arrays share a constant $Px = Py = 500$ nm and $H = 50$ nm. Figure 4-3 (e) shows the unpolarized spectra for these arrays characterized via the same dark-field spectrometer. As the period increases from 400 nm for the NR array to 500 nm in this case, the spectrum outlines a set of Bragg grating peaks at ~575 nm. The characteristic of the Bragg modes is that the peak position is only related to the period and is independent of the geometric size, while the resonance width increases with the diameter. We have now confirmed that in Figure 4-2, the narrow peaks at wavelengths from 530 to 600 nm at $\varepsilon > 21\%$ are grating modes (i.e., Bragg reflection modes), [80, 163] as the strain-induced period variations satisfy the resonance conditions. The redshift trends also indicate that the initial grating modes for the three NR arrays are located in the ultra-violet region, which is beyond the detection scope of the current spectrometer. Furthermore, NR1 and NR3 arrays show similar redshifts to ~600 nm at $\varepsilon = 45\%$, while the NR2 array with a thicker width reduces the grating development under strain, leading to only a redshift to ~ 545 nm in the final state. In addition, the spectra of NR3-LP present a coupling between the Bragg and LSPR mode at $\varepsilon \geq 38\%$. The resulting Surface Lattice Resonances (SLR) are then discussed in Chapter 5.
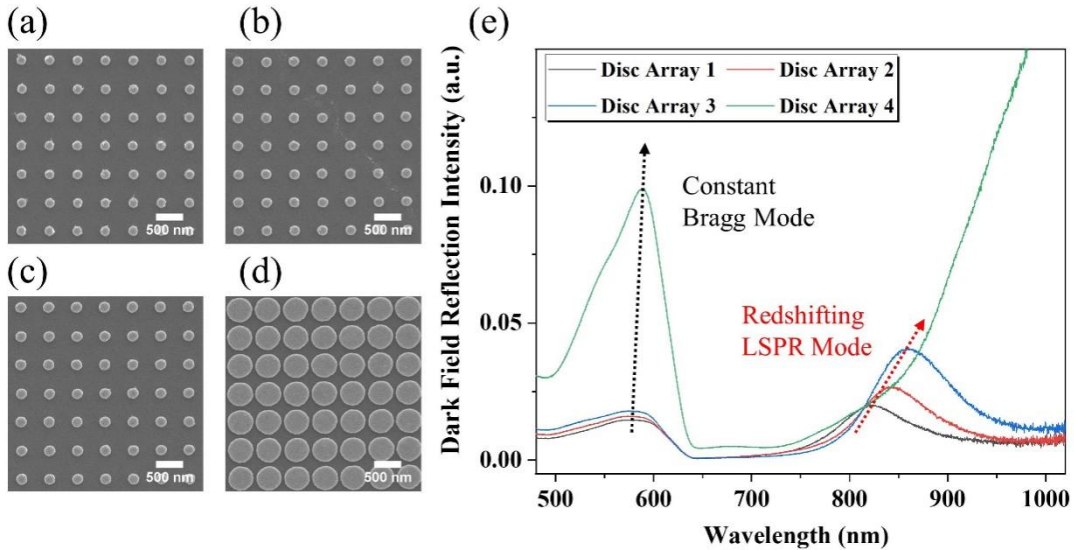
Figure 4-3 Set of disc arrays on a glass/indium-tin-oxide substrate, with respective diameters of $(173 \pm 3)$ nm (a); $(188 \pm 3)$ nm (b); $(203 \pm 7)$ nm (c); and $(463 \pm 11)$ nm (d). Their periods are maintained at 500 nm. Dark-field reflection spectra of the four disc arrays (e), indicating a basically constant Bragg mode and redshifting LSPR mode. The figure is modified after Ref [161].

## 4.2 In-situ SEM characterization on PDMS

Through a comparison of the spectra of NR1 and NR2, it is known that the thinner NR1 array presents a larger grating development under strain, and its LSPR mode exhibits a merging and redshifting trend as the strain increases further. We speculate the reason may be the strain-induced change in the aspect ratio (AR) of NR1, despite of the huge modulus difference between ~69.1 GPa for nanostructured Au and ~2.6 MPa for PDMS. [164-165] Therefore, an in-situ SEM characterization on PDMS for the three NR arrays is necessary to confirm the shape-altering deformability. Figures 4-4 (a-c) show the SEM images of the three NR arrays on Si/Cr before transferring, and on PDMS at engineering strain values of $\varepsilon_{engr}$ = 0, 20%, 40%, respectively. Although these SEM images drift a lot, a slight shape change in NR1 is outlined by the red ellipse at $\varepsilon_{engr = }$ 40%. Therefore, Figures 4-4 (d-f) show a quantitative evaluation of the NRs' diameters in the three arrays, where the longitudinal and transverse ones refer to those parallel or perpendicular to the stretching. It is noted that both transverse and longitudinal diameters of the three NRs do not differ considerably on Si/Cr, but after transfer, the transverse diameters of all three NRs are significantly larger than the longitudinal ones. This is possibly due to the image drifts over SEM

measurements, which produce artifacts along the transverse direction. In this context, an approximately linear increase in the longitudinal diameter of NR1 and a decrease in transverse diameter can still be observed, resulting in a steady increase in AR under strain. However, NR2 with an increased width does not deform under strain, while the transverse and longitudinal diameters show only fluctuations. In addition, the AR of NR3 increases from $AR_{\varepsilon=0} = 275.5 / 317.9 = 0.87$ to $AR_{\varepsilon=20\%} = 282.8 / 299.7 \approx 0.94$ at low strain values, while it remains constant ($AR_{\varepsilon=40\%} = 274.1 / 291.5 \approx 0.94$) as strain further increases. The relatively low deformability of NR3 may be attributed to the reduction in the "free space" along the uniaxial tension, i.e., grating period minus diameter. Finally, it should be noted that the deformability of NRs on PDMS is significantly limited due to the hardening of PDMS under SEM imaging and the existence of the rigid conductive layer. By fabricating another NR array with a thin width, the shape-altering ability under applied strain to PDMS is also confirmed in Section 4.4. (Acknowledgement to Dr. Florian Laible for conducting the PDMS imaging using the *Philips* SEM)
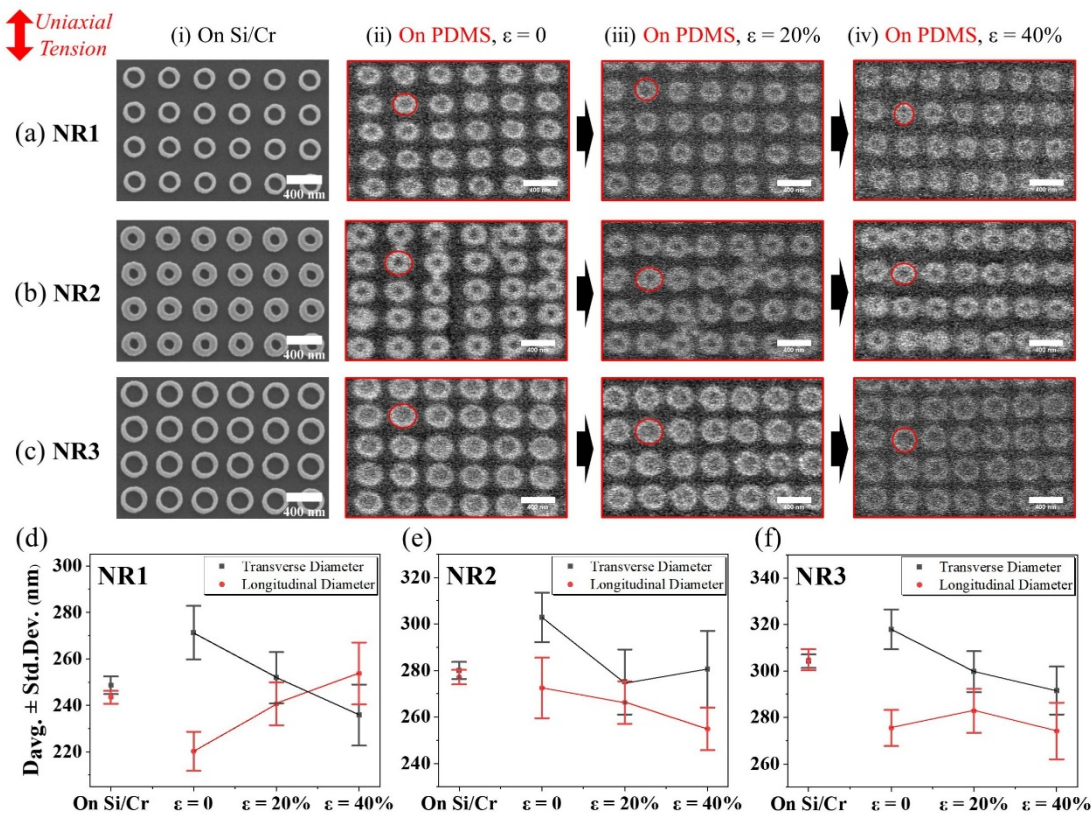


Figure 4-4 Set of SEM images of the three NR arrays with controlled scale bar of 400 nm, where column (i) displays to the structures on Si/Cr before transfer and (ii-iv) depict those on PDMS at different strain values. The red lines in column (ii-iv) outline the shapes of individual NRs within their grating. The statistical evaluation of the

three NRs (d-f), where the diameter here is defined as the distance between the outer walls of the NRs. The figure is adapted from Ref [161].

## 4.3 Numerical simulations

### 4.3.1 NR1 under normal incidence

We start by discussing the optical behaviors of linear antennas such as nanorods. The LSPR modes for nanorods with a negligible width under normal incidence (with polarization along its long axis) can be described by the standing-wave model as follows, [53, 166-167]

$$\lambda_{nanorods} = \frac{2Ln}{m} \tag{4-1}$$

where L, m and n are the geometric length, multipolar order (e.g., m = 1 refers to a dipolar mode), and surrounding refractive index, respectively. A nanoring (NR) can be considered as a bent nanorod with a head-to-tail connection. Then, the LSPR bonding modes of NRs follow a similar description of the standing-wave model:

$$\lambda_{NRs} = \frac{2L^*n}{m} \tag{4-2}$$

where $L^*$ refers to the effective length of NRs. The geometric length for a nanorod is schematically depicted in Figure 4-5 (a); while the effective length for a NR can be approximated as either a central circle or an ellipse connecting the outer and inner walls of a NR, as shown in Figure 4-5 (b). [53, 167] Note that the difference between the two approximations in effective lengths is due to the non-negligible widths of NR antennas.
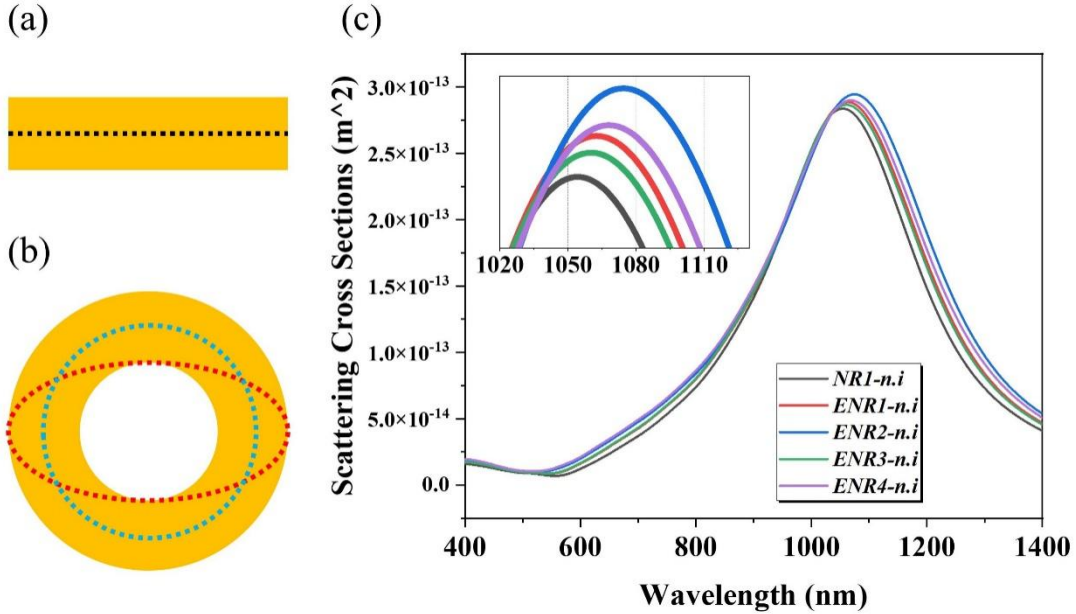
Figure 4-5 Schematic of effective lengths of a nanorod (a) and NR (b). The black dotted line shows the geometric length of a nanorod, while red and blue ones denote the path of the charges as a center circle or an ellipse connecting the NR's outer and inner walls. These models are taken from references by Apter et al. [167] and Cai et al. [53]. Simulated spectra of NR1 and set of ENRs under excitation at normal incidences polarized along the horizontal axis (c). Figures (a-b) is modified after Ref [161].

Therefore, when the AR of a NR increases (i.e., NR changes to ENR), the redshift effect of the LSPR reported in the literature may be due to the change in the effective length of the NR. [159] Hence, we design four different ENRs evolving from the geometrical parameters of NR1, and perform FDTD simulations for these systems under an excitation at normal incidence polarized along the ENR's long axis. Their geometric parameters are shown in Table 4-2, and corresponding spectra are presented in Figure 4-5 (c). We approximate the perimeter of the ellipse ($P$) using the Euler equation as follows, where $a$ and $b$ refer to the radii of the long and short axes of the ellipse. [168]

$$P \approx \pi * \sqrt{2(a^2 + b^2)} \qquad (4-3)$$

From NR1 to ENR1 and ENR2, we maintain a constant center perimeter and increase $Dx$ from 200 to 220 nm. The resulting ellipse perimeter increases from 1266.4 to 1282.9 nm leading to a slight redshift of the LSPR peak from 1054 to 1062 nm, as shown in Figure 4-5 (c). In contrast, the ellipse perimeter remains unchanged from NR1 to ENR3 and ENR4, while one can still observe a redshift in the spectra from

1054 to 1074 nm regardless of the decreasing center perimeter. Our simulation results partially confirm the previous work by Cai et al. [53] that the LSPR redshift could result from the increase of the elliptical charge path of NR. In addition, Valle et al. concluded that the increasing bending level (i.e. AR) results in a bending of the plasmonic currents, [169] and consequently, the enhanced magnetic response in ENRs forbids the electric radiation, leading to a spectral redshift as a function of the increasing AR. This qualitative description can well explain the results observed in simulations, but the quantitative analysis is also necessary in future work.

Table 4-2 Geometric parameters and simulation results of NR1 and set of ENRs.

| NPs | T [nm] | H [nm] | Dx [nm] | Dy [nm] | Aspect Ratio | Center Perimeter [nm] | Ellipse Perimeter [nm] | LSPR peak [nm] |
|---|---|---|---|---|---|---|---|---|
| NR1 | 50 | 50 | 200 | 200 | 1 | 1256.6 | 1266.4 | 1054 |
| ENR1 | 50 | 50 | 210 | 189.5 | 1.11 | 1256.7 | 1274.5 | 1060 |
| ENR2 | 50 | 50 | 220 | 177.8 | 1.24 | 1256.7 | 1282.9 | 1062 |
| ENR3 | 50 | 50 | 210 | 186.3 | 1.13 | 1247.2 | 1266.4 | 1068 |
| ENR4 | 50 | 50 | 220 | 170.7 | 1.29 | 1237.2 | 1266.4 | 1074 |

Apart from the bonding modes, in NRs with a non-negligible width a high-energy antibonding LSPR mode can also be excited. Building on the previous work by Prodan et al, [170] we plot a Plasmonic Hybridization (PH) diagram of NRs excited by normal incidence in Figure 4-6. In line with literature, the antibonding and dipolar bonding modes are due to hybridization between cavity and disc plasmons in NRs, while the multipolar bonding modes are derived from the standing-wave model. The diagram is also supported by Ref [53, 171].
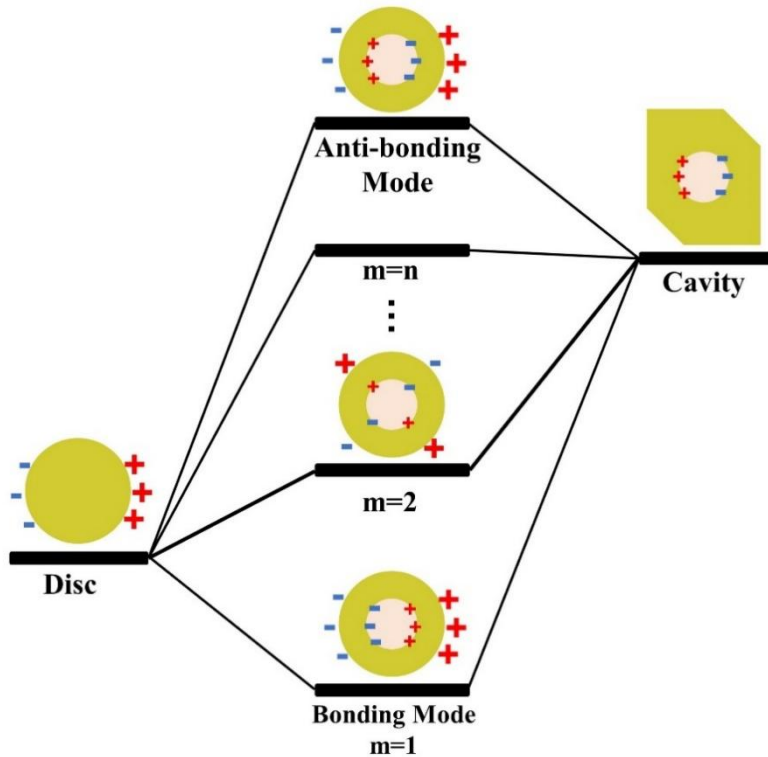
Figure 4-6 Energy diagram of the anti-bonding and set of bonding modes of NRs resulting from the plasmonic hybridization between disc and cavity plasmons. The figure is modified after Ref [170].

**4.3.2 NR1 under dark-field incidence**

The above results suggest that, under normal incidence, the increasing AR of NR1 leads to a spectral redshift of its LSPR mode. However, the simulation results do not directly indicate the experimentally observed LSPR modes as shown in Figure 4-2. The underlying reason is that the excitation of NRs under dark-field incidence cannot be simplified to normal excitation. As illustrated in Ref [166], the oblique incidence will excite additional LSPR modes (with even bonding level m) for linear nanorods, which is more dominant for bent nanorods, particularly for the high-curvature NRs. Here, in line with literature, [172] we approximate cone-shaped dark-field illumination as four separate oblique plane-wave beams with incidence angles of $\theta = 56.75°$ to the normal (corresponding to the average angle of the darkfield condenser), as depicted in Figure 4-7 (a). Among these beams, the front and back ones are s-polarized where the E-fields are aligned with the x-direction, while the beams on the left and right are p-polarized and their E-fields direction presents a $\theta$ angle with the object plane. As shown in Figure 4-7 (b), the simulation curve agrees well with the experimental one, indicating two respective LSPR peaks at 675 and 759 nm. The surface charge maps in

Figure 4-7 (c) show the same bonding levels of m = 2 for the two LSPR modes. The main LSPR peak reveals a radially symmetric charge distribution, while the second mode has an asymmetric distribution.
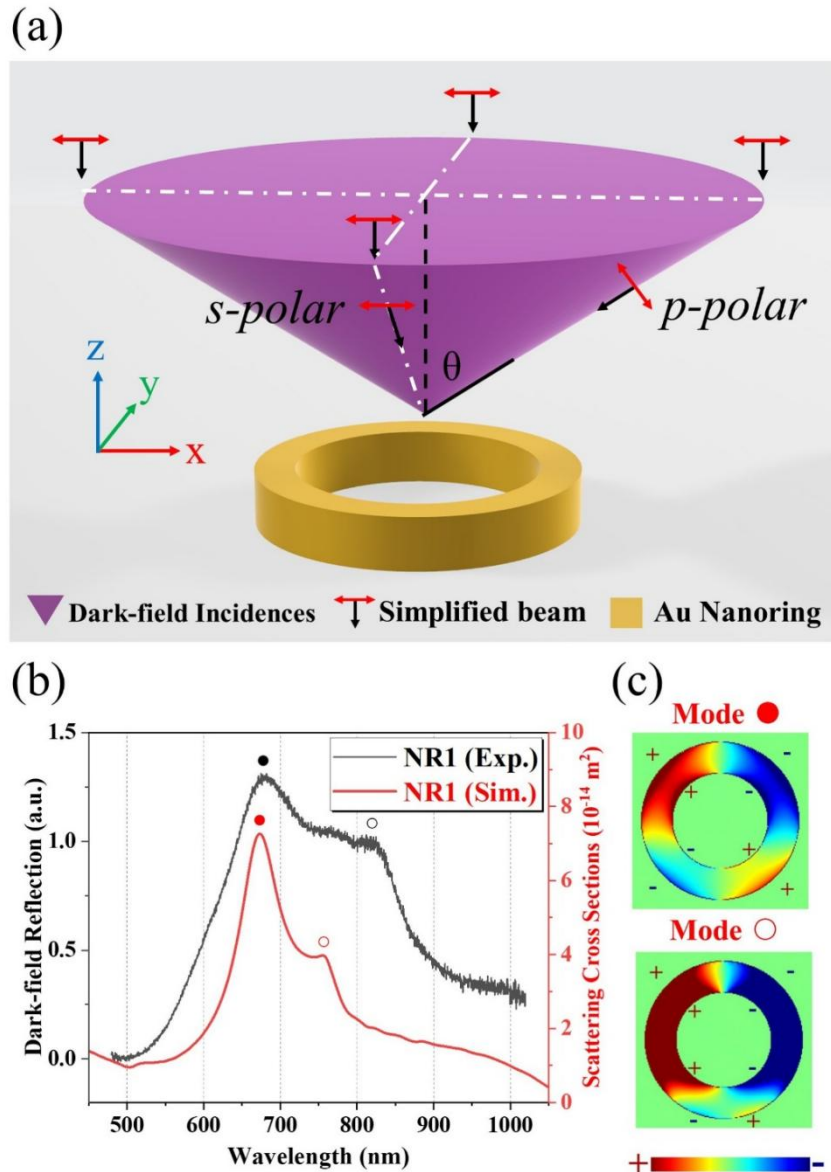


Figure 4-7 (a) Schematic of the dark-field illumination, where the cone-shaped dark-field incidence is simplified as four separate beams. (b) Comparison spectra between experiment and simulation for NR1-TP (b), and (c) surface charge distributions for the two simulation LSPR modes. The figure is modified after Ref [161].

## 4.3.2 NR1 array under strain

To simulate the spectral evolution of NR1 arrays on PDMS when subjected to strain, we consider two main influencing factors: the spacing variation between adjacent NRs and shape variation in NRs. The spacing variation is obtained by calculating the average of the strain-induced lattice period under strain. Due to the high elasticity of PDMS at the strain $\varepsilon < 100\%$, consistent with previous research, [79, 81] we assume that the longitudinal and transverse periods of NR arrays under strain ($Px^\varepsilon$ and $Py^\varepsilon$) follow an elastic relationship:

$$Px^\varepsilon = Px * (1 + \varepsilon) \qquad (4\text{-}4)$$

$$Py^\varepsilon = Py * (1 - \nu\varepsilon) \qquad (4\text{-}5)$$

where $Px$ and $Py$ are the initial array period of 400 nm, and $\nu = 0.5$ sets the constant Poisson ratio of PDMS. The continuous grating development can be confirmed by either measuring the linear redshift of the Bragg mode or by directly observing the grating development during the optical tests (e.g., Figure 3-3 (c, f)).

On the other hand, due to the PDMS hardening effect under SEM imaging and the presence of the rigid conductive layer, capturing the exact shape-altering states of NR1 at each strain shows significant challenges. To examine the shape-altering effect, we conduct two different simulation studies: *deformed* and *undeformed* NR arrays. Figure 4-8 shows the top-view simulation models with a finite 5 * 5 array introduced for the two cases, which share the same elastic grating development under strain, as described above.
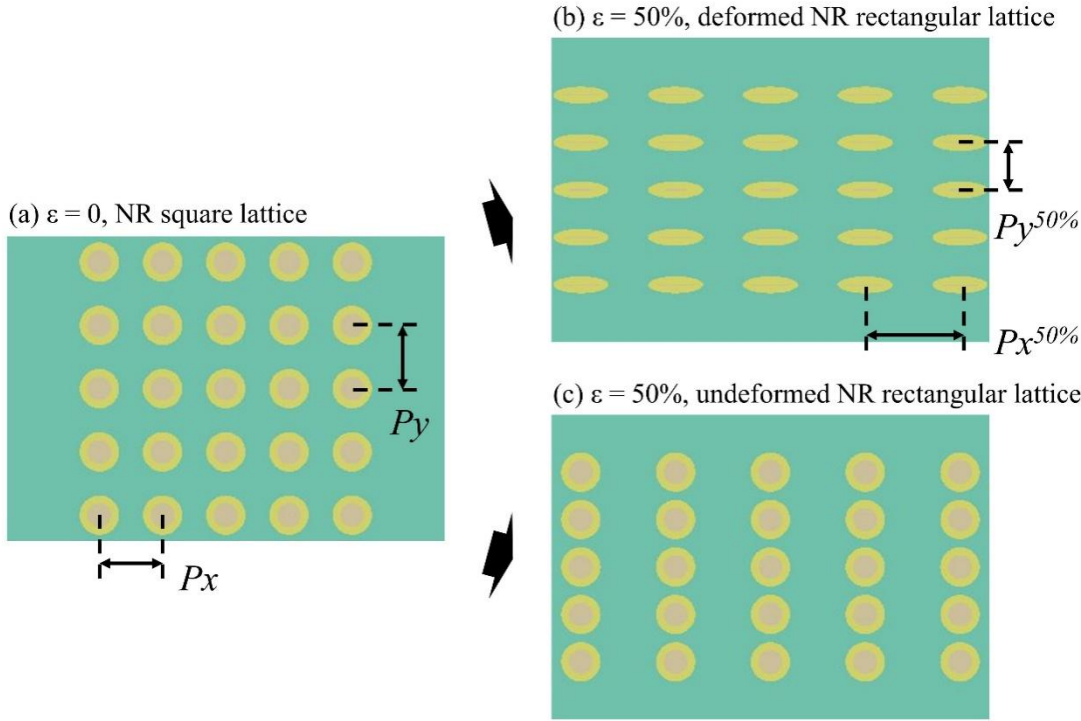
Figure 4-8 Elastic grating development of a finite 5 * 5 NR array depicted by the software layout of *Lumerical FDTD solutions*. Figure (a) sets the initial state of the NR grating, where (b) assumes shape changes for individual NRs, and (c) suggests undeformed NRs under strain. The figure is adapted from Ref [161].

In order to study the shape-altering ability of the deformed NR1 arrays, we make several assumptions as follows. Specifically, (1) the width *W*, the height *H*, and the central perimeter *P* of NR1 remain constant over strain owing to the high modulus of Au; (2) the longitudinal diameter aligned to the uniaxial tension ($Dx^\varepsilon$) deforms elastically under strain; and therefore (3) the transverse diameter ($Dy^\varepsilon$) is calculated by Euler approximation by introducing the constant P and the deformed $Dx^\varepsilon$. Therefore, the shape-altering ability is quantitatively described by $Dx^\varepsilon$ and $Dy^\varepsilon$ using the following equations, and is depicted in Figure 4-9.

$$Dx^\varepsilon = Dx * (1 + \varepsilon) \tag{4-6}$$

$$Dy^\varepsilon = \sqrt{\frac{P^2}{2\pi^2} - \left(Dx^\varepsilon\right)^2} \tag{4-7}$$

(a) $\varepsilon = 0$   (b) $\varepsilon = 10\%$   (c) $\varepsilon = 20\%$

(f) $\varepsilon = 50\%$   (e) $\varepsilon = 40\%$   (d) $\varepsilon = 30\%$

$Dx^{50\%}$   $Dy^{40\%}$   constant $P$ under strain
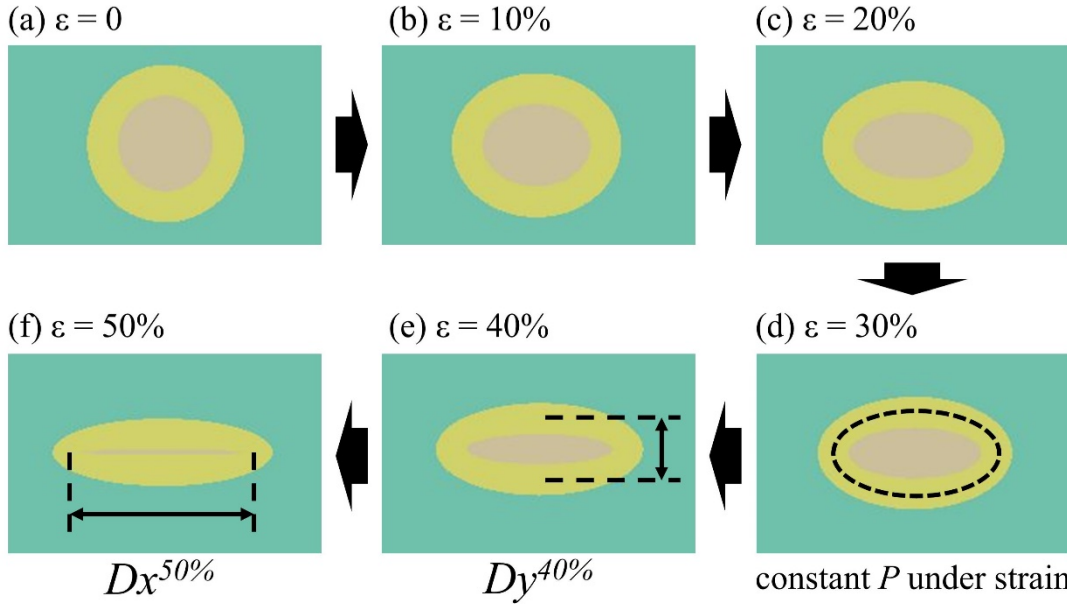
Figure 4-9 Shape-altering of NR1 for the simulation of *deformed* NR arrays, depicted by the software layout of *Lumerical FDTD solutions*. The figure is adapted from Ref [161].

Finally, Figure 4-10 presents the comparison between the experimental NR1-TP spectral and simulation results of *deformed* and *undeformed* NR1 arrays. The simulation curve is obtained by calculating the overall scattering cross section of the 5*5 array under the excitation of a single s-polarized beam under transverse polarization. The simulated spectral evolution for *deformed* NR1 arrays in Figure 4-10 (b) shows a good agreement with the experiment results in (a). Despite the fact the main LSPR modes (marked with red solid circles) remain constant at low strain values (peaking at 670 nm at $\varepsilon = 0$, 10% and 20%), it rapidly redshifts from 670 nm at $\varepsilon = 30\%$ to 735 nm at $\varepsilon = 50\%$ due to abrupt shape changes at high strain values as shown in Figure 4-9. In addition, the second LSPR mode of the *deformed* NR array (red open circles) witnesses a gradual weakening trend under strain, and eventually disappears at $\varepsilon = 30\%$. By contrast, the simulation curve for *undeformed* NR1 array in Figure 4-10 (c) shows only a slight redshift from 670 nm at $\varepsilon = 0$ to 683 nm at $\varepsilon = 50\%$ for the main LSPR mode, and an unchanged second mode over strain. It is obvious that the spectral evolution of *undeformed* NRs is more in line with that of NR2-TP in Figure 4-2. Since NR2 with thicker width limits the strain-induced grating development, it results in a milder gap-altering redshift effect for the main LSPR mode in NR2, which eventually behaves as a constant mode under strain, as shown in Figure 4-2. Furthermore, by comparing Figure 4-7 (b) and Figure 4-10 (b), it is

confirmed that when NRs develop into ENRs under strain, the radially symmetric bonding mode exhibits a significant redshift with the increasing AR of the NR. Meanwhile, the asymmetric bonding mode is more sensitive to the circularity of NRs, and it tends to subside with an increasing AR of ENRs. These observations highlight the dependence of LSPRs on the morphology of NPs. More importantly, the plots in Figure 4-10 (b) and (c) also illustrate that the high redshift effect for NR1-TP (2.85 nm per 1% strain) is mainly due to the shape change of NR1 rather than the spacing variation. This result suggests that shape-altering flexible plasmonics have strong potential in spectral guiding compared to conventional gap-altering ones.
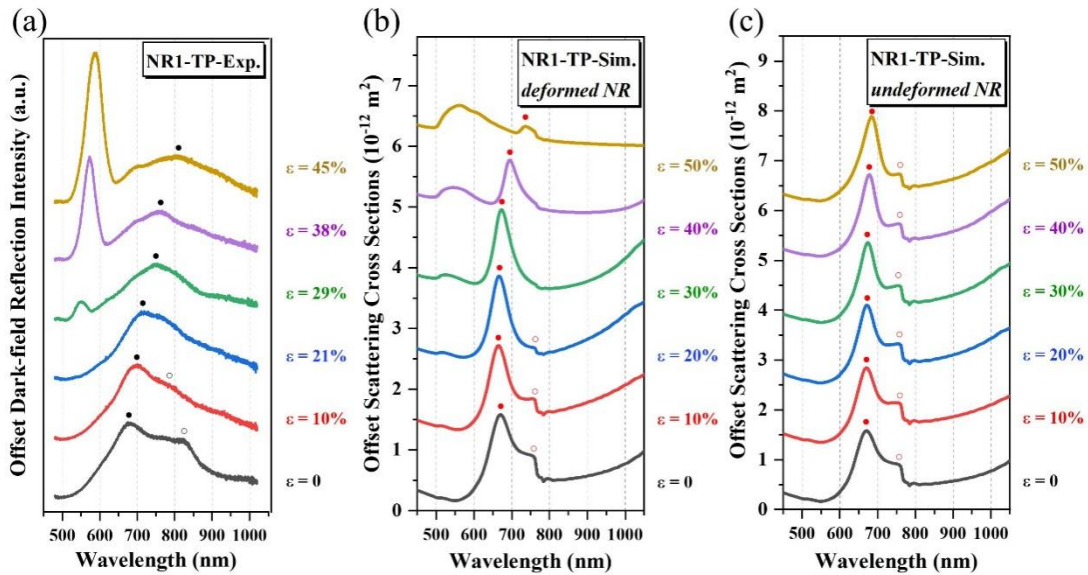


Figure 4-10 Comparison between NR1-TP spectra in experiments (a) and simulations of *deformed* (b) and *undeformed* NR arrays (c). The figure is adapted from Ref [161].

## 4.4 A mechanical squeezing model for explaining the shape-altering ability

### 4.4.1 NR arrays with a large period

By comparing the spectral evolution in experiments and simulations and performing SEM testing of NRs on PDMS, the above sections demonstrate the strain-induced shape-altering capability of NRs with thinner widths and proper "free space" (i.e. grating period minus diameter). Although NR1-TP exhibits a larger redshift for LSPR peaks, its grating modes with higher intensity hinder prospects in potential sensing applications. To address this, we utilize the same fabrication method to prepare another three NR arrays with increased period of Px = Py = 2000 nm, namely A1, A2,

and A3 arrays, on PDMS. The SEM characterization of these arrays on Si/Cr substrates is shown in Figure 4-11 and the parameters are listed in Table 4-3. The experimental spectra of the three arrays in Figure 4-11 do not present obvious grating modes under strain due to the increased period. As for the LSPR, at $\varepsilon = 0$, all the experimental curves are in qualitative agreement with the simulation results, confirming the transfer feasibility and spectral reliability. However, no obvious LSPR shift is found for the three arrays under strain.
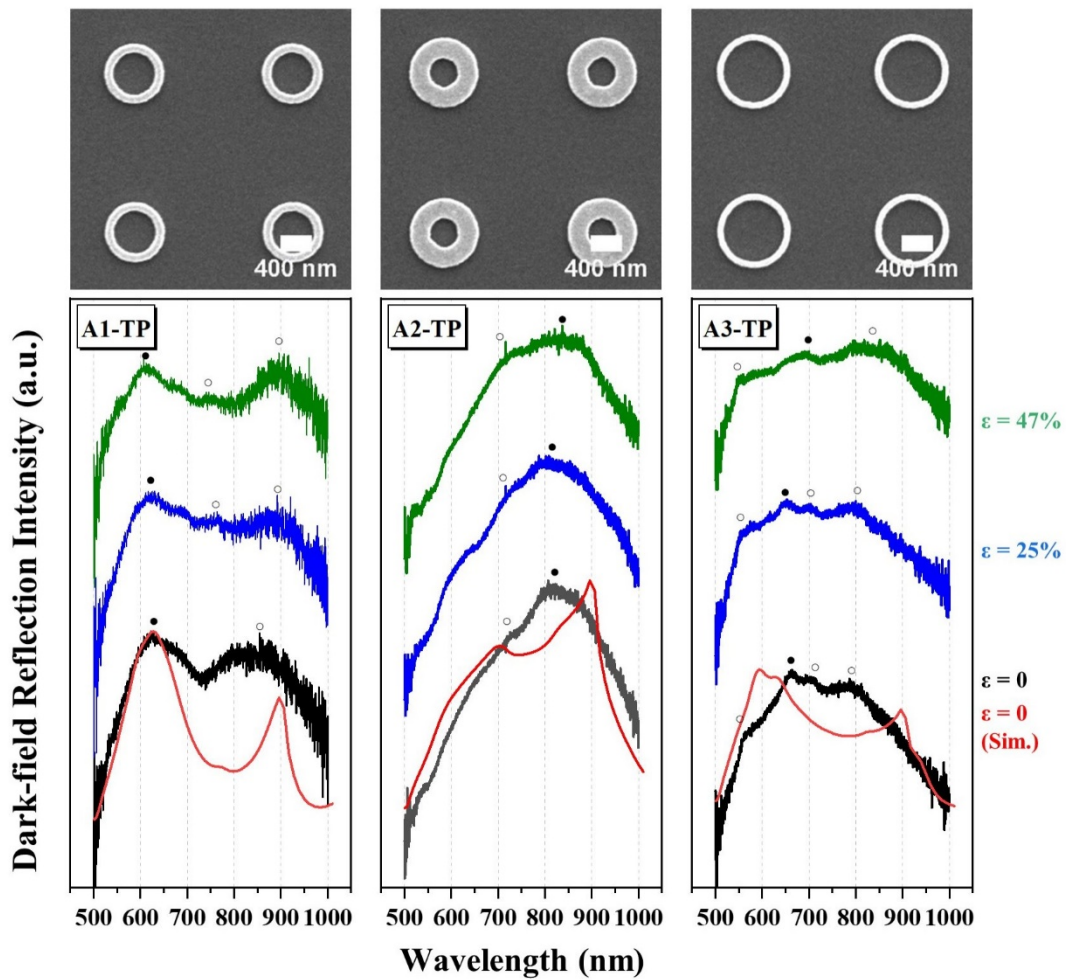


Figure 4-11 SEM images (top figures) and corresponding dark-field reflection spectra of A1, A2 and A3 NR arrays under strain. The scale bar for images is maintained at 400 nm. The red curves in the bottom plots are the normalized simulation results of single NRs.

Table 4-3 Geometric parameters of A1, A2, A3, and A4 NR arrays

| NR arrays | Designed Px [nm] | Designed Py [nm] | Designed Dx [nm] | Designed Dy [nm] | Controlled H [nm] | W [nm] |
|---|---|---|---|---|---|---|
| A1 | 2000 | 2000 | 325 | 325 | 50 | $117 \pm 6$ |
| A2 | 2000 | 2000 | 325 | 325 | 50 | $263 \pm 7$ |
| A3 | 2000 | 2000 | 425 | 425 | 50 | $82 \pm 5$ |
| A4 | 2000 | 2000 | 425 | 425 | 50 | $38 \pm 4$ |

Based on the spectral evolution, we suspected that none of the three NR arrays undergo obvious shape-altering when strain is applied to their substrate. To confirm this, we use the CCD camera in the microscope to observe the A3 array at a 20x magnification under different strains, as shown in Figure 4-12 (a). Despite the inability to capture shape changes in NRs, we are able to distinguish individual NRs in the A3 array due to the increased period. These figures confirm a uniform grating development as strain increases. However, by calculating the longitudinal and transverse strain separately based on Equations (4-4) and (4-5), it is found that the percentage change of the strain value derived from the transverse shrinkage is smaller than that of the longitudinal elongation. This non-elastic deformation for the NR grating indicates localized confinements of individual Au NRs owing to its high modulus compared to PDMS. Furthermore, we fabricate an A4 array on PDMS with geometries listed in Table 4-3. The abrupt decrease in the width of $(38 \pm 4)$ nm enables a direct observation on the NRs' shape at 100x magnification. The results in Figure 4-12 (b) show that for the thinner A4 NR array, its shape does not produce any significant deformation even at a strain reaching 57%. Through a comparison of the deformable NR1 and the undeformable A4 arrays, we propose a mechanical "squeezing" model to explain the shape-altering ability of Au NRs on PDMS. A sufficient condition for the shape-altering of Au NRs is that the embedded NRs in PDMS should be densely distributed. As the stretching PDMS leads to a grating development, it is possible for the NRs to squeeze each other to overcome local confinement and deform in the shapes. The squeezing model is supplemented in Section 4.4.2.
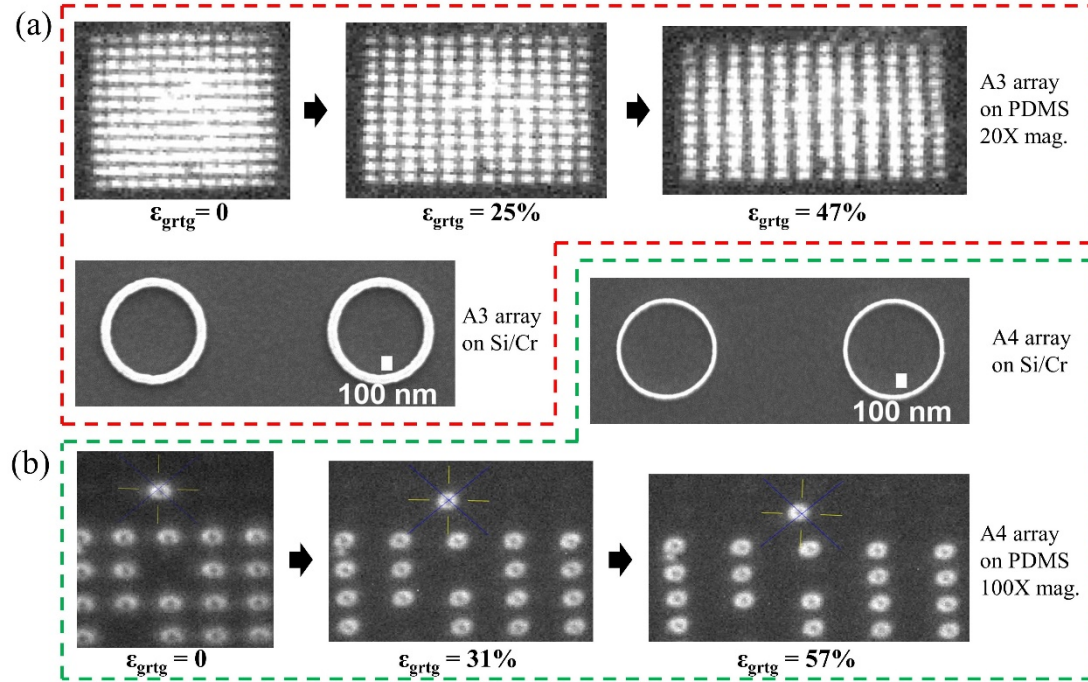
Figure 4-12 Optical microscope imaging on A3 with strains under 20X magnification (a), and A4 under 100x magnification (b). For both figures, the applied strain is aligned with the horizontal direction.

## 4.4.2 NR arrays fabricated via a cured modeling

As an extension of the fluid transfer method, we employ the cured transfer technique to fabricate a series of NR arrays onto PDMS, i.e., B1, B2 and B3 arrays, as show in Figure 4-13. Note that for the cured transfer method, NRs are deposited on the PDMS surface instead of being embedded. Table 4-4 lists the geometric parameters of these arrays, which share a same period of 400 nm. The spectral evolution for these arrays in Figure 4-13 exhibits similar Bragg modes that redshift with increasing strain. However, the intensity of these grating modes is significantly lower than that of the fluid-transferred NR1, NR2 and NR3 arrays. Meanwhile, the LSPR modes for these arrays remain unchanged under strain. Based on previous discussions, we understand that the shapes of NRs within these arrays do not deform under strain despite the grating development observed in these arrays.

Table 4-4 Geometric parameters of the three NR arrays in Figure 4-1

| NR arrays | Designed Px [nm] | Designed Py [nm] | Designed Dx [nm] | Designed Dy [nm] | Controlled H [nm] | W [nm] |
|---|---|---|---|---|---|---|
| B1 | 400 | 400 | 175 | 175 | 50 | $41 \pm 2$ |
| B2 | 400 | 400 | 175 | 175 | 50 | $65 \pm 7$ |
| B3 | 400 | 400 | 200 | 200 | 50 | $46 \pm 4$ |
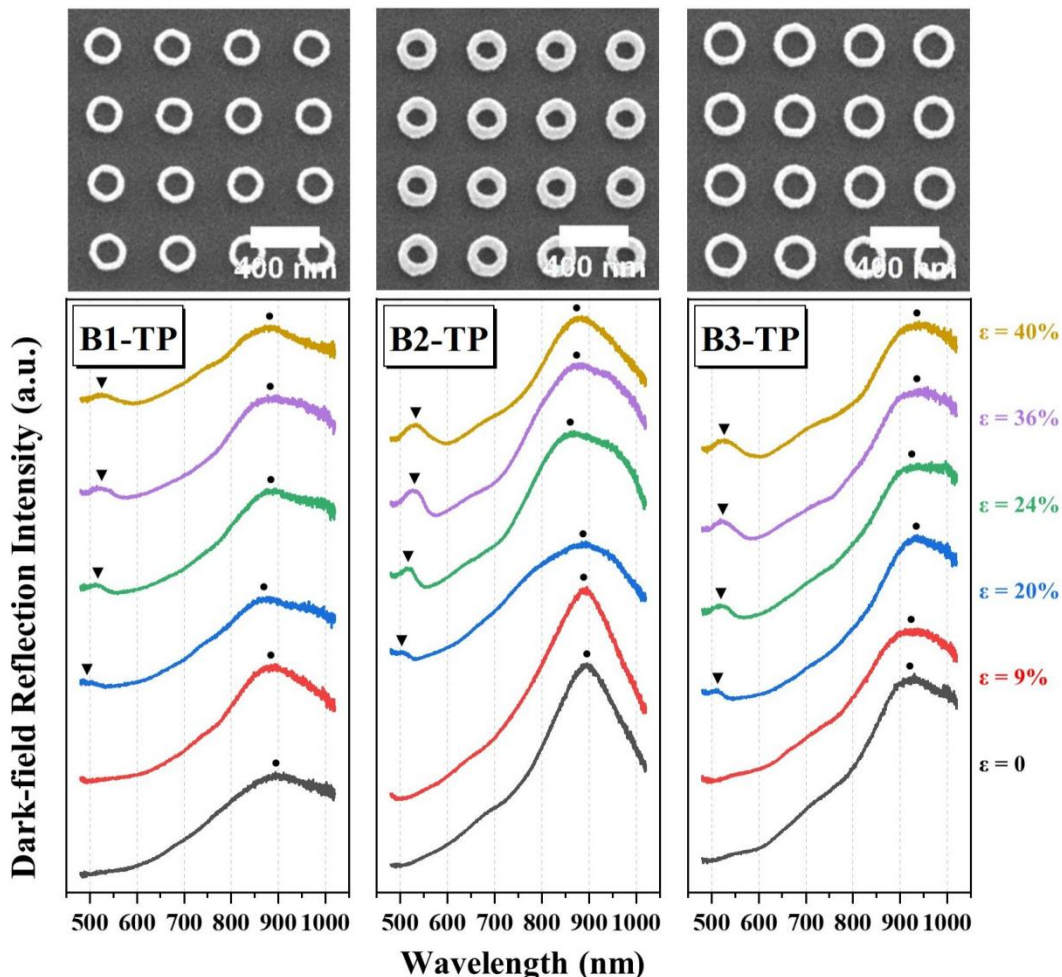


Figure 4-13 SEM images (top figures) and corresponding dark-field reflection spectra (bottom figures) of B1, B2 and B3 NR arrays under strain. The triangles and circles in the spectra refer to Bragg and LSPR modes, respectively.

To investigate the difference in the shape-altering of NRs, we refabricate two NR arrays with the same geometries as NR1, and transfer them onto PDMS using the two modeling methods. Both samples are coated with 50 nm thick Au film and stretched to $\varepsilon = 30\%$ for SEM testing without any optical measurement. Figure 4-14 (a) shows

the result of the cured transfer, indicating no obvious shape development in NRs. In contrast, the result of fluid transfer in Figure 4-14 (b) suggests obvious shape changes for NRs. For instance, the red frame box 3 outlines an AR of 1.17 for the resulting ENR. Moreover, the splitting of the sputtered Au layer (see horizontal cracks) indicates a limited shape-altering for NRs. In addition, we conduct COMSOL simulations to calculate the strain distribution of the NR arrays upon stretching. The 3 * 3 NR arrays have the same geometry parameters as NR1, and are distributed either on top of (Figures c-e) or embedded in (Figures f-h) the PDMS surface, referring to the cured or fluid transfer, respectively. Both results indicate a similar variation in periods under strain, and clearly neither of them displays any observable modifications in the NR shapes when the PDMS is subjected to strain. This limitation arises from the fact that the PDMS and Au NRs within the simulation model share a comparable size scale, where the NRs possessing a significant modulus resist any alterations in their shapes. However, in real-world scenarios, the PDMS sample and Au patterns exhibit different dimensions of approximately 4 cm and 250 nm, respectively. The localized stress induced by stretching the PDMS can potentially induce alternations in the distribution or shape of the Au NRs. Specifically, as suggested for the cured-transfer sample at $\varepsilon = 50\%$ in Figure 4-14 (e), the strain concentrates at the interface between NRs and PDMS along the tensile direction. This may cause the NRs to detach during the strain-induced mutual squeezing, resulting in either horizontal sliding as indicated by the red frame box 1 in Figure 4-14 (a), or vertical sliding as shown in the red frame box 2, which is not conducive to the in-situ shape deformation. In contrast, the fluid-transfer sample shown in Figures 4-14 (h-i) indicates that the local strain is dispersed within the "shallow surface" of PDMS to prevent sliding. Consequently, the embedded NRs lead to an effective mutual squeezing and potential in-situ shape-altering under strain in reality. In general, this squeezing model aligns with our experimental observations and provides insight into mechanisms governing the shape-altering of NRs or other hollow NPs on flexible substrates.
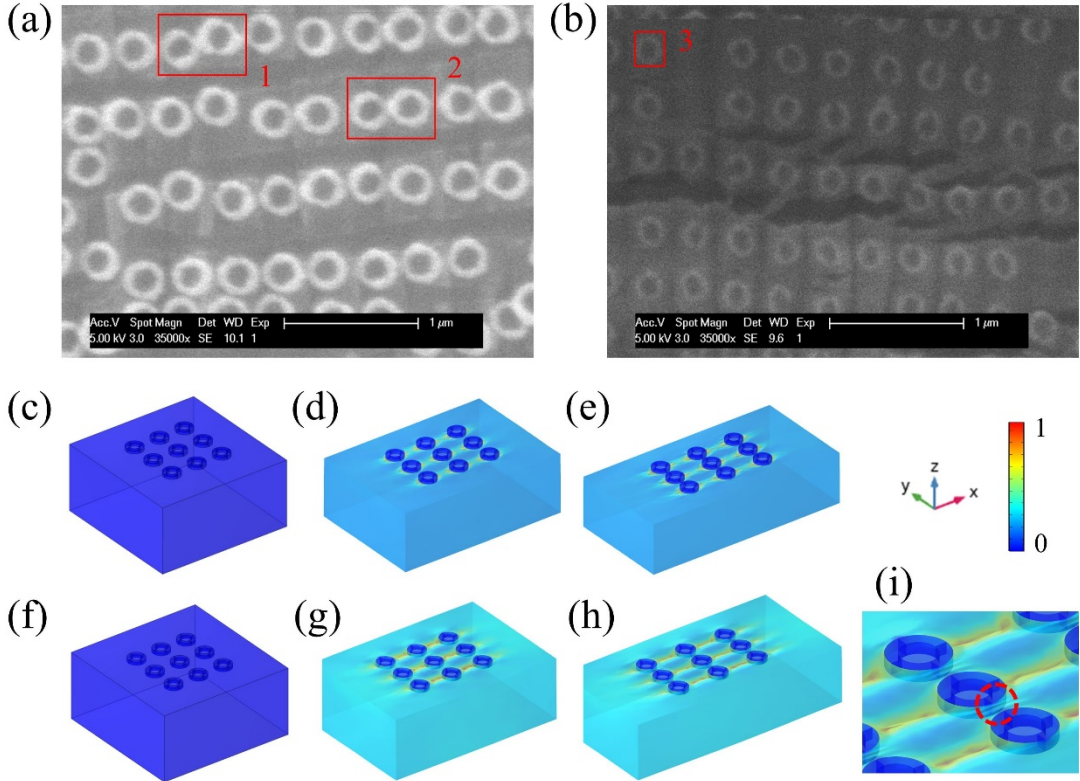
Figure 4-14. Top-view SEM images for NRs on PDMS at ε=30% by the fluid (a) and cured (b) transfer. Figures (c-e) refer to the first strain distribution of NRs distributed on the surface of PDMS at ε=0, 25% and 50%, respectively. Figures (f-h) show the strain distribution of NRs embedded in PDMS at the same strain values, while figure (i) displays a zoom-in layout of (h).

## 4.5 Summary

In this Chapter, we explore the potential of shape-altering plasmonics in Au NR arrays embedded in PDMS with applied strain. By measuring the far-field reflection spectra, we demonstrate that the shape-altering from initial NR to final ENR for the thinner NR1 array serves as an effective strain sensor with a stronger spectral redshift versus strain for the main LSPR peak. The observed shift value of 2.85 nm per 1% elongation provides high sensitivity compared with previous gap-altering flexible devices. To confirm the shape variations under strain, we perform also an in-situ SEM test on PDMS, indicating the shape-altering ability significantly depends on the NRs' width. Additionally, we use the standing-wave model to explain the redshift effect of the LSPR mode, attributing it to the variation in the elliptical charge path as the shape

changes. We also introduce assumptions concerning the grating development and shape-altering of individual NRs under strain, and qualitatively reproduce the spectral evolution for the thinner NR1 and thicker NR2 arrays via FDTD simulations. Our results indicate that the radially symmetric bonding mode is sensitive to the aspect ratio of NRs, and the resulting redshift is mainly due to the shape-altering of NRs instead of the grating development under strain.

Furthermore, we extend our study by measuring the optical spectra of NRs with large periodicity or NRs fabricated via the second approach of cured modeling. Based on constant LSPR modes and corresponding SEM observations, we propose a "squeezing" model to explain the deformability of rigid Au on the flexible PDMS. Specifically, thinner NRs should be densely embedded within an array on PDMS, and the strain-induced bulk shrinkage leads to a mutual squeezing among NRs, enabling them to deform their shapes. Future studies may include exploring this mechanism to optimize the geometry for NRs or other 2D hollow structures in view of their optical properties, which indicates potential applications in shape-altering flexible plasmonics such as strain sensors and flexible/wearable devices.

# Chapter 5 Active Tuning of LSPR and SLR for Elliptical Nanoring Metasurfaces on PDMS

In the previous chapter, we fabricated NR square arrays on PDMS and discussed their LSPR and Bragg optical modes under strain. It is found that different NR arrays show similar grating modes under the two polarization conditions, but NR3-LP presents a SLR coupling under high strain, as depicted in Figure 4-2. In fact, due to the limitations of bottom-up colloidal synthesis, a significant number of studies on SLRs reported in the literature are constrained to arrays comprising isotropic or regular nanoparticles (NPs). [146, 173-174] In this context, we extend the previous chapter by investigating the optical responses of both square and regular triangular arrays of Au ENRs under strain. Since ENRs have different diameters and mutual gaps in the two polarized directions compared to NRs, the composed ENR array exhibits different LSPR and SLR modes depending on the polarization and grating distribution. Therefore, the primary objective of this chapter is to study the optical behavior of arrays consisting of symmetry-breaking NPs under strain. This work not only provides guidance for future large-scale nanofabrication using other techniques, such as nanostencil and nanosphere lithography, but also explores the potential applications of flexible metasurfaces with polarization-dependent functionalities.

## 5.1 ENR square array

Figure 5-1 (a) schematically presents the geometry of a single ENR, consisting of four parameters, i.e., the outer/inner diameter along its long axis ($Lx$ and $lx$), and that along the short axis ($Ly$ and $ly$, respectively). Figures 5-1 (b-c) show the strain-induced grating development for the ENR square and regular triangular arrays. The lattice periods along the x- and y-direction are denoted as $Px_{sq}$, $Py_{sq}$, $Px_{tri}$, and $Py_{tri}$, respectively. The center-to-center distances for the two arrays remain constant at 500 nm, which yields $Py_{tri} = 500$ nm * sin 60° ≈ 433 nm. Note that the out-of-plane heights for all ENRs are maintained at H = 50 nm, and the applied uniaxial strain in this chapter is always along the short axis of the ENRs (y-axis). The grating development under strain for the two cases follows the same elastic description as discussed in Section 4.3.2.
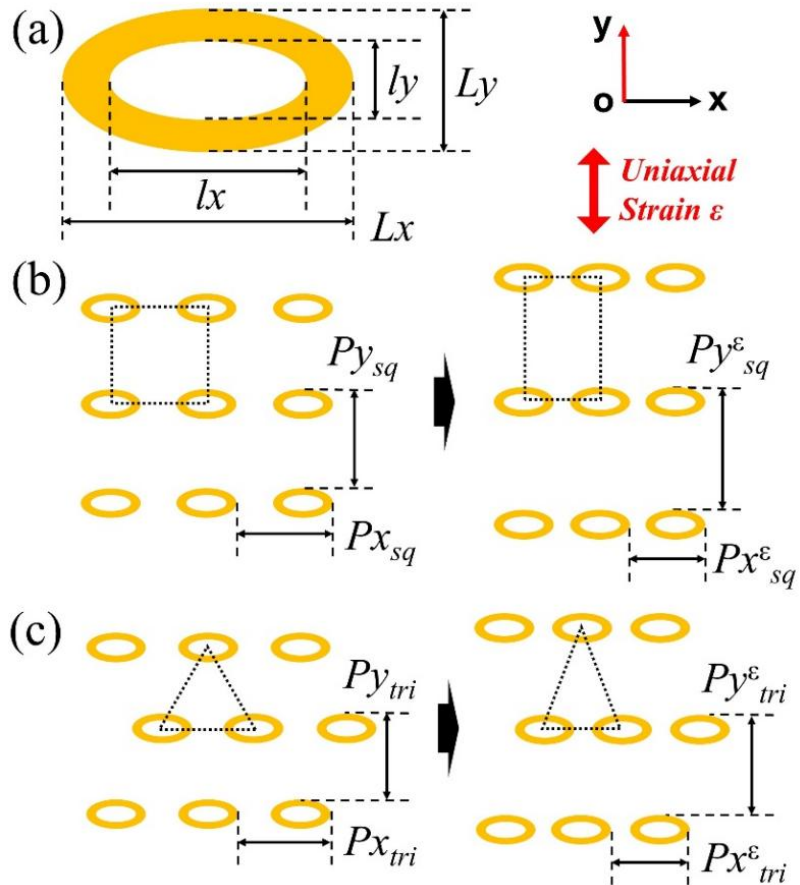
Figure 5-1 Schematics of the ENR (a), ENR square array under strain (b), and ENR regular triangular array under strain (c).

We start by examining the optical characteristics of the ENR square array on PDMS. To assess the transfer quality and grating development under strain, Figure 5-2 (a) and (b) show the SEM images of the array on Si/Cr, and on PDMS after transfer and subsequent stretching at $\varepsilon_{engr} = 40\%$. The specific geometries for both cases are summarized in Table 5-1. The statistical data are obtained by averaging the measurements of the 5*5 array located in the upper-left corner of the SEM image. These rules also apply to Tables 5-2 and 5-3. The results indicate that the EBL-fabricated ENRs exhibit some irregularity after transfer and stretching, as evidenced by the increased standard deviation in various parameters and the geometrical discrepancies in the size denoted by $Lx$ and $Ly$ and in the thickness denoted by $Tx$ and $Ty$. In addition, by comparing the grating development in the stretching direction (Py), one can calculate that the corresponding strain is $\varepsilon_{SEM} = 13.8\%$, which is significantly lower than $\varepsilon_{engr} = 40\%$ and the grating strain of $\varepsilon = \varepsilon_{grtg} = 39.3\%$ during the optical measurements. This difference primarily arises from the

hardening effect observed in the electron-exposed imaging region, as discussed in Section 3.5.1. Therefore, we assume that the geometric variation in ENRs in Figures 5-2 (a-b) results from both the hardening effect and transfer process, i.e., uncontrollable Cr etching. Nevertheless, the successful pattern transfer and uniform grating development confirm the reliability of in-situ optical measurements performed on the flexible substrate.
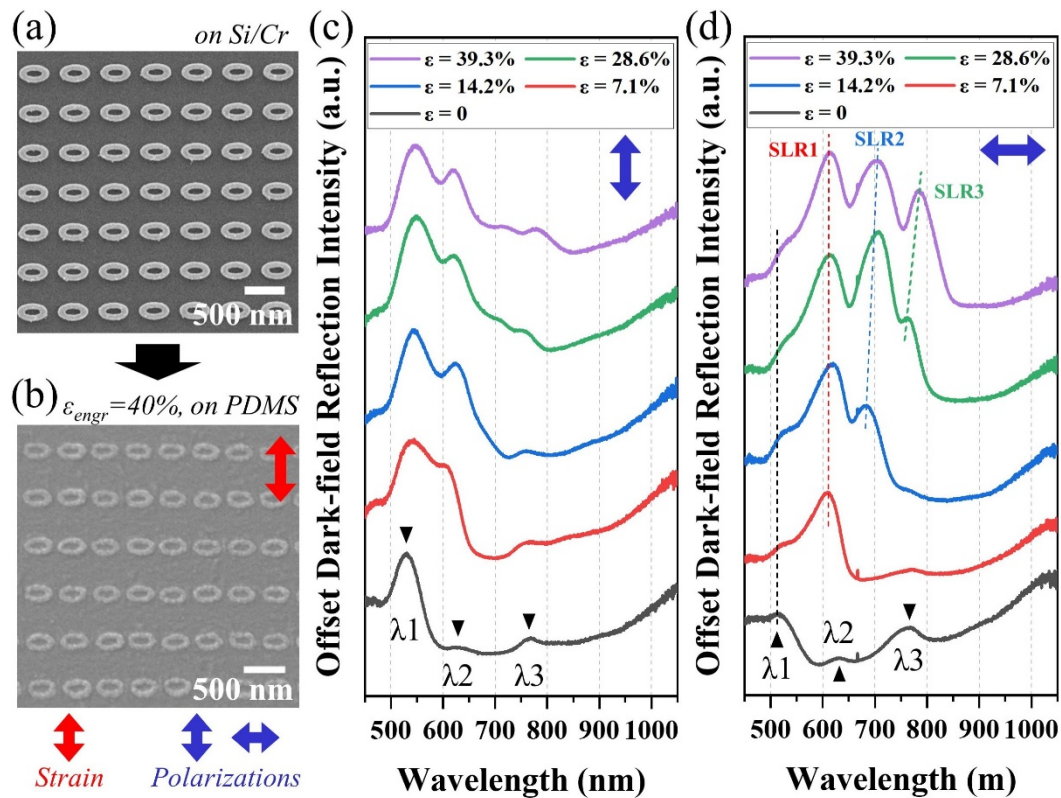


Figure 5-2 SEM images of the ENR square array on Si/Cr (a), and on PDMS at $\varepsilon_{engr}$ = 40% (b). The red and blue arrows set the uniaxial stretching and polarization directions. Spectral evolution of the ENR square array under longitudinal (c) and transverse (d) polarizations. The LSPR modes at $\varepsilon = 0$ are marked with triangles, while SLRs are highlighted by dashed lines, respectively.

Table 5-1 Geometric parameters of the ENR square array in Figure 5-2

| Parameters | ENR @ Si/Cr | ENR @ PDMS with $\varepsilon_{engr}$ = 40% |
|:---:|:---:|:---:|
| Lx [nm] [a] | 373.9 ± 4.5 | 339.4 ± 12.6 |
| lx [nm] | 179.2 ± 4.0 | 186.7 ± 14.0 |
| Ly [nm] | 225.7 ± 3.2 | 204.1 ± 8.6 |
| ly [nm] | 73.1 ± 3.7 | 80.0 ± 7.3 |
| Tx = Lx – lx | 97.4 ± 2.9 | 76.3 ± 6.3 |
| Ty = Ly – ly | 76.3 ± 2.4 | 62.0 ± 5.5 |
| Px [nm] | 499.3 ± 1.1 | 412.0 ± 3.9 |
| Py [nm] | 500.0 ± 0.5 | 569.1 ± 3.1 |

[a](Avg ± Sd, where Avg and Sd are the average and standard deviation values)

Figures 5-2 (c-d) depict the offset dark-field reflection spectra of the ENR square array with polarizations parallel and perpendicular to the strain, denoted as longitudinal and transverse polarizations. The red and blue arrows indicate the tensile and polarization directions, respectively. In contrast to the regular NR square array shown in Figure 4-2, the ENR square array exhibits distinct polarization dependence in spectral evolution under strain. At the strain-less ($\varepsilon = 0$) state, the spectra suggest three peaks at similar positions under both polarizations, namely $\lambda 1 = 513$ nm, $\lambda 2 = 624$ nm, and $\lambda 3 = 764$ nm. The three peaks correspond to LSPR modes of ENR as illustrated in the simulation section. As strain increases, the spectra under longitudinal polarization display minimal shifts in the positions of these peaks. Minor changes involve intensity variations in $\lambda 2$ under strain, and a weak peak at $\lambda = 715$ nm emerges at $\varepsilon = 28.6\%$ and $39.3\%$. However, significant spectral evolution occurs when the ENR square array is subjected to transverse polarization, as shown in Figure 5-2 (d). Specifically, $\lambda 1$ retains its position across different strain values. At $\varepsilon = 7.1\%$, $\lambda 3$ maintains the same position but with a decrease in intensity, while $\lambda 2$ is "replaced" by a distinct peak. This peak corresponds to the SLR mode, denoted as SLR1 and marked with the red dashed line, resulting from the coupling between the LSPR $\lambda 2$ and the emerged Bragg grating mode at $\varepsilon = 7.1\%$. As strain further develops, $\lambda 1$ and SLR1 exhibit negligible evolution, while the redshifting Bragg mode couples with $\lambda 2$ and $\lambda 3$ to form SLR2 at $\varepsilon = 14.2\%$ and SLR3 at $\varepsilon = 28.6\%$. The two SLR modes, SLR2 and SLR3, also redshift under strain owing to the inherent redshifting Bragg modes. The coupling behaviors are further demonstrated in Section 5.3 through numerical simulations. Note that these SLR modes at high strain values display

distinct Fano features, arising from the spectral interference between the discrete peaks of Bragg modes and the broad continuum of LSPR modes. [135, 175] Consequently, the emergence of SLR modes and the enhanced Fano features distinguish the ENR square arrays from isotropic NP arrays which monitor only the spectral shifts of LSPRs and SLRs under strain.

To ensure the reproducibility of the spectral evolution described above, we conduct a series of replicable experiments as follows. Considering the sizes of the ENR arrays and the detection range of the spectrometer, which are respectively $(25\ \mu m)^2$ and $(5\ \mu m)^2$, Figure 5-3 presents the optical responses measured on two other regions of the same sample under two polarizations. It should be noted that these three tests are conducted sequentially under the same stretching condition, resulting in the same grating strain values. The offset spectra in Figure 5-3 demonstrate that different regions in the array exhibit similar spectral evolution under longitudinal polarization while displaying variations under transverse polarization. Specifically, at higher strains ($\varepsilon > 14.2\%$), despite the similar positions of SLRs, their intensities and contrasts between the Fano peak and dip are rather different. This discrepancy can be attributed to the fact that the LSPR peak represents the average response of individual ENRs in the monitoring area, and it undergoes less variation as there is little or no coupling between it and the Bragg mode under longitudinal polarization. However, influenced by the grating boundary, Bragg modes in different monitoring areas possess similar positions but different intensities and widths. Therefore, the interference between various Bragg modes and LSPRs results in varying Fano features, including intensities and contrast ratios, among these SLRs.
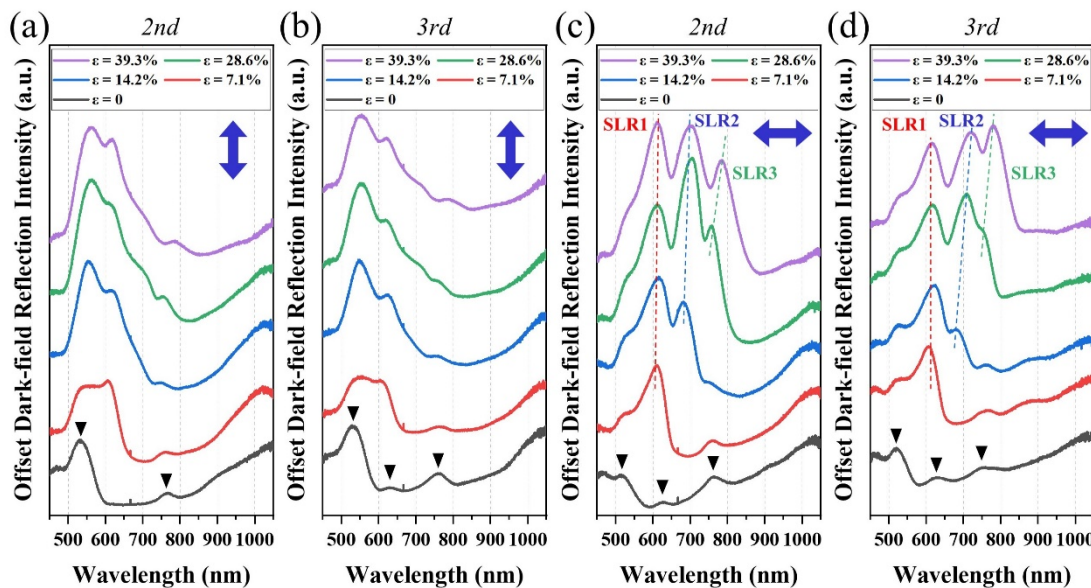
Figure 5-3 Reproducibility tests of the spectral evolution of two other regions in the same ENR square array.

Furthermore, we perform a second set of reproducible experiments by fabricating and monitoring the optical response of a new ENR square array. The SEM and spectral evolution of the second array, along with the corresponding parameters, are shown in Figure 5-4 and Table 5-2, respectively. Similar to the first array as shown in Figure 5-2, this array exhibits three slightly blueshifted LSPR modes at $\varepsilon = 0$ due to geometric variations in ENRs, specifically $\lambda 1 = 511$ nm, $\lambda 2 = 613$ nm, and $\lambda 3 = 744$ nm. As strain increases, the offset spectra of the second array under longitudinal polarization demonstrate similar behavior to that in Figure 5-2. However, under transverse polarization, the Fano features between SLRs are significantly diminished. Besides, the LSPR mode of $\lambda 3$ remains unchanged until $\varepsilon = 19.8\%$, and a weak SLR3 coupled by Bragg and $\lambda 3$ modes is finally found at $\varepsilon = 35.3\%$. Nevertheless, consistent with the first square array, a constant $\lambda 1$ and SLR1 and a redshifting SLR2 can still be observed. These replication tests further affirm the reliability of the optical performance of the ENR square array. The distinctive strain-induced Fano resonance and polarization dependence provide new directions not only for traditional strain sensing, but also for various applications such as flexible color display and polarization-dependent bio/chemical sensing.
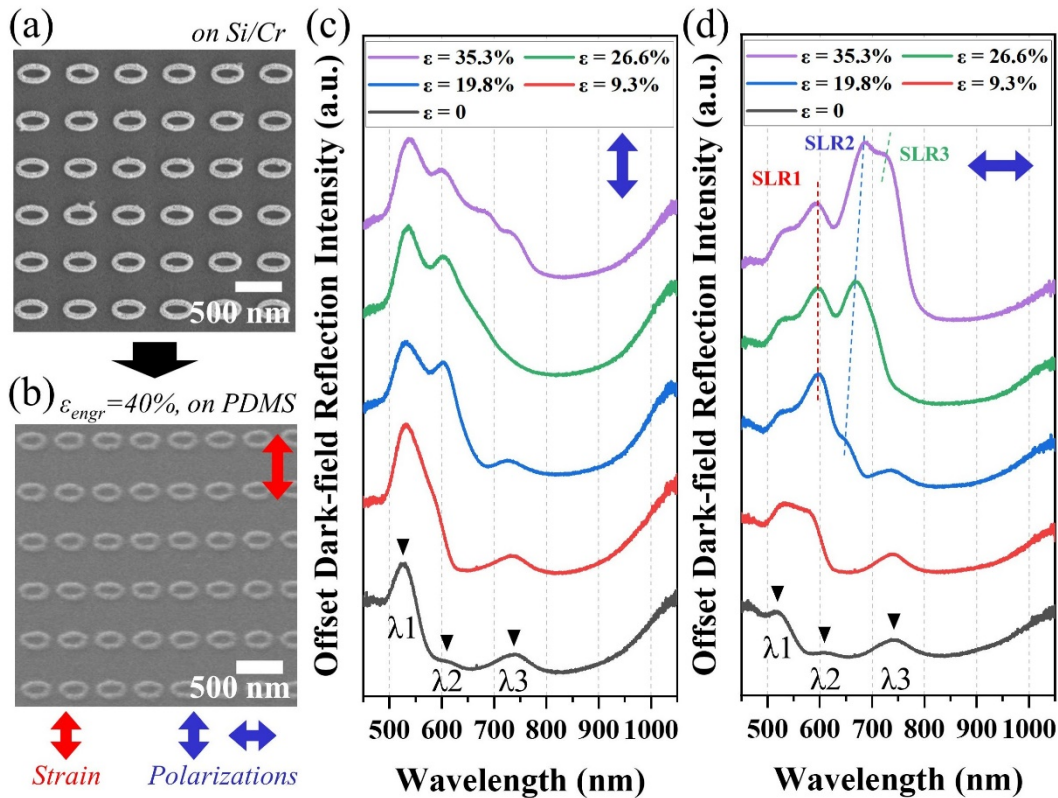
Figure 5-4 Reproducibility tests of the second ENR square array: SEM images on Si/Cr (a) and on PDMS at $\varepsilon_{engr} = 40\%$ (b), and optical characterizations under the two polarizations (c and d).

Table 5-2 Geometric parameters of the ENR arrays in Figure 5-4

| Parameters | ENR @ Si/Cr | ENR @ PDMS with $\varepsilon_{engr} = 40\%$ |
|---|---|---|
| Lx [nm] | 341.8 ± 4.0 | 311.3 ± 8.0 |
| lx [nm] | 226.7 ± 4.8 | 208.1 ± 11.4 |
| Ly [nm] | 216.6 ± 2.4 | 197.0 ± 4.6 |
| ly [nm] | 85.5 ± 2.9 | 91.0 ± 7.0 |
| Tx = Lx − lx | 57.5 ± 3.5 | 51.6 ± 5.2 |
| Ty = Ly − ly | 65.6 ± 1.9 | 53.0 ± 4.5 |
| Px [nm] | 502.1 ± 1.6 | 405.7 ± 2.3 |
| Py [nm] | 500.1 ± 0.6 | 530.6 ± 3.1 |

## 5.2 ENR regular triangular array

The strain-induced optical properties of an ENR regular trianglular array are investigated in this section. Figure 5-5 shows the SEM characterization of the triangle array and its optical properties under strain. The SEM-reflected geometric parameters

are summarized in Table 5-3. In contrast to the ENR square array, the triangular array which maintains the same initial center-to-center spacing of 500 nm does not exhibit pronounced polarization dependence. As shown in Figures 5-5 (c-d), the spectra at ε = 0 display four separate LSPR peaks under both polarizations, namely λ1 = 512 nm, λ2 = 601 nm, λ3 = 726 nm, and λ4 = 744 nm. As strain increases to ε = 19.8%, a SLR peak appears in both spectra at λ = 527 nm, resulting from the coupling between the Bragg and the λ1 mode. At ε = 26.6%, the second SLR2 is observed due to the redshifting Bragg mode coupling to the λ2 mode. Additionally, a side mode of SLR3 emerges at λ= 638 nm under transverse polarization at ε = 35.3%. On the other hand, since the LSPR modes of λ3 and λ4 do not directly couple with the Bragg mode, their spectral evolution is similar under both polarizations despite an intensity difference observed for λ4. Interestingly, the peak position of λ4 remains unchanged with applied strain, while λ3 exhibits a slight blueshift under both polarizations, i.e., Δλ = (695 - 724) nm / 35.3% = -0.82 nm/%.
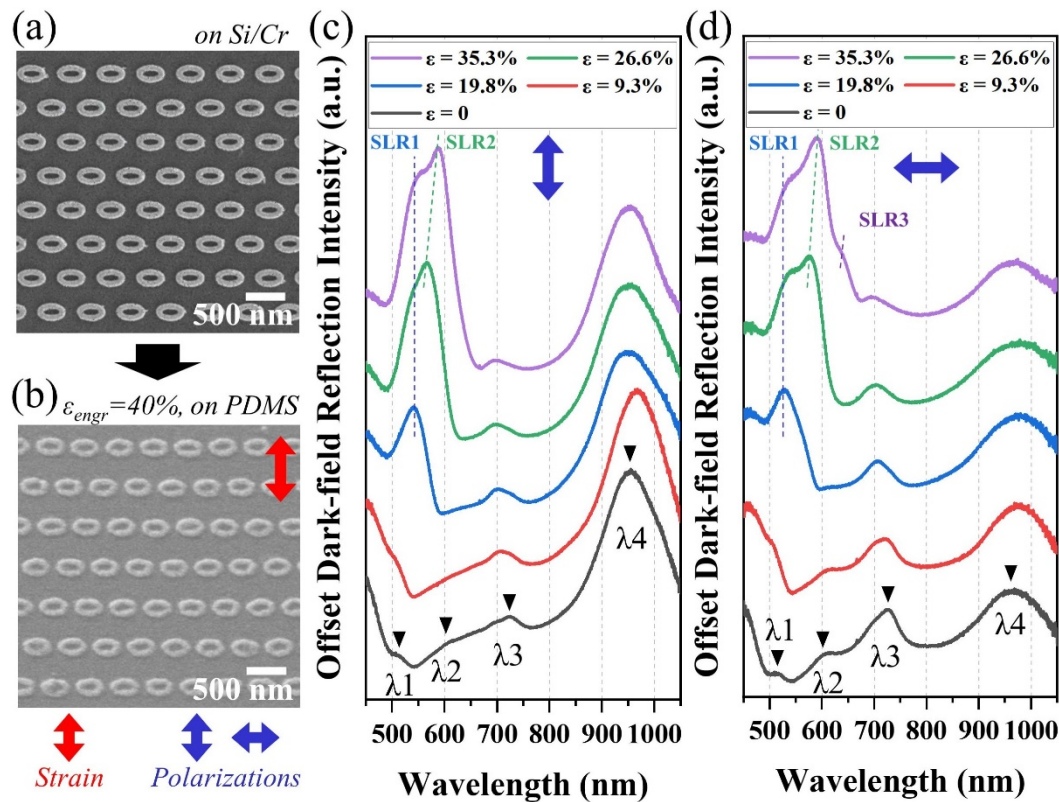


Figure 5-5 SEM images of the ENR regular triangular array on Si/Cr (a), and on PDMS at ε_engr = 40% (b). Spectral evolution of the triangular array under longitudinal (c) and transverse (d) polarizations.

Table 5-3 Geometric parameters of the ENR arrays in Figure 5-5

| Parameters | ENR @ Si/Cr | ENR @ PDMS with $\varepsilon_{engr}$ = 40% |
|---|---|---|
| Lx [nm] | 359.2 ± 6.0 | 324.3 ± 12.2 |
| lx [nm] | 192.6 ± 4.5 | 186.2 ± 14.7 |
| Ly [nm] | 233.6 ± 4.8 | 211.1 ± 7.4 |
| ly [nm] | 64.4 ± 4.3 | 71.4 ± 7.9 |
| Tx = Lx − lx | 83.3 ± 4.0 | 62.7 ± 5.2 |
| Ty = Ly − ly | 84.6 ± 3.4 | 65.2 ± 3.3 |
| Px [nm] | 498.6 ± 1.2 | 412.3 ± 2.6 |
| Py [nm] | 432.1 ± 1.2 | 474.2 ± 2.6 |

Similarly, reproducibility tests are conducted to ensure the universality of the strain-induced spectral behavior of the ENR regular triangular array. Figure 5-6 shows the optical responses of two other regions on the same sample under both polarizations. Compared with transverse polarization, the spectra under longitudinal polarization show less contrast for the LSPR modes at $\varepsilon = 0$, and particularly in Figure 5-6 (a), a side LSPR mode is found at $\lambda = 690$ nm due to the geometric variations in ENRs. As strain develops, the spectral evolution for these LSPR modes is generally in line with that in Figures 5-5 (c-d). Within the coupling region between the inherent Bragg modes and LSPRs modes, one can observe the emergence of SLR peaks at higher strain values. In contrast, LSPR $\lambda 3$ and $\lambda 4$ modes which are beyond the coupling region display similar blueshifting and constant trends under strain, respectively.
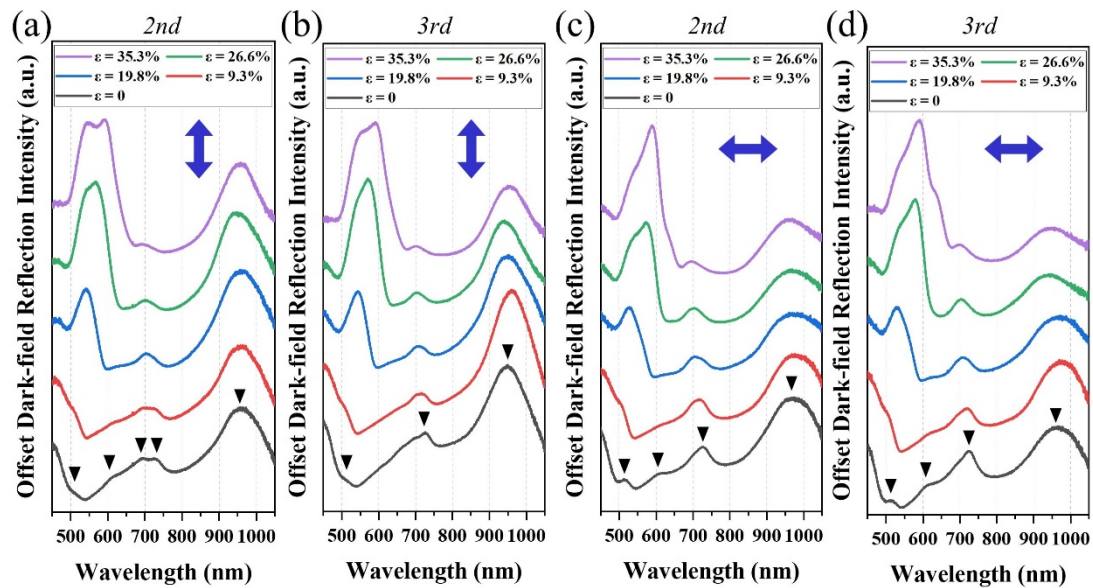
Figure 5-6 Reproducibility tests of the spectral evolution of two other regions in the same ENR regular triangular array.

Another set of ENR regular triangular arrays is fabricated, and their SEM characterizations and spectral evolution are presented in Figure 5-7. Due to significant geometric differences (e.g., the regularity) after transfer and stretching, specific parameters of the ENR array are not elaborated upon. At $\varepsilon = 0$, there are similar LSPR peaks of $\lambda 1$, $\lambda 2$, and $\lambda 3$ as observed in the previous triangular array at shorter wavelengths, while $\lambda 4$ apparently is shifted outside of the detection range due to the increased size. The spectra in Figures 5-7 (c-d) indicate that the broken symmetry/regularity of the transferred ENR geometries lead to weakening SLRs in intensity, but the redshifted Bragg peak and coupled SLR peak are still clear under strain. Moreover, a similar blueshift is observed for the $\lambda 3$ peak due to strain-induced spacing variations. Therefore, we confirm the spectral evolution of ENR regular trianglular arrays under both polarizations. When the Bragg mode of the trianglular array does not directly couple to the specific LSPR $\lambda 3$ mode (i.e., the initial period of the array should not be too large), the offset spectra will exhibit a weak blueshift for $\lambda 3$ under both polarizations with applied strain. In fact, achieving a strain-induced spectral blueshift in 2D regular arrays is rather challenging, as the redshift coupling effect caused by spacing changes is much more pronounced than the blueshift effect. [81] In comparison to square arrays, triangular lattices can be easily realized through either bottom-up self-assembly synthesis or top-down nanosphere lithography. Thus, our work in this section also provides guidance for future large-scale nanofabrication.
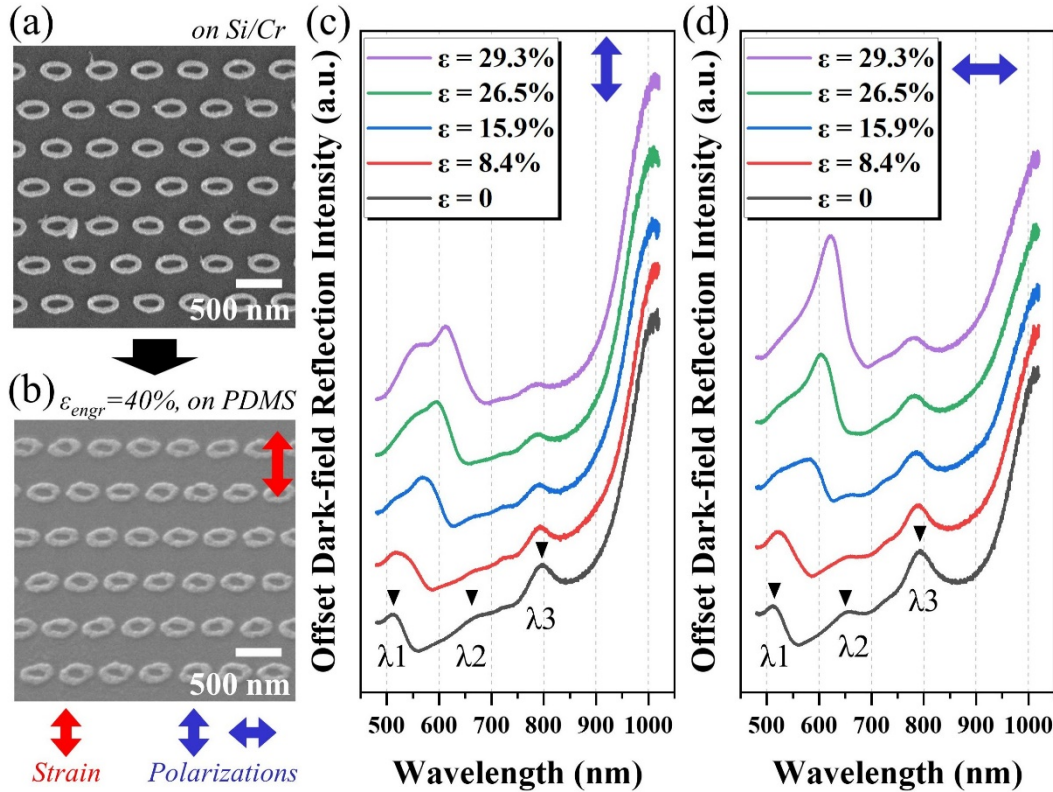
Figure 5-7 Reproducibility tests of the second ENR regular triangular array: SEM images on Si/Cr (a) and on PDMS at $\varepsilon_{engr} = 40\%$ (b), and optical characterizations under the two polarizations (c and d).

## 5.3 Numerical Simulations

In the previous two sections, we experimentally study the optical properties of ENR square and regular triangular arrays, including the strain-induced SLRs, enhanced Fano features between SLRs, and constant/blueshifting LSPR modes. Although reproducibility has been confirmed by a set of experiments, simulation analysis is also necessary as it not only provides the theoretical basis for spectra formation but also supports pattern designing in future work. However, to the best of our knowledge, it remains challenging to simulate both the Bragg/SLR grating modes of the ENR arrays. In Section 4.3.2, we apply the Perfectly Matched Layer (PML) boundary condition and incorporate a finite array into the simulation box to investigate the LSPR modes of a 5x5 array under a single oblique incidence. To simplify the ring-shaped dark-field light source and enhance the convergence of the simulations, the electric field polarization direction of the employed oblique incidence is parallel to the array surface. Although the simulation results, as depicted in Figure 4-10, qualitatively describe the experimental spectra, they fail to adequately capture the Bragg modes of

the NR array. Hence, in this chapter, we study the optical response of the ENR array through the exploration of four distinct simulation methods. Particularly, *Method I* utilizes the aforementioned approach to simulate the scattering cross section of a finite 3 * 3 ENR array, whereas *Method II* considers instead the normal incidence for the simulation. The grating development in the square array under strain is schematically illustrated in Figure 5-1 (b), and elastic deformation is only considered similar to Chapter 4. Since the spectral behavior of SLRs depends also on the array size, we employ Bloch boundary conditions (BC) and Periodic Boundary Conditions (PBC) in *Method III* and *Method IV*, to simulate the reflectance of an infinite array. To facilitate simulation convergence, *Method III* adopts a Broadband Fixed Angle Source Technique (BFAST) plane wave source with the same oblique angle and polarization conditions as in the previous methods, where BFAST provides broadband simulation results at a fixed angle of illumination. In contrast, *Method IV* employs a normal incident source.

In this section, we mainly focused on the simulation of the ENR square array under transverse polarization conditions (i.e., polarization is along the ENR's long axis), and the experimental data are shown in Figure 5-8 (a). In Table 5-1, it is clear that there is a significant size difference in the ENR before and after transfer plus subsequent stretching. This difference arises mainly from the transfer rather than the stretching process, and therefore the simulation model incorporates the parameters measured on PDMS. Additionally, due to the large width of the fabricated ENRs, the influence of strain on its shape variations is neglected in the simulation. Consequently, Figures 5-8 (b) to (e) illustrate the simulated spectra of the ENR array using the four methods. Upon comparison, it is apparent that none of the four simulation curves can fully replicate the experimental results. This highlights shortcomings within our simulation approaches, necessitating further improvements in future work. Nevertheless, we can still explain the observed characteristics of the experimental spectra based on the four simulations. As shown in Figures 5-8 (b,d) vs. (c,e), oblique incidence compared to normal incidence excites additional LSPR modes in the ENR, i.e., $\lambda 5 = 692$ nm and $\lambda 8 = 674$ nm at $\varepsilon = 40\%$. This corresponds to our simulation results in the previous chapter in Figure 4-7 and is consistent with literature. [166] Furthermore, Figures 5-8 (b-d), corresponding to *Methods I* to *III*, indicate three peaks with similar positions which remain also constant under strain, i.e., $\lambda 4 = 580$ nm, $\lambda 6 = 592$ nm, and $\lambda 7 = 581$ nm at $\varepsilon = 40\%$, respectively. In contrast, $\lambda 5$ and $\lambda 8$ exhibit a small blueshift under

strain, i.e., $\Delta\lambda 5 = (677 - 692)$ nm / 40 = -0.375 nm/% and $\Delta\lambda 8 = (674 - 678)$ nm / 40 = -0.1 nm/%, while $\lambda 9$ undergoes a significant redshift, i.e., $\Delta\lambda 9 = (997 - 832)$ nm / 40 = 4.125 nm/%. It is worth noting that a similar blueshift effect as in $\lambda 5$ and $\lambda 8$ is also found for simulations in ENR regular triangular array (not shown here), which corresponds to the blueshifting middle LSPR mode under strain as shown in Figure 5-5, as it does not directly couple with the Bragg mode.
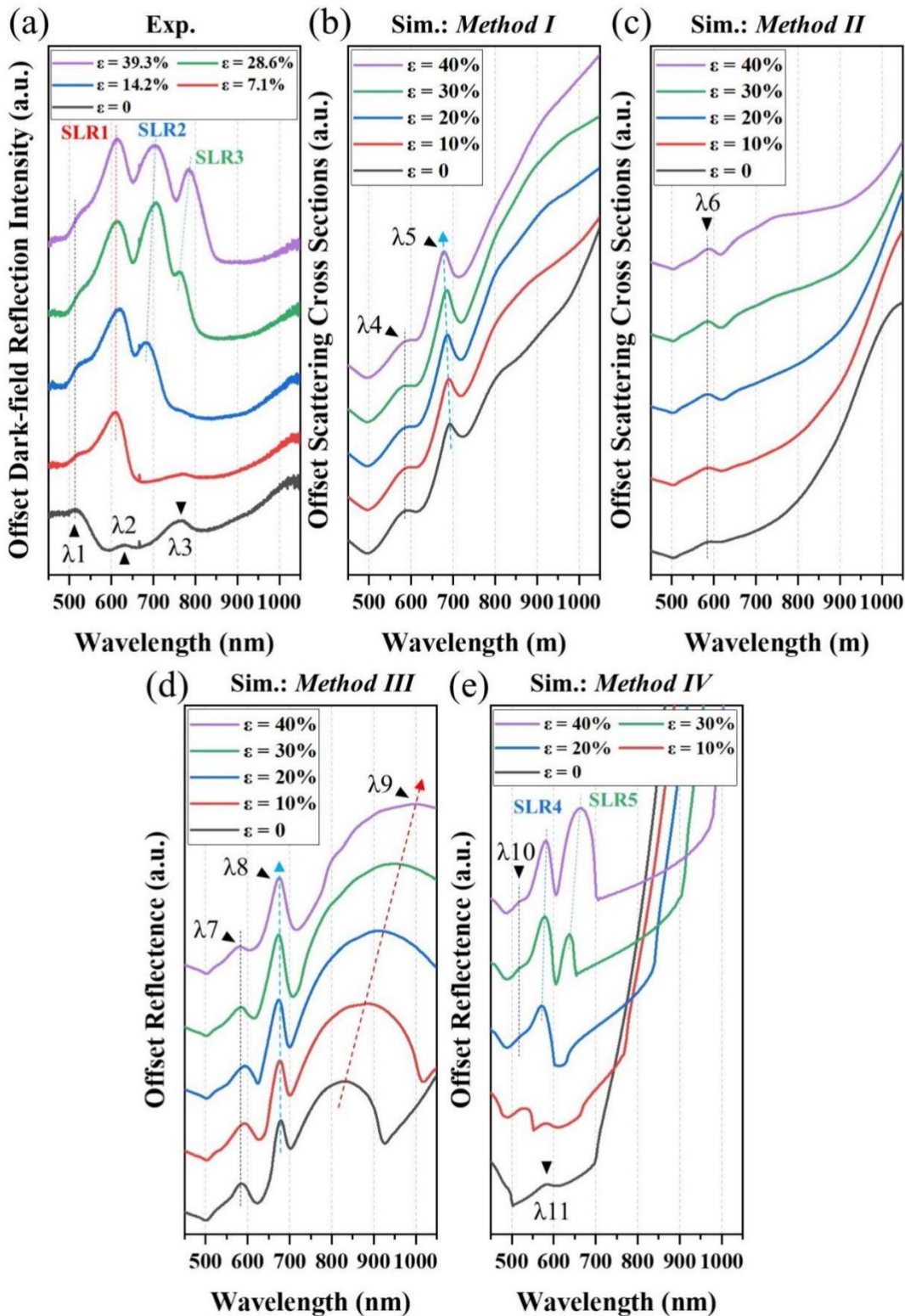
Figure 5-8 Spectral evolution of the ENR square array under transverse polarization induced by strain: experimental (a) and simulation results using *Methods I* to *IV* (b to e), respectively.

To analyze these modes, we plot the electron surface charge and electric field distributions corresponding to these peaks under the ultimate strain ($\varepsilon$ = 40%) in Figures 5-9 (a-f). The charge and field distributions are derived from the top and bottom surfaces of the ENRs, respectively. For the 3 * 3 array, only the distribution of the middle ENR is displayed. Figure 5-9 (c) reveals that $\lambda 6$ excited by normal incidence corresponds to the ENR's LSPR bonding mode with the bonding level m = 3. Due to the symmetry in ENR structure and incidence, the charge and field distributions of $\lambda 6$ exhibit both vertical and horizontal symmetry. Note that the simulation spectra in Figures 5-8 (b-c) suggest also a LSPR dipolar bonding mode (m = 1) for the ENR in the near-infrared region, which is not shown here. In comparison, Figure 5-9 (a) illustrates that the LSPR mode of $\lambda 4$ excited by oblique incidence exhibits similar near-field distributions as $\lambda 6$ excited by normal incidence, corresponding to the same bonding level of m = 3. In Figure 5-9 (b), $\lambda 5$ representing the additional mode excited by oblique incidence shows a bonding level of m = 2. Please note that due to the approximation of using a single oblique incidence to simplify the dark-field light source, the charge and field distributions in Figures 5-9 (a-b) and (d-f) exhibit top-bottom symmetry-breaking to some extent; whereas a real ring-shaped dark-field illumination should guarantee the symmetry in both directions. Similarly, when the ENR periodic structure is excited by oblique incidence, Figures 5-9 (d-e) demonstrate the bonding levels of $\lambda 7$ and $\lambda 8$ are the same as the aforementioned $\lambda 4$ and $\lambda 5$, while $\lambda 9$ exhibits a characteristic LSPR dipolar bonding mode. Since the spectral evolution corresponding to *Method III* does not exhibit the characteristics of SLR, and its LSPR modes resemble those of a finite array (Method *I*), we conclude that the single oblique incidence cannot excite a Bragg/SLR grating mode in periodic ENR structures in the simulation model. Moreover, by comparing the experimental spectra with the spectra obtained from *Methods I* to *III*, the peaks $\lambda 2$ and $\lambda 3$ at $\varepsilon$ = 0 in the experimental spectra are assumed to the LSPR bonding modes excited by the dark-field illumination, with m = 3 and m = 2, respectively.
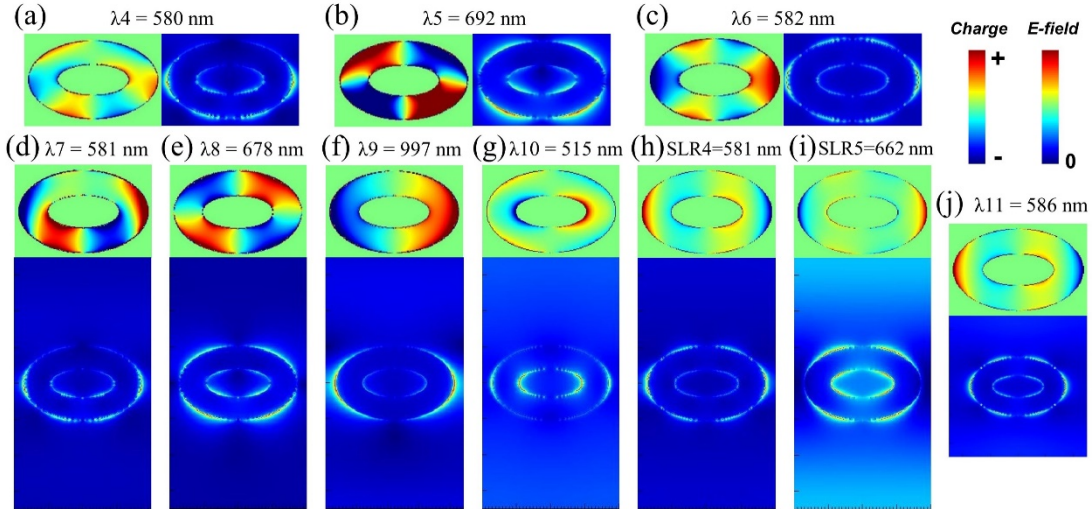
Figure 5-9 The electron surface charge and electric field distribution of a set of peaks indicated in Figure 5-8, namely λ4 to λ10, SLR4, and SLR5, referring to the peaks observed at ε = 40%. Additionally, λ10 corresponds to the peak observed at ε = 0.

Finally, when simulating the ENR periodic structure under normal incidence using *Method IV*, Figure 5-8 (e) exhibits a spectral evolution rather similar to the experimental ones. As strain increases, these peaks show typical grating-mode behaviors as they emerge with increasing intensities and redshifting trends in the wavelength range of 500-800 nm. Figure 5-10 displays the full simulation spectrum corresponding to *Method IV*, revealing a significant difference in intensity between the grating and LSPR dipolar modes in the infrared region. Therefore, in Figure 5-8 (e), the offset spectra are plotted based on the intensity of the grating peaks. At ε = 0, the spectrum displays a peak (λ11 = 586 nm) similar in position to λ6, and Figure 5-9 (j) suggests it to have the same bonding level m = 3. This similarity is attributed to the fact that the Bragg peak of the ENR is not directly coupling with the LSPR peak. However, as strain increases, their coupling leads to a significant difference in the spectral evolution of Figure 5-8 (e) compared to (c). For example, when strain reaches ε = 40%, the spectrum exhibits three distinct peaks, namely λ10 = 515 nm, SLR4 = 581 nm, and SLR5 = 662 nm. From Figure 5-9 (g), it can be observed that λ10 corresponds to the LSPR antibonding mode of the ENR. Due to the width dependence of the antibonding mode, its peak position and intensity remain unchanged at ε = 20%, 30%, and 40%, while the absence of observation at ε = 0% and 10% is speculated to be owing to its coupling with the Bragg modes. Moreover, Figures 5-9 (h-i) display the charge and electric field distribution patterns corresponding to SLR4 and SLR5, showing the same bonding level of m = 3 but phase inversions. Since SLR4 and SLR5

show similar near-field distributions with λ11 but differences in peak intensity and width, we conclude that both of them arise from the coupling between the Bragg and λ11 modes. According to the definition, [146-148] these two peaks belong to SLR peaks. Particularly, the electric field distribution plot in Figure 5-9 (i) reveals that the field enhancement corresponding to SLR5 also propagates along the ENR surface perpendicular to the polarization direction, indicating a characteristic feature of the grating mode. Finally, we summarize that in the experimental spectrum, the formation of SLR1 and SLR2 arises from the coupling of the inherent Bragg and LSPR λ2 peaks, whereas in the simulation spectrum using *Method IV*, SLR4 and SLR5 are formed between Bragg and λ11 modes. The additional SLR3 in the experiment results from the coupling of the Bragg peak and λ3 (LSPR mode, quadrupolar bonding mode, m = 2), which cannot be excited by normal incidence in *Method IV*. Furthermore, our simulations also demonstrate that the inherent Bragg modes excited by a dark-field lillumination can be simplified by using normal incidence, possibly because the normal component of the dark-field illumination is crucial for generating the grating peaks as it propagates only at the interface between ENR and PDMS. In fact, Yang et al. [176] reported the simulation of SLRs in Au nanosphere arrays using normal light sources. Such solid structures typically do not exhibit new LSPR peaks under oblique incidence, indicating that the coupled SLR modes mostly involve Bragg and dipolar modes.
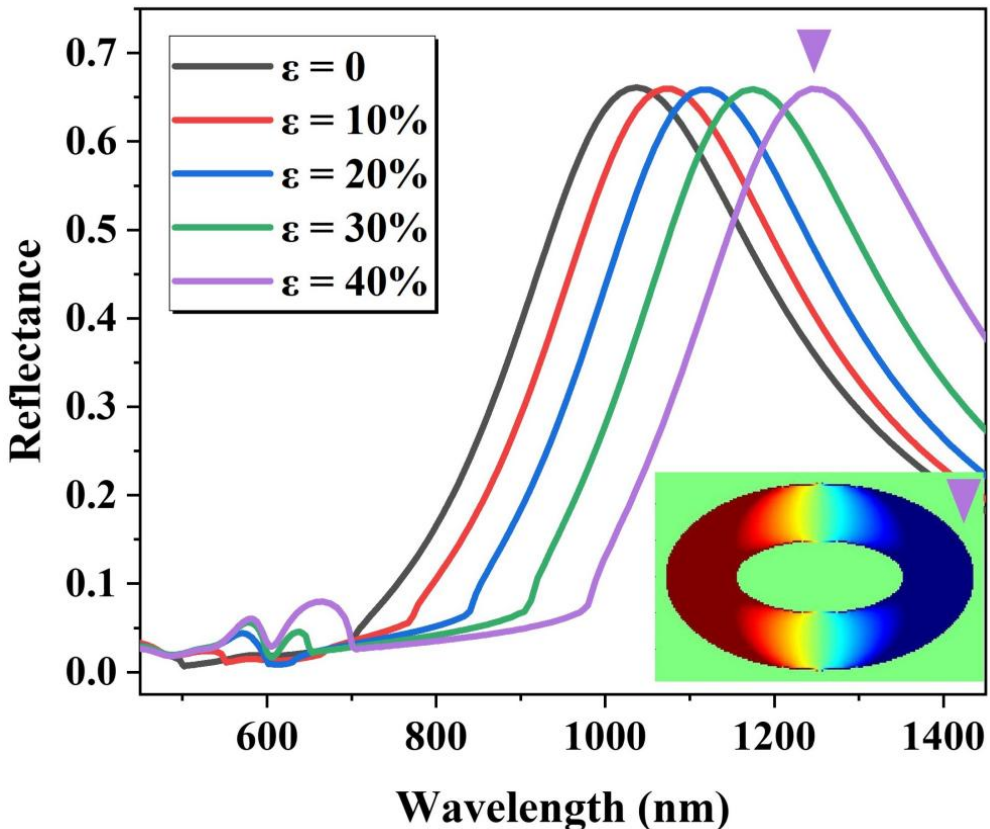
Figure 5-10 Simulation spectra of the periodic ENR square array under normal incidence. The bottom-right electron surface charge refers to the LSPR mode at $\varepsilon$ = 40% ($\lambda$ = 1243 nm).

## 5.4 Summary

In this chapter, we conduct experimental investigations into the spectral evolution of ENRs arranged in square and regular triangular arrays under both transverse and longitudinal polarizations relative to the stretching. Through a series of reproducible tests, we confirm the polarization-dependent behavior of the ENR square array, wherein distinctive Fano-like SLRs are observed under transverse polarizations. In contrast, we demonstrate similar optical behaviors for the ENR triangular arrays irrespective of polarizations. Since the emerging Bragg peaks show less coupling with the middle LSPR mode (i.e., $\lambda 3$ in Figure 5-5), it presents an interesting strain-induced blueshift under both polarizations. These spectral behaviors are effectively explained through the utilization of four simulation methods, thereby illustrating that SLRs arise from the coupling between strain-induced redshifting Bragg peaks and LSPR peaks excited in the ENR under dark-field illumination.

Compared with conventional isotropic nanosphere/nanodisc arrays, this chapter highlights the exceptional capabilities of the ENR flexible metasurface, enabling active manipulation of SLRs and their associated Fano characteristics through external strain and polarization conditions. These findings not only establish a theoretical framework for the design of future metasurfaces but also hold great promise for the development of sensing applications.

# Chapter 6 Outlook for Active Tuning of Fano Resonance for Ring-disc Hybrids

In the preceding chapters, we have discussed different optical responses in Au NR/ENR arrays, including broader LSPR and narrower SLR modes. In contrast to these Lorentzian-shaped resonances, Fano resonances in plasmonic structures with asymmetric and narrow lineshapes have recently emerged as a topic of interest for various sensing applications. [175, 177-179] In particular, Zhang et al. conducted COMSOL simulations to explain the different Fano resonances in Ring-disc cavities (RDC) and ring-disc pair (RDP) systems. [180] Their results in Figure 6-1 suggest that multiple higher-order bonding ring modes can be excited in RDPs, such as octupolar ones, resulting in higher figures of merit (FoM) and contrast ratios (CR) compared to RDCs. The negative curvature of the ring relative to the disc in RDPs also creates an intense hotspot associated with Fano coupling, which is crucial for Fano resonances in plasmonic hybrid structures that rely on near-field hybridization. Furthermore, in the context of flexible plasmonics, it is predicted that the unique RDPs support tunable Fano resonances once they are transferred onto PDMS, as their radiative losses can be easily tailored by narrowing the ring-disc mutual gap. However, it remains a challenge to monitor the optical signals of a single structure against a stretching PDMS, necessitating high-resolution spectrometers and ultra-thin PDMS substrates for focusing. Therefore, in this chapter, we give an outlook into the potential applications of spectral guiding in RDP/PDMS systems, by measuring the optical properties of RDPs on a rigid substrate, such as glass/ITO.

Partial results and related figures (Figures 6-2 to 6-7) have been published in the journal article (Reproduced with permission from Wiley) : [181]

*W. Tao, H. Hu, O. Guillot, T. Maurer, M. Fleischer, Fano resonances in plasmonic ring-disc-pair systems, Advanced Photonics Research 2300012 (2023)*
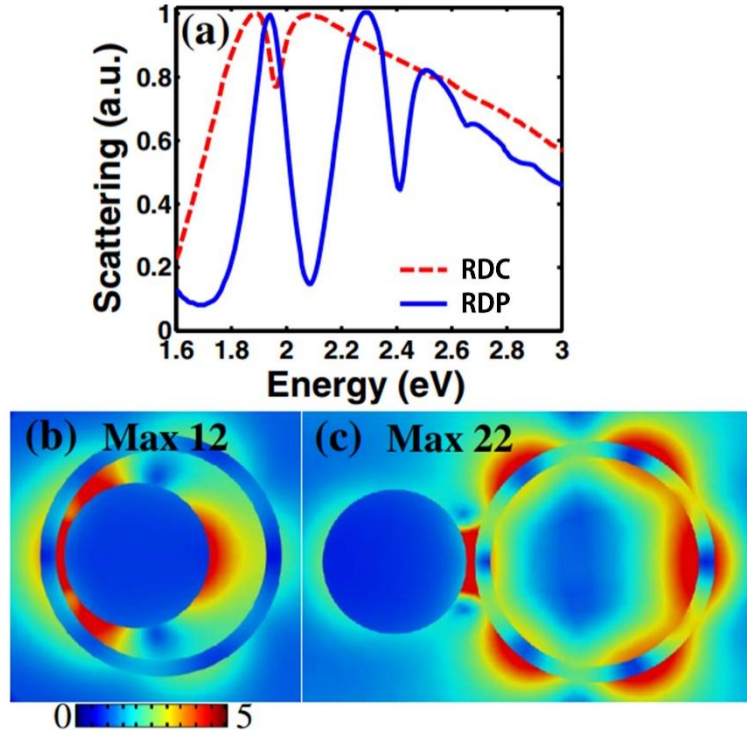
Figure 6-1 (a) Scattering spectra of a RDC and a RDP with the same discs and rings as shown in (b) and (c). The smallest gap for the two cases remains at 10 nm. Respective electric field distributions at the Fano dips of hexapolar resonance modes in the RDC (b) and RDP (c), respectively. The figure is adapted from Ref [180].

## 6.1 Fano resonances in RDP systems

Figure 6-2 schematically depicts a Au ring-disc-pair (RDP) system fabricated on the glass/ITO substrate via EBL. The thickness of the conductive ITO layer is 50 nm. The RDP has several geometric parameters, including the ring's center diameter ($D_{ring}$), ring width ($W$), disc diameter ($D_{disc}$), heights ($H$), and the edge-to-edge gap ($G$). During the EBL process, a pattern file carefully designs the RDPs' center distance and $D_{ring}$, while the electron exposure dose controls $W$ and $D_{disc}$ which further tailors $G$. In order to avoid carbon contamination that affects the RDPs' dark-field spectra, all parameters are characterized via SEM imaging after optical measurements.
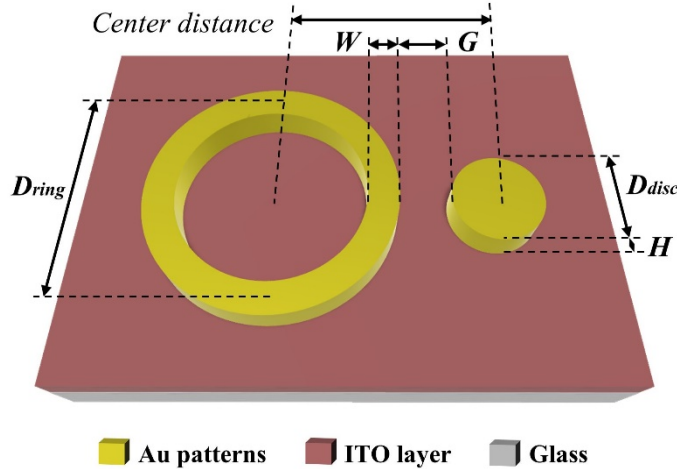
**Figure 6-2** Schematic presenting the geometries of Au RDP on the ITO/glass substrate. The figure is modified after Ref [181].

After fabrication, dark-field scattering spectra are characterized under unpolarized illumination to reduce the influence of slight fabrication defects or misalignment. We first investigate the impact of exposure dose on the optical properties of a single disc, a single ring, and their hybrid RDPs by maintaining $D_{ring}$ at 450 nm and the center distance at 380 nm. The spectra shown in Figure 6-3 reveal that both the single disc and ring demonstrate a general redshift in their spectral features as a function of $D_{disc}$ and $T$ within the wavelength range of 695-850 nm and 575-600 nm, respectively. The spectral redshift effects observed for the disc and ring are consistent with literature and further ensure the reliability of the current experiments. [94, 182] The plasmonic modes for the disc and ring refer to the dipolar disc and anti-bonding ring mode as illustrated subsequently. However, the spectral behavior of the hybrid RDP with narrowing gap changes from an initial superposition to the final interference between the two spectra as the exposure dose increases.
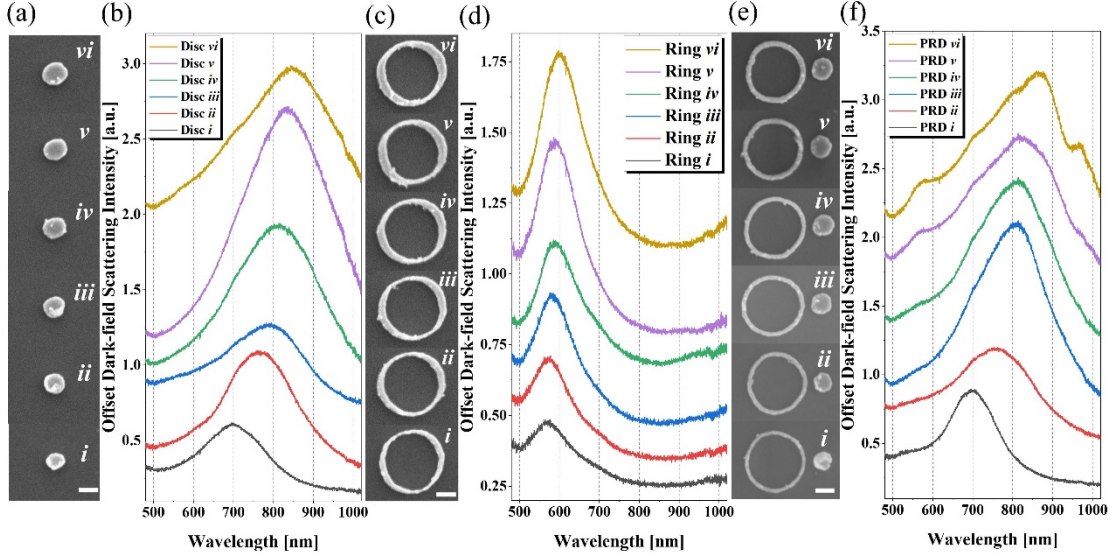
Figure 6-3 EBL dose dependence of the geometric size and optical properties of single discs (a and b), rings (c and d), and hybrid RDPs with controlled $D_{ring}$ of 450 nm and a center distance of 380 nm (e and f). The scalebar is maintained at 150 nm. Each RDP has the same exposure dose as the corresponding single ring and disc. The dipolar disc mode in (b) experiences a redshift as disk size increases. The antibonding dipolar ring mode shown in (d) is dependent on the ring width and undergoes a slight shift towards longer wavelengths with increasing ring thickness. The figure is adapted from Ref [181].

In order to study the spectral interference of RDP *vi* as shown in Figure 6-3, numerical simulations in *Lumerical FDTD solution* are conducted. The experimental scattering spectra are compared with the simulated scattering cross sections in Figure 6-4, where the simulation model is regularly approximated based on the average sizes extracted from SEM imaging, i.e., $D_{ring} = 450$ nm, $W = 45 \pm 6$ nm, $D_{disc} = 180 \pm 9$ nm, and $G = 45$ nm, respectively. The statistical values $W$ and $D_{disc}$ are derived from the average measurements taken four and two times along the two axes on the SEM images. These rules also apply to Table 6-1. The simulated spectra qualitatively reproduce the experimental characteristics and suggest five different peaks at wavelengths of namely 568, 692, 780, 863, and 1028 nm, despite a redshift of ~60 nm for Mode-5. The dashed red line in Figure 6-4 represents a superposition spectrum of the antibonding ring mode at 568 nm and dipolar disc at 840 nm, by separately simulating the spectra for the two parts. From the far-field explanation of Fano resonances, these results illustrate that the dipolar disc mode provides a broad continuum for the spectral interference in RDPs, resulting in four different Fano peaks

of Mode-2 through Mode-5.[135, 138]
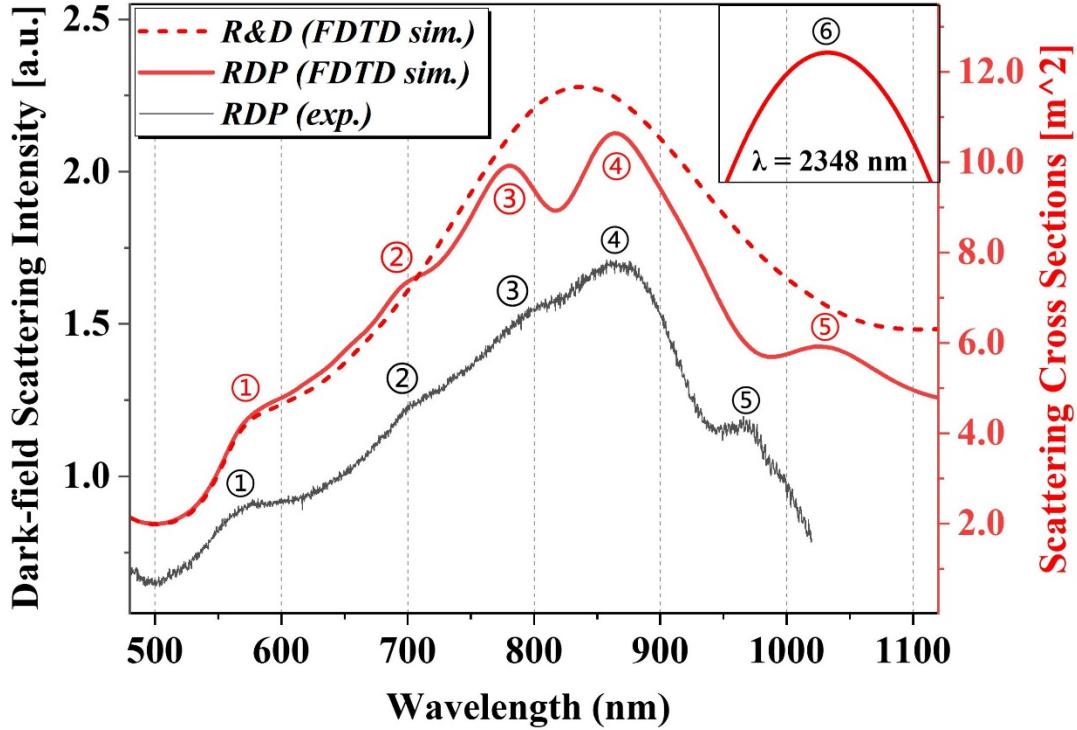


Figure 6-4 (a) Comparison between experimental and simulated spectra in RDP *vi* from Figure 6-3. The top-right figure suggests a simulated peak for RDP *vi* in the near-infrared region at $\lambda$ = 2348 nm. The dashed red-line shows a simulated spectral superposition between the single disc and ring spectra. The figure is modified after Ref [181].

Furthermore, the mechanism of spectral interferences in Fano resonance can be interpreted by the near-field plasmonic hybridization. Figure 6-5 presents surface charge density and electric field distributions of these spectral peaks shown in Figure 6-4. The logarithmic scale plot in row (a) of Figure 6-5 illustrates the charge boundary between opposite polarities and easily reveals the bonding levels for the ring, also confirmed by the linear plot in row (b). These charge plots show that Fano peaks of Mode-2 through -5 result from LSPR coupling between the dipolar disc mode and multipolar bonding ring modes with bonding level m = 5 for Modes 2 and 3, m = 4 for Mode-4, and m = 3 for Mode-5, respectively. The charge of Mode-1 arises from a combined mode of a dipolar antibonding ring and a hybrid disc mode. The hybrid disc charge suggests a combined mode between the in-plane dipolar and the out-of-plane base modes, with opposite charges distributed on the left/right and top/bottom edges of the disc, respectively. Outside the experimental detection range, the simulation

curve in the top-right figure of Figure 6-4 shows that these RDPs present a Mode-6 at $\lambda$ = 2348 nm, resulting from a coupling between the dipolar bonding ring and a weak dipolar disc mode, suggested by the charge plots. Furthermore, since the enhanced electric field in the vicinity of RDPs results from the oscillations of free electrons on the surface, a comparison of rows (a-b) and (c) reveals a consistent correspondence between the surface charge and the electric field distributions. Specifically, Mode-1 shows a superposition in the electric field between the dipolar disc and anti-bonding ring mode without strong gap coupling. Modes 2 through 5 display bonding ring modes with different polar-orders excited by a dipolar disc mode. In Mode-6, the field enhancement is more concentrated on the ring since no obvious enhancement is found on the right side of the disc. Note that the enhancement effect by the dipolar disc is weak in Mode-2, resulting in not only a weaker Fano peak with lower CRs but also a stronger dependence on the ring's regularity rather than the coupling effect by the nearby disc. This may explain why the experimental spectra (with irregular geometries) in Figure 6-6 do not present the Fano peak at a wavelength of ~675 nm as suggested by the simulation.
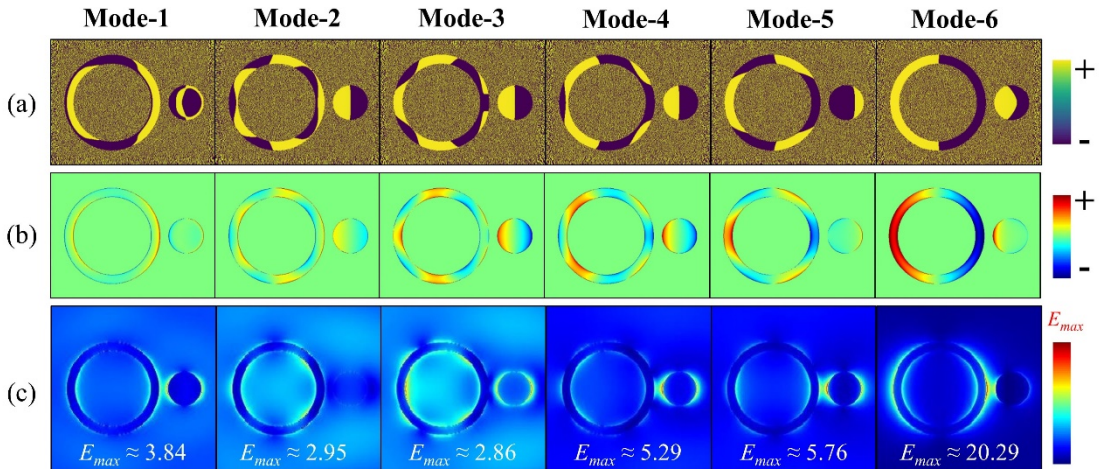


Figure 6-5 Simulated surface charge distributions for peaks in Figure 6-4, in both logarithmic (a) and linear (b) scale, and corresponding linearly plotted electric field distributions (c). These figures are calculated on the top surface of the RDPs. The figure is modified after Ref [181].

The above discussion highlights the occurrence of plasmonic hybridization in RDPs. Particularly, when the wavelength ($\lambda$) sits between ~650 and ~1100 nm, the strong near-field coupling effect gives rise to a dipolar-disc background/continuum, resulting in the emergence of various multipolar bonding ring modes. These near-field hybridizations in turn lead to the formation of far-field Fano resonances. In contrast,

for wavelengths away from the dipolar disc continuum, the coupling effects from the disc significantly reduce. As a result, both the antibonding ($\lambda = 568$ nm) and dipolar ring ($\lambda = 2348$ nm) modes remain mostly unaffected in the far-field spectra, while the high-energy antibonding ring mode excites an additional and weak base mode for the disc at shorter wavelengths.

## 6.2 Perspectives of RDPs in flexible plasmonics

In the above section, we theoretically explain the Fano resonances in a RDP system resulting from the near-field hybridization. In order to explore the potential gap-altering sensing applications, we take advantage of the state-of-the-art EBL method to fabricate a set of RDPs, with controlled $D_{ring}$ and $D_{disc}$, $H$, and $W$ under varying $G$. The SEM-characterized geometries are listed in Table 6-1.

Table 6-1 SEM-characterized geometric parameters of the six RDPs in Figure 6-6

| RDPs | Designed $D_{ring}$ [nm] | $D_{disc}$ [nm] | W [nm] | G [nm] |
|---|---|---|---|---|
| RDP *i* | 450 | $178.7 \pm 7.2$ | $47.3 \pm 10.5$ | 74.4 |
| RDP *ii* | 450 | $176.7 \pm 6.4$ | $43.9 \pm 10.3$ | 60.0 |
| RDP *iii* | 450 | $176.3 \pm 7.9$ | $42.8 \pm 5.8$ | 46.3 |
| RDP *iv* | 450 | $171.7 \pm 6.0$ | $44.7 \pm 3.3$ | 23.8 |
| RDP *v* | 450 | $180.0 \pm 8.3$ | $41.8 \pm 7.3$ | 20.0 |
| RDP *vi* | 450 | $175.4 \pm 6.5$ | $41.0 \pm 7.4$ | /[a] |

[a] (In PRD *vi*, the ring and disc are connected with each other)

As shown Table 6-1 and Figure 6-6 (a), we study the impact of $G$ in RDPs on their Fano resonance, spanning from 74.4 nm to the final connection. To simulate the connected state for RDP *vi* in Figure 6-6 (a), an overlapping RDP system with a gap of -10 nm is considered. By comparing Figures 6-6 (b) and (c), one can find the main difference in the spectral superposition of RDP *i* and *ii* observed in experiment and the weak Fano coupling in simulation is mainly due to signal loss or system noise during the measurement. Apart from this difference, both experimental and simulated plots illustrate a stable position of Fano peaks independent of gap variation. Here, we mark the most distinguishable Fano features with solid triangles, and in Figure 6-6 (d) present the electric field distribution for the main Fano dips with $G = 74.4$, 46.3 and

20.0 nm, respectively. It is found that the coupling modes for these dips remain constant between a bonding ring mode with m = 4 and the dipolar disc mode, where the coupling strength is gradually enhanced with increasing $E_{max}$. As $G$ keeps decreasing, finally, the connected RDP $vi$ shows a set of resonance peaks (e.g., $\lambda_1 =$ 717.1 nm, $\lambda_2 =$ 769.4 nm, and $\lambda_3 =$ 841.6 nm in experiments), resulting from the redistributed surface charges by the metal junction instead of a coupling between the disc and ring. [183] In addition, simulation studies in Figure 6-7 (a) indicate that the dipolar ring mode (outside the experimental detection range) in the near-infrared regime undergoes a weak redshift as $G$ decreases, where the connected RDP vi shows instead a broad peak at $\lambda = \sim$2500 nm.
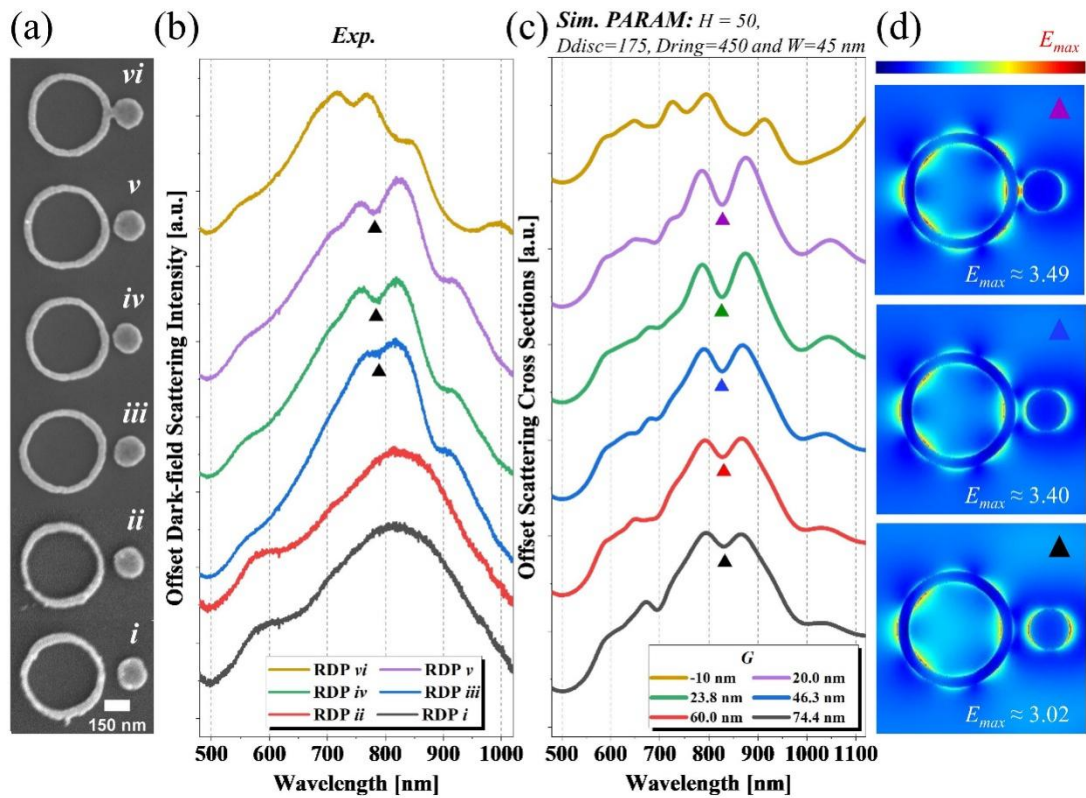


Figure 6-6 (a) Top-view SEM images and (b) experimental dark-field scattering spectra of the six RDPs with decreasing $G$ until RDP $vi$. (c) Simulated scattering cross sections of the six RDPs with decreasing edge-to-edge gap. Note that the simulated structures are regularly modeled. (d) Electric field distribution plots with $G$ of 74.4, 46.3, and 20.0 nm, respectively. The figure is adapted from Ref [[181]].

The above discussion demonstrates that Fano resonances in RDPs with varying $G$ exhibit similar coupling behaviors, justifying a quantitative analysis of their spectral evolution vs. $G$. In Figure 6-7 (b), we plot the positions of Fano dips and their

corresponding contrast ratios (CRs) as a function of gap distance ($G$), based on experimental (solid lines) and simulation results (dashed lines). We define the CR as the ratio of the intensity difference between two adjacent peaks and their intermediate Fano dip to the intensity of the two peaks (i.e., $CR_1 = (I_{left\text{-}peak} - I_{dip}) / I_{left\text{-}peak}$ and $CR_2 = (I_{right\text{-}peak} - I_{dip}) / I_{right\text{-}peak}$), and calculate an average value ($CR_{avg} = (CR_1 + CR_2) / 2$) and error bars (representing $CR_1$ and $CR_2$) for each data point. In general, the overall trends between the experimental and simulated plots in dip positions and CRs remain consistent. Notably, the simulated Fano behaviors exhibit a constant dip position over gap variations at $\lambda = 828$ nm, and their CRs follow an exponential decay with respect to G, fitting as $CR = -0.017 + 0.357 * e^{(-0.020*G/ nm)}$, as depicted by the blue dotted line. The exponential growth in Fano coupling vs. decreasing G suggests that RDPs, owing to their unique structure compared with conventional RDCs, can function as nano-emitter sensors, such as the surface-enhanced Raman scattering (SERS) sensing. [184-185] In Figure 6-7 (c), we present SERS analyses by comparing the Raman spectra of Rhodamine 6G (R6G) acquired from various structures, including a single nanodisc, a nanoring, a hybrid RDP with a mutual gap of 150 nm (RDP_G150), and an RDP with a gap of 45 nm (RDP_G45), respectively. The corresponding SEM images maintain a consistent scale bar of 200 nm. The peaks ranging from ~1400 to ~1700 cm$^{-1}$ correspond to the vibrational modes of C–C stretching of R6G. [184] By comparing these spectra, we observe that the single nanoring yields slightly stronger signals than the single nanodisc, and their hybrid structure of RDP_G150 presents only a "superposition" signal due to the weaker coupling effect. However, once the gap is reduced, e.g., to 45 nm, a significant enhancement of C–C stretching Raman signals can be observed due to strong Fano coupling. In general, these results suggest potential and reliable applications of RDPs as active flexible plasmonic sensors, where the appearance/enhancement of Fano resonances and SERS signals can be monitored by varying the gap with applied strains once the RDPs are transferred onto flexible substrates. [85, 186-187] (Acknowledgment to Dr. Quan Liu and Liangxuan Wang for the SERS measurements, which were conducted as part of the research group led by Prof. Alfred J. Meixner at EKUT.)
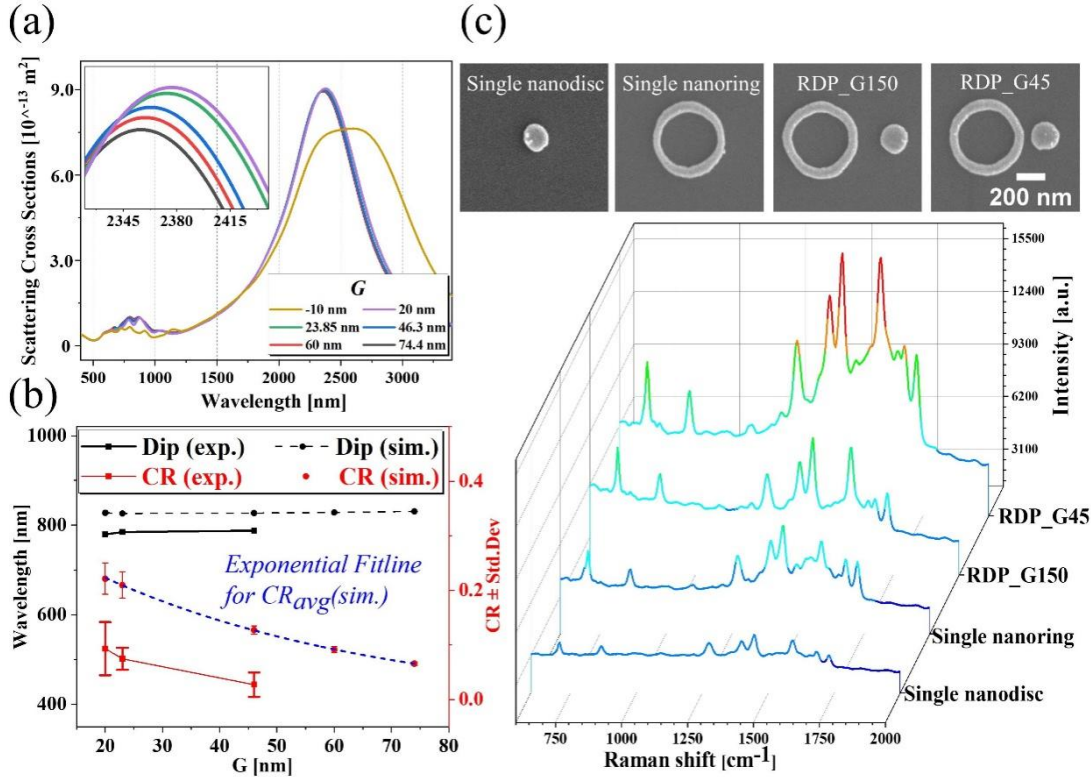
Figure 6-7 (a) Simulated scattering cross section of RDPs with varying *G* from 74.4 nm to a connected state, and the top-left figure shows a weak redshift as *G* decreases. (b) Quantitative studies on the dip positions and CRs in experimental (solid lines) and simulated (dashed lines) spectra for Fano resonances in Figure 6-6. (c) Set of R6G Raman spectra of single nanodisc, nanoring, RDP_G150, and RDP_G45. The scale bar for the SEM images is 200 nm. Figures (a-b) are modified after Ref [181].

## 6.3 Summary

In summary, we demonstrate that the coupled ring-disc-pair (RDP) enables plasmonic hybridization between the multipolar bonding ring and dipolar disc modes in the near-field, leading to the formation of a series of Fano peaks within the dipolar disc background observed in the far-field. Our experimental results show that the quality (e.g., contrast ratios) of these Fano resonances can be improved by reducing the mutual gaps. Furthermore, the SERS analysis suggests that the decreasing gaps can enhance the Raman signals of RDPs due to the strong Fano coupling effect. Compared to the conventional RDCs described in the literature, our work highlights the potential of RDPs in future applications such as far-field spectra/SERS signals evolutions for flexible plasmonics with tunable gaps by transferring RDPs onto stretchable substrate.

# Chapter 7 Conclusion

In this thesis, we have successfully fabricated and characterized flexible metasurfaces composed of gold nanoring (NR) and elliptical nanoring (ENR) arrays embedded in polydimethylsiloxane (PDMS). Our study highlights the active tuning of optical properties in NR/ENR metasurfaces, including larger localized surface plasmonic resonance (LSPR) spectral shifts and emerging surface lattice resonances (SLRs) under strain, and distinct Fano lineshapes for SLRs at higher strain values. The feasibility of the nanofabrication and the reliability of optical measurements have been confirmed through subsequent SEM characterizations.

Specifically, we demonstrate the in-situ shape alteration of thin-walled Au NRs on a stretched PDMS, confirmed by in-situ optical/SEM measurements and numerical simulation. The shape-altering NRs can serve as an effective strain sensor, exhibiting a significant spectral redshift for the main LSPR mode (2.85 nm/1% strain) higher than previous gap-altering flexible devices (up to 2 nm/1%). Simulation results illustrate that such significant spectral shifts come from the radially symmetric bonding mode in NRs, while the side peak referring to the asymmetric bonding mode tends to diminish as the shape develops under strain. Moreover, based on the optical/SEM characterizations for NRs with a large periodicity or those fabricated by a cured modeling, we propose a "squeezing" model to explain the deformability of rigid Au NRs on the flexible PDMS. As the substrate is subjected to uniaxial stretching, the transverse shrinkage causes the densely distributed NR arrays to squeeze each other, and embedded NRs with thin width overcome the modulus difference to achieve the in-situ shape development. This work explores the geometric optimization of hollow nanoparticles for enhanced optical properties and highlights the potential for sensing applications based on shape-altering behaviors.

Furthermore, we investigate the strain-induced spectral behaviors of square and regular triangular arrays of Au ENRs on PDMS. The spectral evolution of the square array exhibits strong polarization dependence, showing the emergence of SLRs and a distinct Fano features for different SLRs at higher strain values when transverse polarization is applied during stretching. In contrast, the triangular arrays exhibit similar behaviors under both polarizations, including redshifting SLRs and blueshifting LSPR modes. These results are supported by a set of reproducible tests

and are theoretically explained by numerical simulations, providing insights into metasurface design with respect to SLRs and LSPRs under strain. This work illustrates that the functionalities of flexible metasurfaces significantly depend on the lattice arrangements and suggests the potential for metasurfaces composed of anisotropic nanoparticles.

Lastly, we demonstrate the Fano coupling in Au ring-disc-pair (RDP) systems on rigid substrates, where the Fano features arise from the interference between the discrete peaks of multi-polar rings and the broad continuum of the dipolar disc. Our results indicate that a decreasing gap in RDPs can significantly enhance the quality of these Fano resonances (e.g., contrast ratios) and Raman signals. Such hybrid RDPs hold interest for future research, such as monitoring far-field spectra or surface-enhanced Raman scattering (SERS) signals in gap-altering flexible devices once they are transferred onto a stretchable substrate.

To conclude, this thesis presents a state-of-the-art nanofabrication method by combining the flexibility of EBL in pattern design and the processibility of wet-etching in transfer. Optical measurements further reveal the outstanding spectral evolution for NR/ENR metasurfaces and potential for RDPs, distinct from traditional disc/sphere arrays. Given the strong and sensitive spectral behaviors under strain, this thesis lays a solid foundation for future applications, such as strain sensing, flexible color display, and wearable electronics.

# References

1. Hutter, E.; Fendler, J. H., Exploitation of localized surface plasmon resonance. *Advanced Materials* **2004,** *16* (19), 1685-1706.

2. Sherry, L. J.; Jin, R.; Mirkin, C. A.; Schatz, G. C.; Van Duyne, R. P., Localized surface plasmon resonance spectroscopy of single silver triangular nanoprisms. *Nano Letters* **2006,** *6* (9), 2060-2065.

3. Willets, K. A.; Van Duyne, R. P., Localized surface plasmon resonance spectroscopy and sensing. *Annu. Rev. Phys. Chem.* **2007,** *58,* 267-297.

4. Mayer, K. M.; Hafner, J. H., Localized surface plasmon resonance sensors. *Chemical Reviews* **2011,** *111* (6), 3828-3857.

5. Petryayeva, E.; Krull, U. J., Localized surface plasmon resonance: Nanostructures, bioassays and biosensing—A review. *Analytica Chimica Acta* **2011,** *706* (1), 8-24.

6. Ditlbacher, H.; Krenn, J. R.; Schider, G.; Leitner, A.; Aussenegg, F. R., Two-dimensional optics with surface plasmon polaritons. *Applied Physics Letters* **2002,** *81* (10), 1762-1764.

7. Zayats, A. V.; Smolyaninov, I. I., Near-field photonics: surface plasmon polaritons and localized surface plasmons. *Journal of Optics A: Pure and Applied Optics* **2003,** *5* (4), S16.

8. Zayats, A. V.; Smolyaninov, I. I.; Maradudin, A. A., Nano-optics of surface plasmon polaritons. *Physics Reports* **2005,** *408* (3-4), 131-314.

9. Pitarke, J.; Silkin, V.; Chulkov, E.; Echenique, P., Theory of surface plasmons and surface-plasmon polaritons. *Reports on Progress in Physics* **2006,** *70* (1), 1.

10. Zhang, J.; Zhang, L.; Xu, W., Surface plasmon polaritons: physics and applications. *Journal of Physics D: Applied Physics* **2012,** *45* (11), 113001.

11. Thomson, J. J., Discovery of the electron. *Philosophical Magazine* **1897,** *44,* 93.

12. Sommerfeld, A., Ueber die Fortpflanzung elektrodynamischer Wellen längs eines Drahtes. *Annalen der Physik* **1899,** *303* (2), 233-290.

13. Mie, G., Beiträge zur Optik trüber Medien, speziell kolloidaler Metallösungen. *Annalen der Physik* **1908,** *330* (3), 377-445.

14. Pines, D.; Bohm, D., A collective description of electron interactions: II. Collective vs individual particle aspects of the interactions. *Physical Review* **1952,** *85* (2), 338.

15. Sziklas, E. A., Collective Oscillations in a Dense Electron Gas Containing a Fixed Point Charge. *Physical Review* **1965,** *138* (4A), A1070.

16. Bennett, A. J., Influence of the electron charge distribution on surface-plasmon dispersion. *Physical Review B* **1970,** *1* (1), 203.

17. Feuerbacher, B.; Fitton, B., Investigation of Collective Electron Oscillations in Cd, Mg, and Zn by Photoemission. *Physical Review Letters* **1970,** *24* (10), 499.

18. Simon, H.; Mitchell, D.; Watson, J., Optical second-harmonic generation with surface plasmons in silver films. *Physical Review Letters* **1974,** *33* (26), 1531.

19. Leamy, H., Charge collection scanning electron microscopy. *Journal of Applied Physics* **1982,** *53* (6), R51-R80.

20. Seiler, H., Secondary electron emission in the scanning electron microscope. *Journal of Applied Physics* **1983,** *54* (11), R1-R18.

21. Goodhew, P. J.; Humphreys, J., Electron microscopy and analysis. *CRC Press* **2000**.

22. Crowell, J.; Chen, J.; Yates Jr, J., Surface sensitive spectroscopic study of the interaction of oxygen with Al (111)-low temperature chemisorption and oxidation. *Surface Science* **1986,** *165* (1), 37-64.

23. Kruit, P.; Venables, J., High-spatial-resolution surface-sensitive electron spectroscopy using a magnetic parallelizer. *Ultramicroscopy* **1988,** *25* (3), 183-193.

24. Sullivan, D. M., Frequency-dependent FDTD methods using Z transforms. *IEEE Transactions on Antennas and Propagation* **1992,** *40* (10), 1223-1230.

25. Sullivan, D. M., Z-transform theory and the FDTD method. *IEEE Transactions on Antennas and Propagation* **1996,** *44* (1), 28-34.

26. Okoniewski, M.; Mrozowski, M.; Stuchly, M., Simple treatment of multi-term dispersion in FDTD. *IEEE Microwave and Guided Wave Letters* **1997,** *7* (5), 121-123.

27. Sullivan, D. M., Electromagnetic simulation using the FDTD method. *John Wiley & Sons* **2013**.

28. Yang, W. H.; Schatz, G. C.; Van Duyne, R. P., Discrete dipole approximation for calculating extinction and Raman intensities for small particles with arbitrary shapes. *The Journal of Chemical Physics* **1995,** *103* (3), 869-875.

29. Piller, N. B.; Martin, O. J., Increasing the performance of the coupled-dipole approximation: A spectral approach. *IEEE Transactions on Antennas and Propagation* **1998,** *46* (8), 1126-1137.

30. Jensen, T. R.; Duval, M. L.; Kelly, K. L.; Lazarides, A. A.; Schatz, G. C.; Van Duyne, R. P., Nanosphere lithography: effect of the external dielectric medium on the surface plasmon resonance spectrum of a periodic array of silver nanoparticles. *The Journal of Physical Chemistry B* **1999,** *103* (45), 9846-9853.

31. Rajarajan, M.; Themistos, C.; Rahman, B. A.; Grattan, K. T., Characterization of metal-clad TE/TM mode splitters using the finite element method. *Journal of Lightwave Technology* **1997,** *15* (12), 2264-2269.

32. Rindzevicius, T.; Alaverdyan, Y.; Dahlin, A.; Höök, F.; Sutherland, D. S.; Käll, M., Plasmonic sensing characteristics of single nanometric holes. *Nano Letters* **2005,** *5* (11), 2335-2339.

33. Stewart, M. E.; Anderton, C. R.; Thompson, L. B.; Maria, J.; Gray, S. K.; Rogers, J. A.; Nuzzo, R. G., Nanostructured plasmonic sensors. *Chemical Reviews* **2008,** *108* (2), 494-521.

34. Tong, L.; Wei, H.; Zhang, S.; Xu, H., Recent advances in plasmonic sensors. *Sensors* **2014,** *14* (5), 7959-7973.

35. Yu, H.; Shan, X.; Wang, S.; Chen, H.; Tao, N., Plasmonic imaging and detection of single DNA molecules. *ACS Nano* **2014,** *8* (4), 3427-3433.

36. Ye, W.; Long, R.; Huang, H.; Xiong, Y., Plasmonic nanostructures in solar energy conversion. *Journal of Materials Chemistry C* **2017,** *5* (5), 1008-1021.

37. Ozbay, E., Plasmonics: merging photonics and electronics at nanoscale dimensions. *Science* **2006,** *311* (5758), 189-193.

38. Wang, L.; Ng, R. J. H.; Safari Dinachali, S.; Jalali, M.; Yu, Y.; Yang, J. K., Large area plasmonic color palettes with expanded gamut using colloidal self-assembly. *ACS Photonics* **2016,** *3* (4), 627-633.

39. Mayer, M.; Schnepf, M. J.; König, T. A.; Fery, A., Colloidal Self-Assembly Concepts for Plasmonic Metasurfaces. *Advanced Optical Materials* **2019,** *7* (1), 1800564.

40. Juan, M. L.; Righini, M.; Quidant, R., Plasmon nano-optical tweezers. *Nature Photonics* **2011,** *5* (6), 349-356.

41. Crozier, K. B., Quo vadis, plasmonic optical tweezers? *Light: Science & Applications* **2019,** *8* (1), 35.

42. Vesseur, E. J. R.; De Waele, R.; Lezec, H.; Atwater, H.; García de Abajo, F. J.; Polman, A., Surface plasmon polariton modes in a single-crystal Au nanoresonator fabricated using focused-ion-beam milling. *Applied Physics Letters* **2008,** *92* (8), 083110.

43. Chen, Y.; Bi, K.; Wang, Q.; Zheng, M.; Liu, Q.; Han, Y.; Yang, J.; Chang, S.; Zhang, G.; Duan, H., Rapid focused ion beam milling based fabrication of plasmonic nanoparticles and assemblies via "sketch and peel" strategy. *ACS Nano* **2016,** *10* (12), 11228-11236.

44. Near, R.; Tabor, C.; Duan, J.; Pachter, R.; El-Sayed, M., Pronounced effects of anisotropy on plasmonic properties of nanorings fabricated by electron beam lithography. *Nano Letters* **2012,** *12* (4), 2158-2164.

45. Horák, M.; Bukvišová, K.; Švarc, V.; Jaskowiec, J.; Křápek, V.; Šikola, T., Comparative study of plasmonic antennas fabricated by electron beam and focused ion beam lithography. *Scientific Reports* **2018,** *8* (1), 9640.

46. Manfrinato, V. R.; Camino, F. E.; Stein, A.; Zhang, L.; Lu, M.; Stach, E. A.; Black, C. T., Patterning Si at the 1 nm length scale with aberration-corrected electron-beam lithography: tuning of plasmonic properties by design. *Advanced Functional Materials* **2019,** *29* (52), 1903429.

47. Kazanskiy, N.; Khonina, S.; Butt, M., Plasmonic sensors based on Metal-insulator-metal waveguides for refractive index sensing applications: A brief review. *Physica E: Low-dimensional Systems and Nanostructures* **2020,** *117*, 113798.

48. Chen, S.; Lin, C., Sensitivity comparison of graphene based surface plasmon resonance biosensor with Au, Ag and Cu in the visible region. *Materials Research Express* **2019,** *6* (5), 056503.

49. Dal Forno, S.; Ranno, L.; Lischner, J., Material, size, and environment dependence of plasmon-induced hot carriers in metallic nanoparticles. *The Journal of Physical Chemistry C* **2018,** *122* (15), 8517-8527.

50. Ding, W.; Hsu, L.-Y.; Heaps, C. W.; Schatz, G. C., Plasmon-coupled resonance energy transfer II: Exploring the peaks and dips in the electromagnetic coupling factor. *The Journal of Physical Chemistry C* **2018,** *122* (39), 22650-22659.

51. Dao, T. D.; Hoang, C. V.; Nishio, N.; Yamamoto, N.; Ohi, A.; Nabatame, T.; Aono, M.; Nagao, T., Dark-field scattering and local SERS mapping from plasmonic aluminum bowtie antenna array. *Micromachines* **2019,** *10* (7), 468.

52. Bhattarai, A.; O'Callahan, B. T.; Wang, C.-F.; Wang, S.; El-Khoury, P. Z., Spatio-spectral characterization of multipolar plasmonic modes of Au nanorods via tip-enhanced Raman scattering. *The Journal of Physical Chemistry Letters* **2020,** *11* (8), 2870-2874.

53. Cai, Y.; Li, Y.; Nordlander, P.; Cremer, P. S., Fabrication of elliptical nanorings with highly tunable and multiple plasmonic resonances. *Nano Letters* **2012,** *12* (9), 4881-4888.

54. Aizpurua, J.; Hanarp, P.; Sutherland, D.; Käll, M.; Bryant, G. W.; De Abajo, F. G., Optical properties of gold nanorings. *Physical review Letters* **2003,** *90* (5), 057401.

55. Zhou, H.; Li, P.; Fang, Y., Single-phase-lag thermoelastic damping models for

rectangular cross-sectional micro-and nano-ring resonators. *International Journal of Mechanical Sciences* **2019,** *163*, 105132.

56. Chao, C.-T. C.; Chau, Y.-F. C.; Chiang, H.-P., Highly sensitive metal-insulator-metal plasmonic refractive index sensor with a centrally coupled nanoring containing defects. *Journal of Physics D: Applied Physics* **2021,** *54* (11), 115301.

57. Xu, T.; Geng, Z.; Su, Y., A potential plasmonic biosensor based asymmetric metal ring cavity with extremely narrow linewidth and high sensitivity. *Sensors* **2021,** *21* (3), 752.

58. Chen, Z.; Cui, L.; Song, X.; Yu, L.; Xiao, J., High sensitivity plasmonic sensing based on Fano interference in a rectangular ring waveguide. *Optics Communications* **2015,** *340*, 1-4.

59. Chen, F.; Zhang, H.; Sun, L.; Li, J.; Yu, C., Temperature tunable Fano resonance based on ring resonator side coupled with a MIM waveguide. *Optics & Laser Technology* **2019,** *116*, 293-299.

60. Hao, F.; Nordlander, P.; Burnett, M. T.; Maier, S. A., Enhanced tunability and linewidth sharpening of plasmon resonances in hybridized metallic ring/disk nanocavities. *Physical Review B* **2007,** *76* (24), 245417.

61. Cetin, A. E.; Altug, H., Fano resonant ring/disk plasmonic nanocavities on conducting substrates for advanced biosensing. *ACS Nano* **2012,** *6* (11), 9989-9995.

62. Fu, Y. H.; Zhang, J. B.; Yu, Y. F.; Luk'yanchuk, B., Generating and manipulating higher order Fano resonances in dual-disk ring plasmonic nanostructures. *ACS Nano* **2012,** *6* (6), 5130-5137.

63. Halpern, A. R.; Corn, R. M., Lithographically patterned electrodeposition of gold, silver, and nickel nanoring arrays with widely tunable near-infrared plasmonic resonances. *ACS Nano* **2013,** *7* (2), 1755-1762.

64. Chow, T. H.; Lai, Y.; Cui, X.; Lu, W.; Zhuo, X.; Wang, J., Colloidal gold nanorings and their plasmon coupling with gold nanospheres. *Small* **2019,** *15* (35), 1902608.

65. Zhang, J.; ElKabbash, M.; Wei, R.; Singh, S. C.; Lam, B.; Guo, C., Plasmonic metasurfaces with 42.3% transmission efficiency in the visible. *Light: Science & Applications* **2019,** *8* (1), 53.

66. Jung, C.; Kim, G.; Jeong, M.; Jang, J.; Dong, Z.; Badloe, T.; Yang, J. K.; Rho, J., Metasurface-driven optically variable devices. *Chemical Reviews* **2021,** *121* (21), 13013-13050.

67. Thrane, P. C.; Meng, C.; Ding, F.; Bozhevolnyi, S. I., MEMS Tunable Metasurfaces Based on Gap Plasmon or Fabry–Pérot Resonances. *Nano Letters* **2022,** *22* (17), 6951-6957.

68. Meng, C.; Thrane, P. C.; Ding, F.; Bozhevolnyi, S. I., Full-range birefringence control with piezoelectric MEMS-based metasurfaces. *Nature Communications* **2022,** *13* (1), 2071.

69. Humphrey, A. D.; Barnes, W. L., Plasmonic surface lattice resonances on arrays of different lattice symmetry. *Physical Review B* **2014,** *90* (7), 075404.

70. Fitzgerald, J. P.; Karg, M., Plasmon resonance coupling phenomena in self-assembled colloidal monolayers. *Physica Status Solidi (a)* **2017,** *214* (8), 1600947.

71. Wang, W.; Ramezani, M.; Väkeväinen, A. I.; Törmä, P.; Rivas, J. G.; Odom, T. W., The rich photonic world of plasmonic nanoparticle arrays. *Materials Today* **2018,** *21* (3), 303-314.

72. Cherqui, C.; Bourgeois, M. R.; Wang, D.; Schatz, G. C., Plasmonic surface lattice resonances: Theory and computation. *Accounts of Chemical Research* **2019,** *52* (9), 2548-2558.

73. Bin-Alam, M. S.; Reshef, O.; Mamchur, Y.; Alam, M. Z.; Carlow, G.; Upham, J.; Sullivan, B. T.; Ménard, J.-M.; Huttunen, M. J.; Boyd, R. W., Ultra-high-Q resonances in plasmonic metasurfaces. *Nature Communications* **2021,** *12* (1), 974.

74. Liu, J.; Shi, M.; Chen, Z.; Wang, S.; Wang, Z.; Zhu, S., Quantum photonics based on metasurfaces. *Opto-Electronic Advances* **2021,** *4* (9), 200092-1-200092-13.

75. Krasnok, A.; Tymchenko, M.; Alù, A., Nonlinear metasurfaces: a paradigm shift in nonlinear optics. *Materials Today* **2018,** *21* (1), 8-21.

76. Kamali, S. M.; Arbabi, E.; Arbabi, A.; Horie, Y.; Faraon, A., Highly tunable elastic dielectric metasurface lenses. *Laser & Photonics Reviews* **2016,** *10* (6), 1002-1008.

77. Zhang, S.; Wong, C. L.; Zeng, S.; Bi, R.; Tai, K.; Dholakia, K.; Olivo, M., Metasurfaces for biomedical applications: imaging and sensing from a nanophotonics perspective. *Nanophotonics* **2020,** *10* (1), 259-293.

78. Baffou, G.; Quidant, R., Thermoplasmonics in World Scientific Handbook of Metamaterials and Plasmonics: Volume 4: Recent Progress in the Field of Nanoplasmonics. *World Scientific* **2018,** 379-407.

79. Yang, A.; Hryn, A. J.; Bourgeois, M. R.; Lee, W.-K.; Hu, J.; Schatz, G. C.; Odom, T. W., Programmable and reversible plasmon mode engineering. *Proceedings of the National Academy of Sciences* **2016,** *113* (50), 14201-14206.

80. Gupta, V.; Probst, P. T.; Goßler, F. R.; Steiner, A. M.; Schubert, J.; Brasse, Y.; König, T. A.; Fery, A., Mechanotunable surface lattice resonances in the visible optical range by soft lithography templates and directed self-assembly. *ACS Applied Materials & Interfaces* **2019,** *11* (31), 28189-28196.

81. Brasse, Y.; Gupta, V.; Schollbach, H. T.; Karg, M.; König, T. A.; Fery, A., Mechanotunable plasmonic properties of colloidal assemblies. *Advanced Materials Interfaces* **2020,** *7* (5), 1901678.

82. Kang, L.; Jenkins, R. P.; Werner, D. H., Recent progress in active optical metasurfaces. *Advanced Optical Materials* **2019,** *7* (14), 1801813.

83. Fu, R.; Lu, Y.; Cheng, W., Soft plasmonics: design, fabrication, characterization, and applications. *Advanced Optical Materials* **2022,** *10* (1), 2101436.

84. Shiohara, A.; Langer, J.; Polavarapu, L.; Liz-Marzán, L. M., Solution processed polydimethylsiloxane/gold nanostar flexible substrates for plasmonic sensing. *Nanoscale* **2014,** *6* (16), 9817-9823.

85. Laible, F.; Gollmer, D. A.; Dickreuter, S.; Kern, D. P.; Fleischer, M., Continuous reversible tuning of the gap size and plasmonic coupling of bow tie nanoantennas on flexible substrates. *Nanoscale* **2018,** *10* (31), 14915-14922.

86. Wang, K.; Sun, D.-W.; Pu, H.; Wei, Q.; Huang, L., Stable, flexible, and high-performance SERS chip enabled by a ternary film-packaged plasmonic nanoparticle array. *ACS Applied Materials & Interfaces* **2019,** *11* (32), 29177-29186.

87. Grzelak, D.; Tupikowska, M.; Vila-Liarte, D.; Beutel, D.; Bagiński, M.; Parzyszek, S.; Góra, M.; Rockstuhl, C.; Liz-Marzán, L. M.; Lewandowski, W., Liquid crystal templated chiral plasmonic films with dynamic tunability and moldability. *Advanced Functional Materials* **2022,** *32* (16), 2111280.

88. Mittal, G.; Rhee, K. Y.; Mišković-Stanković, V.; Hui, D., Reinforcements in multi-scale polymer composites: Processing, properties, and applications. *Composites Part B: Engineering* **2018,** *138*, 122-139.

89. Song, S.; Ma, X.; Pu, M.; Li, X.; Liu, K.; Gao, P.; Zhao, Z.; Wang, Y.; Wang, C.; Luo, X., Actively tunable structural color rendering with tensile substrate. *Advanced Optical Materials* **2017,** *5* (9), 1600829.

90. Peng, W.; Wu, H., Flexible and stretchable photonic sensors based on modulation of light transmission. *Advanced Optical Materials* **2019,** *7* (12), 1900329.

91. Du, K.; Wathuthanthri, I.; Liu, Y.; Xu, W.; Choi, C.-H., Wafer-scale pattern transfer of metal nanostructures on polydimethylsiloxane (PDMS) substrates via holographic nanopatterns. *ACS Applied Materials & Interfaces* **2012,** *4* (10),

5505-5514.

92. Tseng, M. L.; Yang, J.; Semmlinger, M.; Zhang, C.; Nordlander, P.; Halas, N. J., Two-dimensional active tuning of an aluminum plasmonic array for full-spectrum response. *Nano Letters* **2017,** *17* (10), 6034-6039.

93. Gao, L.; Zhang, Y.; Zhang, H.; Doshay, S.; Xie, X.; Luo, H.; Shah, D.; Shi, Y.; Xu, S.; Fang, H., Optics and nonlinear buckling mechanics in large-area, highly stretchable arrays of plasmonic nanostructures. *ACS Nano* **2015,** *9* (6), 5968-5975.

94. Su, K.-H.; Wei, Q.-H.; Zhang, X.; Mock, J.; Smith, D. R.; Schultz, S., Interparticle coupling effects on plasmon resonances of nanogold particles. *Nano Letters* **2003,** *3* (8), 1087-1090.

95. Cataldi, U.; Caputo, R.; Kurylyak, Y.; Klein, G.; Chekini, M.; Umeton, C.; Bürgi, T., Growing gold nanoparticles on a flexible substrate to enable simple mechanical control of their plasmonic coupling. *Journal of Materials Chemistry C* **2014,** *2* (37), 7927-7933.

96. Steiner, A. M.; Mayer, M.; Seuss, M.; Nikolov, S.; Harris, K. D.; Alexeev, A.; Kuttner, C.; König, T. A.; Fery, A., Macroscopic strain-induced transition from quasi-infinite gold nanoparticle chains to defined plasmonic oligomers. *ACS Nano* **2017,** *11* (9), 8871-8880.

97. Rodrigues, M. S.; Borges, J.; Vaz, F., Plasmonic Strain Sensors Based on Au-TiO2 Thin Films on Flexible Substrates. *Sensors* **2022,** *22* (4), 1375.

98. Kumari, S.; Mohapatra, S.; Moirangthem, R. S., Development of flexible plasmonic plastic sensor using nanograting textured laminating film. *Materials Research Express* **2017,** *4* (2), 025008.

99. Zhu, J.; Wang, Z.; Lin, S.; Jiang, S.; Liu, X.; Guo, S., Low-cost flexible plasmonic nanobump metasurfaces for label-free sensing of serum tumor marker. *Biosensors and Bioelectronics* **2020,** *150*, 111905.

100. Jackson, J. D., Classical electrodynamics. *American Association of Physics Teachers* **1999**.

101. Griffiths, D. J., Introduction to electrodynamics. *American Association of Physics Teachers* **2005**.

102. Zangwill, A., Modern electrodynamics. *Cambridge University Press* **2013**.

103. Maier, S. A., Plasmonics: fundamentals and applications. *Springer* **2007,** Vol. 1.

104. Bohren, C. F.; Huffman, D. R., Absorption and scattering of light by small particles. *John Wiley & Sons* **2008**.

105. Kreibig, U.; Vollmer, M., Optical properties of metal clusters. *Springer Science*

*& Business Media* **2013,** Vol. 25.

106. Mundy, W.; Roux, J.; Smith, A., Mie scattering by spheres in an absorbing medium. *JOSA* **1974,** *64* (12), 1593-1597.

107. Lentz, W. J., Generating Bessel functions in Mie scattering calculations using continued fractions. *Applied Optics* **1976,** *15* (3), 668-671.

108. Grehan, G.; Gouesbet, G., Mie theory calculations: new progress, with emphasis on particle sizing. *Applied Optics* **1979,** *18* (20), 3489-3493.

109. Fowler, B. W., Expansion of Mie-theory phase functions in series of Legendre polynomials. *JOSA* **1983,** *73* (1), 19-22.

110. Kreibig, U.; Vollmer, M.; Kreibig, U.; Vollmer, M., Theoretical considerations in Optical Properties of Metal Clusters. *Springer-Verlag Berlin Heidelberg* **1995**, 13-201.

111. Jain, P. K.; El-Sayed, M. A., Noble metal nanoparticle pairs: effect of medium for enhanced nanosensing. *Nano Letters* **2008,** *8* (12), 4347-4352.

112. You, E.-M.; Chen, Y.; Yi, J.; Meng, Z.-D.; Chen, Q.; Ding, S.-Y.; Duan, H.; Moskovits, M.; Tian, Z.-Q., Nanobridged rhombic antennas supporting both dipolar and high-order plasmonic modes with spatially superimposed hotspots in the mid-infrared. *Opto-Electronic Advances* **2021,** *4* (12), 210076-1-210076-14.

113. Heßler, A.; Wahl, S.; Leuteritz, T.; Antonopoulos, A.; Stergianou, C.; Schön, C.-F.; Naumann, L.; Eicker, N.; Lewin, M.; Maß, T. W., $In_3SbTe_2$ as a programmable nanophotonics material platform for the infrared. *Nature Communications* **2021,** *12* (1), 924.

114. Jain, P. K.; Huang, W.; El-Sayed, M. A., On the universal scaling behavior of the distance decay of plasmon coupling in metal nanoparticle pairs: a plasmon ruler equation. *Nano Letters* **2007,** *7* (7), 2080-2088.

115. Gunnarsson, L.; Rindzevicius, T.; Prikulis, J.; Kasemo, B.; Käll, M.; Zou, S.; Schatz, G. C., Confined plasmons in nanofabricated single silver particle pairs: experimental observations of strong interparticle interactions. *The Journal of Physical Chemistry B* **2005,** *109* (3), 1079-1087.

116. Tabor, C.; Murali, R.; Mahmoud, M.; El-Sayed, M. A., On the use of plasmonic nanoparticle pairs as a plasmon ruler: the dependence of the near-field dipole plasmon coupling on nanoparticle size and shape. *The Journal of Physical Chemistry A* **2009,** *113* (10), 1946-1953.

117. Ghosh, S. K.; Pal, T., Interparticle coupling effect on the surface plasmon resonance of gold nanoparticles: from theory to applications. *Chemical Reviews* **2007,**

*107* (11), 4797-4862.

118. Scholl, J. A.; García-Etxarri, A.; Koh, A. L.; Dionne, J. A., Observation of quantum tunneling between two plasmonic nanoparticles. *Nano Letters* **2013,** *13* (2), 564-569.

119. Zuloaga, J.; Prodan, E.; Nordlander, P., Quantum description of the plasmon resonances of a nanoparticle dimer. *Nano Letters* **2009,** *9* (2), 887-891.

120. Cha, H.; Yoon, J. H.; Yoon, S., Probing quantum plasmon coupling using gold nanoparticle dimers with tunable interparticle distances down to the subnanometer range. *ACS Nano* **2014**, 8 (8), 8554-8563.

121. Deng, T.-S.; Parker, J.; Yifat, Y.; Shepherd, N.; Scherer, N. F., Dark plasmon modes in symmetric gold nanoparticle dimers illuminated by focused cylindrical vector beams. *The Journal of Physical Chemistry C* **2018,** *122* (48), 27662-27672.

122. Tamaru, H.; Kuwata, H.; Miyazaki, H. T.; Miyano, K., Resonant light scattering from individual Ag nanoparticles and particle pairs. *Applied Physics Letters* **2002,** *80* (10), 1826-1828.

123. Rechberger, W.; Hohenau, A.; Leitner, A.; Krenn, J.; Lamprecht, B.; Aussenegg, F., Optical properties of two interacting gold nanoparticles. *Optics Communications* **2003,** *220* (1-3), 137-141.

124. Hooshmand, N.; El-Sayed, M. A., Collective multipole oscillations direct the plasmonic coupling at the nanojunction interfaces. *Proceedings of the National Academy of Sciences* **2019,** *116* (39), 19299-19304.

125. Zhou, Y.; Zhu, J.; Xi, J.; Li, K.; Huang, W., Quantitative Insights into a Plasmonic Ruler Equation from the Perspective of Enhanced Near Field. *The Journal of Physical Chemistry A* **2022,** *127* (1): 390-399.

126. Clerk, A.; Waintal, X.; Brouwer, P., Fano resonances as a probe of phase coherence in quantum dots. *Physical Review Letters* **2001,** *86* (20), 4636.

127. Göres, J.; Goldhaber-Gordon, D.; Heemeyer, S.; Kastner, M.; Shtrikman, H.; Mahalu, D.; Meirav, U., Fano resonances in electronic transport through a single-electron transistor. *Physical Review B* **2000,** *62* (3), 2188.

128. Song, J.; Ochiai, Y.; Bird, J., Fano resonances in open quantum dots and their application as spin filters. *Applied Physics Letters* **2003,** *82* (25), 4561-4563.

129. Fano, U., Sullo spettro di assorbimento dei gas nobili presso il limite dello spettro d'arco. *Il Nuovo Cimento (1924-1942)* **1935,** *12* (3), 154-161.

130. Fano, U., Effects of configuration interaction on intensities and phase shifts. *Physical Review* **1961,** *124* (6), 1866.

131. Joe, Y. S.; Satanin, A. M.; Kim, C. S., Classical analogy of Fano resonances. *Physica Scripta* **2006,** *74* (2), 259.

132. Miroshnichenko, A. E.; Flach, S.; Kivshar, Y. S., Fano resonances in nanoscale structures. *Reviews of Modern Physics* **2010,** *82* (3), 2257.

133. Dai, F.; Horrer, A.; Adam, P. M.; Fleischer, M., Accessing the hotspots of cavity plasmon modes in vertical metal–insulator–metal structures for surface enhanced Raman scattering. *Advanced Optical Materials* **2020,** *8* (7), 1901734.

134. Chen, Z.; Zhang, S.; Chen, Y.; Liu, Y.; Li, P.; Wang, Z.; Zhu, X.; Bi, K.; Duan, H., Double Fano resonances in hybrid disk/rod artificial plasmonic molecules based on dipole-quadrupole coupling. *Nanoscale* **2020,** *12* (17), 9776-9785.

135. Luk'Yanchuk, B.; Zheludev, N. I.; Maier, S. A.; Halas, N. J.; Nordlander, P.; Giessen, H.; Chong, C. T., The Fano resonance in plasmonic nanostructures and metamaterials. *Nature Materials* **2010,** *9* (9), 707-715.

136. Cui, Y.; Zhou, J.; Tamma, V. A.; Park, W., Dynamic tuning and symmetry lowering of Fano resonance in plasmonic nanostructure. *ACS Nano* **2012,** *6* (3), 2385-2393.

137. Dregely, D.; Hentschel, M.; Giessen, H., Excitation and tuning of higher-order Fano resonances in plasmonic oligomer clusters. *ACS nano* **2011,** *5* (10), 8202-8211.

138. Hao, F.; Sonnefraud, Y.; Dorpe, P. V.; Maier, S. A.; Halas, N. J.; Nordlander, P., Symmetry breaking in plasmonic nanocavities: subradiant LSPR sensing and a tunable Fano resonance. *Nano Letters* **2008,** *8* (11), 3983-3988.

139. Hao, F.; Nordlander, P.; Sonnefraud, Y.; Dorpe, P. V.; Maier, S. A., Tunability of subradiant dipolar and Fano-type plasmon resonances in metallic ring/disk cavities: implications for nanoscale optical sensing. *ACS Nano* **2009,** *3* (3), 643-652.

140. Maradudin, A.; Simonsen, I.; Polanco, J.; Fitzgerald, R., Rayleigh and Wood anomalies in the diffraction of light from a perfectly conducting reflection grating. *Journal of Optics* **2016,** *18* (2), 024004.

141. Darweesh, A. A.; Bauman, S. J.; Debu, D. T.; Herzog, J. B., The role of Rayleigh-Wood anomalies and surface plasmons in optical enhancement for nano-gratings. *Nanomaterials* **2018,** *8* (10), 809.

142. Wood, R. W., XLII. On a remarkable case of uneven distribution of light in a diffraction grating spectrum. *The London, Edinburgh, and Dublin Philosophical Magazine and Journal of Science* **1902,** *4* (21), 396-402.

143. Ekşioğlu, Y.; Cetin, A. E.; Petráček, J., Optical response of plasmonic nanohole arrays: comparison of square and hexagonal lattices. *Plasmonics* **2016,** *11*, 851-856.

144. Utyushev, A. D.; Zakomirnyi, V. I.; Ershov, A. E.; Gerasimov, V. S.; Karpov, S. V.; Rasskazov, I. L., Collective lattice resonances in all-dielectric nanostructures under oblique incidence. *Photonics*, MDPI, **2020,** *7* (2), 24.

145. Gao, H.; McMahon, J.; Lee, M.; Henzie, J.; Gray, S.; Schatz, G.; Odom, T., Rayleigh anomaly-surface plasmon polariton resonances in palladium and gold subwavelength hole arrays. *Optics Express* **2009,** *17* (4), 2334-2340.

146. Auguié, B.; Barnes, W. L., Collective resonances in gold nanoparticle arrays. *Physical Review Letters* **2008,** *101* (14), 143902.

147. Chu, Y.; Schonbrun, E.; Yang, T.; Crozier, K. B., Experimental observation of narrow surface plasmon resonances in gold nanoparticle arrays. *Applied Physics Letters* **2008,** *93* (18), 181108.

148. Vecchi, G.; Giannini, V.; Rivas, J. G., Surface modes in plasmonic crystals induced by diffractive coupling of nanoantennas. *Physical Review B* **2009,** *80* (20), 201401.

149. Pease, R., Electron beam lithography. *Contemporary Physics* **1981,** *22* (3), 265-290.

150. Vieu, C.; Carcenac, F.; Pepin, A.; Chen, Y.; Mejias, M.; Lebib, A.; Manin-Ferlazzo, L.; Couraud, L.; Launois, H., Electron beam lithography: resolution limits and applications. *Applied Surface Science* **2000,** *164* (1-4), 111-117.

151. Levy, P. M.; Zhang, S.; Fert, A., Electrical conductivity of magnetic multilayered structures. *Physical Review Letters* **1990,** *65* (13), 1643.

152. Ren, Y.; Liu, P.; Liu, R.; Wang, Y.; Wei, Y.; Jin, L.; Zhao, G., The key of ITO films with high transparency and conductivity: Grain size and surface chemical composition. *Journal of Alloys and Compounds* **2022,** *893*, 162304.

153. Frazer, R. Q.; Byron, R. T.; Osborne, P. B.; West, K. P., PMMA: an essential material in medicine and dentistry. *Journal of Long-term Effects of Medical Implants* **2005,** *15* (6).

154. Oleksandrov, S.; Lee, J.; Lee, S.; Lee, M.-G.; Choi, H. Y.; Chung, C.-H., Fabrication of micro-and nano-scale gold patterns on glass by transfer printing. *Journal of Nanoscience and Nanotechnology* **2009,** *9* (12), 7481-7484.

155. Pan, S.; Liu, Z.; Wang, M.; Jiang, Y.; Luo, Y.; Wan, C.; Qi, D.; Wang, C.; Ge, X.; Chen, X., Mechanocombinatorially screening sensitivity of stretchable strain sensors. *Advanced Materials* **2019,** *31* (35), 1903130.

156. Leyden, D. E.; Atwater, J. B., Hydrolysis and condensation of alkoxysilanes investigated by internal reflection FTIR spectroscopy. *Journal of Adhesion Science*

*and Technology* **1991,** *5* (10), 815-829.

157. Simo, P. C.; Laible, F.; Horneber, A.; Burkhardt, C. J.; Fleischer, M., Hexagonal arrays of plasmonic gold nanopyramids on flexible substrates for surface-enhanced Raman scattering. *Nanotechnology* **2021,** *33* (9), 095303.

158. Johnson, P. B.; Christy, R.-W., Optical constants of the noble metals. *Physical Review B* **1972,** *6* (12), 4370.

159. Tsai, C.-Y.; Chang, K.-H.; Wu, C.-Y.; Lee, P.-T., The aspect ratio effect on plasmonic properties and biosensing of bonding mode in gold elliptical nanoring arrays. *Optics Express* **2013,** *21* (12), 14090-14096.

160. Pedersen, T. G., Plasmons and magnetoplasmon resonances in nanorings. *Physical Review B* **2021,** *103* (8), 085419.

161. Tao, W.; Laible, F.; Hmima, A.; Maurer, T.; Fleischer, M., Shape-altering flexible plasmonics of in-situ deformable nanorings. *Nano Convergence* **2023,** *10* (1), 15.

162. Marae-Djouda, J.; Gontier, A.; Caputo, R.; Lévêque, G.; Bercu, B.; Madi, Y.; Montay, G.; Adam, P.-M.; Molinari, M.; Stagon, S., Dense brushes of tilted metallic nanorods grown onto stretchable substrates for optical strain sensing. *ACS Applied Nano Materials* **2018,** *1* (5), 2347-2355.

163. Rosenberger, M.; Eisenbeil, W.; Schmauss, B.; Hellmann, R., Simultaneous 2D strain sensing using polymer planar Bragg gratings. *Sensors* **2015,** *15* (2), 4264-4272.

164. Salvadori, M.; Brown, I.; Vaz, A.; Melo, L.; Cattani, M., Measurement of the elastic modulus of nanostructured gold and platinum thin films. *Physical review B* **2003,** *67* (15), 153404.

165. Wang, Z.; Volinsky, A. A.; Gallant, N. D., Crosslinking effect on polydimethylsiloxane elastic modulus measured by custom-built compression instrument. *Journal of Applied Polymer Science* **2014,** *131* (22).

166. Neubrech, F.; Kolb, T.; Lovrincic, R.; Fahsold, G.; Pucci, A.; Aizpurua, J.; Cornelius, T.; Toimil-Molares, M.; Neumann, R.; Karim, S., Resonances of individual metal nanowires in the infrared. *Applied Physics Letters* **2006,** *89* (25), 253104.

167. Apter, B.; Guilatt, O.; Efron, U., Ring-type plasmon resonance in metallic nanoshells. *Applied Optics* **2011,** *50* (28), 5457-5464.

168. Barnard, R. W.; Pearce, K.; Schovanec, L., Inequalities for the perimeter of an ellipse. *Journal of Mathematical Analysis and Applications* **2001,** *260* (2), 295-306.

169. Della Valle, G.; Søndergaard, T.; Bozhevolnyi, S. I., Efficient suppression of radiation damping in resonant retardation-based plasmonic structures. *Physical Review B* **2009,** *79* (11), 113410.

170. Prodan, E.; Radloff, C.; Halas, N. J.; Nordlander, P., A hybridization model for the plasmon response of complex nanostructures. *Science* **2003,** *302* (5644), 419-422.

171. Hao, F.; Larsson, E. M.; Ali, T. A.; Sutherland, D. S.; Nordlander, P., Shedding light on dark plasmons in gold nanorings. *Chemical Physics Letters* **2008,** *458* (4-6), 262-266.

172. Jiang, L.; Yin, T.; Dong, Z.; Liao, M.; Tan, S. J.; Goh, X. M.; Allioux, D.; Hu, H.; Li, X.; Yang, J. K., Accurate modeling of dark-field scattering spectra of plasmonic nanostructures. *ACS Nano* **2015,** *9* (10), 10039-10046.

173. Kravets, V.; Schedin, F.; Grigorenko, A., Extremely narrow plasmon resonances based on diffraction coupling of localized plasmons in arrays of metallic nanoparticles. *Physical Review Letters* **2008,** *101* (8), 087403.

174. Guo, R.; Hakala, T. K.; Törmä, P., Geometry dependence of surface lattice resonances in plasmonic nanoparticle arrays. *Physical Review B* **2017,** *95* (15), 155423.

175. Rahmani, M.; Luk'yanchuk, B.; Hong, M., Fano resonance in novel plasmonic nanostructures. *Laser & Photonics Reviews* **2013,** *7* (3), 329-349.

176. Yang, F.; Chen, Q.; Wang, J.; Chang, J. J.; Dong, W.; Cao, W.; Ye, S.; Shi, L.; Nie, Z., Fabrication of Centimeter-Scale Plasmonic Nanoparticle Arrays with Ultranarrow Surface Lattice Resonances. *ACS Nano* **2022,** *17* (1), 725-734.

177. Lovera, A.; Gallinet, B.; Nordlander, P.; Martin, O. J., Mechanisms of Fano resonances in coupled plasmonic systems. *ACS Nano* **2013,** *7* (5), 4527-4536.

178. Cao, G.; Dong, S.; Zhou, L. M.; Zhang, Q.; Deng, Y.; Wang, C.; Zhang, H.; Chen, Y.; Qiu, C. W.; Liu, X., Fano resonance in artificial photonic molecules. *Advanced Optical Materials* **2020,** *8* (10), 1902153.

179. Cerjan, B.; Gerislioglu, B.; Link, S.; Nordlander, P.; Halas, N. J.; Griep, M. H., Towards scalable plasmonic Fano-resonant metasurfaces for colorimetric sensing. *Nanotechnology* **2022,** *33* (40), 405201.

180. Zhang, Y.; Jia, T.; Zhang, H.; Xu, Z., Fano resonances in disk–ring plasmonic nanostructure: strong interaction between bright dipolar and dark multipolar mode. *Optics Letters* **2012,** *37* (23), 4919-4921.

181. Tao, W.; Hu, H.; Guillot, O.; Maurer, T.; Fleischer, M., Fano Resonances in Plasmonic Ring-Disc-Pair Systems. *Advanced Photonics Research* **2023**, 2300012.

182. Forcherio, G. T.; Blake, P.; DeJarnette, D.; Roper, D. K., Nanoring structure, spacing, and local dielectric sensitivity for plasmonic resonances in Fano resonant square lattices. *Optics Express* **2014,** *22* (15), 17791-17804.

183. Eschimèse, D.; Vaurette, F.; Ha, C.; Arscott, S.; Mélin, T.; Lévêque, G., Strong and weak polarization-dependent interactions in connected and disconnected plasmonic nanostructures. *Nanoscale Advances* **2022,** *4* (4), 1173-1181.

184. Lamberti, A.; Virga, A.; Angelini, A.; Ricci, A.; Descrovi, E.; Cocuzza, M.; Giorgis, F., Metal–elastomer nanostructures for tunable SERS and easy microfluidic integration. *RSC Advances* **2015,** *5* (6), 4404-4410.

185. Das, A.; Pant, U.; Cao, C.; Moirangthem, R. S.; Kamble, H. B., Fabrication of plasmonic nanopyramidal array as flexible SERS substrate for biosensing application. *Nano Research* **2022**, 1-9.

186. Maurer, T.; Marae-Djouda, J.; Cataldi, U.; Gontier, A.; Montay, G.; Madi, Y.; Panicaud, B.; Macias, D.; Adam, P.-M.; Lévêque, G., The beginnings of plasmomechanics: towards plasmonic strain sensors. *Frontiers of Materials Science* **2015,** *9* (2), 170-177.

187. Laible, F.; Horneber, A.; Fleischer, M., Mechanically Tunable Nanogap Antennas: Single-Structure Effects and Multi-Structure Applications. *Advanced Optical Materials* **2021,** *9* (20), 2100326.

# Appendix *Résumé de la Thèse en Français*

## A.1 Introduction

En tant que branche récente de l'optique, la plasmonique étudie les oscillations collectives des électrons libres excités par la lumière, localisées à la surface de nanoparticules (NPs) métalliques sub-longueur d'onde ou des ondes électromagnétiques se propageant à une interface diélectrique-métal, appelées résonances plasmoniques de surface localisées (LSPRs) et polaritons de surface plasmonique (SPPs). L'application des LSPRs peut être retracée jusqu'aux vitraux colorés de l'époque romaine, cependant, ce n'est que récemment qu'a émergé une compréhension scientifique de la façon dont les impuretés telles que l'or et le cobalt suspendues dans le verre jouent un rôle dans l'affichage des couleurs plasmoniques. D'un point de vue historique, la découverte de l'électron en 1897 a stimulé l'étude de son comportement électrodynamique dans les matériaux, établissant ainsi une base théorique pour la plasmonique. Les premiers travaux peuvent inclure, sans s'y limiter, la description mathématique des fonctions d'onde de surface se propageant sur les surfaces métalliques par Sommerfeld en 1899, et la théorie de Mie sur l'absorption par des nanosphères d'or excitées par une incidence d'onde plane en 1908. Après un demi-siècle de développement, les pionniers Pines et Bohm ont décrit pour la première fois en 1952 le comportement collectif du gaz d'électrons comme des oscillations "plasma". Depuis lors, le concept de résonance plasmonique liée à l'oscillation collective des électrons est largement accepté.

En avançant rapidement jusqu'à aujourd'hui, la nanofabrication de pointe des structures LSPR a réalisé des avancées significatives, en utilisant à la fois l'auto-assemblage colloïdal ascendant et des méthodes descendantes telles que les pinces optiques, la gravure par faisceau ionique et la lithographie par faisceau d'électrons (EBL). Ces techniques de fabrication, combinées à des simulations numériques, permettent un contrôle géométrique précis des NPs plasmoniques et une compréhension approfondie des propriétés à la fois de renforcement du champ proche et du champ lointain en fonction de l'indice de réfraction du milieu, des compositions des NPs, des tailles géométriques et en particulier de leurs formes. Par rapport à l'impulsion dipolaire des nanosphères plasmoniques traditionnelles, les nanobâtonnets ou les nano-anneaux (NRs) présentant un rapport longueur/périmètre sur largeur élevé possèdent des modes LSPR multipolaires complexes s'étendant sur la région visible et infrarouge moyen lorsqu'ils sont excités par une polarisation linéaire. De plus, la géométrie en anneau permet un renforcement uniforme du champ proche dans la cavité, des effets d'amortissement plasmonique plus faibles et une sensibilité relativement élevée à l'indice de réfraction, ce qui suscite un vif intérêt pour les applications de détection. De plus, les NRs peuvent être facilement intégrés à d'autres structures nanophotoniques telles que des guides d'ondes et des résonateurs pour obtenir des résonances de Fano nettes et réaliser des fonctionnalités plus complexes.

Étant donné les avancées dans la nanofabrication, un autre domaine de recherche

porte sur les métasurfaces plasmoniques composées de résonateurs bidimensionnels en réseau, d'une épaisseur sous-longueur d'onde. Contrairement aux nanoparticules plasmoniques individuelles, un réseau de résonateurs permet un couplage fort entre la LSPR des nanoparticules individuelles et leur mode de diffraction, et la résonance de réseau de surface (SLR) qui en résulte présente un renforcement plus marqué du champ proche et des caractéristiques ultra-étroites dans le spectre du champ lointain. Par conséquent, les métasurfaces présentent des avantages remarquables dans différents domaines tels que la plasmonique quantique, l'optique non linéaire, les lentilles ultra-minces et les sciences biomédicales. Cependant, les métasurfaces conventionnelles sont généralement conçues sur des substrats plans et rigides, ce qui limite les applications potentielles en biotechnologie, en technologie portable et en électronique flexible. Récemment, la demande de contrôle actif des propriétés optiques par le biais de stimuli macroscopiques (tels que la lumière, la chaleur, l'électricité, la chimie et la mécanique) a motivé la recherche sur les métasurfaces flexibles. Le domaine de la plasmonique flexible étudie la réponse optique dynamique des nanoparticules plasmoniques soumises à une flexion, une torsion et une étirement mécaniques, en les intégrant sur des substrats flexibles tels que le polydiméthylsiloxane (PDMS), le polyéthylène téréphtalate (PET) et les cristaux liquides. Parmi ceux-ci, le PDMS est largement utilisé en raison de sa bonne transparence optique, de sa ductilité mécanique et de sa compatibilité bio/chimique. Cependant, en raison de l'effet d'accumulation de charge sur les surfaces diélectriques des substrats flexibles, la plupart des méthodes de fabrication ascendante telles que l'EBL ne sont pas réalisables. Par conséquent, la littérature récente a exploré diverses techniques de transfert de motifs sur différents substrats, où la géométrie de la métasurface est bien contrôlée par photolithographie initiale ou synthèse colloïdale.

Dans cette thèse, nous présentons une méthode de fabrication de métasurfaces flexibles en adoptant l'EBL sur un substrat en silicium (Si) rigide revêtu d'une couche sacrificielle de chrome (Cr), suivie d'un transfert par gravure humide sur PDMS. Comparée à la méthode d'épluchage mentionnée ci-dessus, cette technique de pointe offre une approche plus universelle pour transférer tout motif 2D ordonné. Après la fabrication, l'échantillon de PDMS est soumis à un étirement uniaxial, et les spectres de réflexion en champ sombre des motifs transférés sont mesurés in situ. La qualité du transfert et la fiabilité des mesures optiques sont confirmées par des tests ultérieurs effectués avec un microscope électronique à balayage (MEB) sur le PDMS. Contrairement aux métasurfaces flexibles classiques sensibles à l'espace composées de nanoparticules solides/isotropes, cette thèse se concentre sur l'étude de la réponse optique induite par la contrainte des réseaux de nanoanneaux d'or (NR), des réseaux d'anneaux nanométriques elliptiques (ENR) anisotropes et des systèmes hybrides anneau/disque. En surveillant les décalages spectraux distincts des LSPR sous l'effet de l'altération de la forme des NR, les SLR et le couplage Fano sous contrainte, nous visons à ouvrir une nouvelle voie dans le domaine de la plasmonique flexible. L'organisation de cette thèse est la suivante. Dans les deux premières sections, nous présentons une introduction générale et les méthodes expérimentales de la thèse. Les techniques de fabrication concernant l'EBL et les transferts sont brièvement

présentées. Les dispositifs optiques comprenant des spectromètres de réflexion/transmission en champ sombre et des tests au MEB sont également discutés. Les sections A.3 et A.4 explorent expérimentalement le potentiel de la plasmonique flexible dans différents efforts. En fabriquant un réseau de NR carrés de faible largeur, la section A.3 démontre une métasurface de NR altérable en forme sur PDMS avec un important décalage spectral vers le rouge sous contrainte. La section A.4 aborde l'évolution spectrale induite par la contrainte des signaux LSPR et SLR des réseaux d'ENR carrés et triangulaires réguliers. De plus, la section A.5 se concentre sur le couplage Fano dans un système hybride anneau/disque. Malgré le fait que les spectres de transmission soient surveillés sur un substrat en verre/indium-étain-oxyde (verre/ITO) rigide, le fort couplage Fano dépendant de l'espace et les améliorations SERS prédisent un fort guidage spectral sur le PDMS dans les travaux futurs. Enfin, dans la dernière section A.6, nous concluons le travail de thèse et donnons une perspective sur les travaux futurs.

## A.2 Méthodes expérimentales et de caractérisation

### A.2.1 Préparation des échantillons

Les méthodes expérimentales pour fabriquer des métasurfaces flexibles comprennent la lithographie par EBL, la fonctionnalisation de surface, la modélisation du PDMS et le transfert par gravure humide. La fabrication par EBL comprend principalement six étapes comme suit. (1) Préparation des substrats rigides. Dans les sections A.3 et A.4, le substrat rigide initial en chrome/silicium (Cr/Si) est fabriqué en évaporant une couche de Cr d'une épaisseur de 200 nm sur une tranche de Si. Dans la section A.5, une couche d'indium-étain-oxyde (ITO) d'une épaisseur de 30 nm est évaporée thermiquement sur un substrat en verre propre. (2) Dépôt par centrifugation de la résine photosensible. Le substrat rigide initial est enduit d'une solution de PMMA/méthylisobutylcétone (MIBK) diluée à 5 v%, qui est ensuite cuite à 150 °C pendant la nuit pour former une couche de PMMA d'environ 200 nm. (3) Lithographie. Un microscope électronique à balayage JEOL JSM-6500F associé à un générateur de motifs XENOS est utilisé pour réaliser la lithographie. La forme des nanostructures est conçue à travers un motif auto-fabriqué comprenant des points d'exposition répétés régulièrement disposés. La largeur ou la taille est ensuite contrôlée en ajustant le temps de séjour et la dose pendant l'exposition électronique. (4) Développement. Une solution de MIBK / IPA à 25 v% est utilisée comme révélateur pour le PMMA. La région exposée est sélectivement dissoute dans le solvant ci-dessus, laissant le PMMA non exposé sur le substrat. Le temps de développement de 75 secondes est soigneusement choisi pour optimiser les motifs conçus. (5) Évaporation de l'or. Une couche d'or d'environ 50 nm d'épaisseur est ensuite évaporée thermiquement sur le substrat développé à l'aide d'un évaporateur Balzers BA510. (6) Décollage. L'échantillon ci-dessus est ensuite plongé dans de l'acétone pendant la nuit pour enlever toutes les zones non exposées. Enfin, les motifs d'or d'environ 50 nm

d'épaisseur sur le substrat rigide sont formés, présentant une haute résolution et une fidélité au motif conçu. Les dimensions des structures résultantes sur Si/Cr sont confirmées par des caractérisations supplémentaires au MEB.

Pour transférer les motifs EBL du substrat initial en Cr/Si sur les substrats de PDMS, les procédures séquentielles suivantes sont effectuées. Le (3-mercaptopropyl)triéthoxysilane (MPTS) est utilisé comme molécule de liaison pour former une liaison chimique entre le PDMS et l'or évaporé et pour améliorer leur adhérence. Tout d'abord, l'échantillon EBL est immergé dans une solution de 5 v% de MPTS/n-hexane pendant 2 heures, permettant au groupe thiol (-SH) du MPTS de se combiner avec l'or évaporé. Le groupe de liaison Au-MPTS est ensuite formé de manière solide. Ensuite, l'échantillon est placé dans une solution de 50 v% de chloroforme/n-hexane pendant au moins 3 minutes pour faciliter la réaction de substitution nucléophile $S_N2$. Dans cette réaction, le groupe éthoxy (-OCH3) du MPTS est remplacé par un groupe hydroxyle (-OH), ce qui est nécessaire pour le processus ultérieur de modélisation car cela permet la formation d'une liaison siloxane (Si-O-Si) entre le PDMS et le MPTS par une réaction de condensation.

En ce qui concerne les approches de modélisation, tout d'abord, trois plaquettes de silicium supplémentaires sont préparées pour fixer l'échantillon EBL comme indiqué dans la Figure A-1 (a). Quelques gouttes de PDMS peuvent être placées entre les deux plaquettes de support et la plaquette de base, puis durcies pour former un adhésif. Ensuite, un gabarit de tension en téflon personnalisé est fixé à l'échantillon EBL et maintenu en place avec deux pinces, comme indiqué dans la Figure A-1 (b). Notez que les motifs EBL doivent être placés exactement au milieu pour obtenir une déformation élastique uniforme sous contrainte à l'avenir. Ensuite, le même mélange de PDMS est lentement versé dans le moule, dégazé plus loin dans une chambre à vide, et durci à 120 °C pendant 12 minutes. Ensuite, le gabarit en téflon est soigneusement retiré, laissant un échantillon moulé en PDMS comme indiqué dans la Figure A-1 (c). Afin de retirer la couche sacrificielle de Cr, l'échantillon de modélisation est soigneusement plongé dans le révélateur de Cr (solution TechniStrip Cr01), comme indiqué dans la Figure A-1 (d). L'échantillon est également pressé sous une plaque de verre et recouvert pour empêcher l'évaporation de la solution. Le processus de gravure peut durer une ou deux semaines, et on peut décider visuellement si la couche de Cr est complètement dissoute. Une fois la gravure terminée, les systèmes Au/MPTS/PDMS peuvent être facilement décollés des substrats d'origine et sont prêts pour des tests optiques ou mécaniques après rinçage et séchage.
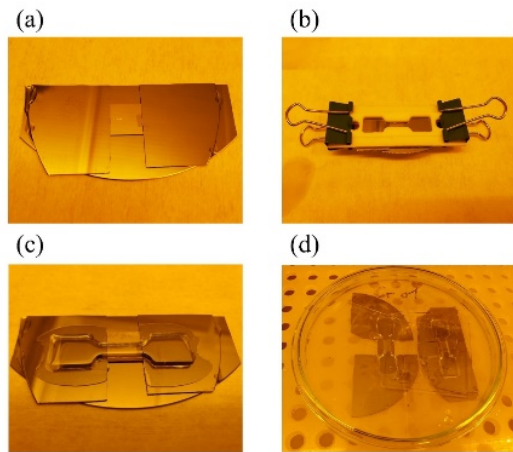
Figure A-1 Ensemble de photos expliquant le processus de modélisation du PDMS fluide. La Figure (a) montre l'échantillon EBL qui a été fixé par des plaquettes supplémentaires ; la Figure (b) montre le système de modélisation fluide en versant le PDMS fluide dans le moule ; la Figure (c) montre un échantillon détaché du moule une fois que le PDMS est durci ; et la Figure (d) indique le processus de gravure humide pour le transfert du motif.

## A.2.2 Caractérisation optique

Dans cette thèse, nous surveillons les spectres de réflexion en champ sombre des réseaux d'or sur PDMS à différentes déformations dans les sections A.3 et A.4. En revanche, dans la section A.5, nous utilisons une lentille à huile à haute magnification pour améliorer la résolution et effectuer les spectres de diffusion en champ sombre.

Pour la mesure de réflexion en champ sombre, un microscope de réflexion Zeiss Axio Scope A1 combiné à un spectromètre à réseau LOT SR-303i-B est utilisé pour analyser la diffusion plasmonique des réseaux de structures en or sur PDMS dans le champ sombre. La Figure A-2 (a) présente son schéma, qui comprend principalement une lampe halogène de 100 W, un polariseur linéaire, un diviseur de faisceau, une lentille d'objectif et un spectromètre, respectivement. La lumière de la source halogène traverse des bloqueurs, des miroirs et des objectifs pour former des incidences en champ sombre en forme d'anneau avec un angle oblique de 56,75 ± 2,25°. La Figure A-2 (b) montre le principe de fonctionnement de l'objectif Zeiss EC EPIPLAN 20x/0,4, qui focalise le champ sombre incident sur le plan de l'objet et collecte sa lumière rétrodiffusée. Le signal collecté est ensuite analysé par le spectromètre à réseau à travers une lentille de focalisation. En général, la zone de focalisation de l'objectif est d'environ 25 $\mu m^2$ et la plage de détection de longueur d'onde effective du spectromètre est d'environ 500 à 1000 nm. Ainsi, pour les réseaux de structures en or avec une période de 400 ou 500 nm, à la fois les résonances plasmoniques et les résonances de réseau peuvent être surveillées.
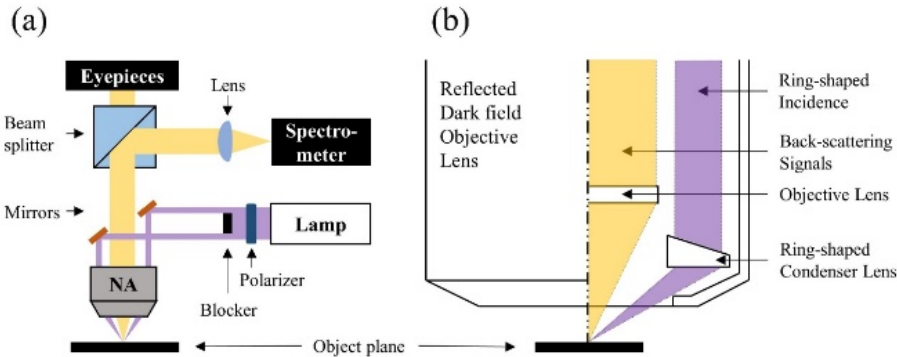
Figure A-2 Schéma du trajet optique pour la spectroscopie de réflexion en champ sombre (a), et principe de fonctionnement de l'objectif en champ sombre (b).

Pour la mesure de transmission en champ sombre, un microscope inversé de transmission Nikon Eclipse Ti avec un condenseur externe en champ sombre Nikon (sec 0.95-0.80) est utilisé pour détecter la lumière diffusée vers l'avant à partir des échantillons d'or. Le schéma du trajet optique est similaire à la Figure A-2 (a), la même source lumineuse halogène et le même spectromètre sont utilisés, mais la lumière diffusée est collectée à partir de l'arrière des échantillons. Pour améliorer la résolution optique, nous utilisons un objectif à fort grossissement tel qu'un objectif Nikon Plan Fluor 100x/0.5-1.3 à immersion dans de l'huile (indice de réfraction de 1.518) et traitons l'échantillon avec de l'huile. Étant donné que la zone de détection effective de cet objectif est d'environ 1 μm$^2$, l'effet de diffraction des structures en or avec une période de 5 μm peut être négligé.

Pour éliminer les effets du bruit de fond de l'échantillon ($I_{bg}$), des sources lumineuses ($I_{lamp}$) et du courant sombre ($I_{dc}$) sur les spectres des structures en or, les données brutes ($I_{raw}$) de tous les signaux diffusés collectés vers l'arrière ou vers l'avant sont normalisées de la manière suivante.

$$I_{nor} = \frac{I_{raw} - I_{bg}}{I_{lamp} - I_{dc}} \tag{A-1}$$

### A.2.3 Caractérisation par MEB

La microscopie électronique à balayage (MEB) permet une imagerie à haute résolution des surfaces des matériaux. Cependant, lors de la numérisation d'un échantillon de polymère, les électrons de haute énergie peuvent soit endommager l'échantillon, soit provoquer une dérive de l'image en raison de l'accumulation de charge. Dans cette thèse, nous adoptons deux méthodes pour imager des échantillons d'or sur des surfaces de PDMS, à savoir le revêtement d'une couche conductrice et le fonctionnement à basse tension.

En ce qui concerne le revêtement d'une couche conductrice, un pulvérisateur Agar est utilisé pour pulvériser un film d'or sur la surface de PDMS afin de réduire

l'accumulation d'électrons. Après immersion dans de l'acétone et soufflage à l'azote, le micro-étireur est monté avec l'échantillon de PDMS et placé à l'intérieur de la chambre de la MEB. Un MEB Philips XL30 est utilisé pour l'imagerie sur PDMS. Une tension d'accélération de 5,0 kV est sélectionnée et un mode de balayage rapide est appliqué pour éviter les artefacts dus aux dérives d'image.

Alternativement, un MEB Zeiss Crossbeam Auriga 40 est utilisé pour l'imagerie sur PDMS. Pour réduire les effets de charge, une tension d'accélération de 1 kV est utilisée. La moyenne des trames avec compensation de dérive est appliquée pour enregistrer les images présentées. Cependant, afin de mesurer correctement les dimensions des nanostructures, des images sans moyenne sont utilisées pour éviter les artefacts dus à la charge ou à la dérive.

## A.3 Propriétés optiques des métasurfaces à nanoanneaux d'or modifiant la forme in-situ sur PDMS

### A.3.1 Caractérisation de la réflexion en champ sombre

La géométrie des réseaux de nanoanneaux d'or (NR) est représentée schématiquement dans la figure A-3 (a), contrôlée par des périodes le long des axes x et y, $Px$ et $Py$, des diamètres centraux $Dx$ et $Dy$, une hauteur $H$ et une largeur $W$. En supposant que l'axe x soit la direction future d'étirement, le rapport d'aspect (AR) d'un NR est déterminé par AR = $Dx$ / $Dy$. Les figures A-3 (b-d) montrent des images MEB en vue de dessus pour trois réseaux de NR déposés sur des plaquettes Si/Cr, à savoir NR1, NR2 et NR3. Le tableau A-1 présente les paramètres géométriques nominaux et mesurés des trois NR. Les paramètres $Px$, $Py$, $Dx$ et $Dy$ sont conçus à l'aide de fichiers de motifs en lithographie électronique. Le paramètre $H$ est contrôlé par l'évaporateur, tandis que W représente les largeurs moyennes de tous les anneaux mesurées dans les axes horizontal et vertical sur les trois images MEB représentées dans la figure A-3. Notez que les caractérisations en MEB sont réalisées sur Si/Cr, et les mesures optiques sont effectuées une fois que ces réseaux de NR sont transférés sur PDMS.



123
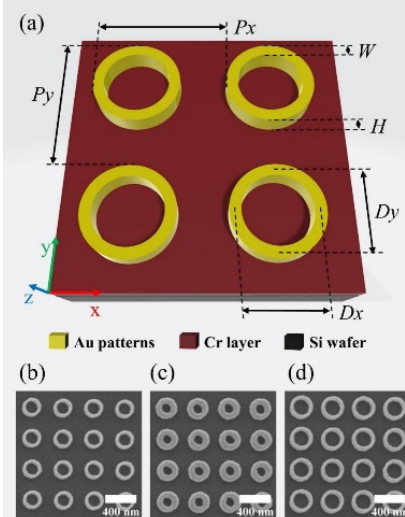
Figure A-3 : Schéma des réseaux de nanoanneaux d'or déposés sur le substrat Si/Cr (a). Images MEB des trois réseaux de nanoanneaux sur Si/Cr, nommés NR1 (b), NR2 (c) et NR3 (d).

**Table A-1** Paramètres géométriques des trois réseaux de nanoanneaux dans la Figure A-3

| NR réseaux | Px [nm] | Py [nm] | Dx [nm] | Dy [nm] | H [nm] | W [a)] [nm] |
|---|---|---|---|---|---|---|
| NR1 | 400 | 400 | 200 | 200 | 50 | 49 ± 7 |
| NR2 | 400 | 400 | 200 | 200 | 50 | 83 ± 6 |
| NR3 | 400 | 400 | 250 | 250 | 50 | 56 ± 6 |

[a)](W = Avg ± Sd, où Avg et Sd représentent les valeurs moyennes et l'écart-type.)

Les trois réseaux de nanoanneaux sont ensuite transférés sur PDMS, qui est ensuite monté dans un micro-étireur pour mesurer leurs propriétés optiques sous contrainte. Deux polarisations linéaires sont introduites lors des caractérisations optiques, où les polarisations transversale et longitudinale (TP et LP) font référence aux directions de polarisation qui sont perpendiculaires ou parallèles à l'étirement uniaxial. La Figure A-4 montre des graphiques de décalage des spectres de réflexion en champ sombre des trois réseaux de nanoanneaux sous contrainte, avec les conditions de polarisation schématiquement illustrées dans les figures en haut à droite. Sauf indication contraire, les valeurs de contrainte dans les graphiques spectraux dans les sections A.3 et A.4 se réfèrent exactement aux contraintes du réseau avec un pas de 10 % de la valeur de contrainte d'ingénierie (par exemple, $\varepsilon = \varepsilon_{grtg} = 45$ % fait référence à $\varepsilon_{engr} = 50$ %). D'une part, les spectres dans la Figure A-4 mettent en évidence un ensemble de modes LSPR (Localized Surface Plasmon Resonance) larges indiqués par des cercles, où les cercles pleins indiquent les intensités LSPR les plus élevées. En plus du mode LSPR principal atteignant son maximum à 680 nm, NR1 montre également un second mode LSPR (marqué d'un cercle ouvert, à 820 nm) à une contrainte de $\varepsilon = 0$ sous les deux polarisations. Ces deux modes fusionnent progressivement en un seul pic avec l'application de contraintes, qui se décale ensuite vers une longueur d'onde plus grande à mesure que la contrainte augmente. La valeur moyenne du décalage vers le rouge des modes LSPR principaux pour NR1-TP peut être quantifiée à 2,85 nm pour 1 % de contrainte ($\Delta\lambda = (804 - 675,8)$ nm / 45 % = 2,85 nm/%), ce qui est plus élevé que ce qui est observé dans les dispositifs plasmoniques flexibles conventionnels modifiant l'espace entre les nanostructures, c'est-à-dire jusqu'à ~2 nm/%.

Une tendance spectrale similaire peut être observée pour NR1-LP, tandis que l'effet de décalage vers le rouge montre moins de sensibilité à une valeur de contrainte élevée ($\varepsilon \geq 29$ %). De plus, il est observé que les comportements spectraux dépendent significativement des géométries des NR. L'augmentation de la largeur de ~49 nm (NR1) à ~83 nm (NR2) entraîne des modes LSPR constants lorsqu'ils sont soumis à une contrainte, situés à ~750 nm pour NR2-TP et ~760 nm pour NR2-LP, respectivement. Étant donné que NR3 partage la même période et une largeur similaire à NR1, son réseau et le développement de la forme des NR présentent des

similitudes sous contrainte (discutées dans les sections suivantes). Un diamètre accru de NR3 de 200 à 250 nm entraîne l'apparition de trois modes LSPR à $\varepsilon = 0$, qui présentent des fluctuations dans leurs positions de pic à mesure que la contrainte se développe. Cependant, en termes de pondération de l'intensité, une tendance discernable de décalage vers le rouge peut toujours être observée pour les modes LSPR principaux sous les deux polarisations.
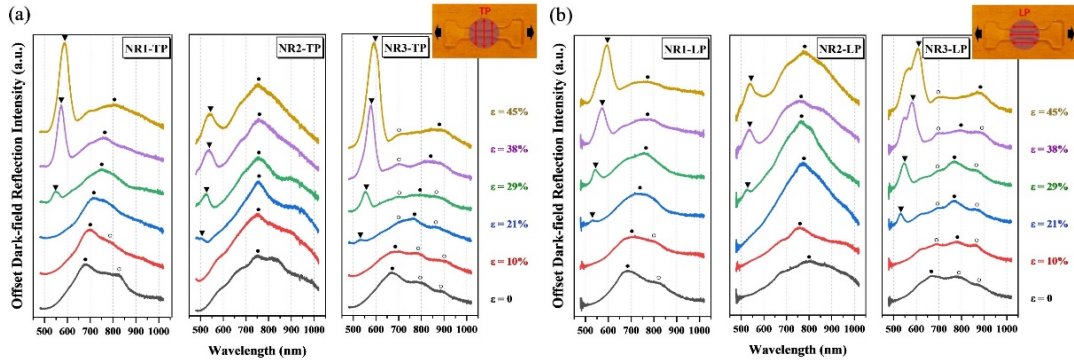


Figure A-4 Graphiques de l'évolution des spectres en champ sombre pour les réseaux NR1, NR2 et NR3 sous polarisations transversales (a) et longitudinales (b), avec les modes de réseau et LSPR marqués par des triangles et des cercles. Les cercles pleins et ouverts indiquent les modes LSPR principaux et secondaires. Les figures en haut à droite dans (a) et (b) affichent la direction de l'étirement et les conditions de polarisation à l'aide de flèches noires et rouges, respectivement.

Pour distinguer entre les pics plus étroits et les modes LSPR tels qu'illustrés dans la Figure A-4, nous réalisons un autre test optique sur des réseaux de disques en or fabriqués par EBL déposés sur un substrat rigide en verre/ITO. Les figures A-5 (a-d) montrent les images MEB en vue de dessus des quatre réseaux, indiquant des diamètres de (173 ± 3), (188 ± 3), (203 ± 7) et (463 ± 11) nm respectivement. Ces valeurs statistiques sont obtenues en mesurant et en faisant la moyenne des diamètres de tous les disques dans les images MEB dans les directions horizontale et verticale. Ces réseaux partagent une période constante $Px = Py = 500$ nm et $H = 50$ nm. La figure A-5 (e) montre les spectres non polarisés de ces réseaux caractérisés via le même spectromètre en champ sombre. À mesure que la période augmente de 400 nm pour le réseau NR à 500 nm dans ce cas, le spectre met en évidence un ensemble de pics de réseau de Bragg à ~575 nm. Les caractéristiques des modes de Bragg sont que la position du pic est uniquement liée à la période et est indépendante de la taille géométrique, tandis que la largeur de résonance augmente avec le diamètre. Nous avons maintenant confirmé que dans la Figure 4-4, les pics étroits aux longueurs d'onde de 530 à 600 nm à $\varepsilon > 21\%$ sont des modes de réseau (c'est-à-dire des modes de réflexion de Bragg), car les variations de période induites par la contrainte satisfont aux conditions de résonance. Les tendances de décalage vers le rouge indiquent également que les modes de réseau initiaux des trois réseaux NR se trouvent dans la région de l'ultraviolet, qui est au-delà de la portée de détection du spectromètre actuel. De plus, les réseaux NR1 et NR3 présentent des décalages vers le rouge similaires à ~600 nm à $\varepsilon = 45\%$, tandis que le réseau NR2 avec une largeur plus épaisse réduit le

développement du réseau sous contrainte, conduisant uniquement à un décalage vers le rouge à ~545 nm à l'état final. De plus, les spectres de NR3-LP présentent un couplage entre le mode de Bragg et le mode LSPR à $\varepsilon \geq 38\%$. Les Résonances de Réseau de Surface (SLR) résultantes sont ensuite discutées dans la Section A.4.
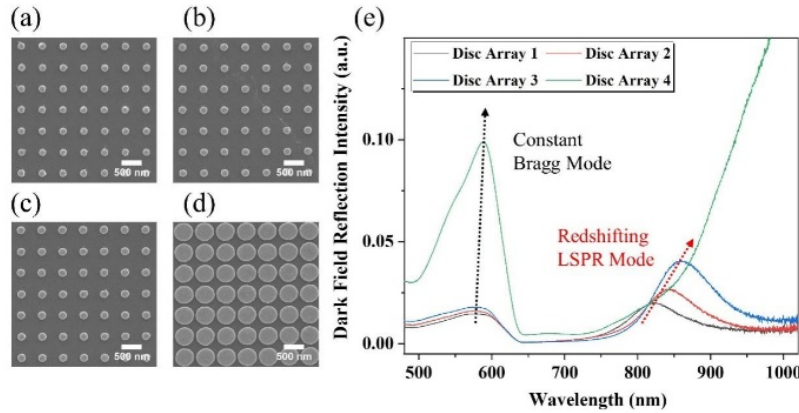


Figure A-5 Ensemble de réseaux de disques sur un substrat en verre/indium-étain-oxyde, avec des diamètres respectifs de $(173 \pm 3)$ nm (a) ; $(188 \pm 3)$ nm (b) ; $(203 \pm 7)$ nm (c) ; et $(463 \pm 11)$ nm (d). Leur période est maintenue à 500 nm. Spectres de réflexion en champ sombre des quatre réseaux de disques (e), indiquant un mode de Bragg essentiellement constant et un mode LSPR décalé vers le rouge.

## A.3.2 Caractérisation en temps réel par MEB sur PDMS

En comparant les spectres de NR1 et NR2, on observe que la matrice NR1 plus fine présente un développement plus important de la structure en réseau sous contrainte, et son mode LSPR montre une tendance de fusion et de décalage vers le rouge à mesure que la contrainte augmente davantage. Nous émettons l'hypothèse que la raison en est le changement induit par la contrainte du rapport d'aspect (AR) de NR1, malgré la différence considérable de module entre environ 69,1 GPa pour l'or nanostructuré et environ 2,6 MPa pour le PDMS. Par conséquent, une caractérisation MEB in-situ sur PDMS pour les trois ensembles NR est nécessaire pour confirmer la déformabilité de la forme. Les figures A-6 (a-c) montrent les images MEB des trois ensembles NR sur Si/Cr avant le transfert, et sur PDMS à des valeurs de contrainte d'ingénierie de $\varepsilon_{engr} = 0$, 20%, 40%, respectivement. Bien que ces images MEB dérivent considérablement, un léger changement de forme dans NR1 est indiqué par l'ellipse rouge à $\varepsilon_{engr} = 40\%$. Par conséquent, les figures A-6 (d-f) présentent une évaluation quantitative des diamètres des NR dans les trois ensembles, où les diamètres longitudinaux et transversaux se réfèrent à ceux parallèles ou perpendiculaires à l'étirement. Il est noté que les diamètres transversaux et longitudinaux des trois NR ne diffèrent pas considérablement sur Si/Cr, mais après le transfert, les diamètres transversaux des trois NR sont significativement plus grands que les diamètres longitudinaux. Cela est probablement dû aux dérives d'image lors des mesures MEB, qui produisent des artefacts le long de la direction transversale.

Dans ce contexte, on peut encore observer une augmentation approximativement linéaire du diamètre longitudinal de NR1 et une diminution du diamètre transversal, entraînant une augmentation régulière du rapport d'aspect sous contrainte. Cependant, NR2 avec une largeur accrue ne se déforme pas sous contrainte, tandis que les diamètres transversaux et longitudinaux montrent seulement des fluctuations. De plus, le rapport d'aspect de NR3 passe de $AR_{\varepsilon=0} = 275,5 / 317,9 = 0,87$ à $AR_{\varepsilon=20\%} = 282,8 / 299,7 \approx 0,94$ à de faibles valeurs de contrainte, tandis qu'il reste constant ($AR_{\varepsilon=40\%} = 274,1 / 291,5 \approx 0,94$) à mesure que la contrainte augmente davantage. La déformabilité relativement faible de NR3 peut être attribuée à la réduction de l'"'espace libre" le long de l'étirement uniaxial, c'est-à-dire la période du réseau moins le diamètre. Enfin, il convient de noter que la déformabilité des NR sur PDMS est significativement limitée en raison du durcissement du PDMS lors de l'imagerie MEB et de l'existence de la couche conductrice rigide.
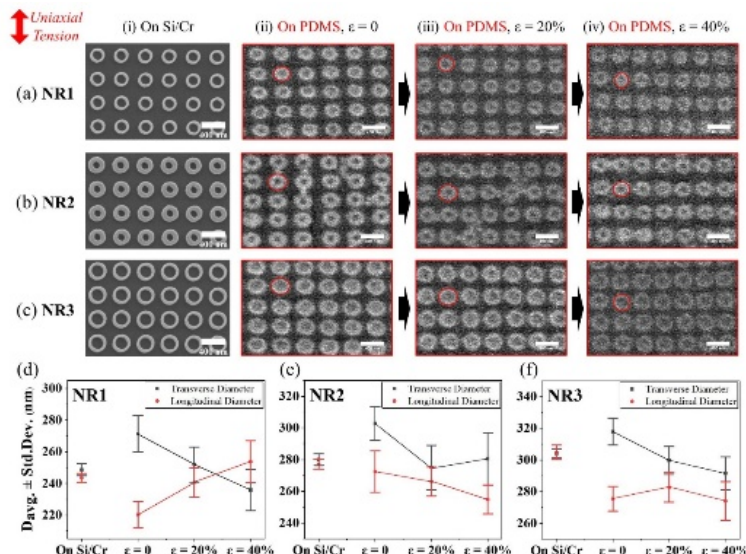


Figure A-6 Ensemble d'images MEB des trois ensembles NR avec une échelle graduée de 400 nm, où la colonne (i) montre les structures sur Si/Cr avant le transfert et les colonnes (ii-iv) représentent celles sur PDMS à différentes valeurs de contrainte. Les lignes rouges dans les colonnes (ii-iv) soulignent les formes des NR individuels dans leur réseau. L'évaluation statistique des trois NR (d-f), où le diamètre est défini comme la distance entre les parois extérieures des NR.

### A.3.3 Simulation numérique

Nous commençons par simuler les spectres de NR1-TP à $\varepsilon = 0$. Comme illustré dans la Figure A-7 (a), l'éclairage en champ sombre en forme de cône est approximé par quatre faisceaux d'ondes planes obliques séparées, avec des angles d'incidence moyens de $\theta = 56,75°$ par rapport à la normale. Parmi ces faisceaux, ceux de l'avant et de l'arrière sont polarisés en s, où les champs électriques sont alignés avec la direction x, tandis que les faisceaux de gauche et de droite sont polarisés en p et leurs champs électriques présentent un angle $\theta$ avec le plan de l'objet. Dans la Figure A-7 (b), la

courbe de simulation correspond bien à celle expérimentale, indiquant deux pics LSPR respectifs à 675 et 759 nm. Les cartes de charge de surface dans la Figure A-7 (c) montrent les mêmes niveaux de liaison pour m = 2 pour les deux modes LSPR. Le pic LSPR principal révèle une distribution de charge radialement symétrique, tandis que le deuxième mode présente une distribution asymétrique.
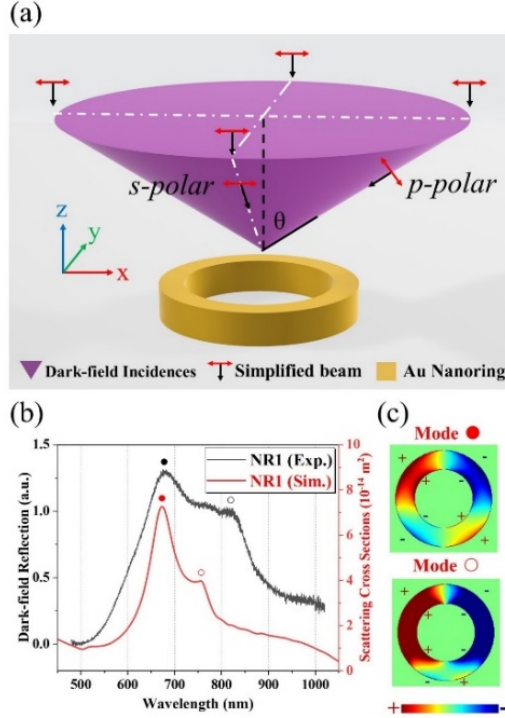


Figure A-7 (a) Schéma de l'éclairage en champ sombre, où l'incidence en champ sombre en forme de cône est simplifiée en quatre faisceaux distincts. (b) Comparaison des spectres entre l'expérience et la simulation pour NR1-TP, et (c) distributions de charge de surface pour les deux modes LSPR simulés.

Pour simuler l'évolution spectrale des réseaux NR1 sur PDMS soumis à une contrainte, nous prenons en compte deux principaux facteurs influents : la variation d'espacement entre les NR adjacents et la variation de forme des NR. La variation d'espacement est obtenue en calculant la moyenne de la période de réseau induite par la contrainte. En raison de l'élasticité élevée du PDMS à une contrainte $\varepsilon < 100\%$, nous supposons que les périodes longitudinale et transversale des réseaux NR sous contrainte ($Px^\varepsilon$ et $Py^\varepsilon$) suivent une relation élastique :

$$Px^\varepsilon = Px*(1+\varepsilon) \tag{A-2}$$

$$Py^\varepsilon = Py*(1-\nu\varepsilon) \tag{A-3}$$

où Px et Py sont les périodes initiales du réseau de 400 nm, et $\nu = 0.5$ fixe le rapport de Poisson constant du PDMS. Le développement continu du réseau peut être confirmé soit en mesurant le décalage linéaire vers le rouge du mode de Bragg, soit en observant directement le développement du réseau lors des tests optiques.

D'autre part, pour examiner l'effet de modification de la forme, nous menons

deux études de simulation différentes : des réseaux de nanoanneaux inaltérés et déformés. Les deux réseaux partagent le même développement élastique du réseau sous contrainte tel que décrit dans les équations (A-2) et (A-3). La capacité de modification de la forme du réseau déformé est considérée selon les hypothèses suivantes : (1) la largeur $W$, la hauteur $H$ et le périmètre central $P$ de NR1 restent constants sous contrainte en raison du module élevé de l'or ; (2) le diamètre longitudinal aligné sur la tension uniaxiale ($Dx^\varepsilon$) se déforme élastiquement sous contrainte ; et donc (3) le diamètre transversal ($Dy^\varepsilon$) est calculé par approximation d'Euler en introduisant la constante P et le $Dx^\varepsilon$ déformé. Par conséquent, la capacité de modification de la forme est décrite quantitativement par $Dx^\varepsilon$ et $Dy^\varepsilon$ en utilisant les équations suivantes.

$$Dx^\varepsilon = Dx * (1 + \varepsilon) \qquad (A\text{-}4)$$

$$Dy^\varepsilon = \sqrt{\frac{P^2}{2\pi^2} - \left(Dx^\varepsilon\right)^2} \qquad (A\text{-}5)$$

Enfin, la Figure A-8 présente la comparaison entre les résultats expérimentaux du spectre NR1-TP et les résultats de simulation des réseaux NR1 déformés et non déformés. La courbe de simulation est obtenue en calculant la section efficace de diffusion globale du réseau 5*5 sous l'excitation d'un seul faisceau polarisé s en polarisation transverse. L'évolution spectrale simulée pour les réseaux NR1 déformés dans la Figure A-8 (b) montre une bonne concordance avec les résultats expérimentaux de la Figure (a). Malgré le fait que les modes LSPR principaux (marqués de cercles rouges pleins) restent constants à de faibles valeurs de contrainte (atteignant un pic à 670 nm à ε = 0, 10% et 20%), ils subissent rapidement un décalage vers le rouge, passant de 670 nm à ε = 30% à 735 nm à ε = 50% en raison de changements de forme abrupts à des valeurs de contrainte élevées. De plus, le second mode LSPR du réseau NR déformé (cercles rouges ouverts) présente une tendance d'affaiblissement progressif sous contrainte, et disparaît finalement à ε = 30%. En revanche, la courbe de simulation pour le réseau NR1 non déformé dans la Figure A-8 (c) montre seulement un léger décalage vers le rouge, passant de 670 nm à ε = 0 à 683 nm à ε = 50% pour le mode LSPR principal, et un deuxième mode inchangé sous contrainte. Il est évident que l'évolution spectrale des NRs non déformés correspond davantage à celle du NR2-TP dans la Figure A-4. Étant donné que le NR2 avec une largeur plus importante limite le développement du réseau induit par la contrainte, il en résulte un effet de décalage vers le rouge plus doux pour le mode LSPR principal dans le NR2, qui finit par se comporter comme un mode constant sous contrainte, comme le montre la Figure A-4. De plus, en comparant la Figure A-7 (b) et la Figure A-8 (b), il est confirmé que lorsque les NR se développent en NRDEs sous contrainte, le mode liant symétrique radial présente un décalage vers le rouge significatif avec l'augmentation du rapport d'aspect du NR. En même temps, le mode de liant asymétrique est plus sensible à la circularité des NRs, et tend à diminuer avec l'augmentation du rapport d'aspect des NRDEs. Ces observations mettent en évidence la dépendance des LSPRs vis-à-vis de la morphologie des nanoparticules. Plus

important encore, les graphiques de la Figure A-8 (b) et (c) montrent également que l'effet de décalage vers le rouge élevé pour NR1-TP (2,85 nm par 1% de contrainte) est principalement dû au changement de forme du NR1 plutôt qu'à la variation de l'espacement. Ce résultat suggère que les plasmoniques flexibles à modification de forme ont un fort potentiel en termes de guidage spectral par rapport aux systèmes classiques
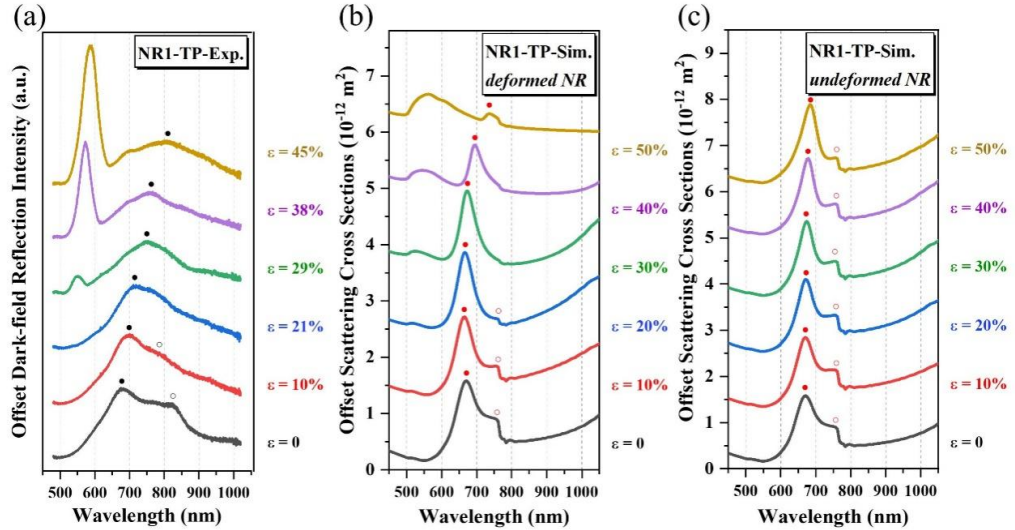


Figure A-8 Comparaison entre les spectres NR1-TP en expérimentation (a) et les simulations des réseaux NR déformés (b) et non déformés (c).

## A.4 Propriétés optiques des méta-surfaces à anneau nanométrique elliptique sur PDMS

### A.4.1 Réseau carré d'ENR

La figure A-9 (a) présente schématiquement la géométrie d'un ENR individuel, comprenant quatre paramètres, à savoir le diamètre extérieur/intérieur le long de son grand axe ($Lx$ et $lx$) et celui le long de son petit axe ($Ly$ et $ly$ respectivement). Les figures A-9 (b-c) montrent le développement de la structure de réseau induit par la contrainte pour les réseaux carrés d'ENR et triangulaires réguliers. Les périodes du réseau le long des directions x et y sont désignées respectivement par $Px_{sq}$, $Py_{sq}$, $Px_{tri}$, et $Py_{tri}$. Les distances centre-à-centre pour les deux réseaux restent constantes à 500 nm, ce qui donne $Py_{tri} = 500$ nm $*$ sin $60° \approx 433$ nm. Notez que les épaisseurs pour tous les ENR sont maintenues à $H = 50$ nm et la contrainte uniaxiale appliquée dans cette section est toujours le long de l'axe court des ENR (axe y). Le développement de la structure de réseau sous contrainte pour les deux cas suit la même description élastique que celle discutée dans la section A.4.3.
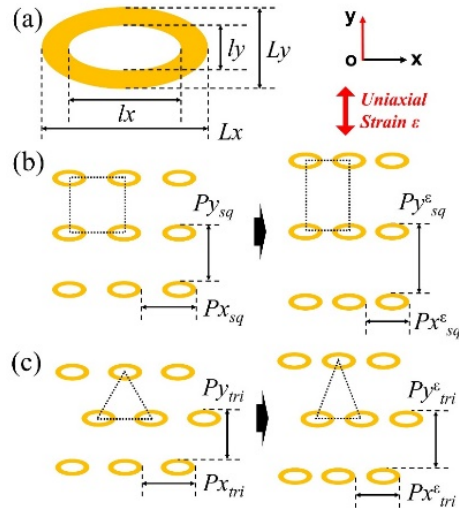
Figure A-9 Schémas de l'ENR (a), du réseau carré d'ENR sous contrainte (b) et du réseau triangulaire régulier d'ENR sous contrainte (c).

Nous commençons par examiner les caractéristiques optiques du réseau carré d'ENR sur PDMS. Pour évaluer la qualité du transfert et le développement du réseau sous contrainte, les figures A-10 (a) et (b) montrent les images MEB du réseau sur Si/Cr et sur PDMS après le transfert et l'étirement ultérieur à $\varepsilon_{engr}$ = 40%. Les géométries spécifiques pour les deux cas sont résumées dans le tableau A-2. Les données statistiques sont obtenues en faisant la moyenne des mesures du réseau 5*5 situé dans le coin supérieur gauche de l'image MEB. Ces règles s'appliquent également au tableau A-3. Les résultats indiquent que les ENRs fabriqués par EBL présentent une certaine irrégularité après le transfert et l'étirement, comme en témoignent l'augmentation de l'écart-type dans divers paramètres et les disparités géométriques de taille notées par Lx et Ly. De plus, en comparant le développement du réseau dans la direction d'étirement (Py), on peut calculer que la contrainte correspondante est $\varepsilon_{MEB}$ = 13,8%, ce qui est nettement inférieur à $\varepsilon_{engr}$ = 40% et à la contrainte du réseau $\varepsilon = \varepsilon_{grtg}$ = 39,3% lors des mesures optiques. Cette différence est principalement due à l'effet de durcissement observé dans la région d'imagerie exposée aux électrons. Par conséquent, nous supposons que la variation géométrique des ENRs dans les figures A-10 (a-b) résulte à la fois de l'effet de durcissement et du processus de transfert, c'est-à-dire de la gravure non contrôlée du Cr. Néanmoins, le succès du transfert de motif et du développement uniforme du réseau confirme la fiabilité des mesures optiques in-situ effectuées sur le substrat flexible.
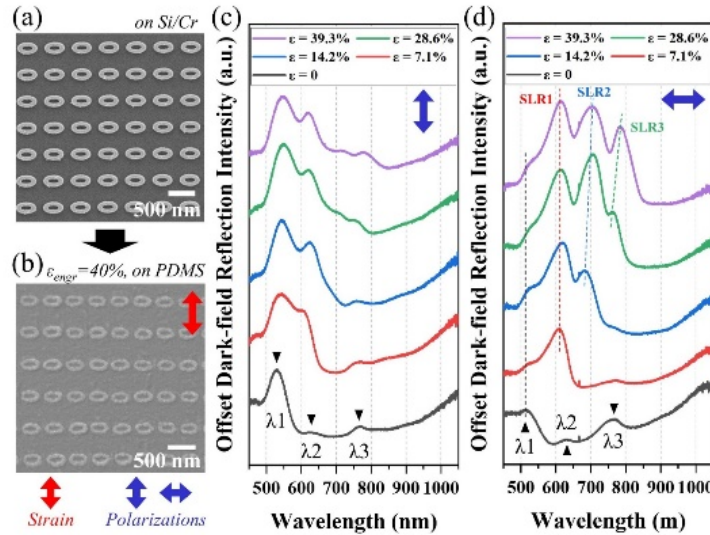
Figure A-10 Images MEB du réseau carré d'ENR sur Si/Cr (a), et sur PDMS à $\varepsilon_{engr}$ = 40% (b). Les flèches rouges et bleues définissent les directions d'étirement uniaxial et de polarisation. Évolution spectrale du réseau carré d'ENR sous polarisations longitudinale (c) et transversale (d). Les modes LSPR à $\varepsilon = 0$ sont marqués par des triangles, tandis que les SLR sont mis en évidence par des lignes en pointillés, respectivement.

Table A-2 Paramètres géométriques du réseau carré d'ENR dans la Figure A-10

| Paramètres | ENR @ Si/Cr | ENR @ PDMS avec $\varepsilon_{engr}$ = 40% |
|---|---|---|
| Lx [nm] [a)] | 373.9 ± 4.5 | 339.4 ± 12.6 |
| lx [nm] | 179.2 ± 4.0 | 186.7 ± 14.0 |
| Ly [nm] | 225.7 ± 3.2 | 204.1 ± 8.6 |
| ly [nm] | 73.1 ± 3.7 | 80.0 ± 7.3 |
| Px [nm] | 499.3 ± 1.1 | 412.0 ± 3.9 |
| Py [nm] | 500.0 ± 0.5 | 569.1 ± 3.1 |

[a)](Avg ± Sd, où Avg et Sd représentent les valeurs moyennes et l'écart-type.)

Les figures A-10 (c-d) représentent les spectres de réflexion en champ sombre décalés de l'ensemble d'ENR carrés avec des polarisations parallèles et perpendiculaires à la contrainte, désignées respectivement comme polarisations longitudinale et transversale. Les flèches rouges et bleues indiquent les directions de traction et de polarisation, respectivement. Contrairement à l'ensemble régulier d'ENR carrés présenté dans la Figure A-4, l'ensemble d'ENR carrés présente une évolution spectrale distincte en fonction de la polarisation sous contrainte. À l'état sans contrainte ($\varepsilon = 0$), les spectres suggèrent trois pics à des positions similaires sous les deux polarisations, à savoir $\lambda 1$ = 513 nm, $\lambda 2$ = 624 nm et $\lambda 3$ = 764 nm. Les trois pics correspondent aux modes LSPR des ENR tels qu'illustrés dans la section de simulation. À mesure que la contrainte augmente, les spectres sous polarisation longitudinale montrent des déplacements minimes dans les positions de ces pics. Des changements mineurs impliquent des variations d'intensité dans $\lambda 2$ sous contrainte, et

un faible pic à $\lambda$ = 715 nm émerge à $\varepsilon$ = 28,6% et 39,3%. Cependant, une évolution spectrale significative se produit lorsque l'ensemble des ENR carrés est soumis à une polarisation transversale, comme le montre la Figure A-10 (d). Plus précisément, $\lambda 1$ conserve sa position pour différentes valeurs de contrainte. À $\varepsilon$ = 7,1%, $\lambda 3$ conserve la même position mais avec une diminution de l'intensité, tandis que $\lambda 2$ est "remplacée" par un pic distinct. Ce pic correspond au mode SLR, désigné SLR1 et marqué par la ligne pointillée rouge, résultant du couplage entre le LSPR $\lambda 2$ et le mode de réseau de Bragg émergent à $\varepsilon$ = 7,1%. À mesure que la contrainte se développe, $\lambda 1$ et SLR1 présentent une évolution négligeable, tandis que le mode de Bragg à décalage vers le rouge se couple avec $\lambda 2$ et $\lambda 3$ pour former SLR2 à $\varepsilon$ = 14,2% et SLR3 à $\varepsilon$ = 28,6%. Les deux modes SLR, SLR2 et SLR3, se décalent également vers le rouge sous contrainte en raison des modes de Bragg intrinsèquement décalés vers le rouge. Les comportements de couplage sont ensuite démontrés dans la Section 5.3 à l'aide de simulations numériques. Notez que ces modes SLR à des valeurs de contrainte élevées présentent des caractéristiques distinctes de Fano, résultant de l'interférence spectrale entre les pics discrets des modes de Bragg et le continuum large des modes LSPR. Par conséquent, l'émergence des modes SLR et les caractéristiques améliorées de Fano distinguent les ensembles d'ENR carrés des ensembles de NPs isotropes traditionnels qui n'induisent que desdécalages spectraux des LSPRs et des SLRs sous contrainte.

## A.4.2 Réseau triangulaire régulier d'ENR

La section suivante examine les propriétés optiques induites par la contrainte d'un ensemble régulier d'ENR triangulaires. La Figure A-11 montre la caractérisation MEB de l'ensemble triangulaire et ses propriétés optiques sous contrainte. Les paramètres géométriques réfléchis par MEB sont résumés dans le Tableau A-3. Contrairement à l'ensemble carré d'ENR, l'ensemble triangulaire, qui maintient un espacement initial constant centre-à-centre de 500 nm, n'exhibe pas de dépendance prononcée vis-à-vis de la polarisation. Comme le montrent les Figures A-11 (c-d), les spectres à $\varepsilon$ = 0 présentent quatre pics séparés de LSPR sous les deux polarisations, à savoir $\lambda 1$ = 512 nm, $\lambda 2$ = 601 nm, $\lambda 3$ = 726 nm et $\lambda 4$ = 744 nm. À mesure que la contrainte augmente jusqu'à $\varepsilon$ = 19,8%, un pic SLR apparaît dans les deux spectres à $\lambda$ = 527 nm, résultant du couplage entre le mode de Bragg et le mode $\lambda 1$. À $\varepsilon$ = 26,6%, le deuxième pic SLR2 est observé en raison du couplage du mode de Bragg décalé vers le rouge avec le mode $\lambda 2$. De plus, un mode latéral SLR3 émerge à $\lambda$ = 638 nm sous polarisation transversale à $\varepsilon$ = 35,3%. D'autre part, puisque les modes LSPR $\lambda 3$ et $\lambda 4$ ne se couplent pas directement avec le mode de Bragg, leur évolution spectrale est similaire sous les deux polarisations, malgré une différence d'intensité observée pour $\lambda 4$. Fait intéressant, la position du pic $\lambda 4$ reste inchangée avec la contrainte appliquée, tandis que $\lambda 3$ présente une légère dérive vers le bleu sous les deux polarisations, c'est-à-dire $\Delta\lambda$ = (695 - 724) nm / 35,3% = -0,82 nm/%.
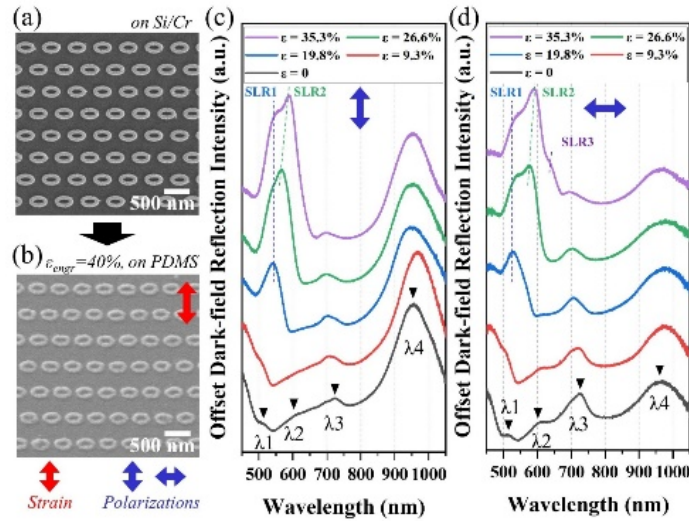
Figure A-11 Images MEB du réseau triangulaire régulier d'ENR sur Si/Cr (a), et sur PDMS à $\varepsilon_{engr}$ = 40% (b). Évolution spectrale du réseau triangulaire sous polarisations longitudinales (c) et transversales (d).

Table A-3 Geometric parameters of the ENR arrays in Figure A-11

| Paramètres | ENR @ Si/Cr | ENR @ PDMS avec $\varepsilon_{engr}$ = 40% |
|---|---|---|
| Lx [nm] | 359.2 ± 6.0 | 324.3 ± 12.2 |
| lx [nm] | 192.6 ± 4.5 | 186.2 ± 14.7 |
| Ly [nm] | 233.6 ± 4.8 | 211.1 ± 7.4 |
| ly [nm] | 64.4 ± 4.3 | 71.4 ± 7.9 |
| Px [nm] | 498.6 ± 1.2 | 412.3 ± 2.6 |
| Py [nm] | 432.1 ± 1.2 | 474.2 ± 2.6 |

## A.4.3 Simulation numérique

Dans les deux sections précédentes, nous avons étudié expérimentalement les propriétés optiques des réseaux carrés et triangulaires réguliers d'ENR, notamment les SLRs induits par la contrainte, les caractéristiques Fano améliorées entre les SLRs et les modes LSPR constants ou à décalage vers le bleu. Cependant, à notre connaissance, la simulation reste un défi pour reproduire à la fois les modes de réseau de Bragg/SLR des réseaux ENR. Dans la section 4.3.2, nous avons appliqué la condition limite Perfectly Matched Layer (PML) et incorporé un réseau fini dans la boîte de simulation pour étudier les modes LSPR d'un réseau 5 * 5 sous une incidence oblique unique. Bien que les résultats de simulation, tels que ceux présentés dans la Figure A-8, décrivent qualitativement les spectres expérimentaux, ils ne parviennent pas à capturer adéquatement les modes de Bragg du réseau NR. Par conséquent, dans cette section, nous étudions la réponse optique du réseau ENR à travers l'exploration de quatre méthodes de simulation distinctes. En particulier, la méthode I utilise l'approche mentionnée précédemment pour simuler la section efficace de diffusion d'un réseau ENR fini de taille 3 * 3, tandis que la méthode II considère une incidence

normale pour la simulation. Le développement du réseau carré sous contrainte est schématiquement illustré dans la Figure A-9 (b), et seule la déformation élastique est prise en compte, similaire à la Section A.4.3. Étant donné que le comportement spectral des SLR dépend également de la taille du réseau, nous utilisons les conditions aux limites de Bloch (BC) et les conditions aux limites périodiques (PBC) dans les méthodes III et IV pour simuler le coefficient de réflexion d'un réseau infini. Pour faciliter la convergence de la simulation, la méthode III utilise une source d'onde plane BFAST avec les mêmes conditions d'angle oblique et de polarisation que dans les méthodes précédentes, tandis que la méthode IV utilise une source incidente normale.

Dans cette section, nous nous sommes principalement concentrés sur la simulation du réseau carré ENR dans des conditions de polarisation transverse (c'est-à-dire, la polarisation est le long de l'axe long de l'ENR), et les données expérimentales sont présentées dans la Figure A-12 (a). Dans le Tableau A-2, il est clair qu'il y a une différence de taille significative dans l'ENR avant et après le transfert, ainsi que l'étirement ultérieur. Cette différence provient principalement du processus de transfert plutôt que du processus d'étirement, et donc le modèle de simulation intègre les paramètres mesurés sur le PDMS. De plus, en raison de la grande largeur des ENR fabriqués, l'influence de la contrainte sur les variations de forme est négligée dans la simulation. Par conséquent, les figures A-12 (b) à (e) illustrent les spectres simulés du réseau ENR en utilisant les quatre méthodes. En les comparant, il est évident qu'aucune des quatre courbes de simulation ne peut reproduire pleinement les résultats expérimentaux. Cela met en évidence les limites de nos approches de simulation, ce qui nécessite des améliorations supplémentaires dans les travaux futurs. Néanmoins, nous pouvons toujours expliquer les caractéristiques observées des spectres expérimentaux en nous basant sur les quatre simulations. Comme le montrent les figures A-12 (b,d) vs (c,e), une incidence oblique par rapport à une incidence normale excite des modes LSPR supplémentaires dans l'ENR, c'est-à-dire $\lambda_5 = 692$ nm à $\varepsilon = 40\%$. Cela correspond à nos résultats de simulation dans la section précédente, figure A-7. De plus, les figures A-12 (b-d), correspondant aux méthodes I à III, indiquent trois pics avec des positions similaires qui restent constants sous contrainte, c'est-à-dire $\lambda_4 = 580$ nm, $\lambda_6 = 592$ nm et $\lambda_7 = 581$ nm à $\varepsilon = 40\%$, respectivement. En revanche, $\lambda_5$ et $\lambda_8$ présentent un léger décalage vers le bleu sous contrainte, c'est-à-dire $\Delta\lambda_5 = (677 - 692)$ nm / 40 = -0.375 nm/% et $\Delta\lambda_8 = (674 - 678)$ nm / 40 = -0.1 nm/%, tandis que $\lambda_9$ subit un important décalage vers le rouge, c'est-à-dire $\Delta\lambda_9 = (997 - 832)$ nm / 40 = 4.125 nm/%. Il est à noter qu'un effet de décalage vers le bleu similaire à celui observé pour $\lambda_5$ et $\lambda_8$ est également trouvé pour les simulations dans le réseau triangulaire régulier ENR (non montré ici), ce qui correspond au mode LSPR central avec décalage vers le bleu sous contrainte tel qu'illustré dans la figure A-11, car il ne se couple pas directement avec le mode de Bragg.
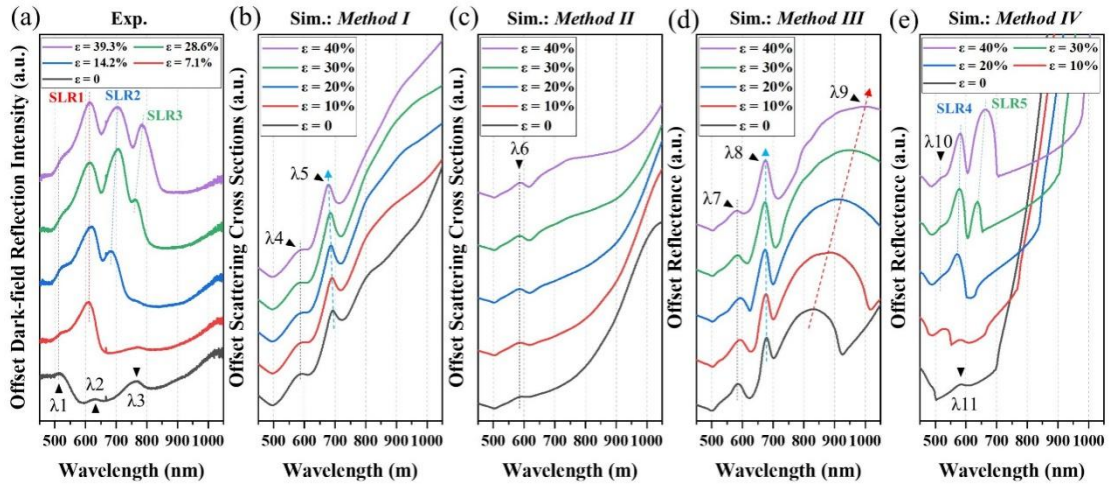
Figure A-12 Évolution spectrale du réseau carré ENR sous polarisation transverse induite par contrainte : résultats expérimentaux (a) et résultats de simulation utilisant les méthodes I à IV (b à e), respectivement.

Figure A-13 Distribution de charge de surface électronique et de champ électrique correspondant à ces pics sous la contrainte ultime (ε = 40%) dans les figures A-13 (a-f). Les distributions de charge et de champ sont dérivées des surfaces supérieure et inférieure des ENR, respectivement. Pour le réseau 3 * 3, seule la distribution de l'ENR central est affichée. La figure A-13 (c) révèle que λ6 excité par une incidence normale correspond au mode de liant LSPR de l'ENR avec le niveau liant m = 3. En raison de la symétrie de la structure de l'ENR et de l'incidence, les distributions de charge et de champ de λ6 présentent à la fois une symétrie verticale et horizontale. Notez que les spectres de simulation dans les figures A-12 (b-c) suggèrent également un mode liant dipolaire LSPR (m = 1) pour l'ENR dans la région proche infrarouge, qui n'est pas montré ici. En comparaison, la figure A-13 (a) illustre que le mode LSPR de λ4 excité par une incidence oblique présente des distributions de champ proches de celles de λ6 excité par une incidence normale, correspondant au même niveau de liant m = 3. Dans la figure A-13 (b), λ5 représentant le mode additionnel excité par une incidence oblique montre un niveau de liant de m = 2. Veuillez noter que, en raison de l'approximation de l'utilisation d'une seule incidence oblique pour simplifier la source de lumière en champ sombre, les distributions de charge et de champ dans les figures A-13 (a-b) et (d-f) présentent une brisure de symétrie haut-bas dans une certaine mesure ; alors qu'une véritable illumination en champ sombre en forme d'anneau devrait garantir la symétrie dans les deux directions. De même, lorsque la structure périodique de l'ENR est excitée par une incidence oblique, les figures A-13 (d-e) montrent que les niveaux liants de λ7 et λ8 sont les mêmes que ceux de λ4 et λ5 mentionnés précédemment, tandis que λ9 présente un mode liant dipolaire caractéristique LSPR. Étant donné que l'évolution spectrale correspondant à la méthode III ne présente pas les caractéristiques des SLR et que ses modes LSPR ressemblent à ceux d'un réseau fini (méthode I), nous concluons qu'une seule incidence oblique ne peut pas exciter un mode de réseau de Bragg/SLR dans les structures périodiques ENR dans le modèle de simulation. De plus, en comparant les

spectres expérimentaux avec les spectres obtenus à partir des méthodes I à III, les pics $\lambda 2$ et $\lambda 3$ à $\varepsilon = 0$ dans les spectres expérimentaux sont supposés être les modes liants LSPR excités par l'illumination en champ sombre, avec m = 3 et m = 2, respectivement.
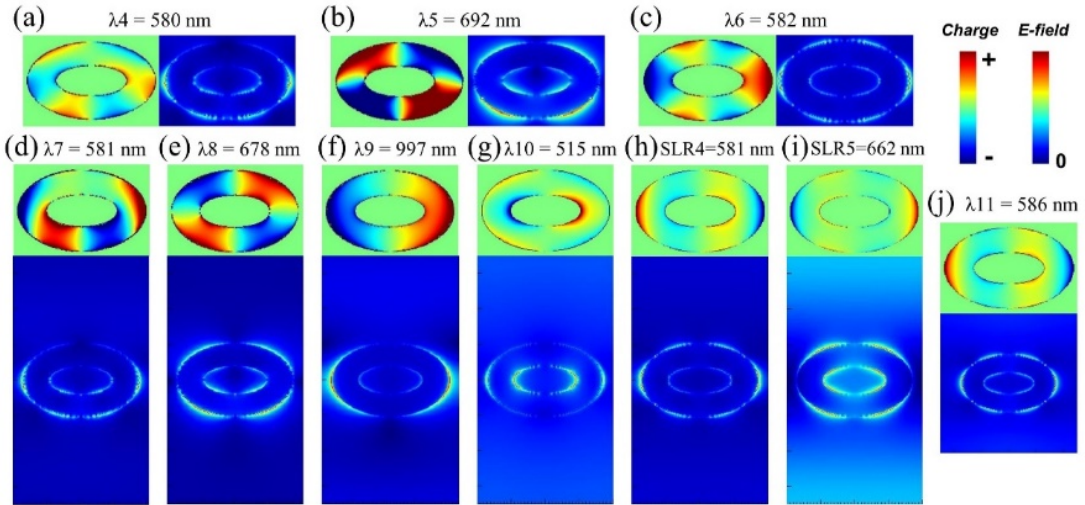


Figure A-13 Distribution de charge de surface électronique et de champ électrique des pics indiqués dans la Figure A-12, à savoir $\lambda 4$ à $\lambda 10$, SLR4 et SLR5, correspondant aux pics observés à $\varepsilon = 40\%$. De plus, $\lambda 10$ correspond au pic observé à $\varepsilon = 0$.

Enfin, lors de la simulation de la structure périodique ENR sous une incidence normale en utilisant la méthode IV, la Figure A-12 (e) présente une évolution spectrale assez similaire aux résultats expérimentaux. À mesure que la contrainte augmente, ces pics montrent des comportements typiques des modes de réseau, émergeant avec des intensités croissantes et des tendances de décalage vers le rouge dans la plage de longueurs d'onde de 500 à 800 nm. À $\varepsilon = 0$, le spectre affiche un pic ($\lambda 11 = 586$ nm) similaire en position à $\lambda 6$, et la Figure A-13 (j) suggère qu'il a le même niveau liant m = 3. Cette similarité est attribuée au fait que le pic de Bragg de l'ENR ne se couple pas directement avec le pic LSPR. Cependant, à mesure que la contrainte augmente, leur couplage entraîne une différence significative dans l'évolution spectrale de la Figure A-12 (e) par rapport à (c). Par exemple, lorsque la contrainte atteint $\varepsilon = 40\%$, le spectre présente trois pics distincts, à savoir $\lambda 10 = 515$ nm, SLR4 = 581 nm et SLR5 = 662 nm. À partir de la Figure A-13 (g), on peut observer que $\lambda 10$ correspond au mode antibondissant LSPR de l'ENR. En raison de la dépendance de la largeur du mode antibondissant, sa position et son intensité de pic restent inchangées à $\varepsilon = 20\%$, 30% et 40%, tandis que l'absence d'observation à $\varepsilon = 0\%$ et 10% est spéculée comme étant due à son couplage avec les modes de Bragg. De plus, les Figures A-13 (h-i) affichent les schémas de distribution de charge et de champ électrique correspondant à SLR4 et SLR5, montrant le même niveau liant m = 3 mais des inversions de phase. Étant donné que SLR4 et SLR5 présentent des distributions de champ proche similaires à $\lambda 11$ mais des différences en termes d'intensité et de largeur de pic, nous concluons que tous deux résultent du couplage entre les modes de Bragg et $\lambda 11$. Selon la définition du couplage entre le mode de Bragg du réseau et les modes LSPR des

particules individuelles, ces deux pics appartiennent aux pics SLR. En particulier, le tracé de la distribution du champ électrique dans la Figure A-13 (i) révèle que l'amplification du champ correspondant à SLR5 se propage également le long de la surface de l'ENR perpendiculaire à la direction de polarisation, ce qui indique une caractéristique propre au mode de réseau. En résumé, dans le spectre expérimental, la formation de SLR1 et SLR2 résulte du couplage des pics intrinsèques de Bragg et LSPR $\lambda 2$, tandis que dans le spectre de simulation utilisant la méthode IV, SLR4 et SLR5 sont formés entre les modes de Bragg et $\lambda 11$. Le pic supplémentaire SLR3 dans l'expérience résulte du couplage entre le pic de Bragg et $\lambda 3$ (mode LSPR, mode liant quadrupolaire, m = 2), qui ne peut pas être excité par une incidence normale avec la méthode IV. De plus, nos simulations démontrent également que les modes de Bragg inhérents excités par une illumination en champ sombre peuvent être simplifiés en utilisant une incidence normale, probablement parce que la composante normale de l'illumination en champ sombre est cruciale pour générer les pics de réseau car elle se propage uniquement à l'interface entre l'ENR et le PDMS. De telles structures solides n'exhibent généralement pas de nouveaux pics LSPR sous une incidence oblique, ce qui indique que les modes SLR couplés impliquent principalement des modes de Bragg et dipolaires.

## A.5 Résonance de Fano pour les hybrides à anneau-disque

### A.5.1 Résonance de Fano dans les systèmes RDP

La Figure A-14 illustre de manière schématique un système à anneau-disque-paire (RDP) en or fabriqué sur un substrat en verre/ITO par EBL. L'épaisseur de la couche conductrice ITO est de 50 nm. Le RDP possède plusieurs paramètres géométriques, notamment le diamètre central de l'anneau ($D_{ring}$), la largeur de l'anneau ($W$), le diamètre du disque ($D_{disc}$), les hauteurs ($H$) et l'écart bord à bord ($G$). Lors du processus d'EBL, un fichier de motif conçoit soigneusement la distance centrale des RDP et $D_{ring}$, tandis que la dose d'exposition électronique contrôle $W$ et $D_{disc}$, ce qui ajuste également $G$. Afin d'éviter les contaminations carbonées qui affectent les spectres en champ sombre des RDP, tous les paramètres sont caractérisés par imagerie MEB après les mesures optiques.
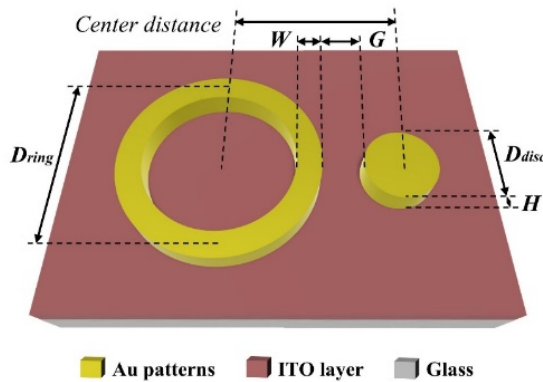
Figure A-14 présente de manière schématique les géométries d'un RDP en or sur le substrat ITO/verre.

Après la fabrication, les spectres de diffusion en champ sombre sont caractérisés sous un éclairage non polarisé afin de réduire l'influence des légers défauts de fabrication ou de désalignement. Nous examinons d'abord l'impact de la dose d'exposition sur les propriétés optiques d'un seul disque, d'un seul anneau et de leurs hybrides RDP en maintenant $D_{ring}$ à 450 nm et la distance centrale à 380 nm. Les spectres présentés dans la Figure A-15 révèlent que tant le disque seul que l'anneau seul montrent un décalage vers le rouge général dans leurs caractéristiques spectrales en fonction de $D_{disc}$ et T dans la plage de longueurs d'onde de 695-850 nm et 575-600 nm, respectivement. Les décalages spectraux observés pour le disque et l'anneau garantissent la fiabilité des expériences actuelles. Les modes plasmoniques pour le disque et l'anneau font référence au mode dipolaire du disque et au mode anti-liant de l'anneau, comme illustré par la suite. Cependant, le comportement spectral du RDP hybride avec un rétrécissement de l'espace varie d'une superposition initiale à une interférence finale entre les deux spectres à mesure que la dose d'exposition augmente.
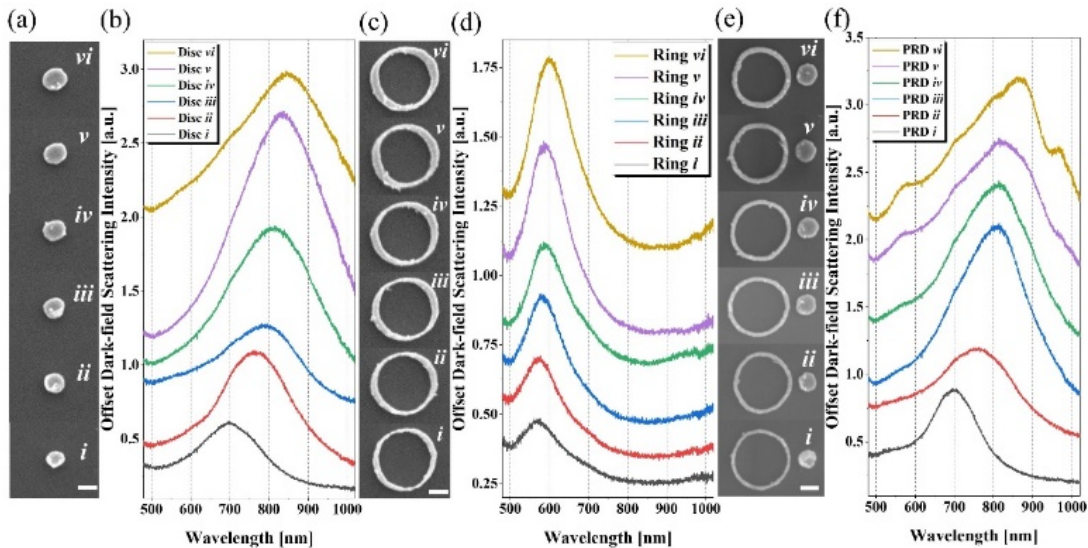


Figure A-15 Dépendance de la dose EBL sur la taille géométrique et les propriétés optiques de disques simples (a et b), d'anneaux (c et d) et de RDP hybrides avec un Dring contrôlé de 450 nm et une distance centrale de 380 nm (e et f). Chaque RDP a la même dose d'exposition que l'anneau et le disque simple correspondant. Le mode dipolaire du disque dans (b) subit un décalage vers le rouge à mesure que la taille du disque augmente. Le mode dipolaire anti-liant de l'anneau, montré dans (d), dépend de la largeur de l'anneau et subit un léger décalage vers des longueurs d'onde plus grandes avec l'augmentation de l'épaisseur de l'anneau.

Afin d'étudier l'interférence spectrale de RDP vi comme indiqué dans la Figure A-15, des simulations numériques sont réalisées à l'aide du logiciel Lumerical FDTD. Les spectres de diffusion expérimentaux sont comparés aux sections efficaces de

diffusion simulées dans la Figure A-16, où le modèle de simulation est approximé de manière régulière en se basant sur les tailles moyennes extraites des images de MEB, c'est-à-dire Dring = 450 nm, W = 45 ± 6 nm, Ddisc = 180 ± 9 nm et G = 45 nm, respectivement. Les valeurs statistiques W et Ddisc sont dérivées des mesures moyennes prises quatre et deux fois le long des deux axes sur les images de MEB. Ces règles s'appliquent également à la Table A-4. Les spectres simulés reproduisent qualitativement les caractéristiques expérimentales et suggèrent cinq pics différents aux longueurs d'onde de 568, 692, 780, 863 et 1028 nm, malgré un décalage vers le rouge d'environ 60 nm pour le Mode-5. La ligne rouge en pointillés dans la Figure A-16 représente un spectre de superposition du mode anti-liant de l'anneau à 568 nm et du mode dipolaire du disque à 840 nm, en simulant séparément les spectres des deux parties. À partir de l'explication des résonances de Fano en champ lointain, ces résultats illustrent que le mode du disque dipolaire fournit un continuum large pour l'interférence spectrale dans les RDPs, ce qui donne quatre pics de Fano différents allant du Mode-2 au Mode-5.
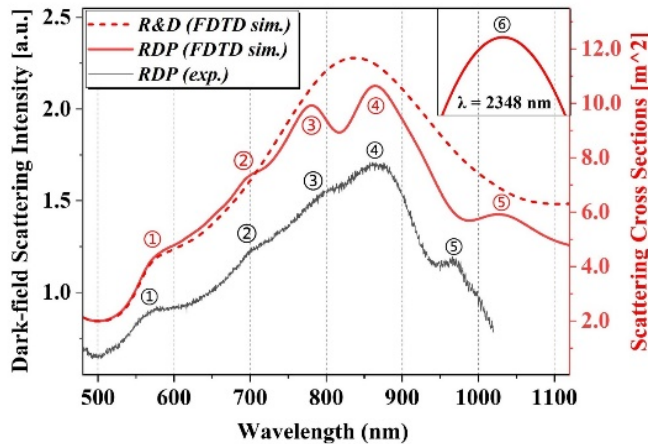


Figure A-16 (a) Comparaison entre les spectres expérimentaux et les spectres simulés dans RDP vi à partir de la Figure A-15. La figure en haut à droite suggère un pic simulé pour RDP vi dans la région du proche infrarouge à λ = 2348 nm. La ligne rouge en pointillés montre une superposition spectrale simulée entre les spectres du disque unique et de l'anneau.

De plus, le mécanisme des interférences spectrales dans la résonance de Fano peut être interprété par l'hybridation plasmonique des champs proches. La Figure A-17 présente la densité de charge en surface et les distributions du champ électrique de ces pics spectraux montrés dans la Figure 6-4. Le tracé à échelle logarithmique dans la rangée (a) de la Figure A-17 illustre la frontière de charge entre les polarités opposées et révèle facilement les niveaux liants pour l'anneau, confirmés également par le tracé linéaire dans la rangée (b). Ces tracés de charge montrent que les pics de Fano des Modes 2 à 5 résultent du couplage LSPR entre le mode dipolaire du disque et les modes d'anneau liants multipolaire avec un niveau liant m = 5 pour les Modes 2 et 3, m = 4 pour le Mode-4, et m = 3 pour le Mode-5, respectivement. La charge du Mode-1 provient d'un mode combiné d'un anneau anti-liant dipolaire et d'un mode de

disque hybride. La charge hybride du disque suggère un mode combiné entre le mode dipolaire dans le plan et le mode de base hors du plan, avec des charges opposées distribuées sur les bords gauche/droit et haut/bas du disque, respectivement. En dehors de la plage de détection expérimentale, la courbe de simulation dans la figure en haut à droite de la Figure A-16 montre que ces RDP présentent un Mode-6 à $\lambda$ = 2348 nm, résultant d'un couplage entre le mode dipolaire d'anneau liant et un mode de disque dipolaire faible, suggéré par les tracés de charge. De plus, étant donné que le champ électrique amélioré à proximité des RDP résulte des oscillations des électrons libres à la surface, une comparaison des rangées (a-b) et (c) révèle une correspondance cohérente entre la distribution de charge en surface et les distributions de champ électrique. Plus précisément, le Mode-1 montre une superposition dans le champ électrique entre le mode dipolaire du disque et le mode d'anneau anti-liant sans couplage fort de l'écart. Les Modes 2 à 5 présentent des modes d'anneau liants avec différents ordres polaires excités par un mode dipolaire du disque. Dans le Mode-6, l'amplification du champ est plus concentrée sur l'anneau puisqu'aucune amplification évidente n'est trouvée sur le côté droit du disque. Notez que l'effet d'amplification par le disque dipolaire est faible dans le Mode-2, entraînant non seulement un pic Fano plus faible avec des rapports de contraste plus bas, mais également une dépendance plus forte à la régularité de l'anneau plutôt qu'à l'effet de couplage par le disque voisin. Cela peut expliquer pourquoi les spectres expérimentaux (avec des géométries irrégulières) dans la Figure A-18 ne présentent pas le pic Fano à une longueur d'onde d'environ 675 nm, comme suggéré par la simulation.
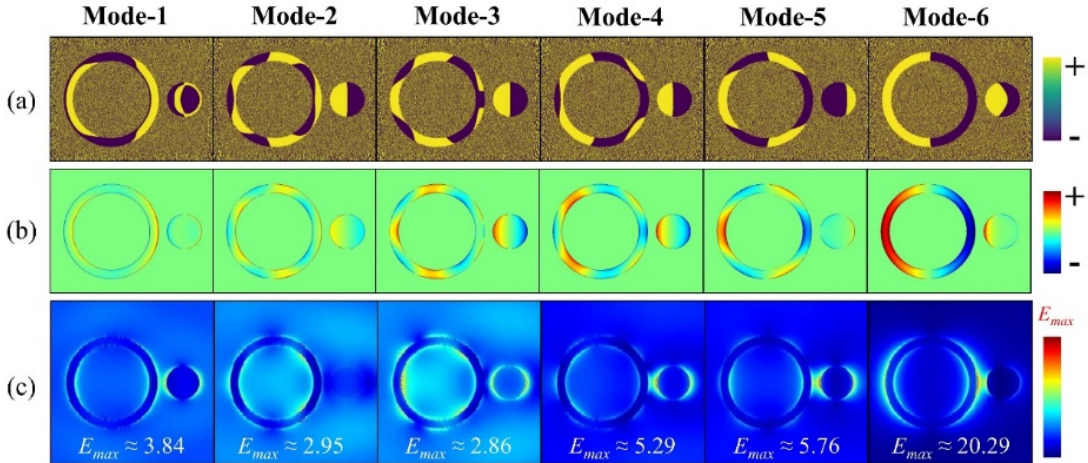


Figure A-17 Distribution de charge de surface simulée pour les pics de la Figure A-16, à la fois en échelle logarithmique (a) et linéaire (b), et distributions de champ électrique correspondantes tracées linéairement (c). Ces figures sont calculées sur la surface supérieure des RDPs.

La discussion précédente met en évidence l'occurrence de l'hybridation plasmonique dans les RDPs. En particulier, lorsque la longueur d'onde ($\lambda$) se situe entre environ 650 et 1100 nm, l'effet de couplage fort dans le champ proche donne lieu à un fond/continuum dipolaire-disc, ce qui entraîne l'émergence de différents modes multipolaires de couplage des anneaux. Ces hybridations dans le champ proche

conduisent ensuite à la formation de résonances de Fano dans le champ lointain. En revanche, pour les longueurs d'onde situées en dehors du continuum dipolaire-disc, les effets de couplage provenant du disque diminuent significativement. Par conséquent, à la fois le mode anti-liant($\lambda$ = 568 nm) et le mode annulaire dipolaire ($\lambda$ = 2348 nm) restent principalement inchangés dans les spectres du champ lointain, tandis que le mode annulaire anti-liant d'énergie élevée excite un mode de base supplémentaire et faible pour le disque à des longueurs d'onde plus courtes.

## A.5.2 Perspective des RDPs dans la plasmonique flexible

Dans la section précédente, nous expliquons théoriquement les résonances de Fano dans un système RDP résultant de l'hybridation dans le champ proche. Afin d'explorer les applications potentielles de détection avec modification de l'espace, nous tirons parti de la méthode EBL de pointe pour fabriquer un ensemble de RDPs, avec un contrôle de $D_{ring}$, $D_{disc}$, $H$ et $W$, tout en faisant varier $G$. Les géométries caractérisées par MEB sont répertoriées dans le tableau A-4.

**Table A-4** Paramètres géométriques caractérisés par MEB des six RDPs dans la Figure A-18

| RDPs | $D_{ring}$ conçus [nm] | $D_{disc}$ [nm] | W [nm] | G [nm] |
|---|---|---|---|---|
| **RDP *i*** | 450 | $178.7 \pm 7.2$ | $47.3 \pm 10.5$ | 74.4 |
| **RDP *ii*** | 450 | $176.7 \pm 6.4$ | $43.9 \pm 10.3$ | 60.0 |
| **RDP *iii*** | 450 | $176.3 \pm 7.9$ | $42.8 \pm 5.8$ | 46.3 |
| **RDP *iv*** | 450 | $171.7 \pm 6.0$ | $44.7 \pm 3.3$ | 23.8 |
| **RDP *v*** | 450 | $180.0 \pm 8.3$ | $41.8 \pm 7.3$ | 20.0 |
| **RDP *vi*** | 450 | $175.4 \pm 6.5$ | $41.0 \pm 7.4$ | /[a] |

[a] (Dans PRD vi, l'anneau et le disque sont connectés entre eux.)

Comme indiqué dans le Tableau A-4 et la Figure A-18 (a), nous étudions l'impact de G sur les résonances de Fano dans les RDPs, allant de 74,4 nm à 0 mn (connexion des structures). Pour simuler l'état connecté du RDP vi dans la Figure A-18 (a), un système RDP superposé avec un écart de -10 nm est pris en compte. En comparant les Figures A-18 (b) et (c), on peut constater que la principale différence dans la superposition spectrale des RDPs i et ii observée en expérimentation et le faible couplage de Fano en simulation est principalement due à la perte de signal ou au bruit du système pendant la mesure. Mis à part cette différence, les tracés expérimentaux et simulés illustrent tous deux une position stable des pics de Fano indépendante de la variation de l'écart. Ici, nous marquons les caractéristiques de Fano les plus distinctives avec des triangles pleins, et dans la Figure A-18 (d), nous présentons la distribution du champ électrique pour les principaux creux de Fano avec $G$ = 74,4 nm, 46,3 nm et 20,0 nm, respectivement. On constate que le mode de couplage pour ces creux reste constant entre un mode d'anneau liant avec m = 4 et le mode de disque dipolaire, où la force de couplage est progressivement augmentée avec l'augmentation

de Emax. À mesure que *G* diminue, finalement, le RDP *vi* connecté montre un ensemble de pics de résonance (par exemple, $\lambda_1$ = 717,1 nm, $\lambda_2$ = 769,4 nm et $\lambda_3$ = 841,6 nm en expérimentation), résultant de la redistribution des charges de surface par la jonction métallique au lieu d'un couplage entre le disque et l'anneau. De plus, des études de simulation dans la Figure A-19 (a) indiquent que le mode d'anneau dipolaire (en dehors de la plage de détection expérimentale) dans le régime du proche infrarouge subit un léger décalage vers le rouge à mesure que G diminue, où le RDP *vi* connecté montre à la place un large pic à $\lambda$ = ~2500 nm.
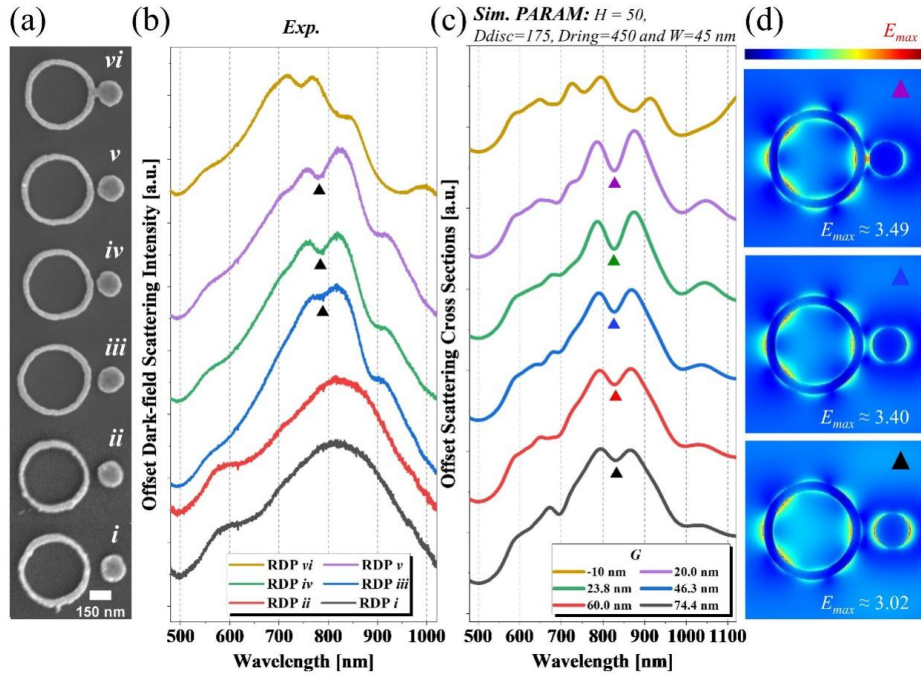


Figure A-18 (a) Images MEB en vue de dessus et (b) spectres de diffusion en champ sombre expérimentaux des six RDP avec un G décroissant jusqu'au RDP *vi*. (c) Sections efficaces de diffusion simulées des six RDP avec un écart d'extrémité à extrémité décroissant. Notez que les structures simulées sont modélisées de manière régulière. (d) Tracés de distribution du champ électrique avec un *G* de 74,4 nm, 46,3 nm et 20,0 nm, respectivement.

La discussion précédente démontre que les résonances de Fano dans les RDP présentant un *G* variable présentent des comportements de couplage similaires, justifiant une analyse quantitative de leur évolution spectrale par rapport à *G*. Dans la Figure A-19 (b), nous représentons les positions des creux de Fano et leurs rapports de contraste (CR) correspondants en fonction de la distance entre les gaps (*G*), basés sur les résultats expérimentaux (lignes solides) et les résultats de simulation (lignes en pointillés). Nous définissons le CR comme le rapport entre la différence d'intensité entre deux pics adjacents et leur creux de Fano intermédiaire et l'intensité des deux pics (c'est-à-dire $CR_1 = (I_{pic\text{-}gauche} - I_{creux}) / I_{pic\text{-}gauche}$ et $CR_2 = (I_{pic\text{-}droit} - I_{creux}) / I_{pic\text{-}droit}$), et calculons une valeur moyenne ($CR_{moyen} = (CR_1 + CR_2) / 2$) et des barres d'erreur (représentant $CR_1$ et $CR_2$) pour chaque point de données. En général, les tendances générales entre les tracés expérimentaux et simulés des positions des creux et des CR

restent cohérentes. Notamment, les comportements simulés de Fano présentent une position constante du creux sur les variations de gap à $\lambda = 828$ nm, et leurs CR suivent une décroissance exponentielle par rapport à G, s'ajustant à CR = -0,017 + 0,357 * $e^{(-0,020*G/nm)}$, comme représenté par la ligne pointillée bleue. La croissance exponentielle du couplage de Fano par rapport à la diminution de $G$ suggère que les RDP, en raison de leur structure unique par rapport aux RDC conventionnels, peuvent fonctionner comme des capteurs de nano-émetteurs, tels que la détection de diffusion Raman améliorée en surface non linéaire (SERS). Dans la Figure A-19 (c), nous présentons des analyses de SERS en comparant les spectres Raman de Rhodamine 6G (R6G) obtenus à partir de différentes structures, notamment un nanodisque unique, un nanoring, un RDP hybride avec un gap mutuel de 150 nm (RDP_G150) et un RDP avec un gap de 45 nm (RDP_G45), respectivement. Les images MEB correspondantes conservent une échelle de 200 nm cohérente. Les pics allant d'environ 1400 à environ 1700 cm$^{-1}$ correspondent aux modes vibratoires de l'étirement C-C de R6G. En comparant ces spectres, nous observons que le nanoring unique produit des signaux légèrement plus forts que le nanodisque unique, et leur structure hybride de RDP_G150 présente uniquement un signal de "superposition" en raison de l'effet de couplage plus faible. Cependant, une fois que l'écart est réduit, par exemple à 45 nm, une augmentation significative des signaux de vibration C-C de Raman peut être observée en raison d'un fort couplage de Fano. En général, ces résultats suggèrent des applications potentielles et fiables des RDP en tant que capteurs plasmoniques flexibles actifs. L'apparition/l'amélioration des résonances de Fano et des signaux SERS peuvent être surveillées en variant l'écart avec des contraintes appliquées une fois que les RDP sont transférées sur des substrats flexibles.
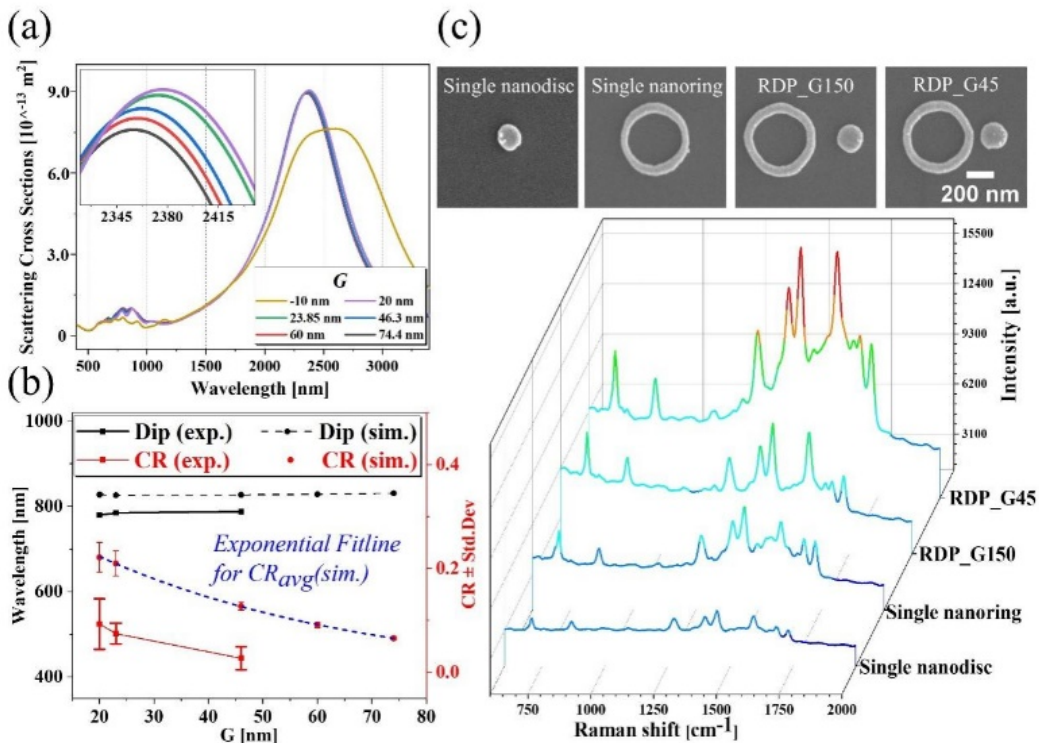


Figure A-19 (a) Section efficace de diffusion simulée des RDP avec des valeurs de G

variables de 74,4 nm jusqu'à un état connecté, et la figure en haut à gauche montre un léger décalage vers le rouge lorsque G diminue. (b) Études quantitatives sur les positions des creux et les CR (taux de contraste) dans les spectres expérimentaux (lignes pleines) et simulés (lignes en pointillés) pour les résonances de Fano dans la Figure A-18. (c) Ensemble de spectres Raman du R6G pour un seul nanodisque, un nanocercle, RDP_G150 et RDP_G45. L'échelle de barre pour les images MEB est de 200 nm.

## A.6 Conclusion

Dans cette thèse, nous avons réussi à fabriquer et caractériser des métasurfaces flexibles composées de réseaux de nanoanneaux (NR) en or et d'anneaux nanométriques elliptiques (ENR) intégrés dans du polydiméthylsiloxane (PDMS). Notre étude met en évidence le réglage actif des propriétés optiques dans les métasurfaces NR/ENR, comprenant des décalages spectraux plus importants de la résonance plasmonique de surface localisée (LSPR) et l'émergence de résonances de réseau de surface (SLR) sous contrainte, ainsi qu'un couplage Fano distinct entre les SLR à des valeurs de contrainte plus élevées. La faisabilité de la nanofabrication et la fiabilité des mesures optiques ont été confirmées par des caractérisations MEB ultérieures.

Plus précisément, nous démontrons l'altération de la forme in situ de NRs en or à paroi mince sur un PDMS étiré, confirmée par des mesures optiques/MEB in situ et une simulation numérique. Les NRs modifiant leur forme peuvent servir de capteur de contrainte efficace, présentant un décalage spectral significatif pour le mode principal de LSPR (2,85 nm/1% de contrainte), supérieur aux dispositifs flexibles à modification de l'espace entre les éléments précédents (jusqu'à 2 nm/1%). Les résultats de la simulation illustrent que de tels décalages spectraux importants proviennent du mode liant symétrique radialement dans les NRs, tandis que le pic latéral correspondant au mode liant asymétrique a tendance à diminuer lorsque la forme se développe sous contrainte.

De plus, nous étudions les comportements spectraux induits par la contrainte des réseaux carrés et triangulaires réguliers de ENR en or sur PDMS. L'évolution spectrale du réseau carré présente une forte dépendance de polarisation, montrant l'émergence de résonances de réseau de surface (SLR) et un couplage Fano significatif entre différentes SLR à des valeurs de contrainte plus élevées lorsque la polarisation transversale est appliquée pendant l'étirement. En revanche, les réseaux triangulaires présentent des comportements similaires sous les deux polarisations, y compris des décalages vers le rouge des SLR et des décalages vers le bleu des modes de LSPR. Ces résultats sont expliqués théoriquement par des simulations numériques, fournissant des informations sur la conception de métasurfaces en ce qui concerne les SLR et les LSPR sous contrainte. Ce travail illustre que les fonctionnalités des métasurfaces flexibles dépendent considérablement des agencements de réseau et suggère le potentiel de métasurfaces composées de nanoparticules anisotropes.

Enfin, nous démontrons le couplage de Fano dans des systèmes de anneau-disque-paire (RDP) en or sur des substrats rigides, où les caractéristiques de Fano résultent de l'interférence entre les pics discrets des anneaux multipolaires et le large continuum du disque dipolaire. Nos résultats indiquent qu'un rétrécissement de l'espace dans les RDP peut considérablement améliorer la qualité de ces résonances de Fano (par exemple, les rapports de contraste). Ces RDP hybrides suscitent un intérêt pour des recherches futures, telles que la surveillance des spectres en champ lointain et des signaux SERS dans des dispositifs flexibles à modification d'espace une fois qu'ils sont transférés sur un substrat extensible.

En conclusion, cette thèse présente une méthode de nanofabrication de pointe en combinant la flexibilité de la lithographie électronique (EBL) dans la conception de motifs et la possibilité de gravure humide dans le transfert. Les mesures optiques révèlent en outre l'évolution spectrale exceptionnelle des métasurfaces NR/ENR et leur potentiel pour les RDP, distincts des réseaux de disques/sphères traditionnels. Compte tenu des comportements spectraux forts et sensibles sous contrainte, cette thèse pose des bases solides pour des applications futures telles que la détection de contrainte, les écrans couleur flexibles et l'électronique portable.